

## Emergent rotational dynamics and optical properties of metal–organic frameworks

Gonzalez Nelson, A.M.

**DOI**

[10.4233/uuid:d7e16dc8-8892-4344-aba7-a754298ef8e2](https://doi.org/10.4233/uuid:d7e16dc8-8892-4344-aba7-a754298ef8e2)

**Publication date**

2021

**Document Version**

Final published version

**Citation (APA)**

Gonzalez Nelson, A. M. (2021). *Emergent rotational dynamics and optical properties of metal–organic frameworks*. [Dissertation (TU Delft), Delft University of Technology]. <https://doi.org/10.4233/uuid:d7e16dc8-8892-4344-aba7-a754298ef8e2>

**Important note**

To cite this publication, please use the final published version (if applicable).  
Please check the document version above.

**Copyright**

Other than for strictly personal use, it is not permitted to download, forward or distribute the text or part of it, without the consent of the author(s) and/or copyright holder(s), unless the work is under an open content license such as Creative Commons.

**Takedown policy**

Please contact us and provide details if you believe this document breaches copyrights.  
We will remove access to the work immediately and investigate your claim.



EMERGENT ROTATIONAL DYNAMICS  
AND OPTICAL PROPERTIES OF  
METAL-ORGANIC FRAMEWORKS

ADRIAN GONZALEZ-NELSON

# Emergent rotational dynamics and optical properties of metal-organic frameworks

Adrian Gonzalez-Nelson



# Emergent rotational dynamics and optical properties of metal-organic frameworks

Dissertation

for the purpose of obtaining the degree of doctor

at Delft University of Technology

by the authority of the Rector Magnificus Prof.dr.ir. T.H.J.J. van der Hagen

chair of the Board for Doctorates

to be defended publicly on

Thursday 20 May 2021 at 10:00

by

Adrian Manuel GONZALEZ NELSON

Master of Science in Chemical Engineering, Delft University of Technology, the Netherlands

born in Mexico City, Mexico

This dissertation has been approved by the promotor.

Composition of the doctoral committee:

|                          |  |
|--------------------------|--|
| Rector Magnificus,       | chairperson                              |
| Prof.dr. F. Kapteijn     | Delft University of Technology, promotor |
| Dr.ir. M.A. van der Veen | Delft University of Technology, promotor |
| Independent members:     |  |
| Prof.dr. F.-X. Coudert   | Chimie ParisTech-PSL, France             |
| Prof.dr. S. Furukawa     | Kyoto University, Japan                  |
| Prof.dr. B.L. Feringa    | University of Groningen                  |
| Prof.dr. F.C. Grozema    | Delft University of Technology           |
| Prof.dr. S.J. Picken     | Delft University of Technology           |



The work of Adrian Gonzalez-Nelson forms part of the research programme of DPI, NEWPOL project 731.015.506. Affiliation: DPI, P.O. Box 902, 5600 AX Eindhoven, the Netherlands.

Cover art by Adrián De la Cruz (@droste\_delacroix)

Printed by Ipskamp Printing, Enschede

ISBN: 978-94-6366-414-1

# Contents

|   |    |
|---|----|
| Preface .....   | 7  |
| Chapter 1   Rotational dynamics of linkers in metal–organic frameworks .....  | 11 |
| 1.1. Introduction .....   | 12 |
| 1.2. Types of Rotational Linker Dynamics .....  | 12 |
| 1.2.1. Type A: Complete Rotation .....  | 15 |
| 1.2.2. Type B: Partial Rotation .....   | 24 |
| 1.2.3. Type C: Rotation of Side Groups .....  | 27 |
| 1.2.4. Type D: Rotation of Mechanically Interlocked Molecules .....   | 28 |
| 1.3. Methods for the Study of Linker Dynamics .....   | 29 |
| 1.3.1. Solid-State Nuclear Magnetic Resonance (NMR) .....   | 29 |
| 1.3.2. Dielectric Spectroscopy .....  | 33 |
| 1.3.3. Terahertz Spectroscopy .....   | 35 |
| 1.3.4. Computational Methodologies .....  | 36 |
| 1.4. Implications of Rotational Dynamics on Applications of MOFs .....  | 39 |
| 1.4.1. Diffusion and Adsorption .....   | 39 |
| 1.4.2. Optical Properties .....   | 44 |
| 1.4.3. Mechanical Properties .....  | 45 |
| 1.5. Conclusions .....  | 46 |
| 1.6. References .....   | 48 |
| Chapter 2   Emergence of cooperative rotor dynamics in metal–organic frameworks via tuned steric interactions ..... | 55 |
| 2.1. Introduction .....   | 56 |
| 2.2. Results and discussion .....   | 56 |
| 2.3. Conclusions .....  | 65 |
| 2.4. Data and code availability .....   | 66 |
| 2.5. References .....   | 66 |

|  |     |
|--|-----|
| Chapter 3   Overcoming crystallinity limitations of aluminum metal–organic frameworks by oxalic acid modulated synthesis ..... | 99  |
| 3.1. Introduction.....   | 100 |
| 3.2. Results and discussion .....  | 101 |
| 3.3. Conclusions.....  | 105 |
| 3.4. References.....   | 106 |
| Chapter 4   Pillared cobalt metal–organic frameworks act as chromatic polarizers.....  | 141 |
| 4.1. Introduction.....   | 142 |
| 4.2. Results and discussion .....  | 143 |
| 4.3. Conclusions.....  | 147 |
| 4.4. References.....   | 147 |
| Summary .....  | 155 |
| Samenvatting .....   | 158 |
| Outlook.....   | 161 |
| Acknowledgements .....   | 163 |
| List of publications.....  | 164 |

# Preface

Metal–organic frameworks are stable porous crystalline materials whose structure consists of two basic types of molecular building blocks: one is metal-based, usually metal ions or (oxidic) clusters, and the other a polytopic organic ligand. Since they link at least two of the metal-based units, they are often referred to as linkers. These inorganic and organic building blocks are joined via coordination bonds, which are relatively strong and highly directional. This is what allows well-defined periodic structures, often with extraordinarily large void fractions, to be formed. It is precisely this versatility of combining building blocks that has allowed the MOF structure library to grow up to tens of thousands of frameworks in roughly two decades. Among their most appreciated properties, tunable pore sizes and surface properties have taken the spotlight. An important portion of MOF research has been invested in the interaction between molecules and the framework, aiming for applications such as gas storage and separation,<sup>1–3</sup> as well as catalysis,<sup>4,5</sup> drug delivery,<sup>6</sup> heat exchange,<sup>7</sup> and water harvesting.<sup>8</sup>

MOFs are considered soft or flexible materials, a characteristic that includes structural dynamics or large amplitude deformations.<sup>9–11</sup> This flexibility is usually attributed to the framework's topology and the degrees of freedom between bond angles in the organic linkers, or between the coordination bonds connecting them to the inorganic nodes. However, the linkers themselves may also have degrees of freedom allowing independent molecular dynamics, in particular in the form of rotation. This type of dynamics is particularly favorable in MOFs because their porous architectures often provide enough space for the rotation of a molecular fragment to occur. A striking example of the importance of rotational dynamics of linkers in MOFs is seen when guest molecules that are larger than the apparent pore size may still diffuse through a framework's pore network. This phenomenon, confirmed to be a direct result of linker rotation, has been described as 'door swinging' or 'gate opening'.<sup>12,13</sup>

Rotation of MOF linkers, one of the main topics of this thesis, is a relatively unexplored area of MOF research. However, it has experienced increased growth in interest because of two main reasons: First, linker rotation influences MOF properties, not only when guest molecule interactions are involved, but also in optical and mechanical properties. Development of our knowledge on MOF linker rotation is therefore essential for a more complete understanding of these materials' properties and how they may be modified to enhance a specific trait. Second, the exploitation of linkers' rotational freedom could potentially lead to important technological advances. The latter category may be divided into two general functions: conformational rotation and dynamic rotation. With conformational rotation, we consider cases such as the controllable orientation of linkers (for example, opening or closing pores by external stimuli, or controlling dipolar rotor fragments to obtain ferroelectric frameworks). With dynamic rotation, we can think of producing useful work, such as in molecular machines. This would involve achieving unidirectional rotation.<sup>14,15</sup> In Chapter 1, I present a review of the MOF linker dynamics literature, making a distinction between types of rotation, and including an overview of the techniques and applications of linker dynamics. In Chapter 2, I discuss the intricacies of linker functionalization on

their dynamic behavior in a family of MOFs that allows steric interactions between linkers. This study involved multiple experimental and computational techniques, from which we observed the emergence of inter-linker cooperative rotation. This is a particularly exciting discovery because properly designing materials for cooperative or correlated dynamics is an important milestone in the development of crystalline molecular machines.<sup>16,17</sup>

Even more detailed understanding of a MOF structure, including its dynamics, could be obtained if large single MOF crystals are available. Several important characterization techniques then become applicable. Perhaps the most fundamental is single-crystal XRD, which enables us to obtain the average periodic structure of a framework with great resolution, as well as, in some cases, more local structural details such as correlated defects or other types of domains.

There is a general tradeoff in the MOF stability scale, where more stable frameworks tend to form smaller crystals, and less stable ones form larger crystals. This is a natural result of the MOF formation reaction kinetics, and it is a problem that both I and other researchers investigating properties of stable MOFs have struggled with. Stable MOFs owe their stability to strong bonds between linker and metal, which also results in faster formation kinetics. Faster bond formation also implies that during synthesis, more nucleation will occur, leading to an overall smaller crystal size. On the other hand, less stable frameworks contain more labile bonds, which are broken more often during synthesis, leading to less nucleation and slower growth, both of which are essential for large single crystal synthesis. Chapter 3 will present a solution we found in the context of aluminum MOFs, which are renowned for their stability. By including an additional compound during synthesis that forms a relatively stable complex with unreacted aluminum cations in solution, we achieved a modulating effect that produced large single crystals of frameworks that are otherwise too small to manipulate.

In addition to structural studies, experiments involving functional properties of MOFs become more accessible if large single crystals are available. For example, the investigation of optical or electronic anisotropic properties that would rely on the ensemble of a crystal to a circuit or other type analyzer requiring a precise crystallographic direction. In the last chapter of this thesis, I show a part of my work that demonstrates the detection of visible light transmitted anisotropically through the crystal; a feat that would not be possible without crystals that are visible in a regular optical microscope. In this study, it becomes clear that the diversity and precision of MOF structures makes them excellent candidates to advance already established classes of technological materials. In this particular case, the use of two different linkers produces a framework with the appropriate tetragonal symmetry, where all metal-based chromophores ( $\text{Co}^{2+}$  in this case) are aligned in the same crystallographic direction, producing a rare and captivating optical dichroic effect.

## References

1. Suh, M. P., Park, H. J., Prasad, T. K. & Lim, D.-W. Hydrogen Storage in Metal–Organic Frameworks. *Chem. Rev.* **112**, 782–835 (2012).
2. Sumida, K., Rogow, D. L., Mason, J. A., McDonald, T. M., Bloch, E. D., Herm, Z. R., Bae, T.-H. & Long, J. R. Carbon Dioxide Capture in Metal–Organic Frameworks. *Chem. Rev.* **112**, 724–781 (2012).

3. Li, J.-R., Sculley, J. & Zhou, H.-C. Metal–Organic Frameworks for Separations. *Chem. Rev.* **112**, 869–932 (2012).
4. Yang, D. & Gates, B. C. Catalysis by Metal Organic Frameworks: Perspective and Suggestions for Future Research. *ACS Catal.* **9**, 1779–1798 (2019).
5. Bavykina, A., Kolobov, N., Khan, I. S., Bau, J. A., Ramirez, A. & Gascon, J. Metal-Organic Frameworks in Heterogeneous Catalysis: Recent Progress, New Trends, and Future Perspectives. *Chemical Reviews* vol. 120 8468–8535 (2020).
6. Horcajada, P., Gref, R., Baati, T., Allan, P. K., Maurin, G., Couvreur, P., Férey, G., Morris, R. E. & Serre, C. Metal-organic frameworks in biomedicine. *Chem. Rev.* **112**, 1232–1268 (2012).
7. de Lange, M. F., Verouden, K. J. F. M., Vlugt, T. J. H., Gascon, J. & Kapteijn, F. Adsorption-Driven Heat Pumps: The Potential of Metal–Organic Frameworks. *Chem. Rev.* **115**, 12205–12250 (2015).
8. Liu, X., Wang, X. & Kapteijn, F. Water and Metal-Organic Frameworks: From Interaction toward Utilization. *Chemical Reviews* vol. 120 8303–8377 (2020).
9. Coudert, F.-X. Responsive metal-organic frameworks and framework materials: Under pressure, taking the heat, in the spotlight, with friends. *Chem. Mater.* **27**, 1905–1916 (2015).
10. Schneemann, A., Bon, V., Schwedler, I., Senkovska, I., Kaskel, S. & Fischer, R. A. Flexible metal–organic frameworks. *Chem. Soc. Rev.* **43**, 6062–6096 (2014).
11. Horike, S., Shimomura, S. & Kitagawa, S. Soft porous crystals. *Nature Chemistry* vol. 1 695–704 (2009).
12. Moggach, S. A., Bennett, T. D. & Cheetham, A. K. The Effect of Pressure on ZIF-8: Increasing Pore Size with Pressure and the Formation of a High-Pressure Phase at 1.47 GPa. *Angew. Chemie Int. Ed.* **48**, 7087–7089 (2009).
13. Fairen-Jimenez, D., Moggach, S. A., Wharmby, M. T., Wright, P. A., Parsons, S. & Düren, T. Opening the Gate: Framework Flexibility in ZIF-8 Explored by Experiments and Simulations. *J. Am. Chem. Soc.* **133**, 8900–8902 (2011).
14. Danowski, W., Castiglioni, F., Sardjan, A. S., Krause, S., Pfeifer, L., Roke, D., Comotti, A., Browne, W. R. & Feringa, B. L. Visible-Light-Driven Rotation of Molecular Motors in a Dual-Function Metal–Organic Framework Enabled by Energy Transfer. *J. Am. Chem. Soc.* jacs.0c03063 (2020) doi:10.1021/jacs.0c03063.
15. Kottas, G. S., Clarke, L. I., Horinek, D. & Michl, J. Artificial Molecular Rotors. *Chem. Rev.* **105**, 1281–1376 (2005).
16. Aprahamian, I. The Future of Molecular Machines. *ACS Cent. Sci.* **6**, 347–358 (2020).
17. Vogelsberg, C. S. & Garcia-Garibay, M. A. Crystalline molecular machines: function, phase order, dimensionality, and composition. *Chem. Soc. Rev.* **41**, 1892–1910 (2012).



# Chapter 1

## Rotational dynamics of linkers in metal–organic frameworks

---

Among the numerous fascinating properties of metal–organic frameworks (MOFs), their rotational dynamics is perhaps one of the most intriguing, with clear consequences for adsorption and separation of molecules, as well as for optical and mechanical properties. A closer look at the rotational mobility in MOF linkers reveals that it is not only a considerably widespread phenomenon, but also a fairly diverse one. Still, the impact of these dynamics is often understated. In this chapter, the various mechanisms of linker rotation reported in the growing collection of literature are addressed, followed by a highlight of the methods currently used in their study, concluding with the impacts that such dynamics have on existing and future applications.

---

This chapter is based on the following publication:

Adrian Gonzalez-Nelson, François-Xavier Coudert, and Monique A. van der Veen, Rotational Dynamics of Linkers in Metal–Organic Frameworks. *Nanomaterials* **9**, 330 (2019)

### 1.1. Introduction

Metal–organic frameworks (MOFs) are ordered arrays of polytopic organic ligands, commonly called linkers, interconnecting metal-based inorganic building units via coordination bonds. The assembly of a large number of organic and inorganic building units is what enables a vast array of topologically diverse frameworks.<sup>1</sup> In particular, the choice and design of the organic linkers is an equally important means of endowing these crystalline materials with specific desired capabilities. Often, these organic components confer some type of flexibility, including rotational mobility.<sup>2</sup> Rotational motion in MOFs is a contrasting characteristic with respect to other ordered microporous materials, such as zeolites, which contain no intrinsic rotor components and are especially challenging to functionalize.

Rotor MOFs can be considered a subset of amphidynamic crystals: solids that combine high order with high molecular mobility.<sup>3</sup> In conventional amphidynamic crystals, molecular rotors are assembled in the crystal lattice via non-covalent interactions, and they usually must contain bulky groups that act as spacers to create enough free volume for rotation to occur. In MOFs, however, these needs are overcome as a result of the porosity that is attained via highly directional coordination bonds.

Rotational dynamics is bound to influence several aspects of MOF properties, perhaps most importantly their interaction with guest molecules. As an example, rotational mobility plays a central role in the fascinating behavior of the zeolitic imidazolate framework ZIF-8.<sup>4,5</sup> The linkers in this framework are known to aid in the diffusion of surprisingly large guest molecules through the otherwise small micropores, by swinging, or partially rotating. This gate-opening, as we shall see, occurs in a considerable variety of different rotor MOFs.

Additionally, the possibility to manufacture tailor-made molecular rotors in an ordered scaffold opens up a multitude of options for novel applications, such as sensors, stimuli-responsive materials,<sup>6</sup> and crystalline molecular machines.<sup>7</sup>

In the last years, an increasing number of papers have appeared that elucidate this type of flexibility in MOFs.<sup>8–12</sup> So far, no review on rotational linker dynamics of MOFs exists. Yet, rotation appears to be a rather common type of dynamics in this class of materials, with clear consequences for adsorption and separation of molecules, optical, and mechanical properties. This review begins by addressing the variety of linker rotational motions and their mechanisms (Section 1.2), followed by a highlight of the methods currently used in their study—including experimental and computational (Section 1.3), and finalizing with the impacts of such dynamics on MOF applications (Section 1.4).

### 1.2. Types of Rotational Linker Dynamics

Michl and coworkers<sup>13</sup> conceptualized rotational motions in molecules by defining them as rotor systems analogous to macroscopic machines:

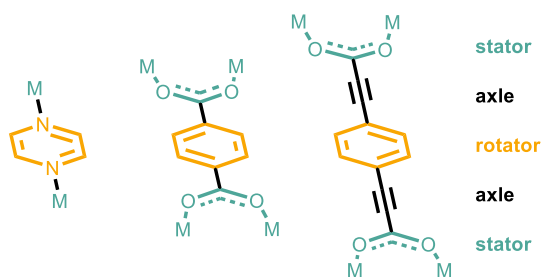
“Molecular rotor: a molecular system in which a molecule or part of a molecule rotates against another part of the molecule

Rotator: the part of the molecule or system that rotates against the rest

Stator: the stationary part of the system with respect to which the rotator turns

Axle: the portion of the molecule that carries the rotator and about which the rotator turns”

For the purpose of this review, we have adapted these definitions to metal–organic frameworks in a manner that will allow us to cover all relevant cases to the best of our knowledge. These definitions were proposed for the broader context of molecular rotors, yet they can be easily applied to metal–organic frameworks when we consider that the inorganic building units, together with the functional groups coordinated thereto, form the stator. Common axes, shown in Scheme 1.1, can be composed of one or more bonds, for example: the nitrogen–metal coordination bond, the covalent bond between the benzene ring and the carboxylate, or the ethynyl ( $-C\equiv C-$ ) group.



**Scheme 1.1.** Common types of axes in metal–organic framework (MOF) rotor linkers.

Within this frame, we categorized rotational dynamics of MOF linkers into four groups (also represented in Figure 1.1):

- A. Complete rotation
- B. Partial rotation
- C. Rotation of side groups
- D. Mechanically interlocked molecule rotation

The first three types of rotation have a common ground in that their axes are covalent bonds. Type A closely resembles the typical case of molecular rotors described by Michl *et al.*, where the axle crosses (approximately) the center of mass of the rotator, and connects it to two stators opposed to each other. We group in this category all rotors that are able to complete  $360^\circ$  torsions.

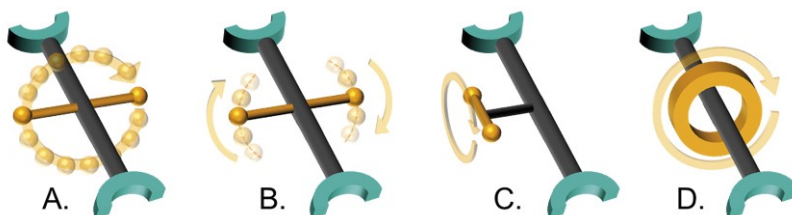


**Figure 1.1.** Illustration of the four types of rotational linker dynamics: **A.** Complete rotation, **B.** Partial rotation, **C.** Side group rotation, **D.** Mechanically interlocked molecule rotation.

Complete rotation often occurs in steps comprising a fraction of the  $360^\circ$  path, which are often referred to as jumps, hops or flips. The nature of these jumps is determined by the torsional potential of the rotor.<sup>13</sup> Figure 1.2 illustrates the torsional potential of a terephthalate rotor. It can be seen that minima in the potential energy are found every  $180^\circ$  of relative rotation between the *para*-phenylene rotator and the coordinated carboxylate stators. These minima determine the starting and ending position of the jumps, which must surpass an energetic barrier,  $E_b$ .

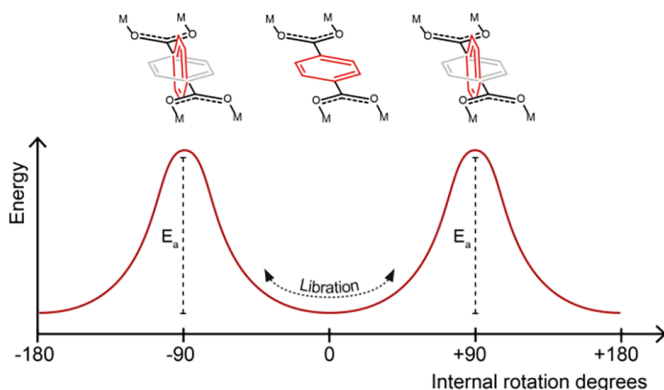


Figure 1.2. Torsional potential curve of a terephthalate rotor.

It is important to note that the jump angles will vary depending on symmetry and structural factors. Furthermore, when the thermal energy of the system is much higher than the energetic barrier, the rotor will rotate freely instead of performing discrete jumps, a scenario that is known as free or diffusional rotation.<sup>10</sup>

Type B rotation involves rotational motions that do not lead to full rotations. We have separated these from Type A since they can be considered a special case where the rotor is greatly hindered, either due to intrinsic or extrinsic restrictions, and  $360^\circ$  rotations do not occur. We can make an important division within this group:

- dynamics where the rotor performs rotational motions about a minimum in a potential energy well, or torsional potential minimum, which are called *librations*.
- dynamics where the rotor overcomes a maximum in potential energy and reaches a second conformation. For the sake of clarity, they will be referred to as *hops* in this section.

Librations are formally torsional vibrational modes, and as such their frequencies are largely determined by the shape of the potential well, while only their amplitude depends on thermal energy.<sup>13</sup> It should be understood that systems that present Type A motions may also exhibit Type B; for example, when a rotator undergoes librations as well as complete rotation. Librations of the phenylene rotator are shown in Figure 1.2 as the arrow centered on a local minimum, representing small-angle partial rotations without exceeding the torsional barrier. Hops, in contrast, do involve a thermally activated transition from one local minimum to another, in the same fashion as already described in Type A, with the condition that they do not achieve  $360^\circ$  rotations.

Due to these fundamental differences, librational and hopping dynamics fall in entirely different timescales. Still, they can in principle be related to each other in a molecular rotor. The librational frequency of a rotor may be considered approximately equal to the attempt frequency,<sup>13</sup> or pre-exponential factor, in the equation describing the rate of a thermally activated rotational hop:

$$\text{rate} = \omega_0 e^{\frac{-E_b}{kT}}, \quad (1)$$

where  $\omega_0$  is the attempt frequency,  $E_b$  is the energetic barrier for rotation,  $k$  is the Boltzmann constant, and  $T$  is the temperature.

It should be noted that the occurrence of rotational hopping entails the existence of librations, although the latter are often not detected. The inverse relation does not hold.

Type C will involve the few reported studies of meta-rotors, or rotors within MOF linkers. The defining characteristic of this group is that the axle and rotator do not play a role in the framework's connectivity; they are a side group on the linking struts. Therefore, the main linker component can be considered the stator, with the functional group attached to it via a covalent bond "axle".

Type D rotation involves systems where the rotator is a separate molecule that is mechanically interlocked to the axle. Here, only weak interactions—such as dispersion forces and hydrogen bonds—are the basis of contact between the two.

### 1.2.1. Type A: Complete Rotation

A list of rotor systems discussed in this sub-section can be found in Table 1.1, together with the relevant information regarding rotation mechanism and energy barriers. We will begin our review of Type A rotations with arguably the most common type of rotor in the MOF field: terephthalate (or 1,4-benzenedicarboxylate; 1,4-BDC) linkers.

The first account of complete rotational motion of linkers in MOFs was published by Gonzalez *et al.*,<sup>14</sup> where the dynamics of the phenylene units in the quintessential MOF-5 were examined. The authors transferred the use of solid-state deuterium nuclear magnetic resonance (NMR), which had so far been used to probe the dynamics of molecules within zeolites, microporous silica, and polymer backbones,<sup>15</sup> to the direct measurement of the dynamics of the perdeuterated phenylene in the terephthalate linkers. It was found that the phenylene groups are static at room temperature (within the timescale of the experiment, i.e., slower than  $\sim 10^3$  Hz), and that they undergo fast 180° rotations ( $\pi$ -flips) at 373 K. These results were later confirmed by Gould *et al.*,<sup>16</sup> who used the same two-fold exchange model to fit the  $^2\text{H}$  NMR data, and applied the Arrhenius relation to assign an activation energy of  $47.3 \pm 8.4$  kJ mol<sup>-1</sup>. This experimental activation energy corroborated the barrier of 52 kJ mol<sup>-1</sup> that had been predicted earlier for this framework using DFT (density functional theory) calculations,<sup>17</sup> where the 90° twist of the benzene ring with respect to the carboxylate plane was indeed found to be the maximum in the potential energy curve.

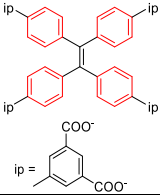
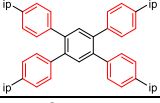
It should be remarked that the MOF-5 structure exerts little steric hindrance on the rotating phenylene rings,<sup>16</sup> and therefore the relatively high rotational barrier can be mainly attributed to

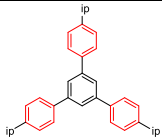
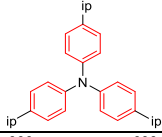
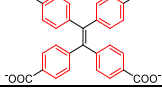
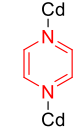
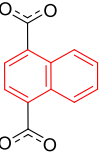
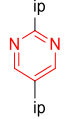
electronic effects. That is, the planar conformation of the terephthalate is stabilized through  $\pi$  electron delocalization, and a  $90^\circ$  rotation of the phenylene implies a complete loss of  $\pi$  system delocalization between the benzene ring and the carboxylate planes.<sup>10</sup>

The same mechanism of complete rotation has been observed in several other terephthalate-based MOFs, including the well-known MIL-47(V), MIL-53,<sup>18–20</sup> and UiO-66<sup>8,21,22</sup> families. The rotational barriers for all these systems are within 30–50 kJ mol<sup>-1</sup>, regardless of the metal centers, which suggests the barrier is in fact intrinsically determined by the linker, with some variations due to metal electronegativity and possible steric effects from the crystal lattice.

Similar findings were reported for the terephthalate rotor in the M<sub>2</sub>(1,4-BDC)<sub>2</sub>(DABCO) pillared MOFs (also known as DMOF series) that consist of 2-D sheets of divalent metal ions (M = Co<sup>2+</sup>, Zn<sup>2+</sup>, Ni<sup>2+</sup>, and Cu<sup>2+</sup>) in the paddlewheel secondary building unit (SBU) linked by terephthalate and pillared by 1,4-diazabicyclo[2.2.2]octane (DABCO) to a 3D structure. With <sup>2</sup>H NMR it was also shown that the phenylene groups performed  $\pi$ -flipping motions that were largely independent of which metal cations were present.<sup>23</sup> The activation energies derived from this <sup>2</sup>H NMR study were in the range of 32–36 kJ mol<sup>-1</sup>.

**Table 1.1. Type A rotor linkers and their rotational barriers.**

| MOF        | Rotator   | Type                       | T/K*                      | Barrier /<br>kJ mol <sup>-1</sup> | $\omega_0$ /Hz                            | Method                                  | Ref. |
|------------|---|----------------------------|---------------------------|-----------------------------------|---|---|------|
| MOF-5      |    | $\pi$ -flip                | 363–435                   | 47.3 $\pm$<br>8.4                 | $1.60 \times 10^{12}$                     | <sup>2</sup> H NMR                      | 16   |
| MOF-5      |   | $\pi$ -flip                | -                         | 51.8                              | -   | DFT                                     | 17   |
| MIL-53(Cr) |   | $\pi$ -flip                | 333–453                   | 41                                | $1.26 \times 10^{11}$                     | <sup>2</sup> H NMR                      | 18   |
| MIL-47(V)  |   | $\pi$ -flip                | 373–483                   | 45                                | $8.80 \times 10^{10}$                     | <sup>2</sup> H NMR                      | 18   |
| MIL-53(Al) |  | $\pi$ -flip                | 359–492                   | 37 $\pm$ 1                        | $0.6 \times 10^{10}$                      | <sup>2</sup> H NMR                      | 19   |
| UiO-66(Zr) |  | $\pi$ -flip                | 213–403                   | 30 $\pm$ 2                        | $0.5 \pm 0.8 \times 10^{12}$              | <sup>2</sup> H NMR                      | 22   |
| MIL-140    |   | $\pi$ -flip                | -                         | 27.4                              | -   | DFT                                     | 24   |
| DMOF       |   | $\pi$ -flip                | 253–359                   | 32–36                             | $0.3\text{--}10 \times 10^{11}$           | <sup>2</sup> H NMR                      | 23   |
| MFM-180    |  | 4-site                     | 223–503                   | 26; 28                            | $1.6 \times 10^{11}$ ;<br>$3 \times 10^7$ | <sup>2</sup> H NMR                      | 9    |
| MFM-181    |  | 4-site                     | 153–473                   | 20; 34                            | $9 \times 10^{11}$ ; $4.6 \times 10^8$    | <sup>2</sup> H NMR                      | 9    |
| BODCA-MOF  |  | 6-site;<br>3-site;<br>free | 6–12;<br>12–50;<br>50–292 | 0.8                               | $4.7 \times 10^{10}$                      | <sup>1</sup> H T <sub>1</sub><br>relax. | 10   |

|   |   |                   |         |        |                                      |                                       |    |
|---|---|-------------------|---------|--------|--------------------------------------|---------------------------------------|----|
| <b>MFM-112a</b>   |    | 4-site            | 123–203 | 8.6    | $3 \times 10^8$ ; $18 \times 10^8$   | $^2\text{H}$ NMR                      | 12 |
| <b>MFM-115a</b>   |    | 4-site;<br>6-site | 203–315 | 14; 40 | $2 \times 10^8$ ; $5 \times 10^{12}$ | $^2\text{H}$ NMR                      | 12 |
| <b>Zn<sub>2</sub>(TCPE)<br/>(DEF)<sub>2</sub></b>               |    | $\pi$ -flip       | 300–421 | 43(6)  | $2.2 \times 10^{11}$                 | $^2\text{H}$ NMR                      | 25 |
| <b>CdNa(2-<br/>stp)(pyz)<sub>0.5</sub>(<br/>H<sub>2</sub>O)</b> |    | 4-site            | 193–293 | 7.7    | $2.40 \times 10^6$                   | $^2\text{H}$ NMR                      | 26 |
| <b>Zn<sub>2</sub>(1,4-<br/>ndc)<sub>2</sub>(DABC<br/>O)</b>     |    | 4-site            | 193–293 | 53     | Not reported                         | $^2\text{H}$ NMR                      | 26 |
| <b>UTSA-76</b>  |    | $\pi$ -flip       | -       | 8.2    | -                                    | DFT                                   | 27 |
| <b>NOTT-101a</b>  |  | $\pi$ -flip       | -       | 20.2   | -                                    | DFT                                   | 27 |
| <b>UCLA-R3</b>  | Figure 1.6  | 3-site            | -       | 56.5   | $8.7 \times 10^{15}$                 | $^2\text{H}$ NMR                      | -  |
| <b>Cu(bbcbo)<br/>(H<sub>2</sub>O)</b>                           | Scheme 1.2  | -                 | -       | 15.5   | -                                    | DFT                                   | 28 |
| <b>Zn-BPEB</b>  | Scheme 1.2  | free              | 150–293 | 2      | $2.2 \times 10^{12}$                 | $^1\text{H}$ T <sub>1</sub><br>relax. | 29 |

\*Temperature range in which the experiments were performed.

Analysis of terephthalate rotors has been extended to cases where the pores are occupied with guest molecules. The presence of molecules in the pores is expected to have a significant effect on the mobility of the linkers lining the pores due to weak interactions as well as steric effects. In the case of MIL-53(Al), the effect of xylene loading was analyzed and found to hinder the phenylene  $\pi$  flips greatly, increasing the activation energy from 37 to above 50 kJ mol<sup>-1</sup>.<sup>19</sup> The  $\pi$ -flipping of UiO-66(Zr) was found to have a strong linear dependence on benzene loading, increasing from 30 kJ mol<sup>-1</sup> in the guest-free framework, to 48 kJ mol<sup>-1</sup> with the highest loading of molecules.<sup>21</sup> Likewise, in the experimental studies of unfunctionalized DMOF systems described

above, the presence of *N,N*-dimethylformamide inside the pores increased the activation energy from 32–36 to 47–55 kJ mol<sup>-1</sup>.<sup>23</sup>

In the Zn-DMOF family, DFT calculations were also employed to model the rotational energy barrier for terephthalate linkers with a series of functionalizations, as well as for 1,4-naphthalenedicarboxylate (1,4-NDC).<sup>30</sup> Using fragment models to approximate the MOF structure, the potential energy surface was scanned while rotating the phenylene group. Drastic differences in estimated rotational barriers were found when analyzing different substituent groups on the benzene ring, ranging from 10 to 58 kJ mol<sup>-1</sup>. The authors attributed the decrease in barrier for rotation to the electrostatic repulsion between electronegative atoms as ring substituents and the oxygen atoms of the carboxylate groups, yet the electron donating/withdrawing effect of the groups was not considered.

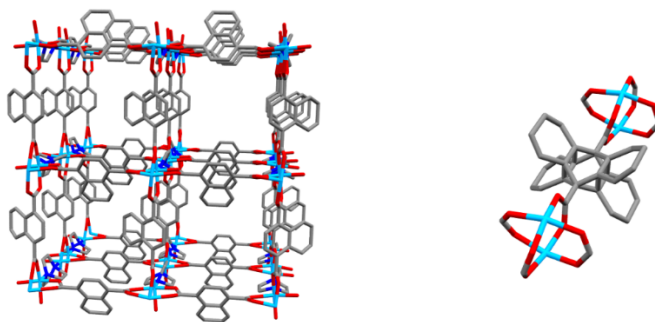


**Figure 1.3.** Structure of pillared DMOF with 1,4-NDC rotors. Adapted with permission from ref. 26. Copyright Wiley-VCH, 2006.

Only the barriers for terephthalate and 1,4-NDC (58 and 22 kJ mol<sup>-1</sup>, respectively) could be compared to available experimental data; the calculation of the terephthalate resulted in an overestimation the rotational barrier of 36 kJ mol<sup>-1</sup> reported by Khudozhitkov *et al.*<sup>23</sup>, while for 1,4-NDC the model underestimated the 53 kJ mol<sup>-1</sup> found previously by Horike *et al.*<sup>26</sup>. The latter <sup>2</sup>H NMR study assumed four-site jumps of the 1,4-NDC rotor, based on their observation of four disorder positions of the rotator in the single crystal X-ray diffraction (XRD) structure (Figure 1.3).

Regardless of the substantial underestimation of the barrier of 1,4-NDC, the computational study confirmed the presence of two maxima in the torsional potential of this rotor, one at 0° and the other at 90° with respect to the carboxylate plane. The energy wells between these maxima in a 360° rotation correspond to the four sites that were used to model the <sup>2</sup>H NMR spectra.

Horike *et al.* also showed that rotational dynamics occur in linkers that are not dicarboxylates.<sup>26</sup> Initially, single crystal XRD studies indicated an equally disordered pyrazine ring over two positions, suggesting that this ligand completes a full 360° rotation in four steps, or jumps, around the N–N axis (precisely at 0°, 76.4°, 180°, and 256.4°) (Figure 1.4a). Therefore, in contrast with the terephthalate rotor  $\pi$ -flip cases, a four-site jump model was used to fit the <sup>2</sup>H NMR spectra, and an activation energy of 7.7 kJ mol<sup>-1</sup> was derived.

Such a striking difference in energetic barriers for rotation between this rotor and the various phenylene-based systems is not surprising. The fact the axle of the pyrazine rotator is a  $\sigma$  bond with no double bond character implies that this type of coordination will exert less electronic limitations than the terephthalate rotors, which have a certain double bond character in the C–C axle due to  $\pi$  electron delocalization.

It is interesting to note that only one activation energy was determined, even though the two sets of jumps used for analysis are geometrically unequal (two short jumps and two large jumps), suggesting the possibility of two barriers. Therefore, it could be inferred that the jumps are either energetically degenerate, or that the differences are too small to be detected.

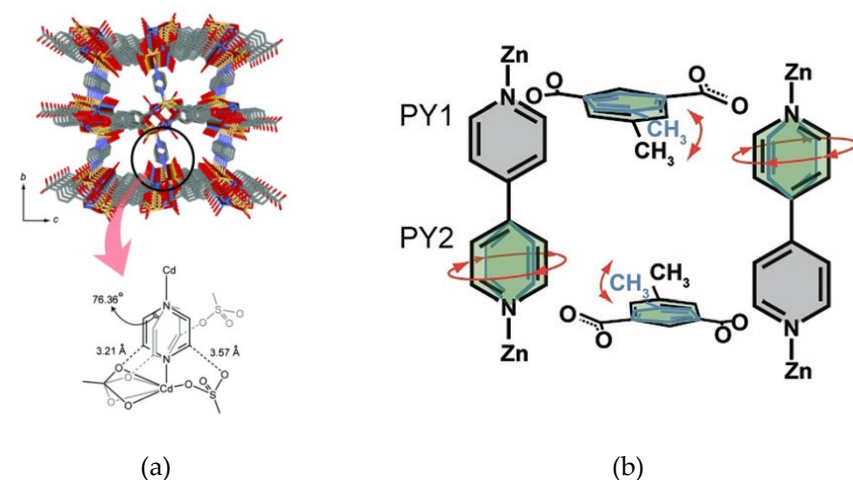


**Figure 1.1.** Structure of two N-linker rotor-based MOFs. (a)  $\text{CdNa}(2\text{-stp})(\text{pyz})0.5(\text{H}_2\text{O})$ , with an illustration of the two disorder positions of the linker; (b) 2D stacked framework,  $\text{Zn}(5\text{-Me-isophthalate})(\text{bipyridine})$ . Reproduced with permission from refs. 26 and 31. Copyright Wiley-VCH, 2006. Copyright Wiley-VCH, 2018.

Inukai *et al.* have researched dynamics of a different type of two-linker 2D stacked framework material,  $\text{Zn}(5\text{-X-isophthalate})(\text{bipyridine})$ , where X stands for methyl, nitro, or methoxy groups.<sup>31,32</sup> These systems were studied with  $^2\text{H}$  NMR to describe the rotational dynamics of each type of ligand. The 4,4'-bipyridine pillar's dynamics were found to be fairly complex (see Figure 1.1b), and dependent on the functional group used on the dicarboxylic linker. With the presence of methyl and nitro groups, one of the rings of the bipyridine was measured to be static, since the functional group of the isophthalate greatly hinders its rotation. The other pyridine ring, however, performed full rotations through a combination of  $\pi$ -flips and 4-site jumps. Unfortunately, no activation energies were reported, and thus no comparison may be made with respect to other N-donor ligands.

The use of 5-methoxyisophthalate, in contrast, brought about enough steric hindrance to block the rotation of both pyridine rings simultaneously. The dynamics of the angled dicarboxylate linker are an interesting example of incomplete rotations and will be addressed in Type B.

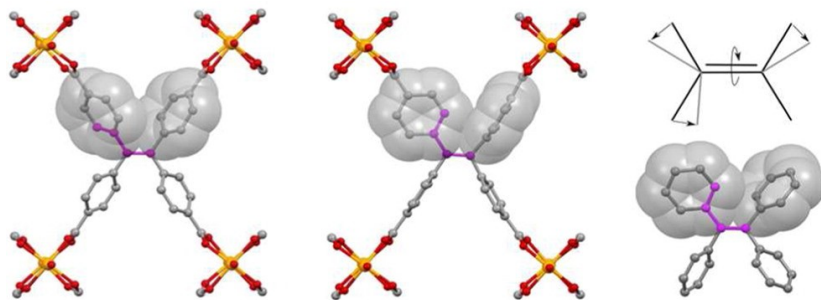


**Figure 1.2.** Linker conformation in tetra(4-carboxy)phenylethylene-based MOF, depicting steric hindrance from neighboring rings (left and center). The comparative case of a free tetraphenylethylene molecule is shown on the right. Reproduced with permission from ref 25. Copyright American Chemical Society, 2012.

Shustova *et al.* investigated phenylene dynamics in a tetra(4-carboxy)phenylethylene-based MOF,<sup>25</sup> whose linker structure is depicted in Figure 1.2. A combined  $^2\text{H}$  solid-state NMR and DFT study revealed that the phenylene rotators undergo rotations via  $\pi$ -flips, with an activation energy of  $43 \text{ kJ mol}^{-1}$ . Although such a high barrier is within the range of terephthalate rotors that we have discussed previously, a comparison of the computed rotational barrier in model molecules (including styrene, benzoic acid, and tetraphenylethylene) led the authors to conclude that, in this case, an important fraction of the rotational barrier is of steric origin. Since the four arms of the linker are tethered to metal nodes, the core is barred from deformations that would otherwise allow for one phenylene to rotate with less interaction with its neighbor (as was observed in the free tetraphenylethylene molecule; right side of Figure 1.2).

A case of four-site jump rotation of phenylene groups was recently reported in two octacarboxylate frameworks, MFM-180 and MFM-181 (Figure 1.3a).<sup>9</sup> Due to their branched structure, both linkers contain only one type of rotator that can undergo complete rotations: a *p*-phenylene in each arm connecting the core of the linker (ethylenyl or benzene ring, respectively) with the benzenedicarboxylate terminal rings.

Detailed analysis of the  $^2\text{H}$  NMR line shape evolution along a wide temperature range allowed the authors to conclude that the mechanism for complete rotation involved a four-site jump-exchange in both MOFs. The four jumps, however, are not equal, since two different rate constants could be derived from the NMR data. In both cases, one of the jumps involves a smaller angle partial rotation and is even activated at 100 K ( $\Delta\phi_1$  jump angle indicated in Figure 1.3b with a green arrow), while a second, wider motion ( $\Delta\phi_2$ ), was only activated at 330 K, allowing for full-rotational movement at these higher temperatures (see blue arrow in Figure 1.3b). Because of the phenylene group's  $C_2$  symmetry,  $\Delta\phi_1$  and  $\Delta\phi_2$  occur twice within a complete  $360^\circ$  rotation.

A closer look at each linker's structure and the possible interactions of the rotating phenylene with neighboring rings revealed the likely origins of such a complex rotational behavior. On the one hand, the smaller barrier for  $\Delta\phi_1$  was attributed to steric hindrance from the site marked with a green arrow in Figure 1.4, where the structural differences explain the large difference in  $\Delta\phi_1$  jump rates between both MOFs. The large barrier for  $\Delta\phi_2$ , on the other hand, which is activated

at approximately 330 K in both frameworks, was proposed to originate from the interactions with the neighbor ring in the vicinity, marked with a blue arrow in Figure 1.4, which is similar in both MOFs.

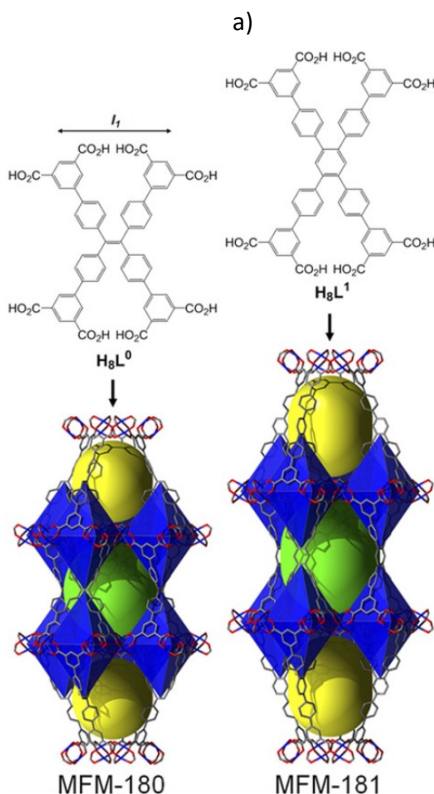


**Figure 1.3.** (a) Structure of MFM-180 and MFM-181 and their respective linkers; (b) rotational trajectory of the *para*-phenylene rotators. Reproduced from ref. 9.

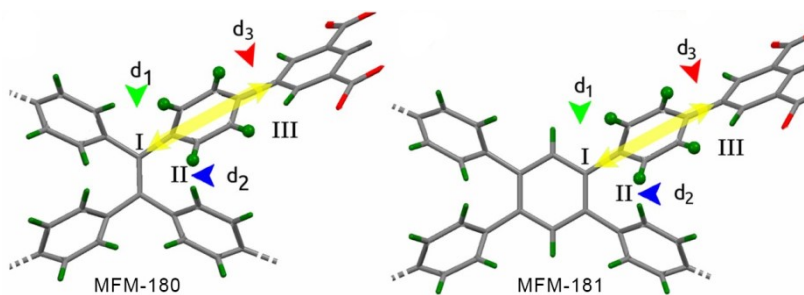


**Figure 1.4.** Rotator environment in MFM-180 and MFM-181. The colored arrows mark the closest steric interactions. Reproduced from ref. 9.

Another branched linker MOF with complete rotational motions was studied in a similar fashion. Three different tri-branched, hexacarboxylate linkers were used to build isostructural frameworks.<sup>12</sup> Two of the members of this series were found to perform full rotations (Figure 1.5, left and center). The third ligand's atracenyliene rotors (Figure 1.5, right), in contrast, could not achieve complete rotations due to its highly hindered environment, and will be discussed in Type B rotations. MFM-112 and MFM-115 differ in that the linker of the former has a benzene ring core, while the latter has a nitrogen core connecting the three dicarboxylate-terminated branches. These systems closely resemble the MFM-180 and -181 previously discussed in that the rotator is a phenylene group connecting the terminal ring to the core of the linker. Likewise, these rotors undergo four-site jumps to complete a 360° rotation.

The authors determined that the *p*-phenylene groups in MFM-115 require significantly more thermal energy to rotate than in MFM-112, which should be expected due to the shorter distances between rotators owing to the smaller center group. Additionally, two different modes of rotation were observed in MFM-115: a slow rotation with a barrier of 14 kJ mol<sup>-1</sup> below 283 K, and a faster motion with higher energy barrier (40 kJ mol<sup>-1</sup>) above 283 K. The authors hypothesized that the low temperature motion corresponds to the collective, gearlike rotation of the three phenylene groups. It is feasible that concerted motion would result in the diminishment of steric hindrance, as well as lower rates of rotation. At higher temperatures, concerted motion becomes less likely, thus increasing the steric hindrance from neighboring rings leading to a higher energetic barrier (40 kJ mol<sup>-1</sup>).



**Figure 1.5.** Structure of rotor linkers used in MFM-112, -115, and -132. Reproduced with permission from ref. 12. <https://pubs.acs.org/doi/10.1021/jacs.7b05453>; further permissions should be directed to the ACS. Copyright American Chemical Society, 2017.

Garcia-Garibay's group reported a framework containing a triptycene rotator with triple bond axles in a Zn-based pillared architecture (see Figure 1.6).<sup>33</sup> Although the triple bond axles were expected to lead to a free rotor system, solvent DMF (*N,N*-dimethylformamide) molecules present in the pores of the MOF were found to strongly hinder the rotation, leading to an apparent barrier of 56.5 kJ mol<sup>-1</sup>.

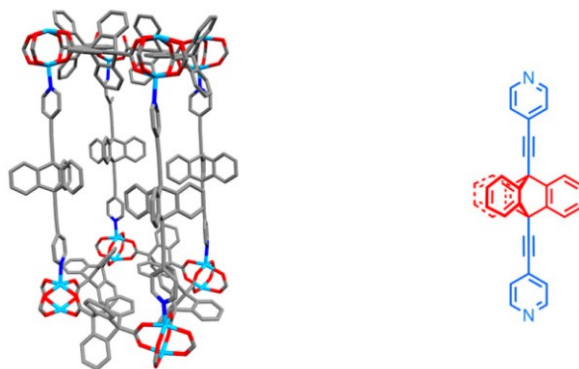
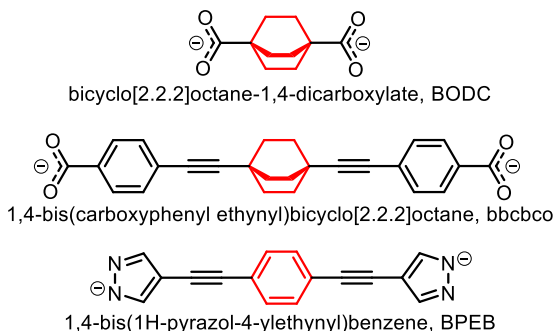


**Figure 1.6.** Crystal structure of UCLA-R3 (left); the triptycene rotator is shown in red (right). Adapted with permission from ref. 33. Copyright American Chemical Society, 2016.

Aiming to achieve lower rotational energy barriers in MOF rotor systems, Garcia-Garibay's research group explored a ditopic linker analogous in connectivity length to the terephthalate, 1,4-bicyclo[2.2.2]octane dicarboxylate (BODC, see Scheme 1.2, top). BODC linkers, in contrast to terephthalates, present no  $\pi$  electron delocalization to provide a double bond character to the C–C bond between rotator and stator (carboxylate). Additionally, the combined symmetry of the  $C_3$  rotor (bicyclo[2.2.2]octane, BCO) and the  $C_2$  stators leads to sixfold degenerate energy potential, meaning that the rotor should be able to perform a full rotation in six jumps of equal activation energy. Altogether, it was demonstrated that the BODC rotors have much lower rotational barriers than terephthalates, emphasized by the fact that unrestricted diffusional rotation was observed down to ca. 20 K, although with increasing contributions of six-fold exchange. Below 13 K, three-fold rotation was observed, while at 6 K the slow exchange regime was detected (frequencies lower than 1 kHz). Since the rotation of the BCO groups was too fast to derive appropriate rate constants from line shape analysis, the authors performed  $^2\text{H}$  and  $^1\text{H}$   $T_1$  relaxation measurements, which yielded activation energies of 0.5–0.77 kJ mol $^{-1}$ .

Another framework containing a bicyclo[2.2.2]octane rotator was constructed by Bastien *et al.*<sup>28</sup> The remarkable length of the axle (linker depicted in Scheme 1.2, center) would have meant that all steric interactions might have been avoided, thus achieving free rotation. However, the framework was found to be interpenetrated, and therefore the expected low rotational barrier could not be achieved. A barrier of 15.5 kJ mol $^{-1}$  was estimated computationally, mostly caused by steric hindrance from neighboring rotators.

A different approach to achieving free rotation in MOF linkers was presented by Bracco *et al.*,<sup>29</sup> where a *p*-phenylene unit was selected as rotator with a triple bond axle coordinated to  $\text{Zn}^{2+}$  centers via pyrazole groups (Scheme 1.2, bottom). Using  $^2\text{H}$  NMR, very fast  $\pi$ -flips were observed down to 150 K, such that the rate constants of rotation could not be determined through line shape modeling. Instead, the  $^1\text{H}$  spin-lattice relaxation times were measured and the Arrhenius equation was used to determine an activation energy of 2 kJ mol $^{-1}$ .



**Scheme 1.2.** Low-barrier rotor linkers. Rotor fragments are shown in red.

Although the majority of cases reported in the literature involve rotation of phenylene groups in terephthalate linkers, several other cases illustrated here show that this type of motion is quite diverse. The rotational barriers associated to complete rotations in MOFs can be found in a wide range, from less than  $1 \text{ kJ mol}^{-1}$  to close to  $50 \text{ kJ mol}^{-1}$ .

We can observe that the great diversity in rotor systems and their mechanisms of rotation arise mainly from variations in the electronic configuration of the rotor and the steric environment in frameworks. The location of maxima and minima along the torsional potential curve determine the partial steps that a rotor must follow, while the height of rotational barriers is related to the rate of rotation. In addition, guest molecules have been shown to significantly hinder rotational dynamics of linkers, a property of great importance for adsorption applications which will be addressed in Section 1.4.

### 1.2.2. Type B: Partial Rotation

Librational motions in MOFs often fall within the THz frequency region, and are thus detectable with spectroscopic techniques such as inelastic neutron scattering and far-infrared spectroscopy. The combination of detailed  $^2\text{H}$  NMR and spin-lattice relaxation analysis, which together can probe an enormous range of frequencies, have established that systems that perform complete rotations may also present librational motions within the same molecular rotator fragment, such as in the case of UiO-66.<sup>8</sup>

Soft modes attributed to libration of phenylene groups in other terephthalate-based frameworks have been discussed in several instances. In the case of MOF-5, this type of motion was initially identified using inelastic neutron scattering and *ab initio* calculations.<sup>17</sup> The well-known “breathing” MIL-53 was suspected to obtain its intriguing bi-stable pore configuration (narrow pore, large pore) as a result of these twisting modes.<sup>34</sup>

Similarly to MIL-53, the MIL-140A framework is built from inorganic 1D chains and terephthalate linkers. However, within the latter structure, there are two different environments for the linkers (A and B, see Figure 1.7). Using a combination of neutron scattering, far-infrared spectroscopy, and *ab initio* quantum chemical calculations, researchers unraveled the contributions of librational motions of phenylene groups in the low-frequency vibrational spectrum.<sup>24</sup> It was found

that each type of linker had phenylene twisting modes at different frequencies, and that the B linker's rotation required higher energies due to steric hindrance of the adjacent linkers. In fact, supporting single-point DFT calculations showed that complete rotation of the hindered B linker is likely impossible.

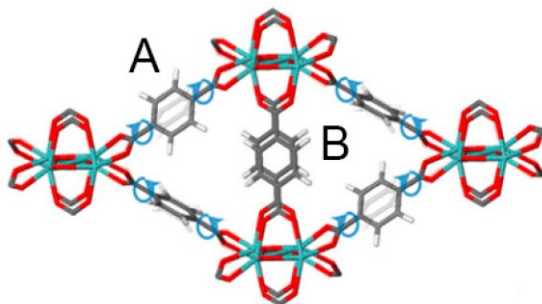


**Figure 1.7.** Structure of MIL-140A, terephthalate linkers in two different positions (A and B). Reproduced with permission from ref. 24. Copyright American Physical Society, 2017.

Revisiting the MFM hexacarboxylate series discussed in Type A, the third member that Yan and co-workers designed, MFM-132, contains a 9,10-anthracenylene moiety on each of the three arms (Figure 1.5, right). Their  $^2\text{H}$  NMR analysis demonstrated that these rotators were not able to perform full rotations even at high temperatures (ca. 573 K) due to the steric hindrance from adjacent groups, yet a small amplitude libration of  $32^\circ$  was observed.

In some instances, the impediment to rotate is a result of a ligand coordination geometry that deviates from  $180^\circ$ . Although not as many such cases have been reported, a remarkable example is found in zeolitic imidazolate frameworks (ZIFs). An imidazolate ligand's bridging coordination angle is approximately  $145^\circ$ , which means any large amplitude rotations will be strongly hampered by the directionality of the coordination bond (see Figure 1.8). However, ample evidence has shown that even small amplitude rotational motions are responsible for the remarkable capacity of MOFs such as ZIF-8 to admit molecules that are seemingly too large to fit through the pore windows.<sup>35</sup>

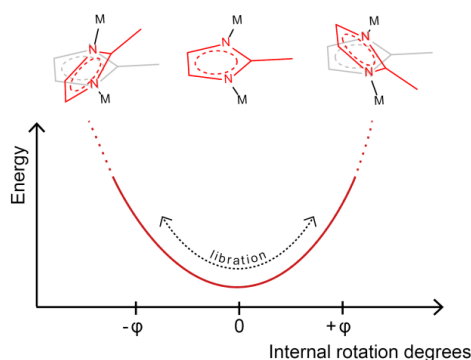


**Figure 1.8.** Illustration of the torsional potential for coordinated imidazolate linkers (as in zeolitic imidazolate framework 8 (ZIF-8)). Large amplitude rotations are hampered by the connectivity angle, yet small-amplitude librations are possible.

The rotational dynamics of the 2-methylimidazolate linker have been studied in detail using  $^2\text{H}$  NMR,<sup>11,36</sup> and multiple modes of rotation have been identified, including fast, small-angle librations (shaded in orange in Figure 1.9a), small-amplitude two-site hopping (blue arrows in Figure 1.9a), and slow, large-amplitude swinging between two sites (Figure 1.9b). In the case of ZIFs, the term swinging has been used to describe partial rotational motions indistinctly, even though they may have different characteristics (e.g., librations or hops). Strikingly different energy barriers have been assigned to the latter two rotational motions:  $1.5\text{ kJ mol}^{-1}$  and  $50\text{--}60\text{ kJ mol}^{-1}$ , respectively. The torsional potential is thus certainly more complex than what is described in Figure 1.8, likely with local minima at different torsion angles.

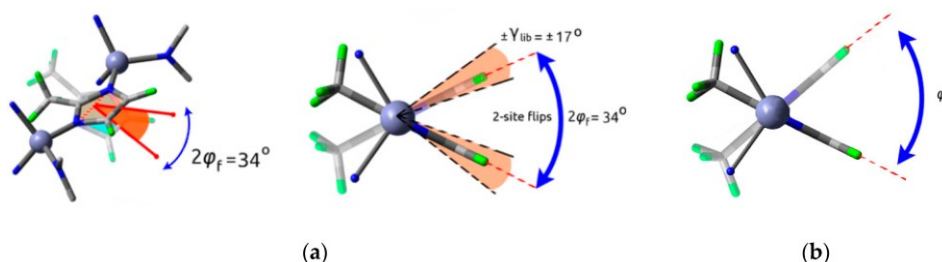
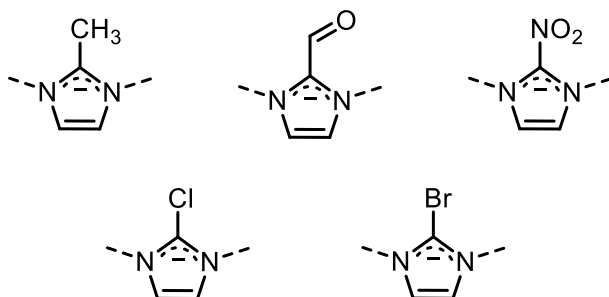


**Figure 1.9.** Diverse dynamics of 2-methylimidazolate linker in ZIF-8. Left: Small-amplitude two-site hopping ( $34^\circ$ ) and fast librations ( $\pm 17^\circ$ ) centered on both hop positions; Right: slow, large-amplitude swing. Adapted with permission from ref. 36.

Structural transitions in isostructural ZIFs have been studied to understand their behavior upon molecule uptake, taking into consideration the effect that the choice of functional group (methyl, carboxaldehyde, and nitro, shown in Scheme 1.3) has on the dynamic responses.<sup>37</sup> Researchers have found that, when subjected to alcohol guest molecules under high hydrostatic pressures, the framework responds by adopting a high-pressure conformation where the imidazolate linkers swing to varying degrees depending on the functional group chosen to substitute the 2- position of the ring. This collective swinging motion leads to changes in pore volume and pore window diameters, with the methyl- and aldehyde-containing linkers this leads to a larger pore window, while the nitro-functionalized linkers rotate in the opposite direction, leading to a smaller pore window.



**Scheme 1.3.** Imidazolate linkers used in ZIF-8 isorecticular frameworks.

Interest in the effect of functionalization on the imidazolate linker's rotational flexibility has motivated a recent study comparing the behavior of ZIF-8 with its 2-Cl and 2-Br functionalized isorecticular analogues.<sup>38</sup> Using first-principles molecular dynamics, the authors found that the 2-chloroimidazolate linkers responded to N<sub>2</sub> adsorption by swinging in a similar manner as the 2-methylimidazolate, while the bromo-substituted linker does not rotate, showing that the framework is more rigid. It was proposed that the bulkiness of the bromo group, and not its electronic effects on the coordination bond, is accountable for this lack of flexibility.

Inukai and coworkers developed a MOF that combines both full rotation of pyridine rings (already discussed in Type A rotation) and libration of a secondary linker.<sup>31</sup> The 5-methylisophthalate group resembles the previously discussed imidazolate linker in that the connectivity is not linear, but angular (120° in this case). Due to this, 1,3-phenylenes cannot perform complete rotations, yet they can still have rotational dynamics in the form of librations. <sup>2</sup>H NMR evidence showed that the linker in this system indeed librates, aiding in guest molecule transport by widening the pore window.

The discussed cases of partial rotational motions should provide evidence that this is a broad category of dynamics, encompassing low-energy vibrational rotations that are expected to occur in any linker with rotational degrees of freedom, and hindered, thermally activated hops along local minima in the torsional potential. In contrast with full rotations, partial rotations have been documented in frameworks with angular linkers. In particular, the importance of this type of dynamics in frameworks such as the prominent ZIF-8 will be highlighted in Section 1.4.

### 1.2.3. Type C: Rotation of Side Groups

A third type of rotational motion occurring in the linker consists in the rotation of a side group that is covalently bonded to the main structural linker. Although a large variety of cases exist where these motions are, in principle, possible, there are only a handful of reported cases.

From the systems discussed in the previous sections, those involving a methyl group attached to the linker, methylimidazolate in ZIF-8 and 5-methylisophthalate in [Zn(5-Me-ip)(bpy)], are a clear example in this category. In both cases, methyl C<sub>3</sub> rotations around the C–C bond were observed in the <sup>2</sup>H NMR line shapes. Methyl rotation has a very low activation barrier estimated at 0.6–0.8 kJ mol<sup>-1</sup> in ZIF-8,<sup>39,40</sup> therefore these fast motions are omnipresent in these systems in all covered temperature ranges,<sup>31,36</sup> and can be detected in the THz range of the vibrational spectrum.

In ZIF-8, methyl rotations are not as accountable for guest molecule transport via gate-opening as are the librations of the whole imidazolate linker. Yet one can imagine that the impact of functional group rotation would increase for bulkier or more complex groups. ZIF-90, an isostructural framework to ZIF-8, the rotation carboxaldehyde group about its axis on position 2 was observed computationally to have an important effect on the angle of the imidazolate linker due to intra-framework interactions with neighboring linkers.<sup>41</sup> In other words, the librational angle is much smaller for ZIF-90 than for ZIF-8. Hence, the authors postulated a driving mechanism where the functional group rotation enhances or restricts the linker swing motion, which would likely have an effect on the gas adsorption process.

IRMOF-3, the amino-functionalized version of MOF-5, was subject of investigations regarding its linker dynamics.<sup>42</sup> The authors succeeded in using  $^1\text{H}$  NMR relaxation measurements to assign a second, lower-energy process besides the ring  $\pi$ -flip: the rotation of the amino group. Since the amino group participates in hydrogen bonding with the nearby carboxylate oxygen, a complex interplay between the amino group rotation and the complete rotations of the phenylene may be expected.

Rotation of linker functional groups adds an additional aspect of design in MOFs. Although few cases have been reported so far, the further study of MOF linker dynamics should unearth more interesting examples in the future with potentially interesting effects on applications.

#### 1.2.4. Type D: Rotation of Mechanically Interlocked Molecules

Metal–organic rotaxane frameworks (MORFs) are a relatively young class of MOF. This type of framework originates from the interest in endowing rotaxanes with a higher degree of order, as their functions had, until recently, mainly been studied in solution.<sup>43</sup> Yaghi and Stoddart<sup>44</sup> highlighted MORFs as central in the exciting prospect of obtaining frameworks capable of dynamics that do not compromise the structural units (*i.e.*, the linkers). Since the rotator and stator are not covalently bonded in this type of rotor systems, supramolecular interactions between the ring and the threading component, as well as between the ring and the surrounding environment, should determine the rotational dynamics.

The first report of rotational dynamics of a [2]rotaxane linker in a MOF came in 2012,<sup>45</sup> where the wheel component mechanically interlocked around a carboxylate functionalized axle in a Cu(II)-based MOF was found to show a transition from a static state to a thermally activated rotational state at 324 K (Figure 1.10). The fact that rotation was only possible in the activated framework (*i.e.*, guest molecule-free) provides evidence of the importance of MOF porosity in achieving dynamic MORFs. In a following study,<sup>46</sup> a different MORF based on the same wheel component ([24]crown-6, or 24C6 macrocycle), a solvation-induced structural transition was also found to provide a means to control the rotation of the wheel about the linker axle.

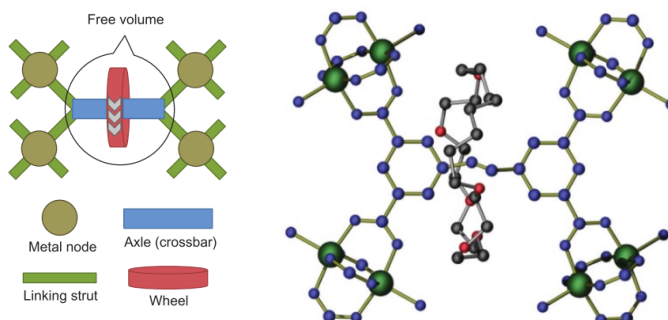


**Figure 1.10.** Left: Illustration of the composition of a metal–organic rotaxane framework (MORF); Right: Crystal structure of the Cu(II) MORF with a [2]rotaxane. Reproduced with permission from ref. 45. Copyright Nature Publishing Group, 2012.

A comparative study that considered three different macrocyclic components of varying sizes, which imply different degrees of free volume allowing for ring dynamics.<sup>47</sup> It was found that only the wheel components without a benzo group ([22]crown-6 and [24]crown-6) were able to perform rotational motions, out of which only the larger wheel could rotate completely around the axle. Another report suggested the variation of weak interactions between wheel and axle components as a rotation control parameter.<sup>48</sup> These results have elucidated the remarkable degree of control that can be achieved through the rational design of rotating moieties in MORFs.

## 1.3. Methods for the Study of Linker Dynamics

### 1.3.1. Solid-State Nuclear Magnetic Resonance (NMR)

The numerous examples of complex linker dynamics in MOFs covered in Section 1.2 evidences the fact that  $^2\text{H}$  solid-state NMR is the leading experimental technique in MOF rotational dynamics research. Deuterium NMR is an outstanding technique to analyze molecular dynamics in the solid state for several reasons. Firstly, since deuterium has a nuclear spin of 1, its NMR properties are largely determined by quadrupolar interactions with the electric field gradient tensor.<sup>49</sup> The electric field gradient on an organic compound deuteron is determined predominantly by the electrons in the C– $^2\text{H}$  bond, therefore axial symmetry along this bond can be assumed.<sup>50</sup> This allows for dynamics to be tracked by analyzing the orientation of individual C– $^2\text{H}$  bonds.<sup>15,51</sup>

It should be noted that natural abundance of the deuterium isotope is too low (0.0156%),<sup>51</sup> making the use of  $^2\text{H}$ -labeled rotator groups compulsory. This is often not a substantial drawback, as simple deuterated linker precursors are commercially available, but it may potentially deter the study of more complex linker architectures. An obvious benefit, however, is that  $^2\text{H}$  NMR is highly selective due to this labelling.<sup>15</sup>

In most of the cases presented in this review, solid echo pulse sequences were used. In some instances, the use of other pulse sequences may allow to probe an extended frequency range. Spin alignment echo technique, for example, allowed Khudozhitkov *et al.* to probe rotational motions of *p*-phenylene below 1 kHz rate,<sup>20</sup> which is the typical lower limit of conventional solid echo experiments.

The spin 1 nucleus of deuterium has three Zeeman energy levels, therefore, its spectra contain two transitions. The splitting between these transitions is determined by the orientation of the C– $^2\text{H}$  bond with respect to the external magnetic field. Since a powder sample contains all possible orientations of C– $^2\text{H}$  bonds, the static  $^2\text{H}$  solid-state NMR spectrum of a powder sample has a characteristic broad, mirrored shape with two horns, called Pake (or powder) pattern.<sup>15</sup> Each half of the line shape is caused by one of the transitions (see Figure 1.11), in combination to all the possible orientations of the bonds. The maximum (the so-called horn), corresponds to the signal when the angle between the C– $^2\text{H}$  bond and external magnetic field is  $90^\circ$ . The shoulders of the line shape correspond to the  $0^\circ$  orientation, and are the least probable orientation in a powder sample.

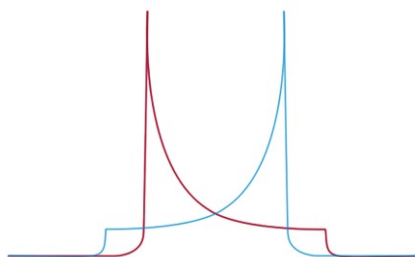


**Figure 1.11.** Pake pattern, displaying the two line shapes that compose it.

The Pake pattern can be highly sensitive to molecular motions that result in reorientation of the C–<sup>2</sup>H bonds. The frequency and trajectory of these variations are the main factors that will determine the distortions on the Pake pattern.<sup>52</sup> As an example, the left column of Figure 1.12 shows the evolution of the <sup>2</sup>H NMR line shape with temperature in deuterium-labelled MIL-53(Al). A two-site  $\pi$ -flip model was used to model the spectra, based on the known symmetry and behavior of terephthalate rotors. The good agreement between the frequency-fitted line shapes (right column of Figure 1.12) and the experimental spectra confirms that the distortions of the Pake pattern are in fact a result of the gradual increase in frequency of  $\pi$ -flipping motions. This example demonstrates that modeling the line shape with respect to possible trajectories is an essential part of analyzing molecular dynamics using <sup>2</sup>H solid-state NMR spectroscopy.

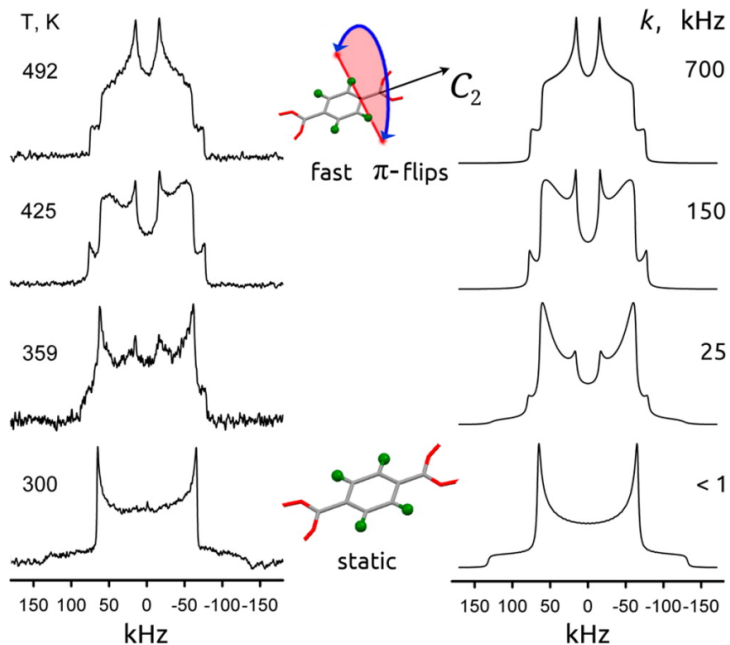


**Figure 1.12.** Experimental (left column) and simulated (right column) <sup>2</sup>H NMR line shapes of the *p*-phenylene rotor in MIL-53(Al) at different temperatures. Reproduced with permission from ref. 19. Copyright American Chemical Society, 2014.

The frequency range of  $^2\text{H}$  NMR measurements can be conveniently divided into three dynamic frequency regions, corresponding to their effects on the Pake pattern: the slow motion limit (SML), for rates of 1 kHz or less; the intermediate motion regime (IMR), when rates are between  $10^3$  and  $10^7$  Hz; and the fast motion limit (FML), when rates are higher than  $10^7$  Hz.<sup>47</sup>

Molecular dynamics of  $\text{C}-^2\text{H}$  bonds that fall in the SML and in the FML regions do not cause further changes in the Pake pattern line shape. Therefore, not much information can be gathered from processes occurring at these frequencies. Indeed, the SML line shape can be modeled with a single set of parameters. In the case of FML line shapes, the complete trajectory of motion must be known.

Dynamics occurring in the IMR, in contrast, cause marked differences in the line shape depending on the geometry of the different deuteron sites, and on the exchange rate between them. Spectra are thus collected at varying temperatures along the range, and the different spectral line shapes must be fitted to a dynamic model. Such a model includes, among other information, the parameters that describe the motion's trajectory through exchange sites, and the exchange rate.

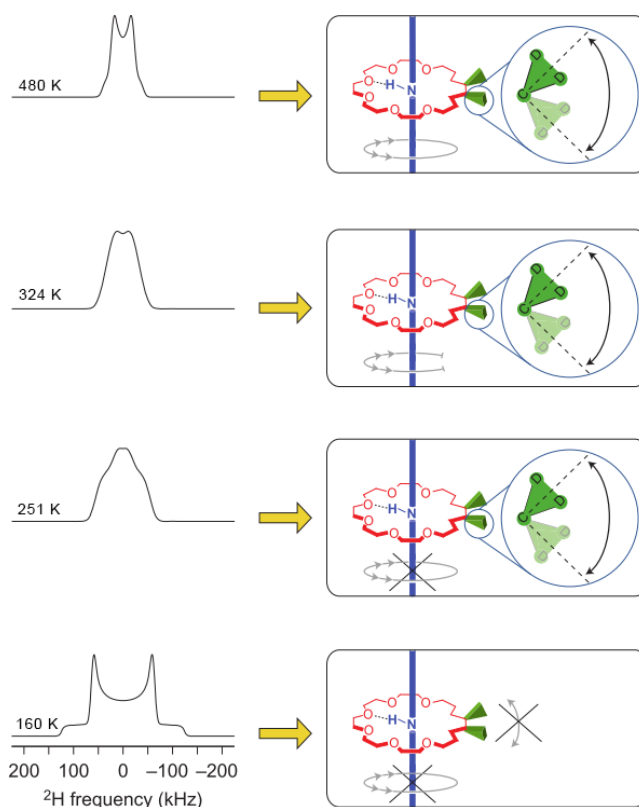


**Figure 1.13.** Simulated  $^2\text{H}$  NMR line shapes of the metal–organic rotaxane framework UWDM-1 at different temperatures. The corresponding models are shown on the right-hand side. Reproduced with permission from ref 45. Copyright Nature Publishing Group, 2012.

The complexity of deuterium NMR line shape analysis may increase when the studied systems have more degrees of freedom in the C–<sup>2</sup>H bonds, or when more than one type of deuterium bond is present. The work by Schurko and Loeb's groups on rotaxane MOFs<sup>45</sup> illustrates one such case (see Figure 1.13). With the help of detailed models, several modes of motion could be identified at different temperatures, including the CD<sub>2</sub> group reorientation, as well as partial and complete rotations of the macrocycle around the axle component.

The work by Inukai *et al.*<sup>32</sup> depicts another interesting case of complexity solved by deuterium NMR, where two pyridyl rings (PY1 and PY2 in Figure 1.14) behave differently depending on their position in the crystal lattice. Good agreement with the experimental line shape (black line on the left of Figure 1.14) was reached by modeling a superposition of the line shapes of the PY1 static ring (gray line shape), and the mobile PY2 ring performing 4-site and 2-site flips (ring shown in green, with the 4-site line in green and the 2-site line in red). Similar modeling was implemented in several other publications addressed in Section 2.<sup>12,19,26,33</sup>

Besides deuterium NMR, some examples of <sup>1</sup>H NMR used to study linker rotational motions in MOFs can be found. Morris *et al.*<sup>42</sup> analyzed <sup>1</sup>H spin-lattice relaxation (*T*<sub>1</sub>) data obtained from IRMOF-3, a framework containing aminoterephthalate linkers. Two different motions were identified: a low-energy motion (activation energy 5.0–7.5 kJ mol<sup>-1</sup>) and a higher energy process with an activation energy of 21 kJ mol<sup>-1</sup>. Based on the frequency behavior these processes, the authors postulated that the low-energy motion should be a libration, and the high-energy motion a π-flipping motion.

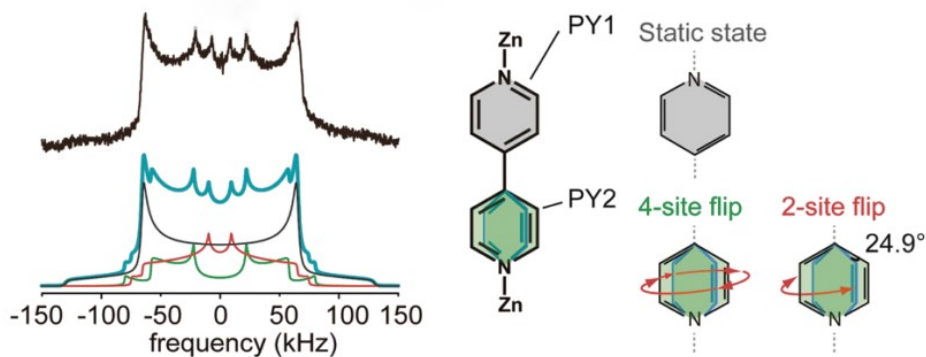


**Figure 1.14.** Experimental (top spectrum) and simulated (bottom spectra) <sup>2</sup>H NMR line shapes. The corresponding models for each of the three rotational situations are shown on the right-hand side. Reproduced with permission from ref. 32. Copyright American Chemical Society, 2015.

<sup>1</sup>H NMR spin-lattice relaxation analysis was further applied in two studies involving ultrafast rotation in MOFs. Bracco *et al.*<sup>29</sup> carried out these measurements on the Zn-BPEB framework to complement <sup>2</sup>H NMR line shape analysis that revealed dynamics belonging to the fast motion limit (>10<sup>7</sup> Hz). Indeed, the rotational frequency at 150 K was found to be in the order of 10<sup>11</sup> Hz, and a fitting of the Kubo–Tomita relation led to an activation energy of 2 kJ mol<sup>-1</sup>.

Vogelsberg *et al.*<sup>10</sup> measured  $T_1$  spin-lattice relaxation times down to much lower temperatures (2.3–80 K) in the BODCA-MOF. They found a single process in the MHz frequency range, which could be fitted to the Kubo–Tomita equation, yielding an activation energy of 0.77 kJ mol<sup>-1</sup>. This motion was confirmed to be the rotation of the BCO moiety by means of <sup>2</sup>H NMR experiments previously addressed in Section 1.2.

More recently, Damron *et al.*<sup>53</sup> introduced the use of a different NMR method to study linker dynamics in MOFs: a separated local field (SLF) type known as DIPSHIFT (which stands for dipolar chemical shift correlation). This technique was applied to a series of the UiO-66 family, and differences in rotational motions could be inferred from the variations in <sup>13</sup>C–<sup>1</sup>H dipolar coupling strength. The analysis relies on the fact that, with faster motions of the benzene ring, the <sup>13</sup>C–<sup>1</sup>H dipolar coupling constant decreases. It was thus found that the dimethyl functionalization vastly increased the rotational mobility of the linker in the MOF, while the presence of hydroxyl groups on the ring had the opposite effect.

In conclusion, solid-state NMR offers an interesting variety of approaches to study molecular dynamics in solids. Deuterium NMR clearly stands out in the field of MOFs due to the unparalleled level of detail that can be drawn from its analysis, especially when trying to discern between different types of rotation. The other types of NMR spectroscopy here discussed offer the advantage of different frequency ranges, and do not require chemical labelling. However, the conclusions that are derived from these techniques usually require additional care, since they can be significantly more ambiguous than deuterium NMR.

### 1.3.2. Dielectric Spectroscopy

Dielectric spectroscopy can provide insight into the dipole moment reorientation dynamics within solids.<sup>54</sup> Typically, the dependence of the complex permittivity (Eq. 2) of a material with respect to frequency and temperature is studied by building a parallel plate capacitor with the dielectric material of interest (*i.e.*, the MOF) enclosed. The capacitance is measured—with respect to a reference capacitor—along a wide range of electric field frequencies and temperatures. The measured capacitance can be readily converted to dielectric permittivity when the dimensions of the capacitor are known.

$$\varepsilon^*(\omega, T) = \varepsilon'(\omega, T) - i\varepsilon''(\omega, T) \quad (2)$$

The most common analysis in MOF literature involves identifying the maxima of the imaginary part of the complex permittivity—also known as the dielectric loss ( $\varepsilon''$ )—with respect to temperature or frequency. These are indicative of dipolar reorientations (also known as relaxations) in response to the applied alternating electric field.<sup>54</sup> Since this type of motion is thermally activated, a characteristic temperature shift in the relaxation peaks is usually observed, with higher frequencies corresponding to higher temperatures. A linear relation between the frequency of maximal  $\varepsilon''$  and the inverse of temperature is often found, from which an activation energy and a pre-exponential factor are obtained, according to the Arrhenius equation (Eq. 3):

$$\omega_p = \omega_0 e^{\frac{-E_a}{kT}}, \quad (3)$$

where  $\omega_p$  is the frequency corresponding to the peak in  $\epsilon''$ ,  $\omega_0$  is the pre-exponential factor (or attempt frequency),  $E_a$  is the activation energy,  $k$  is the Boltzmann constant, and  $T$  is the temperature at which the  $\omega_p$  value is obtained.

In the field of MOFs, dielectric spectroscopy has been used mainly to study rotational motions of functionalized terephthalate linkers. Winston *et al.*<sup>55</sup> compared the response of IRMOF-1 (MOF-5) and IRMOF-2. Although they did not observe dielectric relaxations in the non-polar IRMOF-1, they did identify it in the bromine-substituted analog, and the signal could thus be produced by rotational motion of the permanent dipole present in the bromo-*p*-phenylene moiety. Fitting the spectra to an appropriate model led to an activation energy of 30.5 kJ mol<sup>-1</sup>.

This is the case with some functionalized UiO-66(Zr) frameworks studied by Devautour *et al.*,<sup>56</sup> where the dipole moments generated by the presence of Br and NH<sub>2</sub> functionalities on the rings of the terephthalate linkers produced noticeable dielectric relaxation processes visible in the dielectric spectra.

Frunza *et al.*<sup>57</sup> demonstrated the use of dielectric spectroscopy to characterize rotational motions in MOF-5. Their work suggests that, even in a non-polar framework, deformations in the structure possibly lead to the appearance of dipole moments related to linker rotation. The authors assigned a low activation energy process to bending of the SBUs of MOF-5, and a higher energy process (33.4–37.3 kJ mol<sup>-1</sup>) to phenylene rotational motions.

Dielectric spectroscopy has recently been used in other non-terephthalate-based frameworks. Knebel *et al.*<sup>11</sup> included this technique in their study of the rotational mobility of the 2-methylimidazolate linker in ZIF-8. Using a similar analysis to those in the previously mentioned literature, they found a dielectric relaxation corresponding to an activation energy of 49 kJ mol<sup>-1</sup>. They assigned this motion to the slow linker swinging that could also be observed in <sup>2</sup>H NMR, albeit with a slightly higher activation energy obtained with the latter technique.

Balčiūnas *et al.*<sup>58</sup> reported a comprehensive dielectric study of linker dynamics in ZIF-90—an isorecticular analog of ZIF-8 that has a carboxaldehyde group in place of the methyl group. Their work shows the effect that different gas molecules present in the pores have on the linker's ability to perform partial rotations. The linker rotation in the evacuated ZIF-90 has an activation energy of 22 kJ mol<sup>-1</sup>, which increases to 34.7 and 35.7 kJ mol<sup>-1</sup> in the presence of N<sub>2</sub> and CO<sub>2</sub>, respectively.

It is important to note that dielectric spectroscopy cannot provide the same level of detail as deuterium NMR experiments regarding the nature and trajectory of molecular motions. As observed in the cited articles, no specific conclusions are made as to whether the rotators perform full 360° rotations, or their rotational amplitude in the case of the partial rotations. Nevertheless, dielectric spectroscopy is clearly growing in popularity in the MOF field as it is a powerful and sensitive method to probe dynamics of MOFs with the added benefit of not requiring chemical labelling. Furthermore, it is much more inexpensive than NMR equipment.

### 1.3.3. Terahertz Spectroscopy

Very recently, far-infrared (FIR) spectroscopy in the terahertz range has been applied successfully to study MOF linker dynamics. This vibrational spectroscopy technique is used to study low-energy vibrational modes in solid materials, which tend to be related to structural flexibility.<sup>59</sup> As discussed in Section 1.2, librations are a prevalent form of partial rotational motion in MOF linkers, whose frequencies have been observed in the THz range. This is indeed the range where you expect rotational motions about a minimum in a potential energy. Dynamics of Type A—*i.e.*, involving hopping over an energetic barrier—are thus not detectable by this method.

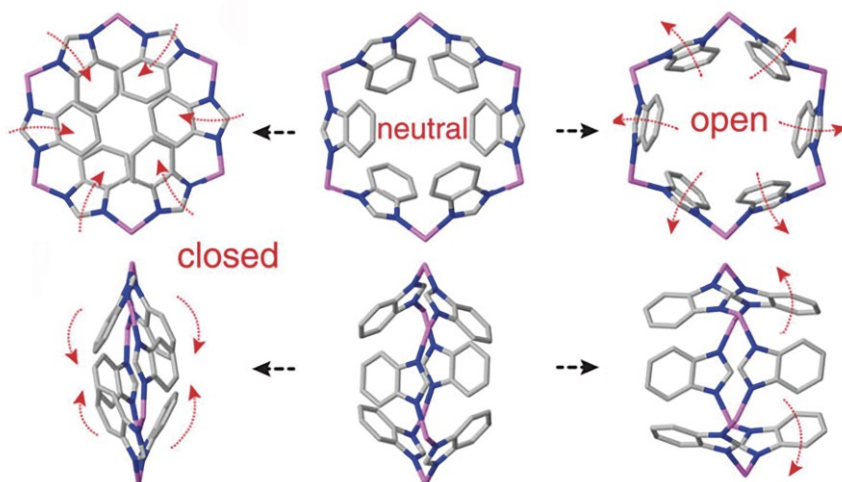


**Figure 1.15.** Illustration of low-energy vibration mode in ZIF-7, causing pore opening and closing. Reproduced with permission from ref 60. Copyright American Physical Society, 2014.

High-quality quantum chemical calculations are usually required in order to interpret the spectra associated to THz spectroscopy. In such a manner, the vibrational modes belonging to linker rotation can be isolated from the various other types of collective modes.

Ryder *et al.*<sup>60</sup> undertook a detailed study of lattice dynamics in three ZIF materials (ZIF-4, ZIF-7, and ZIF-8) using far-infrared spectroscopy. Specifically, they focused on the frequency region below 21 THz, down to 0.6 THz, using synchrotron radiation. Although their report identifies a large array of low-frequency lattice vibrations, the relevant modes for linker rotation were found close to the lower limit of the probed range. Gate-opening modes were found in ZIF-4, ZIF-7, and ZIF-8 at 1, 1.47 and 1 THz, respectively. In all three cases, the modes involve librations of at least some of the imidazolite linkers that form one of the windows of the pore (example of ZIF-7 shown in Figure 1.15). In a similar manner, but using terahertz time-domain spectroscopy (THz-TDS), Tan *et al.*<sup>61</sup> identified vibrational modes involving rotational motion of the linkers in ZIF-8 and ZIF-90 in the same frequency range.

In a subsequent article, Ryder *et al.*<sup>24</sup> applied THz spectroscopy to identify the differences in the librational rotation of two types of terephthalate linkers—one significantly more hindered than the other—that form the MIL-140A framework (addressed in Section 1.2).

Additionally, Li *et al.*<sup>39</sup> used THz-TDS to detect the rotation of the methyl group in ZIF-8—one of the few examples of Type C rotors found in MOF literature.

Terahertz spectroscopy is likely at the start of its application in the field of linker rotation, yet the work discussed here demonstrates its great potential, when coupled with appropriate computational chemistry methods, to expand our understanding of partial rotational dynamics in MOFs.

### 1.3.4. Computational Methodologies

The seminal works of Zhou *et al.* in 2006,<sup>17</sup> Kuc *et al.* in 2007,<sup>62</sup> and Winston *et al.* in 2008<sup>55</sup> were the first to address the issue of linker rotation in metal–organic frameworks from a computational perspective. Zhou *et al.* studied the rotation of the *para*-phenylene units in MOF-5 using density functional theory (DFT) single-point calculations (see Figure 1.16). Their method involved the rotation of only one linker out of the six present in the primitive unit cell, with two-degree steps, from 0° to 180°. The rotational barrier found at 90° is 51.8 kJ mol<sup>-1</sup>. Kuc *et al.* studied the properties of over 30 MOF structures, at the semi-empirical level with Density functional based tight-binding (DFTB) calculations. As part of this larger study, they calculated a rotation barrier for the organic linker in IRMOF-1 (= MOF-5) of 34 kJ mol<sup>-1</sup>, a value significantly lower than that calculated by Zhou, and which can be attributed to the lower-accuracy level of theory chosen. Kuc *et al.* also stated that they observed “nearly free rotation of the linker” at 300 K using DFTB-based molecular dynamics, which is not in agreement with the later experimental findings through <sup>2</sup>H NMR showing that at 300 K the flipping rate is below 1 kHz.<sup>16</sup>

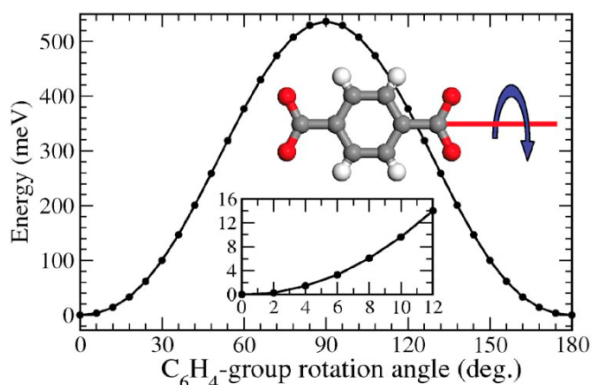


**Figure 1.16.** Energy profile for the rotation of a single *para*-phenylene unit in MOF-5 using density functional theory (DFT) single-point calculations. Reproduced with permission from ref 17. Copyright American Physical Society, 2006.

Winston’s study focused more specifically on the rotation dynamics of the bromo-*p*-phenylene organic linkers— called “dipolar molecular rotors”—in IRMOF-2, by combining experimental and computational methods. In particular, the authors calculated rotational energy barriers by a series of energy calculations with 10° angle increments, at two levels of theory: density functional theory (DFT) using the B3LYP functional, and the post-Hartree–Fock Møller–Plesset (MP2) theory.

However, these studies were performed not on the periodic crystalline structures, but on model clusters composed of a single linker and two metal nodes. The rotation barrier ranges between 20 and 31 kJ mol<sup>-1</sup> depending on the computational method, which is in good agreement with the experimental value of 30.5 kJ mol<sup>-1</sup> determined by the same authors using dielectric spectroscopy.

This methodology is the simplest way to computationally characterize the rotation of a given linker. The computational cost is relatively low, because it corresponds to a series of single-point energy calculations with rotated configurations of the linker (in some studies, the other coordinates are relaxed, but not always). This has been used in several other studies, and can be performed with periodic DFT to take into account the full crystal structure, as has been done for example by Kolokolov *et al.*<sup>63</sup> in their comparison of the dynamics of MIL-53(Cr) and MIL-47(V), two materials with the same diamond-shaped micropores. They used periodic DFT calculations to study the nature of the low-frequency vibration modes of the two materials, identifying the linker rotation modes as well as the corresponding rotational barriers—in agreement with <sup>2</sup>H NMR experimental data. The methodology can also be extended to a full calculation of the rotation energy profile, calculating the potential energy surface  $E(\phi)$  by rotating a linker by an angle  $\phi$ —usually in series of calculations constraining the dihedral angle  $\phi$ . Shustova *et al.*<sup>25</sup> studied in this way the phenyl ring dynamics in a tetraphenylethylene-bridged MOF. In another recent example, Hobday *et al.*<sup>37</sup> looked at the tuning of the swing motion of various functionalized imidazolate linkers in ZIFs. Ryder *et al.*<sup>24</sup> determined the rotational energy profiles for various MIL-140A vibration modes, using DFT calculations, to show that experimentally observed low-energy vibrations in THz spectroscopy originate from the hindered rotations of organic linkers.

However, the rotation of MOF linkers also involves entropic contributions—which are not taken into account in the potential energy surface scans—and can be expected to be significant, given that the soft vibration motions often have low frequency. These effects can be studied with molecular dynamics (MD) simulations at finite temperature  $T$ , where the free dynamics of the ligand will be sampled over time. Burtch *et al.*<sup>64</sup> investigated the framework dynamics of pillared zinc-based MOFs, relying on a classical molecular dynamics approach where an empirical force field is used to describe the various intra- and intermolecular terms of the energy. They also used this approach to study the influence of framework dynamics on water adsorption in these materials, and showed that the dynamics of the linker (DABCO, 1,4-diazabicyclo[2.2.2]octane) is strongly impacted by the presence of water guest molecules. However, the impact of the flexibility itself on total water uptake was found to be negligible.<sup>65</sup>

In a recent paper, Namsani and Yazaydin<sup>66</sup> performed MD simulations of halogen-functionalized IRMOF-1 and IRMOF-7 under the influence of an external electric field. Their study shows that the rotation angle of dipolar linkers may be controlled externally to enhance the diffusion of methane molecules in a specific direction, depending on the orientation of the electrical field.

We note here that several other studies have analyzed the impact of linker rotation on properties such as adsorption of gas or liquid molecules. This can be done either with a full description of the material's flexibility (through MD simulations), or even at a lower level by a cursory look at the geometric impact of the rotation of the linker on the properties—without a full description of the energetics of the rotation itself. The Sholl group has published several studies on the impact of

flexibility in ZIF-8 on adsorption, for example of methane, carbon dioxide,<sup>67</sup> and noble gases.<sup>68</sup> Elsaïdi *et al.*<sup>69</sup> described the impact of ring rotation upon gas adsorption in the nanoporous spaces of SIFSIX-3 pillared square grid networks.

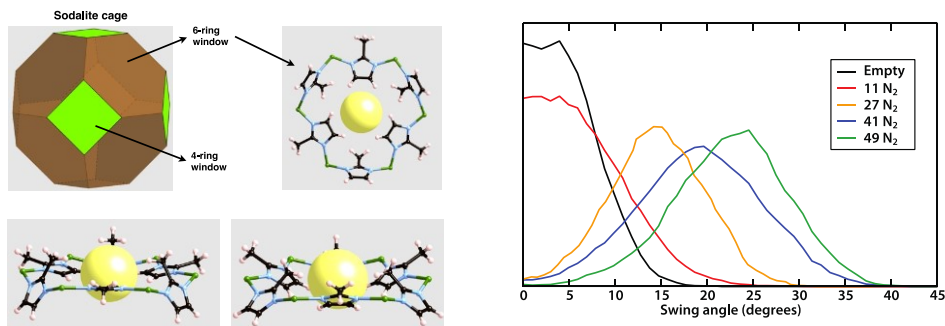


**Figure 1.17.** Left: Depiction of the “out of plane” swinging motion of the methylimidazolate linkers in the 6-ring window of ZIF-8 material, with sodalite topology; Right: distribution of swing angle due to thermal motion at 300 K, in the evacuated material and in presence of N<sub>2</sub> adsorbate molecules. Reproduced with permission from <sup>35</sup>. Copyright Wiley-VCH, 2017.

While classical MD has a relatively low computational cost which allows the sampling of large time and length scales, its accuracy is limited by that of the intra- and intermolecular interaction potentials of its underlying force field. This accuracy can be particularly limited for soft vibration modes—which are of critical importance in soft porous crystals—and large dihedral rotation angles, as Burtch showed in their study.<sup>64</sup> Therefore, there is a need for molecular dynamics simulations based on quantum chemistry calculations of the interatomic forces, a method called *ab initio* molecular dynamics (AIMD). Recent studies have shown that the use of AIMD can shed light into the linker dynamics in MOFs, investigating the nature of the large-amplitude “swinging” motion of the imidazolate linkers that give rise to the flexibility of ZIF-8 (depicted in Figure 1.17a). This showed in particular that the deformation upon adsorption is continuous upon pore loading with nitrogen (see Figure 1.17b),<sup>35</sup> and highlighted the influence of the linker functionalization and the impact of this delicate balance of microscopic interactions on the framework’s overall flexibility.<sup>38</sup>

Finally, direct sampling of the organic linker rotation through MD is suitable for low-barrier rotations that occur spontaneously within the timescale of MD simulations (from ps to ns). It will not be suitable to describe activated rotation events corresponding to high barriers, where free energy methods such as metadynamics will be necessary to sample the free energy profile  $F(\phi)$ .<sup>70</sup> Such methods have been used extensively in the literature on the conformations of organic molecules and biological systems,<sup>71</sup> but their use in the MOF field has been so far relatively rare. Haigis *et al.*<sup>72</sup> used metadynamics in conjunction with AIMD to probe the water-assisted breaking of the linker–metal bond that occurs during hydrothermal breakdown of MIL-53(Ga).

## 1.4. Implications of Rotational Dynamics on Applications of MOFs

### 1.4.1. Diffusion and Adsorption

There are ample studies where guest adsorption leads to a rotational conformational change.<sup>59,73–76</sup> These studies do not directly investigate the dynamics of linker rotation, but the aforementioned observation implies that linker rotation is energetically possible. As discussed in Section 1.2, the presence of guest molecules inside the pores generally decreases the rate of rotational dynamics of the linkers. A clear example of this is reported by Bracco et al.<sup>29</sup> (first discussed in Section 1.2.1, linker structure shown in Scheme 1.2, bottom) where the 180° flip motion of the 1,4-bis(1H-pyrazol-4-ylethynyl)benzene linker coordinated to Zn<sup>2+</sup> decreases from 10<sup>11</sup> Hz to 10<sup>5</sup> Hz, along with an increase in the activation energy from 2 to 19 kJ mol<sup>-1</sup> upon complete pore filling with CO<sub>2</sub> at 150 K. At partial filling of CO<sub>2</sub>, intermittent rotational frequencies due to a combination of static and mobile linker were found. Interestingly, when CO<sub>2</sub> guest molecules are present, the librational motion alongside the flips has a larger amplitude ( $\pm 32$ – $41^\circ$ ) with respect to the libration of the guest-free structure (amplitude of  $\pm 20^\circ$ ). This is an example of the influence of guest molecules on the rotational dynamics. Yet, the question we pose here is: what is the influence of linker rotational dynamics on guest diffusion and adsorption?

An often addressed phenomenon that arises from the interaction between a mobile linker and the guest molecules is the so-called gate-opening effect. It is usually observed as an inflection point, a step, or hysteresis in an adsorption isotherm, as a result of a structural transition in the MOF.<sup>77–79</sup> This structural transition can be due for example to the breathing effect.<sup>80</sup> Here we discuss the gate-opening effect with regard to structural transitions with a change in rotational conformation of the linkers.

The gate-opening can affect guest diffusion. Often the pore size expected based from XRD does not correspond with the size of the molecules that can be adsorbed: molecules larger than expected are able to diffuse into the pores. Two typical examples are ZIF-7 and ZIF-8. This is due to the librational movement of the imidazolate linker (see Section 1.2.2). Energetically the pore opening can easily be enlarged due to the librational motion of the linker, as shown schematically in Figure 1.18.

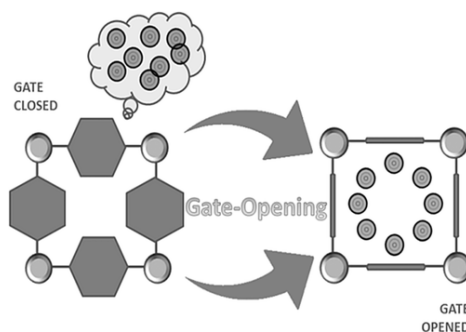


**Figure 1.18.** Illustration of the gate-opening effect. Reproduced with permission from ref. 81. Copyright Wiley-VCH, 2016.

More specifically, in ZIF-8 the 6-membered rings that provide entrance to the cages have a free diameter of ca. 3.0 Å. Many molecules with a kinetic diameter larger than that can penetrate into the pores, *e.g.* O<sub>2</sub>, N<sub>2</sub>, CH<sub>4</sub>.<sup>81</sup> This was first described by Moggach *et al.*,<sup>4</sup> in a study where ZIF-8 crystals were submitted to a pressure up to 1.47 GPa via a 4:1 (methanol:ethanol) hydrostatic mixture. This resulted in a single-crystal to single-crystal phase transition to a previously unobserved phase. This phase transition involves the rotation of the methylimidazolate linker, which leads to an increase in the diameter of the 6-membered rings from 3.0 to 3.6 Å, allowing more methanol and ethanol molecules to enter the pores. Later Fairen-Jimenez *et al.*<sup>5</sup> showed that this same phase transition also takes place upon gas adsorption at lower pressures. For example, for N<sub>2</sub> at 77 K it occurs at ~0.02 bar.<sup>82</sup> Similar gate-opening effects have been reported for ZIF-7, which also presents imidazolate linkers with rotational freedom forming 6-membered rings as pore windows.<sup>83,84</sup>

Recently, Hobday *et al.*<sup>37</sup> compared ZIF-8 and its carboxaldehyde and nitro functionalized analogues (ZIF-90 and ZIF-65, respectively) also under high hydrostatic pressure of a 4:1 methanol:ethanol mixture. At high pressures, the linker in ZIF-90 undergoes a similar rotation as in ZIF-8, which leads to a larger pore opening. In contrast, the linker in ZIF-65 rotates in the opposite direction, leading to a smaller pore opening. This suggests a difference in interaction energies of the –NO<sub>2</sub> groups between each other and with the alcohol molecules, with respect to what occurs with the –CH<sub>3</sub> and –CHO groups. The rotational dynamics of the nitro-functionalized ligand might still be different for other guest molecules.

For a framework constructed from Mn<sup>2+</sup> and isonicotinate, the one-dimensional pores are lined with the isonicotinate linkers, which, in the guest-free conformation of the MOF, are orientated into a closed pore configuration that is too narrow for diffusion of small molecules such as CO<sub>2</sub>. However, adsorption of guest molecules such as CO<sub>2</sub> and propane is associated with rotation of these linkers about their coordination axis into an open pore configuration. This leads to a steep rise in the adsorption curve at the gate-opening pressure. The gate-opening pressure is dependent on the adsorption energy and hence adsorbate dependent.<sup>85</sup>

An intriguing example of a material that is capable of transforming between a gate-closed to gate-open configuration via linker rotation was reported by Kitagawa *et al.*<sup>86</sup> The structure is based on 2-D sheets that are pillared by a ligand with a 180° coordination geometry and an ethylene glycol functionalization (see Figure 1.19). These side chains act as a molecular gate, that can be unlocked by guest interactions. The hydrogen bonds of the ethylene glycol side chain are vital in the mechanism. In the guest-free framework, the side chains form hydrogen bonds with each other that lead to an effectively closed pore configuration: N<sub>2</sub> and O<sub>2</sub> cannot be adsorbed. In contrast, water and methanol can be adsorbed and lead to a gate-opening of the pores. The hydrogen bonds between the ethylene glycol groups are broken as H-bonds with the guest molecules are formed. This leads to a rotation of the linker around its coordination axis leading to a large pore opening (see Figure 1.19). At the vapor pressure upon which this occurs the sorption isotherm shows a step that is typical of a gate-opening effect. For CO<sub>2</sub>, due to its much smaller tendency to form H-bonds with the ethylene glycol groups this happens at a much higher vapor pressure.

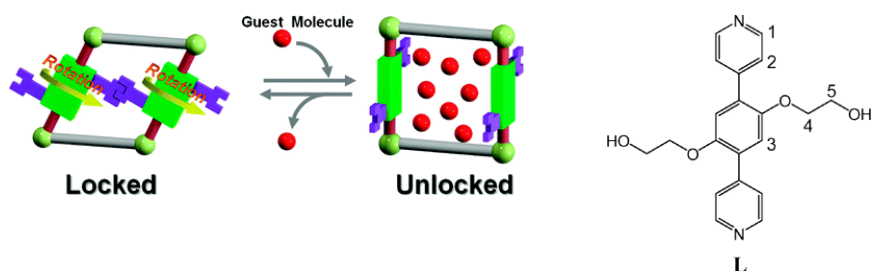


**Figure 1.19.** Left: Illustration of gate-opening effect in 2-D sheet framework with glycol functionalization; Right: Schematic structure of linker. Reproduced with permission from ref. 84. Copyright American Chemical Society, 2009.

In a MOF based on  $\text{Cu}^{2+}$  and 5-diethyl-1,2,4-triazole, the ethyl groups are capable of momentarily moving out of the way to permit the diffusion of guest molecules that are normally too large to fit, such as acetylene and  $\text{CO}_2$ .<sup>87</sup> The structure of the framework is hardly changed upon guest inclusion. This is a clear example of linker molecules, or part thereof, only temporarily moving out of the way.

Zhang et al.<sup>88</sup> studied a framework based on  $\text{Cu}^{2+}$ , which is pillared by hexafluorogermanate or hexafluoronibate as well as a ligand containing two pyridyl rings, 4,4'-dipyridylacetylene or 4,4'-azopyridine more specifically. In the guest-free state one of the pyridyl rings is rotated such as to optimize a favorable  $\text{C}\cdots\text{H}\cdots\text{F}$  hydrogen bond. When solvent molecules are occluded, both pyridyl rings have a close to planar conformation, which leads to a larger pore size. The difference is the largest for the 4,4'-azopyridine ligand, with a difference of  $30^\circ$  in rotational conformation for one pyridyl ring in the guest-free state. The result is that the solvated MOF has larger pore sizes:  $4.2 \text{ \AA}$  instead of  $3 \text{ \AA}$ . This larger pore size of  $4.2 \text{ \AA}$  should allow for butadiene to diffuse through, while the butene isomers that have a larger cross section cannot. Indeed, the authors report both plausible gate-opening in the adsorption isotherm of butadiene, and a good separation between butadiene and butene isomers. Often, MOFs do not perform as well in breakthrough adsorption experiments as expected from the single gas adsorption experiments.<sup>89–91</sup> However, in this case a very good selectivity was retained in the breakthrough experiments.

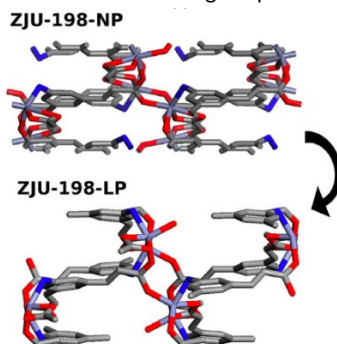


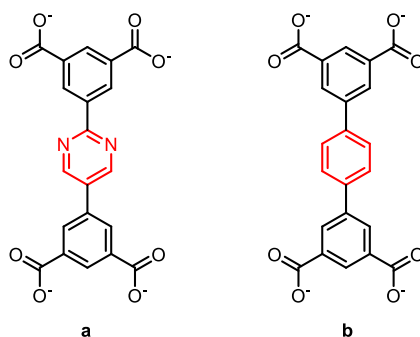
**Figure 1.20.** NP and LP conformations of ZJU-198 framework. Reproduced with permission from ref. 90. Copyright Wiley-VCH, 2018.

For ZJU-198, shown in Figure 1.20 as ZJU-198-NP (NP = narrow pore), it has been shown experimentally that this structure can separate CO<sub>2</sub> from N<sub>2</sub>, acetylene from methane, and, moderately, acetylene from ethylene.<sup>92</sup> This was initially rationalized via the static ZJU-198-NP structure. Yet, many of the adsorbate molecules in fact do not fit into the ZJU-198-NP pores. Via Monte Carlo simulations through grand canonical assemblies and molecular dynamics, Calero *et al.*<sup>93</sup> showed that the structure actually undergoes a phase transition upon guest adsorption, via a linker rotation that leads to large pore cavities. This structure is shown as ZJU-198-LP (LP = large pore) in Figure 1.20. This breathing effect leads to preferential adsorption of molecules that favor the large-pore configuration. In fact, the authors could far better reproduce the experimental adsorption isotherms and selectivity by including this framework flexibility than by assuming a static ZJU-198-NP structure.

So far, we discussed the rotation-induced gate-opening effect that leads to larger effective pore windows than predicted from XRD crystal structures. This can happen if the linkers in the equilibrium guest-filled structure have a different orientational conformation with larger pore size. It can also happen due to transitory linker rotation that allows diffusion of guest molecules, while the equilibrium conformation is very alike that in the guest-free structure. The result of this effect is that molecules larger than expected from the refined guest-free structure can diffuse through the MOF.

Another way in which rotational dynamics can lead to different adsorbate/adsorbent interactions is when a conformational transition of the MOF affords a better packing of the adsorbate molecules, or when it leads to more favorable adsorbate/adsorbent interactions.

The above-discussed gate-opening effect is in fact more intricate than initially thought. A gradual deformation of the ZIF-8 structure takes place during adsorption. In the case of small molecules—such as N<sub>2</sub>, Ar, O<sub>2</sub> or CO—at low temperature, this deformation can lead to stepped isotherms due to packing effects. More specifically, a step occurs when a more favorable packing arrangement of guest molecules becomes possible in the deformed structure. As such, the polarizability and molecular size and shape of the gases play a significant role in the adsorption behavior.<sup>35,94</sup> Recently Coudert *et al.*,<sup>38</sup> via a combination of N<sub>2</sub> sorption and first principles thermodynamics, showed that the isoreticular ZIF-8-Cl (ZIF-8 with the –CH<sub>3</sub> group substituted by –Cl) has similar steps in the low temperature N<sub>2</sub> adsorption. Here too, it is convincingly shown that this is governed by an increasing rotational linker deformation and guest packing effects. In contrast, the isoreticular ZIF-8-Br was shown to be stiff and displays a characteristic type Ia adsorption isotherm.



**Scheme 1.4.** Two rotor linkers used in (a) UTSA-76 and (b) NOTT-101.

In two metal–organic framework based on  $\text{Cu}^{2+}$ -paddle wheels, that contain the linkers shown in Scheme 1.4, a difference in rotational dynamics between these linkers leads to distinct differences in the adsorption of methane.<sup>27</sup> At high loading, the pyrimidine-containing linker has a much higher methane uptake. At low methane pressures, both frameworks show a very similar uptake. DFT calculations show similar adsorption energies for both MOFs. With quasi-elastic neutron scattering, the authors of this study found that the pyrimidine containing linker is far more dynamic, and hence the authors postulated that the central pyrimidine rings can be more easily adjusted and oriented to optimize the methane packing in the MOF at high pressure than that this can happen for the central benzene rings in the other MOF.

In another series of MOFs investigated for methane storage (discussed in Section 1.2.1, see Figure 1.5), a difference in rotational dynamics for the different ligands occurs. However, it is less clear in these structures what the precise effect of rotational dynamics is on the interplay of flexibility, pore shape, and adsorption energies that leads to the observed differences in methane loading.

SIFSIX-3-Ni consists of a network based on square grids of  $\text{Ni}^{2+}$  and pyrazine, which are pillared by  $\text{SiF}_6^{2-}$ . This structure shows a distinct inflection point in the Xe adsorption isotherm that is absent for Kr,  $\text{N}_2$ , and  $\text{CO}_2$ . The pore diameters based on the refined structure are 3.5–3.8 Å, which is close to the kinetic diameter of 4 Å of Xe. Whether the structure is present in vacuum, or fully loaded with He or Xe, the pyrazine rings within the framework have a similar orientation, where each ring is rotated approximately  $16^\circ$  with respect to the square grid plane orientation.<sup>69</sup> Two different orientations ( $-16^\circ$  and  $16^\circ$ ) are possible. The transition that occurs around the inflection point is hence subtler. Aided by DFT calculations, the authors concluded that a disorder-to-order structural transition in the organization of the pyrazine rings takes place, which leads to an organized pattern of aligned  $+16^\circ$  and  $-16^\circ$  pyrazine configurations that can better accommodate Xe guest molecules. In this case, it is not so much a packing effect, but rather a reorganization of the linker conformations to allow for optimal adsorbate/adsorbent interactions.

For an isorecticular structure based on  $\text{Zn}^{2+}$  and  $\text{Ni}^{2+}$  it has also been shown that the rotational dynamics of the pyrazine rings play a role in the adsorption of  $\text{CO}_2$ .<sup>95</sup> Here, intriguingly, a higher uptake of  $\text{CO}_2$  is observed at 298 K than at 195 K.

Gee and Sholl<sup>96</sup> applied molecular dynamics simulation to better grasp what the role of rotational flexibility of MIL-47 and MOF-48 might be on the adsorption selectivity for different pairs of C8 aromatics. These MOFs with one-dimensional pores are based on  $V^{4+}$  coordinated by oxygen and terephthalic acid (MIL-47) or dimethyl terephthalic acid (MOF-48). They compared static Grand Canonical Monte Carlo simulations with GCMC simulations on a series of snapshots taken from flexible molecular dynamics simulations that pertain to a wide set of dihedral angles of the terephthalate linkers. When rotational flexibility was included, the computational results matched the experimentally observed selectivity far better. For these host/guest systems, the simulated selectivity decreased when flexibility was included.

As is clear, the rotational dynamics of linker molecules in MOFs can have a profound effect on the adsorption properties of MOFs. The gate-opening effect shows that the effective pore size that should be considered to predict selectivity based on a molecular sieving effect, is in this case generally larger than the pore size determined from the guest-free refined structure. In addition, the potential for structural transitions based on rotational linker dynamics, can lead to a better packing of guest molecules at high loadings. This is especially the case for small molecules at low temperatures these packing effects may be pronounced.

The examples we discussed show that in fact rotational dynamics has the potential to increase or decrease the adsorption selectivity, depending on the specific interplay between the MOF structure, its flexibility and the guest molecules. In any case, in order to understand the adsorptive properties of MOFs, the rotational dynamics need to be considered.

### 1.4.2. Optical Properties

Rotational dynamics can influence several optical properties of MOFs. One area where this happens is inspired by the recently discovered phenomenon of aggregation-induced emission (AIE).<sup>97</sup> Chromophores that have this property are far more fluorescent as aggregates than when they are present in dilute solutions. In these chromophores, orbitals that are involved in the luminescence decay pathway are present on groups that are rapidly rotating in solution, hence quenching the fluorescence. When aggregated, this rotation is hindered, hence fluorescence is switched on.<sup>98</sup> A typical example is the molecule tetraphenylethylene (TPE), for which fast rotation of phenyl groups and twisting of the C=C group occur in solution, but not upon aggregation.<sup>99</sup> Dinca *et al.*<sup>100</sup> showed that a tight packing of the chromophores is actually not necessary, since simply restraining the mobility via incorporation the chromophore in a matrix can suffice for fluorescence to occur. More specifically, a tetrakis(4-carboxyphenyl)ethylene (TCPE) ligand was built as linker into metal–organic frameworks via either  $Zn^{2+}$  (see Figure 1.21) or  $Cd^{2+}$  ions. Despite the distance between the TPE motifs being significantly larger in the MOF than in the aggregate, and rotation/flipping of the phenyl rings being feasible, the MOFs exhibit fluorescence, both in the solvated and unsolvated state.

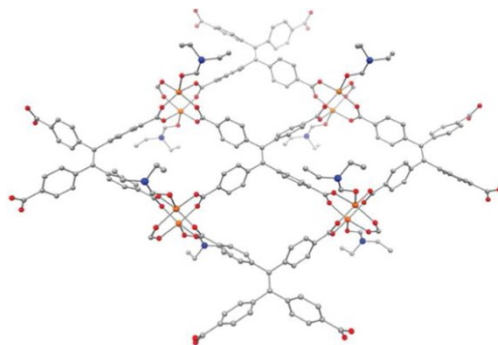


**Figure 1.21.** Crystal structure of the fluorescent  $Zn_2(TCPE)$  framework. Reproduced with permission from ref. 25. Copyright American Chemical Society, 2012.

The same group investigated the effect for the MOF built up with  $Zn^{2+}$  paddle wheels in greater detail via  $^2H$  NMR and DFT modeling of the energy barrier for rotation on a cluster model. With respect to free TPE in the gas phase, the linker in the MOF has twice the energy barrier for ring rotation: 50 kJ/mol versus 25 kJ/mol. This is due to the geometrical constraint the MOF topology poses on the linker which leads to steric hindrance upon ring rotation that is absent from the free TPE.<sup>100</sup> Apparently, these decreased phenyl rotations suffice to retain the fluorescence of the materials. The authors predict that if the MOF topology could be chosen such that the rotational energy barrier could be lowered significantly, they could be interesting sensors. They postulate that in such cases the guest-free MOF should hardly fluoresce, while upon guest inclusion the fluorescence should be switched on.<sup>25</sup>

Correspondingly, Du *et al.*<sup>101</sup> recently hypothesized that the fluorescence enhancement of MIL-53 related MOFs with Au particles attached in the presence of glutathione, is related to a restriction of the rotational dynamics of the terephthalate linkers.

Serra-Crespo *et al.*<sup>102</sup> showed that modulation of linker dynamics can also act as the switch to turn on the non-linear optical (NLO) response of  $NH_2$ -MIL-53(Al).  $NH_2$ -MIL-53 is capable of generating second-order NLO light, which is only allowed for non-centrosymmetric structures, in the closed pore configuration where the linkers experience significant steric hindrance to rotation. When guest molecules were introduced, the structure transformed to an open pore configuration that allowed for linker rotation. This, in turn, led to a randomization of the linker orientation that switched off the NLO response.

In short, linker dynamics can have a pronounced effect on optical properties such as fluorescence and non-linear optical light generation, such that on–off transitions may be realized based on the drastic changes in linker dynamics upon guest adsorption/desorption.

### 1.4.3. Mechanical Properties

Metal–organic frameworks can show intriguing mechanical properties, such as negative thermal expansion or gigantic positive thermal expansion.<sup>103–108</sup> This prompts the question: in what ways does the flexibility that many MOFs have play a role in these phenomena? Within the frame of

this review, what role may rotational linker dynamics play? A few papers have addressed this explicitly.

For MOF-5, which shows negative thermal expansion between at least 80 K and 500 K, it has been shown in an experimental<sup>103</sup> and a computational study<sup>106</sup> that its unit cell contraction with increasing temperature is due to a concerted transverse movement of the linkers and the twisting and vibrations of the carboxylate groups specifically. Yet, the librations of the terephthalate linkers hardly play a role in the phenomenon.

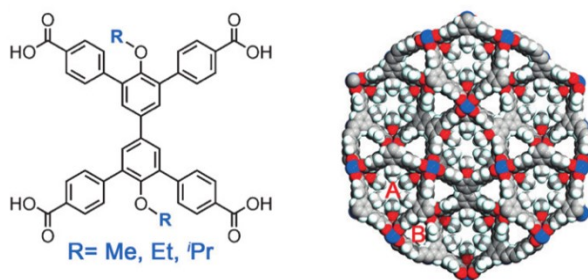


**Figure 1.22.** Structure of the FJI-H11-R framework and its rotor linker. Adapted with permission from ref. 109. Copyright Wiley-VCH, 2016.

The FJI-H11-R MOFs—which consist of  $\text{Cu}_2$  paddle wheels and the rather elaborate linkers depicted in Figure 1.22—show a significant positive thermal expansion,<sup>107</sup> with a slight contraction of 0.6 % of the  $a$ -axis between 100 K and 293 K, but a large positive thermal expansion of 9.4 % along the  $c$ -axis, leading to a pore volume increase of 8.0 %. The authors showed that this is related to rotation of the  $p$ -phenylene groups in the linker, and deformation of the linker.

## 1.5. Conclusions

In this review we categorized rotational linker dynamics in MOFs into four types (A–D), based on geometric and energetic considerations. Type A occurs in linkers with straight axes and low enough rotational barriers, such that they are capable of completing  $360^\circ$  rotations. Type B consists of partial rotations, such as librations (oscillations about a minimum) and hops in energetically constrained rotors. Types C and D are topologically different from the first two, and far fewer examples are reported in literature. In Type C, the rotor is a side functional group that is not involved in the connectivity, while in Type D the rotor is formed by a macrocyclic molecule that is mechanically interlocked around the main linker strut. In general, rotational motions are commonplace in MOFs, with a rich diversity of mechanisms of rotation, as well as complex interplays between the rotor framework and guest molecules.

Given the diverse examples found in the literature, it is evident that electronic configuration of the rotor and the steric environment inside the framework are the two main factors determining the torsional potential. Hence, they are essential parameters in the design of framework rotor systems. For instance, high rotational barriers can be obtained using linkers that feature  $\pi$ -

electron delocalization systems. By contrast, axes with pure single-bond character—or with triple bond moieties—should be chosen in order to reach free rotational motion. Additionally, the coordination geometry of a linker may exclude the possibility of 360° rotations in certain types of MOFs. Steric hindrance on the rotors, arising from the framework itself or from guest molecules in the pores, will lead to increased rotational barriers.

With regard to the set of tools that can be used to study rotational dynamics of linkers, <sup>2</sup>H NMR is evidently the most important in the field. This is due to its specificity and ease of interpretation. It has been used successfully to determine rotation steps, rates, and barriers of numerous and often diverse MOFs. Other methods, such as <sup>1</sup>H NMR spin-lattice relaxation, dielectric spectroscopy, and THz spectroscopy, are becoming more commonplace, but may need further development and/or combination with supporting techniques to avoid ambiguity. Molecular modeling techniques can also be used to provide information on the dynamic nature of the frameworks. Relatively low-cost DFT calculations can be used to characterize the low-energy vibration modes of the materials, as well as the energy profile for linker rotation. More advanced methods, including *ab initio* molecular dynamics and free energy methods (such as metadynamics), are starting to appear in the study of rotational linker dynamics in MOFs, although their computational cost is significantly higher.

In addition to their prevalence in MOFs, these motions can have a drastic impact on their properties and on their performance in several applications. With regard to adsorption and separation, molecules larger than the pore size expected from the XRD refined structure might adsorb. Furthermore, the rotational dynamics allow the frameworks to access different conformational structures that allow better packing and/or more favorable adsorbate/adsorbent interactions for specific molecules. As such, the adsorption selectivity and capacity can be heavily influenced by the rotational dynamics. Still, the majority of adsorption simulations in MOFs treat the adsorbing materials as rigid, which may not capture the actual behavior of the MOF. As the rotational dynamics of the linkers are generally restricted by guest inclusion, it provides a pathway for reversible guest-dependent optical properties, such as switching on of fluorescence and switching-off second-harmonic generation upon guest inclusion.

Even though rotational dynamics are fairly prevalent in MOFs, their impact is often understated or entirely ignored. Traditional microporous materials, such as zeolites and activated carbon cannot display similar rotational dynamics. Yet, other emerging families of microporous materials, like porous organic frameworks (POFs) and porous organic cages should be expected to exhibit similar behavior. So far, research has primarily analyzed the properties that derive from rotation, but we expect growth in the exploitation of rotation as a valuable design factor in functional nanomaterials. In particular, more explicit cases of modulation of gas adsorption based on tunable rotational dynamics can be forecast, as the interplay between these two phenomena is becoming more understood. An especially exciting prospect is the attainment of coherent motion within MOFs, which might enable these ordered microporous materials to behave as artificial nanomachine platforms able to perform useful work.

## 1.6. References

1. Furukawa, H., Cordova, K. E., O’Keeffe, M. & Yaghi, O. M. The Chemistry and Applications of Metal–Organic Frameworks. *Science* **341**, 1230444 (2013).
2. Schneemann, A., Bon, V., Schwedler, I., Senkowska, I., Kaskel, S. & Fischer, R. A. Flexible metal–organic frameworks. *Chem. Soc. Rev.* **43**, 6062–6096 (2014).
3. Khuong, T.-A. A. V, Nunez, J. E., Godinez, C. E., Garcia-Garibay, M. A., Nuñez, J. E., Godinez, C. E. & Garcia-Garibay, M. A. Crystalline molecular machines: A quest toward solid-state dynamics and function. *Acc. Chem. Res.* **39**, 413–422 (2006).
4. Moggach, S. A., Bennett, T. D. & Cheetham, A. K. The Effect of Pressure on ZIF-8: Increasing Pore Size with Pressure and the Formation of a High-Pressure Phase at 1.47 GPa. *Angew. Chemie Int. Ed.* **48**, 7087–7089 (2009).
5. Fairen-Jimenez, D., Moggach, S. A., Wharmby, M. T., Wright, P. A., Parsons, S. & Düren, T. Opening the Gate: Framework Flexibility in ZIF-8 Explored by Experiments and Simulations. *J. Am. Chem. Soc.* **133**, 8900–8902 (2011).
6. Catalano, L. & Naumov, P. Exploiting rotational motion in molecular crystals. *CrystEngComm* **20**, 5872–5883 (2018).
7. Vogelsberg, C. S. & Garcia-Garibay, M. A. Crystalline molecular machines: function, phase order, dimensionality, and composition. *Chem. Soc. Rev.* **41**, 1892–1910 (2012).
8. Khudozhnikov, A. E., Kolokolov, D. I. & Stepanov, A. G. Characterization of Fast Restricted Librations of Terephthalate Linkers in MOF UiO-66(Zr) by <sup>2</sup>H NMR Spin–Lattice Relaxation Analysis. *J. Phys. Chem. C* **122**, 12956–12962 (2018).
9. Moreau, F., Kolokolov, D. I., Stepanov, A. G., Easun, T. L., Dailly, A., Lewis, W., Blake, A. J., Nowell, H., Lennox, M. J., Besley, E., Yang, S. & Schröder, M. Tailoring porosity and rotational dynamics in a series of octacarboxylate metal–organic frameworks. *Proc. Natl. Acad. Sci.* **114**, 3056–3061 (2017).
10. Vogelsberg, C. S., Uribe-Romo, F. J., Lipton, A. S., Yang, S., Houk, K. N., Brown, S. & Garcia-Garibay, M. A. Ultrafast rotation in an amphidynamic crystalline metal organic framework. *Proc. Natl. Acad. Sci.* **114**, 13613–13618 (2017).
11. Knebel, A., Geppert, B., Volgmann, K., Kolokolov, D. I., Stepanov, A. G., Twiefel, J., Heitjans, P., Volkmer, D. & Caro, J. Defibrillation of soft porous metal–organic frameworks with electric fields. *Science* **358**, 347–351 (2017).
12. Yan, Y., Kolokolov, D. I., da Silva, I., Stepanov, A. G., Blake, A. J., Dailly, A., Manuel, P., Tang, C. C., Yang, S. & Schröder, M. Porous Metal–Organic Polyhedral Frameworks with Optimal Molecular Dynamics and Pore Geometry for Methane Storage. *J. Am. Chem. Soc.* **139**, 13349–13360 (2017).
13. Kottas, G. S., Clarke, L. I., Horinek, D. & Michl, J. Artificial Molecular Rotors. *Chem. Rev.* **105**, 1281–1376 (2005).
14. Gonzalez, J., Nandini Devi, R., Tunstall, D. P., Cox, P. A. & Wright, P. A. Deuterium NMR studies of framework and guest mobility in the metal–organic framework compound MOF-5, Zn<sub>4</sub>O(O<sub>2</sub>CC<sub>6</sub>H<sub>4</sub>CO<sub>2</sub>)<sub>3</sub>. *Microporous Mesoporous Mater.* **84**, 97–104 (2005).
15. Spiess, H. W. Molecular dynamics of solid polymers as revealed by deuterium NMR. *Colloid Polym. Sci.* **261**, 193–209 (1983).
16. Gould, S. L., Tranchemontagne, D., Yaghi, O. M. & Garcia-Garibay, M. A. Amphidynamic character of crystalline MOF-5: Rotational dynamics of terephthalate phenylenes in a free-volume, sterically unhindered environment. *J. Am. Chem. Soc.* **130**, 3246–3247 (2008).
17. Zhou, W. & Yildirim, T. Lattice dynamics of metal–organic frameworks: Neutron inelastic scattering and first-principles calculations. *Phys. Rev. B* **74**, 180301 (2006).
18. Kolokolov, D. I., Jobic, H., Stepanov, A. G., Guillermin, V., Devic, T., Serre, C. & Férey, G.

- Dynamics of benzene rings in MIL-53(Cr) and MIL-47(V) frameworks studied by <sup>2</sup>H NMR spectroscopy. *Angew. Chemie - Int. Ed.* **49**, 4791–4794 (2010).
19. Kolokolov, D. I., Stepanov, A. G. & Jobic, H. Guest controlled rotational dynamics of terephthalate phenylenes in metal-organic framework MIL-53(Al): Effect of different xylene loadings. *J. Phys. Chem. C* **118**, 15978–15984 (2014).
  20. Khudozhitkov, A. E., Jobic, H., Freude, D., Haase, J., Kolokolov, D. I. & Stepanov, A. G. Ultraslow Dynamics of a Framework Linker in MIL-53 (Al) as a Sensor for Different Isomers of Xylene. *J. Phys. Chem. C* **120**, 21704–21709 (2016).
  21. Khudozhitkov, A. E., Jobic, H., Kolokolov, D. I., Freude, D., Haase, J. & Stepanov, A. G. Probing the Guest-Mediated Structural Mobility in the UiO-66(Zr) Framework by <sup>2</sup>H NMR Spectroscopy. *J. Phys. Chem. C* **66**, acs.jpcc.7b03259 (2017).
  22. Kolokolov, D. I., Stepanov, A. G., Guillerm, V., Serre, C., Frick, B. & Jobic, H. Probing the dynamics of the porous Zr terephthalate UiO-66 framework using <sup>2</sup>H NMR and neutron scattering. *J. Phys. Chem. C* **116**, 12131–12136 (2012).
  23. Khudozhitkov, A. E., Kolokolov, D. I., Stepanov, A. G., Bolotov, V. A. & Dybtsev, D. N. Metal-Cation-Independent Dynamics of Phenylene Ring in Microporous MOFs: A <sup>2</sup>H Solid-State NMR Study. *J. Phys. Chem. C* **119**, 28038–28045 (2015).
  24. Ryder, M. R., Van De Voorde, B., Civalleri, B., Bennett, T. D., Mukhopadhyay, S., Cinque, G., Fernandez-Alonso, F., De Vos, D., Rudić, S. & Tan, J. C. Detecting Molecular Rotational Dynamics Complementing the Low-Frequency Terahertz Vibrations in a Zirconium-Based Metal-Organic Framework. *Phys. Rev. Lett.* **118**, 1–6 (2017).
  25. Shustova, N. B., Ong, T.-C., Cozzolino, A. F., Michaelis, V. K., Griffin, R. G. & Dincă, M. Phenyl Ring Dynamics in a Tetraphenylethylene-Bridged Metal–Organic Framework: Implications for the Mechanism of Aggregation-Induced Emission. *J. Am. Chem. Soc.* **134**, 15061–15070 (2012).
  26. Horike, S., Matsuda, R., Tanaka, D., Matsubara, S., Mizuno, M., Endo, K. & Kitagawa, S. Dynamic motion of building blocks in porous coordination polymers. *Angew. Chemie - Int. Ed.* **45**, 7226–7230 (2006).
  27. Li, B., Wen, H.-M., Wang, H., Wu, H., Tyagi, M., Yildirim, T., Zhou, W. & Chen, B. A Porous Metal–Organic Framework with Dynamic Pyrimidine Groups Exhibiting Record High Methane Storage Working Capacity. *J. Am. Chem. Soc.* **136**, 6207–6210 (2014).
  28. Bastien, G., Lemouchi, C., Wzietek, P., Simonov, S., Zorina, L., Rodríguez-Fortea, A., Canadell, E. & Batail, P. A crystalline hybrid of paddlewheel copper(II) dimers and molecular rotors: Singlet-triplet dynamics revealed by variable-temperature proton spin-lattice relaxation. *Zeitschrift fur Anorg. und Allg. Chemie* **640**, 1127–1133 (2014).
  29. Bracco, S., Castiglioni, F., Comotti, A., Galli, S., Negroni, M., Maspero, A. & Sozzani, P. Ultrafast Molecular Rotors and Their CO<sub>2</sub> Tuning in MOFs with Rod-Like Ligands. *Chem. - A Eur. J.* **23**, 11210–11215 (2017).
  30. Pakhira, S., Takayanagi, M. & Nagaoka, M. Diverse Rotational Flexibility of Substituted Dicarboxylate Ligands in Functional Porous Coordination Polymers. *J. Phys. Chem. C* **119**, 28789–28799 (2015).
  31. Inukai, M., Tamura, M., Horike, S., Higuchi, M., Kitagawa, S. & Nakamura, K. Storage of CO<sub>2</sub> into Porous Coordination Polymer Controlled by Molecular Rotor Dynamics. *Angew. Chemie Int. Ed.* **57**, 8687–8690 (2018).
  32. Inukai, M., Fukushima, T., Hijikata, Y., Ogiwara, N., Horike, S. & Kitagawa, S. Control of Molecular Rotor Rotational Frequencies in Porous Coordination Polymers Using a Solid-Solution Approach. *J. Am. Chem. Soc.* **137**, 12183–12186 (2015).
  33. Jiang, X., Duan, H.-B., Khan, S. I. & Garcia-Garibay, M. A. Diffusion-Controlled Rotation of Triptycene in a Metal–Organic Framework (MOF) Sheds Light on the Viscosity of MOF-Confined Solvent. *ACS Cent. Sci.* **2**, 608–613 (2016).

34. Liu, Y., Her, J. H., Dailly, A., Ramirez-Cuesta, A. J., Neumann, D. A. & Brown, C. M. Reversible structural transition in MIL-53 with large temperature hysteresis. *J. Am. Chem. Soc.* **130**, 11813–11818 (2008).
35. Coudert, F. X. F.-X. Molecular Mechanism of Swing Effect in Zeolitic Imidazolate Framework ZIF-8: Continuous Deformation upon Adsorption. *CHEMPHYSICHEM* **18**, 2732–2738 (2017).
36. Kolokolov, D. I., Stepanov, A. G. & Jobic, H. Mobility of the 2-Methylimidazolate Linkers in ZIF-8 Probed by <sup>2</sup>H NMR: Saloon Doors for the Guests. *J. Phys. Chem. C* **119**, 27512–27520 (2015).
37. Hobday, C. L., Bennett, T. D., Fairen-Jimenez, D., Graham, A. J., Morrison, C. A., Allan, D. R., Düren, T. & Moggach, S. A. Tuning the Swing Effect by Chemical Functionalization of Zeolitic Imidazolate Frameworks. *J. Am. Chem. Soc.* **140**, 382–387 (2018).
38. Chaplais, G., Fraux, G., Paillaud, J.-L., Marichal, C., Nouali, H., Fuchs, A. H., Coudert, F.-X. & Patarin, J. Impacts of the Imidazolate Linker Substitution (CH 3, Cl or Br) on the Structural and Adsorptive Properties of ZIF-8. *J. Phys. Chem. C* [acs.jpcc.8b08706](https://doi.org/10.1021/acs.jpcc.8b08706) (2018) doi:10.1021/acs.jpcc.8b08706.
39. Li, Q., Zaczek, A. J., Korter, T. M., Zeitler, J. A. & Ruggiero, M. T. Methyl-rotation dynamics in metal–organic frameworks probed with terahertz spectroscopy. *Chem. Commun.* **54**, 5776–5779 (2018).
40. Zhou, W., Wu, H., Udovic, T. J., Rush, J. J. & Yildirim, T. Quasi-Free Methyl Rotation in Zeolitic Imidazolate Framework-8. *J. Phys. Chem. A* **112**, 12602–12606 (2008).
41. Zheng, B., Fu, F., Wang, L. L., Yang, L., Zhu, Y. & Du, H. Investigation of the Linker Swing Motion in the Zeolitic Imidazolate Framework ZIF-90. *J. Phys. Chem. C* **122**, 7203–7209 (2018).
42. Morris, W., Taylor, R. E., Dybowski, C., Yaghi, O. M. & Garcia-Garibay, M. A. Framework mobility in the metal-organic framework crystal IRMOF-3: Evidence for aromatic ring and amine rotation. *J. Mol. Struct.* **1004**, 94–101 (2011).
43. Loeb, S. J. Rotaxanes as ligands: from molecules to materials. *Chem. Soc. Rev.* **36**, 226–235 (2007).
44. Deng, H., Olson, M. A., Stoddart, J. F. & Yaghi, O. M. Robust dynamics. *Nat. Chem.* **2**, 439–443 (2010).
45. Vukotic, V. N., Harris, K. J., Zhu, K., Schurko, R. W. & Loeb, S. J. Metal–organic frameworks with dynamic interlocked components. *Nat. Chem.* **4**, 456–460 (2012).
46. Zhu, K., Vukotic, V. N., O’Keefe, C. A., Schurko, R. W., Loeb, S. J., Okeefe, C. A., Schurko, R. W., Loeb, S. J., O’Keefe, C. A., Schurko, R. W. & Loeb, S. J. Metal–Organic Frameworks with Mechanically Interlocked Pillars: Controlling Ring Dynamics in the Solid-State via a Reversible Phase Change. *J. Am. Chem. Soc.* **136**, 7403–7409 (2014).
47. Vukotic, V. N., O’Keefe, C. A., Zhu, K., Harris, K. J., To, C., Schurko, R. W. & Loeb, S. J. Mechanically Interlocked Linkers inside Metal–Organic Frameworks: Effect of Ring Size on Rotational Dynamics. *J. Am. Chem. Soc.* **137**, 9643–9651 (2015).
48. Farahani, N., Zhu, K., O’Keefe, C. A., Schurko, R. W. & Loeb, S. J. Thermally Driven Dynamics of a Rotaxane Wheel about an Imidazolium Axle inside a Metal–Organic Framework. *Chempluschem* **81**, 836–841 (2016).
49. Karlen, S. D. & Garcia-Garibay, M. A. Amphidynamic Crystals: Structural Blueprints for Molecular Machines. *Mol. Mach.* **262**, 179–227 (2005).
50. Wittebort, R. J., Olejniczak, E. T. & Griffin, R. G. Analysis of deuterium nuclear magnetic resonance line shapes in anisotropic media. *J. Chem. Phys.* **86**, 5411–5420 (1987).
51. Sutrisno, A. & Huang, Y. Solid-state NMR: A powerful tool for characterization of metal-organic frameworks. *Solid State Nucl. Magn. Reson.* **49–50**, 1–11 (2013).
52. Henrichs, P. M., Hewitt, J. M. & Linder, M. Experimental Aspects of Deuterium NMR of

- Solids. *J. Magn. Reson.* **60**, 280–298 (1984).
53. Damron, J. T., Ma, J., Kurz, R., Saalwächter, K., Matzger, A. J. & Ramamoorthy, A. The Influence of Chemical Modification on Linker Rotational Dynamics in Metal–Organic Frameworks. *Angew. Chemie - Int. Ed.* **57**, 8678–8681 (2018).
54. Kremer, F. & Schonhals, A. *Broadband Dielectric Spectroscopy*. (Springer-Verlag: Berlin, Heidelberg, 2003).
55. Winston, E. B., Lowell, P. J., Vacek, J., Chocholoušová, J., Michl, J. & Price, J. C. Dipolar molecular rotors in the metal–organic framework crystal IRMOF-2. *Phys. Chem. Chem. Phys.* **10**, 5188 (2008).
56. Devautour-Vinot, S., Maurin, G., Serre, C., Horcajada, P., Paula Da Cunha, D., Guillemin, V., De Souza Costa, E., Taulelle, F. & Martineau, C. Structure and dynamics of the functionalized MOF type UiO-66(Zr): NMR and dielectric relaxation spectroscopies coupled with DFT calculations. *Chem. Mater.* **24**, 2168–2177 (2012).
57. Frunza, S., Schönhals, A., Frunza, L., Ganea, P., Kosslick, H., Harloff, J. & Schulz, A. Molecular relaxation processes in a MOF-5 structure revealed by broadband dielectric spectroscopy: Signature of phenylene ring fluctuations. *J. Phys. Chem. B* **114**, 12840–12846 (2010).
58. Balčiūnas, S., Šimėnas, M., Pavlovaitė, D., Kinka, M., Shieh, F.-K., Wu, K. C.-W., Banys, J. & Grigalaitis, R. Low-Frequency Dipolar Dynamics and Atmospheric Effects in ZIF-90 Metal–Organic Framework. *J. Phys. Chem. C* **123**, 631–636 (2019).
59. Greaves, G. N., Meneau, F., Majérus, O., Jones, D. G. & Taylor, J. Identifying vibrations that destabilize crystals and characterize the glassy state. *Science* **308**, 1299–302 (2005).
60. Ryder, M. R., Civalleri, B., Bennett, T. D., Henke, S., Rudić, S., Cinque, G., Fernandez-Alonso, F. & Tan, J.-C. Identifying the Role of Terahertz Vibrations in Metal–Organic Frameworks: From Gate-Opening Phenomenon to Shear-Driven Structural Destabilization. *Phys. Rev. Lett.* **113**, 215502 (2014).
61. Tan, N. Y., Ruggiero, M. T., Orellana-Tavra, C., Tian, T., Bond, A. D., Korter, T. M., Fairen-Jimenez, D. & Axel Zeitler, J. Investigation of the terahertz vibrational modes of ZIF-8 and ZIF-90 with terahertz time-domain spectroscopy. *Chem. Commun.* **51**, 16037–16040 (2015).
62. Kuc, A., Enyashin, A. & Seifert, G. Metal–Organic Frameworks: Structural, Energetic, Electronic, and Mechanical Properties. *J. Phys. Chem. B* **111**, 8179–8186 (2007).
63. Kolokolov, D. I., Jobic, H., Stepanov, A. G., Plazanet, M., Zbiri, M., Ollivier, J., Guillemin, V., Devic, T., Serre, C. & Férey, G. Comparison of the dynamics of MIL-53(Cr) and MIL-47(V) frameworks using neutron scattering and DFT methods. *Eur. Phys. J. Spec. Top.* **189**, 263–271 (2010).
64. Burtch, N. C., Torres-Knoop, A., Foo, G. S., Leisen, J., Sievers, C., Ensing, B., Dubbeldam, D. & Walton, K. S. Understanding DABCO Nanorotor Dynamics in Isostructural Metal–Organic Frameworks. *J. Phys. Chem. Lett.* **6**, 812–816 (2015).
65. Burtch, N. C., Dubbeldam, D. & Walton, K. S. Investigating water and framework dynamics in pillared MOFs. *Mol. Simul.* **41**, 1379–1387 (2015).
66. Namsani, S. & Yazaydin, A. O. Electric field induced rotation of halogenated organic linkers in isorecticular metal–organic frameworks for nanofluidic applications. *Mol. Syst. Des. Eng.* **3**, 951–958 (2018).
67. Haldoupis, E., Watanabe, T., Nair, S. & Sholl, D. S. Quantifying Large Effects of Framework Flexibility on Diffusion in MOFs: CH<sub>4</sub> and CO<sub>2</sub> in ZIF-8. *ChemPhysChem* **13**, 3449–3452 (2012).
68. Parkes, M. V., Demir, H., Teich-McGoldrick, S. L., Sholl, D. S., Greathouse, J. A. & Allendorf, M. D. Molecular dynamics simulation of framework flexibility effects on noble gas diffusion in HKUST-1 and ZIF-8. *Microporous Mesoporous Mater.* **194**, 190–199

- (2014).
69. Elsaidi, S. K., Mohamed, M. H., Simon, C. M., Braun, E., Pham, T., Forrest, K. A., Xu, W., Banerjee, D., Space, B., Zaworotko, M. J. & Thallapally, P. K. Effect of ring rotation upon gas adsorption in SIFSIX-3-M (M = Fe, Ni) pillared square grid networks. *Chem. Sci.* **8**, 2373–2380 (2017).
  70. Laio, A. & Gervasio, F. L. Metadynamics: a method to simulate rare events and reconstruct the free energy in biophysics, chemistry and material science. *Reports Prog. Phys.* **71**, 126601 (2008).
  71. Vymětal, J. & Vondrášek, J. Metadynamics As a Tool for Mapping the Conformational and Free-Energy Space of Peptides — The Alanine Dipeptide Case Study. *J. Phys. Chem. B* **114**, 5632–5642 (2010).
  72. Haigis, V., Coudert, F.-X., Vuilleumier, R., Boutin, A. & Fuchs, A. H. Hydrothermal Breakdown of Flexible Metal–Organic Frameworks: A Study by First-Principles Molecular Dynamics. *J. Phys. Chem. Lett.* **6**, 4365–4370 (2015).
  73. Chen, S., Lucier, B. E. G., Boyle, P. D. & Huang, Y. Understanding The Fascinating Origins of CO<sub>2</sub> Adsorption and Dynamics in MOFs. *Chem. Mater.* **28**, 5829–5846 (2016).
  74. Katsoulidis, A. P., Antypov, D., Whitehead, G. F. S., Carrington, E. J., Adams, D. J., Berry, N. G., Darling, G. R., Dyer, M. S. & Rosseinsky, M. J. Chemical control of structure and guest uptake by a conformationally mobile porous material. (2019) doi:10.1038/s41586-018-0820-9.
  75. Yang, W., Davies, A. J., Lin, X., Suyetin, M., Matsuda, R., Blake, A. J., Wilson, C., Lewis, W., Parker, J. E., Tang, C. C., George, M. W., Hubberstey, P., Kitagawa, S., Sakamoto, H., Bichoutskaia, E., Champness, N. R., Yang, S. & Schröder, M. Selective CO<sub>2</sub> uptake and inverse CO<sub>2</sub>/C<sub>2</sub>H<sub>2</sub> selectivity in a dynamic bifunctional metal–organic framework. *Chem. Sci.* **3**, 2993 (2012).
  76. Murdock, C. R., McNutt, N. W., Keffer, D. J. & Jenkins, D. M. Rotating Phenyl Rings as a Guest-Dependent Switch in Two-Dimensional Metal–Organic Frameworks. *J. Am. Chem. Soc.* **136**, 671–678 (2014).
  77. Hyun, S., Lee, J. H., Jung, G. Y., Kim, Y. K., Kim, T. K., Jeoung, S., Kwak, S. K., Moon, D. & Moon, H. R. Exploration of Gate-Opening and Breathing Phenomena in a Tailored Flexible Metal–Organic Framework. *Inorg. Chem.* **55**, 1920–1925 (2016).
  78. Yue, Y., Rabone, J. A., Liu, H., Mahurin, S. M., Li, M.-R., Wang, H., Lu, Z., Chen, B., Wang, J., Fang, Y. & Dai, S. A Flexible Metal–Organic Framework: Guest Molecules Controlled Dynamic Gas Adsorption. *J. Phys. Chem. C* **119**, 9442–9449 (2015).
  79. Sakaida, S., Otsubo, K., Sakata, O., Song, C., Fujiwara, A., Takata, M. & Kitagawa, H. Crystalline coordination framework endowed with dynamic gate-opening behaviour by being downsized to a thin film. *Nat. Chem.* **8**, 377–383 (2016).
  80. Serra-Crespo, P., Gobechiya, E., Ramos-Fernandez, E. V., Juan-Alcañiz, J., Martinez-Joaristi, A., Stavitski, E., Kirschhock, C. E. A., Martens, J. A., Kapteijn, F. & Gascon, J. Interplay of Metal Node and Amine Functionality in NH<sub>2</sub>-MIL-53: Modulating Breathing Behavior through Intra-framework Interactions. *Langmuir* **28**, 12916–12922 (2012).
  81. Bux, H., Liang, F., Li, Y., Cravillon, J., Wiebcke, M. & Caro, J. Zeolitic Imidazolate Framework Membrane with Molecular Sieving Properties by Microwave-Assisted Solvothermal Synthesis. *J. Am. Chem. Soc.* **131**, 16000–16001 (2009).
  82. Fairen-Jimenez, D., Galvelis, R., Torrisi, A., Gellan, A. D., Wharmby, M. T., Wright, P. A., Mellot-Draznieks, C. & Düren, T. Flexibility and swing effect on the adsorption of energy-related gases on ZIF-8: combined experimental and simulation study. *Dalt. Trans.* **41**, 10752 (2012).
  83. Van Den Bergh, J., Gücüyener, C., Pidko, E. A., Hensen, E. J. M., Gascon, J. & Kapteijn, F.

- Understanding the anomalous alkane selectivity of ZIF-7 in the separation of light alkane/alkene mixtures. *Chem. - A Eur. J.* **17**, 8832–8840 (2011).
84. Gücüyener, C., Van Den Bergh, J., Gascon, J. & Kapteijn, F. Ethane/ethene separation turned on its head: Selective ethane adsorption on the metal-organic framework ZIF-7 through a gate-opening mechanism. *J. Am. Chem. Soc.* **132**, 17704–17706 (2010).
85. Banerjee, D., Wang, H., Plonka, A. M., Emge, T. J., Parise, J. B. & Li, J. Direct Structural Identification of Gas Induced Gate-Opening Coupled with Commensurate Adsorption in a Microporous Metal–Organic Framework. *Chem. - A Eur. J.* **22**, 11816–11825 (2016).
86. Seo, J., Matsuda, R., Sakamoto, H., Bonneau, C. & Kitagawa, S. A Pillared-Layer Coordination Polymer with a Rotatable Pillar Acting as a Molecular Gate for Guest Molecules. *J. Am. Chem. Soc.* **131**, 12792–12800 (2009).
87. Zhang, J.-P. & Chen, X.-M. Optimized Acetylene/Carbon Dioxide Sorption in a Dynamic Porous Crystal. *J. Am. Chem. Soc.* **131**, 5516–5521 (2009).
88. Zhang, Z., Yang, Q., Cui, X., Yang, L., Bao, Z., Ren, Q. & Xing, H. Sorting of C 4 Olefins with Interpenetrated Hybrid Ultramicroporous Materials by Combining Molecular Recognition and Size-Sieving. *Angew. Chemie Int. Ed.* **56**, 16282–16287 (2017).
89. Andres-Garcia, E., Oar-Arteta, L., Gascon, J. & Kapteijn, F. ZIF-67 as silver-bullet in adsorptive propane/propylene separation. *Chem. Eng. J.* **360**, 10–14 (2019).
90. Hartmann, M., Böhme, U., Hovestadt, M. & Paula, C. Adsorptive Separation of Olefin/Paraffin Mixtures with ZIF-4. *Langmuir* **31**, 12382–12389 (2015).
91. Böhme, U., Barth, B., Paula, C., Kuhnt, A., Schwieger, W., Mundstock, A., Caro, J. & Hartmann, M. Ethene/Ethane and Propene/Propane Separation via the Olefin and Paraffin Selective Metal–Organic Framework Adsorbents CPO-27 and ZIF-8. *Langmuir* **29**, 8592–8600 (2013).
92. Zhang, L., Jiang, K., Jiang, M., Yue, D., Wan, Y., Xing, H., Yang, Y., Cui, Y., Chen, B. & Qian, G. A highly stable amino-coordinated MOF for unprecedented block off N 2 adsorption and extraordinary CO 2 /N 2 separation. *Chem. Commun.* **52**, 13568–13571 (2016).
93. Luna-Triguero, A., Vicent-Luna, J. M. & Calero, S. Phase Transition Induced by Gas Adsorption in Metal–Organic Frameworks. *Chem. - A Eur. J.* **24**, 8530–8534 (2018).
94. Ania, C. O., García-Pérez, E., Haro, M., Gutiérrez-Sevillano, J. J., Valdés-Solís, T., Parra, J. B. & Calero, S. Understanding gas-induced structural deformation of ZIF-8. *J. Phys. Chem. Lett.* **3**, 1159–1164 (2012).
95. Kanoo, P., Reddy, S. K., Kumari, G., Haldar, R., Narayana, C., Balasubramanian, S. & Maji, T. K. Unusual room temperature CO2 uptake in a fluoro-functionalized MOF: insight from Raman spectroscopy and theoretical studies. *Chem. Commun.* **48**, 8487 (2012).
96. Gee, J. A. & Sholl, D. S. Effect of Framework Flexibility on C 8 Aromatic Adsorption at High Loadings in Metal–Organic Frameworks. *J. Phys. Chem. C* **120**, 370–376 (2016).
97. Hong, Y., Lam, J. W. Y. & Tang, B. Z. Aggregation-induced emission. *Chem. Soc. Rev.* **40**, 5361 (2011).
98. Qin, A., Jim, C. K. W., Tang, Y., Lam, J. W. Y., Liu, J., Mahtab, F., Gao, P. & Tang, B. Z. Aggregation-Enhanced Emissions of Intramolecular Excimers in Disubstituted Polyacetylenes. *J. Phys. Chem. B* **112**, 9281–9288 (2008).
99. Dong, Y., Lam, J. W. Y., Qin, A., Liu, J., Li, Z., Tang, B. Z., Sun, J. & Kwok, H. S. Aggregation-induced emissions of tetraphenylethene derivatives and their utilities as chemical vapor sensors and in organic light-emitting diodes. *Appl. Phys. Lett.* **91**, 011111 (2007).
100. Shustova, N. B., McCarthy, B. D. & Dincă, M. Turn-On Fluorescence in Tetraphenylethylene-Based Metal–Organic Frameworks: An Alternative to Aggregation-Induced Emission. *J. Am. Chem. Soc.* **133**, 20126–20129 (2011).
101. Du, T., Zhang, H., Ruan, J., Jiang, H., Chen, H.-Y. & Wang, X. Adjusting the Linear Range

- of Au-MOF Fluorescent Probes for Real-Time Analyzing Intracellular GSH in Living Cells. *ACS Appl. Mater. Interfaces* 10, 12417–12423 (2018).
102. Serra-Crespo, P., Van Der Veen, M. A., Gobechiya, E., Houthoofd, K., Filinchuk, Y., Kirschhock, C. E. A., Martens, J. A., Sels, B. F., De Vos, D. E., Kapteijn, F. & Gascon, J. NH<sub>2</sub>-MIL-53(Al): A high-contrast reversible solid-state nonlinear optical switch. *J. Am. Chem. Soc.* 134, 8314–8317 (2012).
  103. Balestra, S. R. G., Bueno-Perez, R., Hamad, S., Dubbeldam, D., Ruiz-Salvador, A. R. & Calero, S. Controlling Thermal Expansion: A Metal–Organic Frameworks Route. *Chem. Mater.* 28, 8296–8304 (2016).
  104. Collings, I. E., Tucker, M. G., Keen, D. A. & Goodwin, A. L. Geometric switching of linear to area negative thermal expansion in uniaxial metal–organic frameworks. *CrystEngComm* 16, 3498–3506 (2014).
  105. Lock, N., Wu, Y., Christensen, M., Cameron, L. J., Peterson, V. K., Bridgeman, A. J., Kepert, C. J. & Iversen, B. B. Elucidating Negative Thermal Expansion in MOF-5. *J. Phys. Chem. C* 114, 16181–16186 (2010).
  106. Lock, N., Christensen, M., Kepert, C. J. & Iversen, B. B. Effect of gas pressure on negative thermal expansion in MOF-5. *Chem. Commun.* 49, 789–791 (2013).
  107. Peterson, V. K., Kearley, G. J., Wu, Y., Ramirez-Cuesta, A. J., Kemner, E. & Kepert, C. J. Local Vibrational Mechanism for Negative Thermal Expansion: A Combined Neutron Scattering and First-Principles Study. *Angew. Chemie Int. Ed.* 49, 585–588 (2010).
  108. Wang, L., Wang, C., Sun, Y., Shi, K., Deng, S. & Lu, H. Large negative thermal expansion provided by metal-organic framework MOF-5: A first-principles study. *Mater. Chem. Phys.* 175, 138–145 (2016).
  109. Lock, N., Wu, Y., Christensen, M., Cameron, L. J., Peterson, V. K., Bridgeman, A. J., Kepert, C. J. & Iversen, B. B. Elucidating Negative Thermal Expansion in MOF-5. *J. Phys. Chem. C* 114, 16181–16186 (2010).
  110. Wang, L., Wang, C., Sun, Y., Shi, K., Deng, S. & Lu, H. Large negative thermal expansion provided by metal-organic framework MOF-5: A first-principles study. *Mater. Chem. Phys.* 175, 138–145 (2016).
  111. Pang, J., Liu, C., Huang, Y., Wu, M., Jiang, F., Yuan, D., Hu, F., Su, K., Liu, G. & Hong, M. Visualizing the Dynamics of Temperature- and Solvent-Responsive Soft Crystals. *Angew. Chemie - Int. Ed.* 55, 7478–7482 (2016).

# Chapter 2

## Emergence of cooperative rotor dynamics in metal–organic frameworks via tuned steric interactions

---

The organic components in metal-organic frameworks (MOFs) enjoy a unique situation: they are embedded in a crystalline lattice, yet, as they are separated from each other by tunable free space, a large variety of dynamic behavior can emerge. These rotational dynamics of the organic linkers are especially important due to their influence over properties such as gas adsorption and kinetics of guest release. In order to fully exploit linker rotation, it is necessary to engineer correlated linker dynamics to achieve their cooperative functional motion. This chapter shows that for MIL-53, a topology with closely spaced rotors, the phenylene functionalization allows to tune the rotors' steric environment, shifting linker rotation from completely static to rapid motions at frequencies above 100 MHz. For steric interactions that start to inhibit independent rotor motion, the emergence of correlated rotation modes in linker dynamics is observed. These findings pave the way for function-specific engineering of gearlike cooperative motion in MOFs.

---

This chapter is based on the following (submitted) publication:

Adrian Gonzalez-Nelson, Srinidhi Mula, Mantas Šimėnas, Sergejus Balčiūnas, Adam R. Altenhof, Cameron S. Vojvodin, Jūras Banys, Robert W. Schurko, François-Xavier Coudert, and Monique A. van der Veen, Emergence of cooperative rotor dynamics in metal–organic frameworks via tuned steric interactions, in review for *Journal of the American Chemical Society*, 2021

## 2.1. Introduction

The hybrid nature of metal–organic frameworks (MOFs) goes hand in hand with diverse and often complex behavior. The dynamic traits of these materials are increasingly capturing the curiosity of researchers in the field: MOFs show the potential of displaying intricate dynamics, similar to that observed in other materials built from closely interacting molecules, such as crowded movement of proteins in lipid bilayers<sup>1,2</sup> or concerted molecular motion in liquid crystals.<sup>3</sup> The organic components in MOFs are embedded in a crystalline lattice, yet, in contrast to traditional molecular crystals, they are separated from each other by modifiable free space, providing a handle to tune dynamic behavior in an ordered and stable supramolecular arrangement.<sup>4–6</sup>

A decade ago, Yaghi and Stoddart proposed that ‘robust dynamics’ could be achieved by mechanically interlocking organic components onto the linkers, such that they have the necessary freedom of mobility without compromising the MOF structure.<sup>7</sup> Since then, it has become evident that stable frameworks that display inherent rotational motion are in fact ubiquitous.<sup>8,9</sup> However, not all such frameworks are usable in practice, and the performance of a MOF in specific applications is highly dependent on its dynamic properties, a prime example being adsorption behavior in flexible MOFs.<sup>10–15</sup> Furthermore, MOF-based crystalline molecular machines will require external control of linker motion, making the engineering of correlated dynamics a necessary step to achieve cooperative functional mobility.<sup>5,6,16,17</sup>

Recent achievements in rotor-MOFs include engineering ultrafast rotation by decreasing the rotation energy barrier via molecular design,<sup>18,19</sup> reaching rates as high as those in gas or liquid phases. Additionally, the first example of unidirectional rotation in MOF linkers by the Feringa group<sup>20</sup> represents a crucial step towards attaining nanomotors embedded in a crystalline lattice that can produce useful work.<sup>21</sup> A recent study on rotor-MOFs presented evidence of steric interactions between rotating phenylene units within a single linker.<sup>22</sup> Yet, the understanding, let alone the engineering, of correlated dynamics based on steric interactions between linkers remains extremely limited.

The growing field of rotor-MOFs may benefit from inspiration drawn from the more developed field of crystalline molecular rotors. In many such systems, it has been found that in structures where rotor–rotor distances are small enough, the resulting steric interactions force the rotational dynamics to adopt correlated gearlike mechanisms.<sup>23–26</sup> This chapter demonstrates how correlated motions emerge in linker dynamics as the steric environment of the rotors is gradually modified. Linker functionalization is applied in the MIL-53 family of materials to tune both the pore dimensions and the rotor–rotor interactions. The MIL-53 topology proves to be an excellent choice due to its functionalization-dependent pore size configurations, *i.e.*, the metastability of two phases, large pore and narrow pore. Moreover, terephthalate-based organic linkers are very common among MOFs.

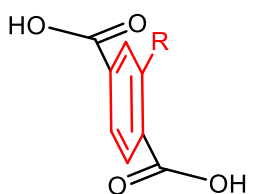
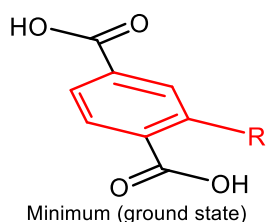
## 2.2. Results and discussion

To start, the intramolecular effects of linker functionalization on rotational motion will be addressed. As explained in Chapter 1, the benzene rings of terephthalate linkers can rotate with

respect to the carboxyl groups, which are fixed due to their coordination to the metal nodes. The maximum energy corresponds to a conformation where the benzene rings form a 90° angle with both carboxyl groups,<sup>27–29</sup> as the overlap between the *p* orbitals in the ring and in the carboxyl groups is minimized.

Density functional theory (DFT) calculations were used to model the intrinsic rotational energy barriers ( $\Delta E_{\text{rot}}$ ) of different functionalized terephthalic acids with different functional groups as the relative energy between the transition state and a planar conformer (Table 2.1 and Scheme 2.1). With respect to the unsubstituted terephthalic acid, most substituent groups decrease the  $\Delta E_{\text{rot}}$  barrier. In these cases, steric repulsion between the substituent group and the closest carboxyl oxygen likely destabilizes the planar configuration,<sup>25,30</sup> decreasing the energy difference between the transition state and the ground state. This effect is particularly significant in the nitro-substituted molecule (Figure A2.8), where the rotation barrier is the lowest at  $\Delta E_{\text{rot}} = 17.1 \text{ kJ mol}^{-1}$ , *i.e.*, less than  $7 k_B T$  at room temperature.

Only electron donating substituents, namely amino and hydroxy groups, cause an increase in  $\Delta E_{\text{rot}}$ . This is in fact mostly due to stabilization via a hydrogen bond with the adjacent carboxyl oxygen (1.93 Å for  $\text{NH}\cdots\text{O}$  and 1.75 Å  $\text{OH}\cdots\text{O}$ , see Figure A2.9). Indeed, simply breaking the H-bond by rotating the hydroxy group by 180° results in an energy penalty of 31 kJ mol<sup>-1</sup>. Conversely, the electron-donating methoxy substituent without H-bond formation shows a slight decrease in  $\Delta E_{\text{rot}}$ .



Maximum (transition state)

Scheme 2.1

Table 2.1. Calculated barriers for 180° rotation on terephthalic acid and its derivatives.

| R group | $\Delta E_{\text{rot}} / \text{kJ mol}^{-1 \dagger}$ |
|---------|--|
| -       | 47.7   |
| hydroxy | 64.2   |
| amino   | 53.7   |
| methoxy | 42.1   |
| cyano   | 34.5   |
| fluoro  | 35.9   |
| chloro  | 25.0   |
| bromo   | 25.1   |
| nitro   | 17.1   |

†The maximum energy state for each molecule ( $E_{90}$ ) is obtained from constrained geometry optimizations, setting the dihedral angles between carboxylic groups and ring to 90°. Relative values were obtained with respect to a planar conformation energy, see Appendix section A2.3.1 for details.

Experimental work on MIL-53<sup>31–33</sup> has established that its *p*-phenylene groups undergo rotation in the form of  $\pi$ -flips, exhibiting similar behavior to several other terephthalate-based MOFs.<sup>29,34–36</sup> The large-pore conformation of MIL-53 suggests that the rotating rings should not be subject to

significant steric effects. The rotator's closest interactions are between contiguous linkers in the same row (or pore wall): their closest ring-to-ring ( $-\text{CH}\cdots\text{HC}-$ ) distance possible is 2.3 Å, which means their van der Waals radii barely overlap. This spacing is limited yet sufficient for unfunctionalized terephthalate rotors to perform full rotations in the form of 180° rotations ( $\pi$ -flips), as evidenced experimentally.<sup>32</sup>

This spacing between the linkers in MIL-53 family is still relatively small, in contrast to other MOFs such as IRMOF and UiO-66 families. This suggests that ring substituents are likely to influence the dynamics of rotors. Based on the DFT calculations of the free linkers, two contrasting groups—nitro and amino—were selected to assess the impact of linker functionalization in the complete framework, a “crowded” environment. Moreover, for MIL-53 materials, functionalization has an important impact on the flexible crystalline conformation: guest-free  $\text{NO}_2$ -MIL-53(Al) and MIL-53(Al) are present in the large-pore form at ambient conditions,<sup>37,38</sup> while guest-free  $\text{NH}_2$ -MIL-53(Al) is present in the denser narrow-pore form (Figure 2.1).<sup>37,39,40</sup> Table 2.2 presents the characteristic distances between rotors in each form of the framework, showing how the difference in pore opening impacts row-to-row distance, but not rotor spacing within a row. The row-to-row distance of the narrow-pore amino-MOF indicates likely inter-row steric effects prohibiting full rotation of rings. For both functionalized frameworks, steric repulsion between neighboring linkers within the same row is expected.

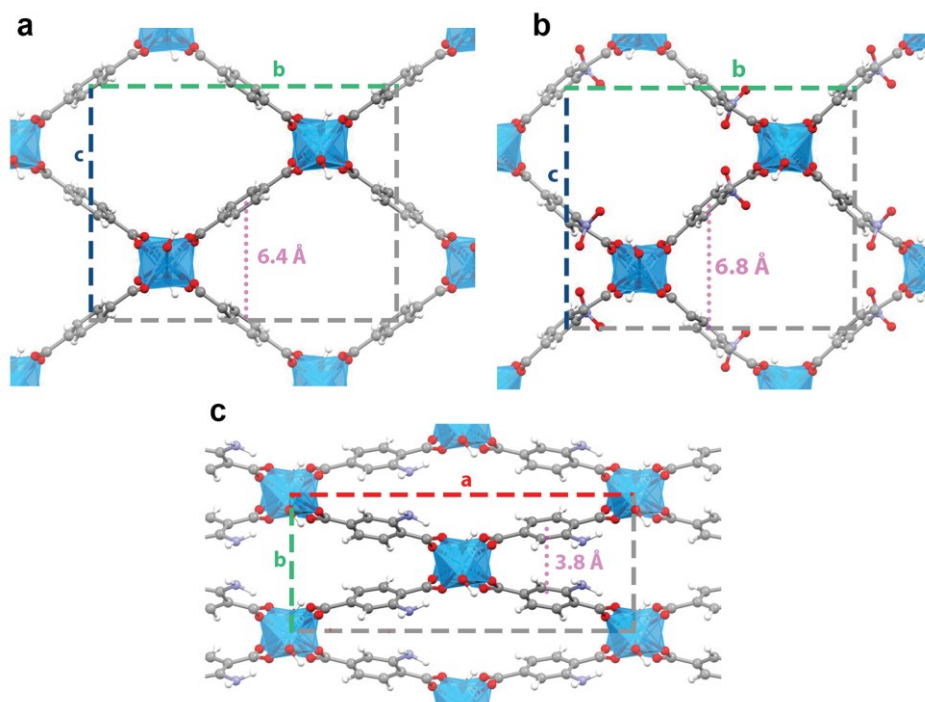


**Figure 2.1.** Structure of three members of the MIL-53 family viewed along the pore direction. **a**, MIL-53(Al), **b**,  $\text{NO}_2$ -MIL-53(Al), and **c**,  $\text{NH}_2$ -MIL-53(Al). This topology is characterized by four distinct rows of linkers per unit cell forming rhombic pores. Closest row distances for each MOF are marked in magenta. For complete unit cell parameters see Table A2.1.

**Table 2.2. Unit cell geometry influence on rotor spacing in MIL-53 frameworks.**

| MOF                         | Rotor spacing within row / Å* | Pore rhombus angle / ° | Row-to-row distance / Å† |
|-----------------------------|-------------------------------|------------------------|--------------------------|
| MIL-53(Al)                  | 6.6                           | 75.0                   | 6.4                      |
| NO <sub>2</sub> -MIL-53(Al) | 6.7                           | 79.5                   | 6.8                      |
| NH <sub>2</sub> -MIL-53(Al) | 6.6                           | 43.8                   | 3.8                      |

\* Defined as distance between neighboring C–C rotation axes, see Appendix section A2.3.2.

† For definition see Appendix section A2.3.2.

Each crystallographic unit cell contains four linkers. To explore the energy associated with linker rotation, rotation steps of ca. 30° on one linker were performed, starting from the global minimum conformation, followed by partial geometry optimization at each step. The rotational space of a nitroterephthalate linker is defined in Figure 2.2b (for aminoterephthalate see Figure A2.10). The obtained potential energy curves (or energy profiles as a function of rotation) are shown in Figure 2.2c. The energy profile of NH<sub>2</sub>-MIL-53 shows a very steep increase upon linker rotation, far larger in magnitude than the barrier calculated for the free linker (54 kJ mol<sup>-1</sup>). This is the result of row-to-row steric hindrance in the tightly packed narrow-pore phase (see Figure A2.11), indicating that large amplitude rotations are unlikely to occur in this MOF. For NO<sub>2</sub>-MIL-53(Al), energy minima are found at ±30° and ±150°, with expected maxima at ±90°, and local maxima at 0° and 180° due to steric effects experienced by the linker in the planar conformation (intramolecular, *vide supra*, and overlap between nitro and a hydrogen atom of the closest adjacent ring). The potential energy maxima of ~40 kJ mol<sup>-1</sup> is in the range of aromatic ring π-flips found in other MOFs,<sup>31,34,35,41,42</sup> which indicates the feasibility of linker rotation.

Nevertheless, these periodic single unit cell calculations force the nitro linkers in a row along [100] to rotate together, as they are periodic images of each other. Such an ordered motion limits other possible interactions between neighboring linkers in the same row. To consider non-synchronous rotation, the energy profile for the rotation of one linker in a 2x1x1 supercell was calculated (Figure 2.2c), where the same-row neighbor linker is not constrained and can move independently. Out of several combinations of nitro positions on the pair of rings, the one where nitro groups are located on identical carbon positions for each of the two cells was considered. This represents the scenario with most impactful steric effects between two rotors.

Here again, both possible directions of rotation were analyzed, and in most of the rotation space, similar values to those of the single cell calculations were found. However, negative rotation beyond -120°, where the two nitro groups of same-row neighbors come into close proximity, shows a very steep energy increase due to head-to-head NO<sub>2</sub> interactions that inhibit the rotational mobility (Figure 2.2d and Figure A2.12). Alternatively, when this part of the rotational space is reached via positive rotation beyond +180°, the same-row neighbor linker is pushed out of the way in a cooperative fashion (Figure A2.13), meaning that the simultaneous rotation of the neighbor linker makes the rotational event energetically feasible. Rotation in this direction could be described as gearlike: both linkers' nitro groups are in contact and they are both required to rotate simultaneously in order to allow movement.

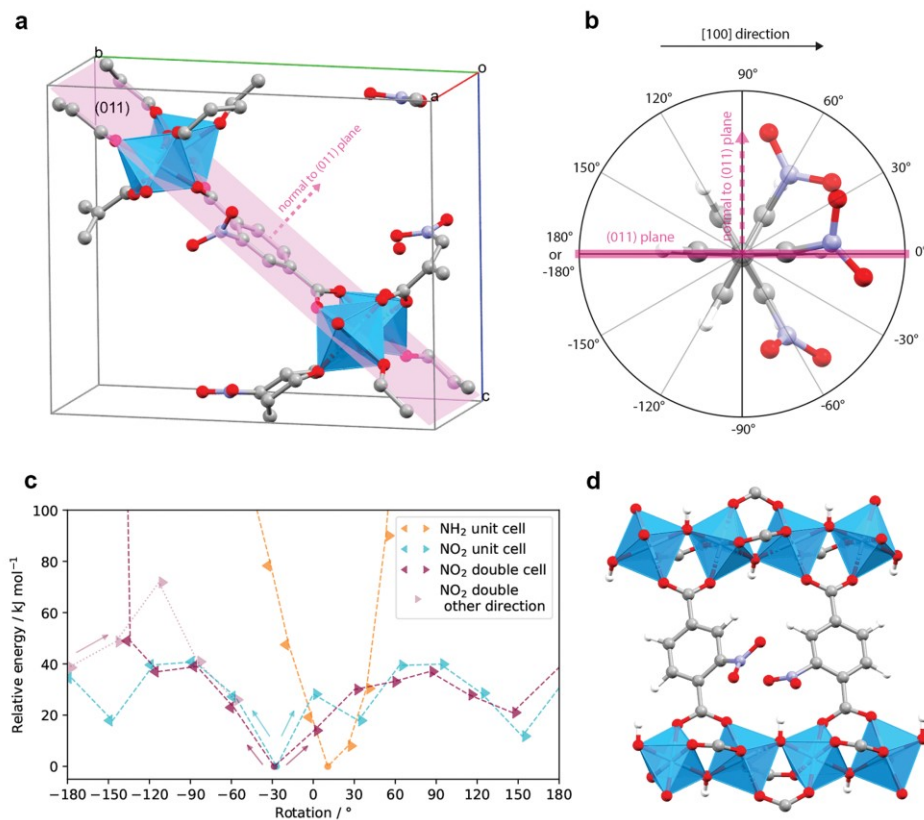


**Figure 2.2.** Effect of linker rotation on the potential energy as studied by DFT. **a**, Unit cell of NO<sub>2</sub>-MIL-53(Al) with central linker in 0° rotation with respect to (011) plane (pink); hydrogens omitted for clarity. **b**, Rotation angle is defined as the angle between benzene ring plane and (011) plane, taking 0° as the conformation with the functional group pointing in the positive [100] direction. The sign of the angle is assigned based on the direction normal of the reference plane. **c**, Potential energy profiles for NH<sub>2</sub>-MIL-53(Al) and NO<sub>2</sub>-MIL-53(Al) single and 2x1x1 supercell. The direction of rotation is indicated by the direction of the marker. **d**, Unfavorable head-to-head nitro group encounter in adjacent linkers in a supercell at -145° rotation.

In the alternative case where nitro groups are not in equivalent carbon positions in the two cells, profiles with significantly lower energies are obtained at angles where the nitro groups approach head-to-head (see Figures A2.14 and A2.15). These results indicate that, in contrast to the case of identical pairs, independent rotation of alternatively positioned nitrophenylene neighbors should not be ruled out. Hence, in a real system with disordered nitro positions, varying degrees of rotational mobility may be expected. Due to the size and positioning of its linkers, NO<sub>2</sub>-MIL-53 is a framework in which full rotations are energetically feasible, yet are unlikely to occur independently and in certain cases will require cooperativity between the motion of same-row linkers.<sup>23,24,26</sup>

Broadband dielectric spectroscopy (BDS) has proven particularly useful for probing the motion of MOF linkers containing polar functional groups.<sup>43–45</sup> The imaginary part ( $\epsilon''$ ) of the complex dielectric permittivity ( $\epsilon^* = \epsilon' - i\epsilon''$ ) contains information about the dynamic relaxation processes

of dipolar moieties in the dielectric material.<sup>46,47</sup> The temperature and frequency dependences of  $\epsilon''$  for MIL-53(Al), NH<sub>2</sub>-MIL-53(Al) and NO<sub>2</sub>-MIL-53(Al) are presented in Figure 2.3 and Figure A2.17. Peaks in  $\epsilon''$  correspond to dielectric losses due to dipolar motion, with the frequency of the maximum of  $\epsilon''$  corresponding to the mean relaxation time of the dipolar motion at that temperature.

NO<sub>2</sub>-MIL-53(Al) shows a strong relaxation process with peaks dispersed in terms of both frequency and temperature (Figure 2.3a and b), a feature typical of dipolar linker relaxations in MOFs.<sup>44,45,48</sup> In contrast, NH<sub>2</sub>-MIL-53(Al) shows no relaxation process (Figure 2.c), confirming a strongly hindered environment of the rotors, in correspondence with our DFT results. MIL-53(Al) (Figure 2.3d) exhibits a very weak dielectric relaxation, even though the mobile *p*-phenylene units do not have a permanent dipole. This may be due to small deformations of the linkers that lead to spontaneous dipole moments, or due to the presence of polar impurities.<sup>47</sup>

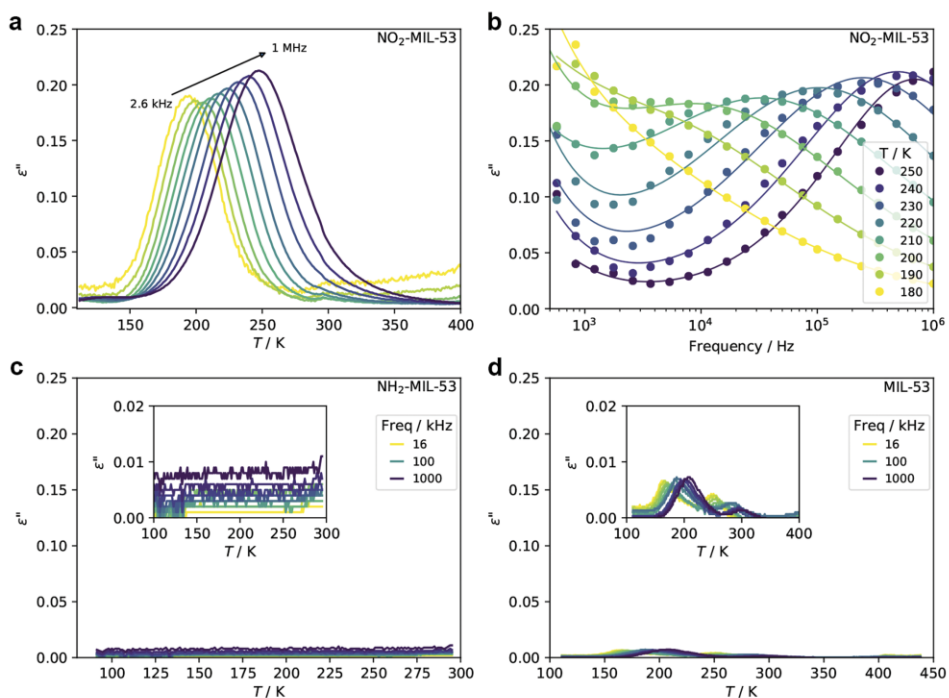


**Figure 2.3.** Dielectric spectra of the three systems. **a,b**, Imaginary part ( $\epsilon''$ ) of  $\epsilon^*$  for NO<sub>2</sub>-MIL-53(Al) with respect to temperature to (a) and frequency (b). The latter includes the fitted Cole-Cole model as continuous lines. **c,d**, Temperature dependence of  $\epsilon''$  for NH<sub>2</sub>-MIL-53(Al) (c) and MIL-53(Al) (d).

As expected, the dispersion frequency of the nitro linker relaxation increases with temperature, more specifically, from 2.6 kHz at 180 K to 1 MHz at 250 K. The frequency dependence of  $\epsilon^*$  at different temperatures was fitted using the Cole-Cole equation (Figure 2.3b and Figure A2.16). The best fits indicate a gradual increase of the dispersion broadness parameter ( $\alpha$ ) as temperature is decreased, from 0.3 at 250 K to 0.55 at 180 K (Figure A2.18). The broadening of the relaxation suggests a larger fraction of interacting dipoles exists when less thermal energy is available. It

should be noted, however, that BDS will not detect linkers whose dynamics fall outside the probed frequency range, in particular static linkers, meaning that potential rotation-impeding interactions such as the one illustrated in the DFT curve may not be covered in the dielectric spectra. Fitting the temperature dependence of the mean relaxation times to the Arrhenius equation delivers an activation energy  $E_a$  of  $32.3 \pm 1.3$  kJ mol<sup>-1</sup> and a pre-exponential factor  $\tau_0$  of  $3.4 \times 10^{-14}$  s (Figure A2.19). This activation energy is in between the DFT-estimated barriers for a single unit cell of this framework, *i.e.*, the smaller barrier at 0° and the larger barrier at ca. 90°. The obtained  $\tau_0$  value, equivalent to  $2.9 \times 10^{13}$  Hz, is larger than the expected attempt frequency based on estimations for *p*-phenylene rotators (usually on the order of  $10^{12}$  Hz).<sup>25</sup> This type of result is not uncommon for functionalized *p*-phenylene rotors,<sup>30,45,49</sup> and it may be interpreted as an indication of a small linear dependence of the rotational barrier with temperature (see Appendix section A2.3.5 for further discussion).<sup>50</sup> In NO<sub>2</sub>-MIL-53(Al), this could hint towards the progressive effect that thermal energy has on the rotor's environment due to increased conformational motions and nitro group rotations.<sup>51</sup>

To obtain specific information about the angular and frequency ranges of the nitro-functionalized linker dynamics, variable-temperature solid-state deuterium NMR (<sup>2</sup>H SSNMR) spectroscopy was employed. Spatial information about the deuterium exchange sites can be extracted from the NMR spectra by using relatively simple geometric models.<sup>52,53</sup> In addition, this technique is sensitive to all deuterium-labelled rings, and not only to the mobile ones. This enables us to obtain experimental information to complement the BDS data, especially for the nitro-functionalized framework, for which dynamics above 250 K could not be probed due to the high frequency limit. The results for ring-labelled MIL-53(Al)-d<sub>4</sub> (Figure A2.20) and NH<sub>2</sub>-MIL-53(Al)-d<sub>3</sub> (Figure A2.21) are in line with literature<sup>42,54,55</sup> as well as our expectations based on the DFT and BDS analyses. The <sup>2</sup>H SSNMR data for MIL-53(Al)-d<sub>4</sub> indicate that the phenylene rings undergo an increased rate of 180° reorientations (“π-flips”) at increased temperatures in the intermediate motion regime (IMR, 1 kHz <  $k$  < 100 MHz, where  $k$  is the rate constant for the exchange between deuterium sites). For NH<sub>2</sub>-MIL-53(Al)-d<sub>3</sub>, only static phenylene ring signals are observed in the slow motion limit (SML,  $k$  < 1 kHz), evidenced by the Pake doublet (Figure A2.21), in line with linker rotation not being possible for this framework.

The variable-temperature <sup>2</sup>H SSNMR spectra for NO<sub>2</sub>-MIL-53(Al)-d<sub>3</sub> are remarkably different from the aforementioned situations (Figure 2.4a). At the lowest temperature, the <sup>2</sup>H spectrum indicates a stationary phenylene ring in the SML, whereas the spectra acquired at 409 K and higher indicate dynamics only in the fast motion limit (FML,  $k$  > 100 MHz). The spectra in the range of 254 to 387 K display a superposition of the SML and FML powder patterns, with progressive increase in integrated intensity of the FML pattern with respect to the SML pattern with increasing temperature. No pattern corresponding to the IMR was detected in the entire temperature range, differing from earlier <sup>2</sup>H SSNMR studies on MOFs with *p*-phenylene rotators;<sup>31,34,35</sup> this is likely due to diminished intensity of IMR spectra when the rates of motion are on the order of the <sup>2</sup>H pattern breadths.<sup>56–59</sup> Furthermore, the fact that contributions from both SML and FML patterns are observed across the entire temperature range indicates the presence of a distribution of correlation times for the dynamics, which further obscures signals arising from IMR motions.<sup>36,52,60</sup> Such broad distributions of rotation rates are rarely found in terephthalate MOFs,<sup>8,30,31,34–36</sup>

though they are more often observed for *p*-phenylene moieties in polymeric systems,<sup>61–63</sup> where structural heterogeneity among the rotors is often cited as the cause of a wide variety of rotation barriers, and consequently, rotation rates. This observation is further supported by the BDS results: there is a very broad distribution of detected frequencies for each temperature in the BDS spectra for NO<sub>2</sub>-MIL-53(Al) (Figure 2.3b). As suggested by the DFT calculations, these broad distributions of rotational rates are a consequence of the varied degree of inter-linker steric interactions, which are unique to the nitro-functionalized MOF among the three frameworks.

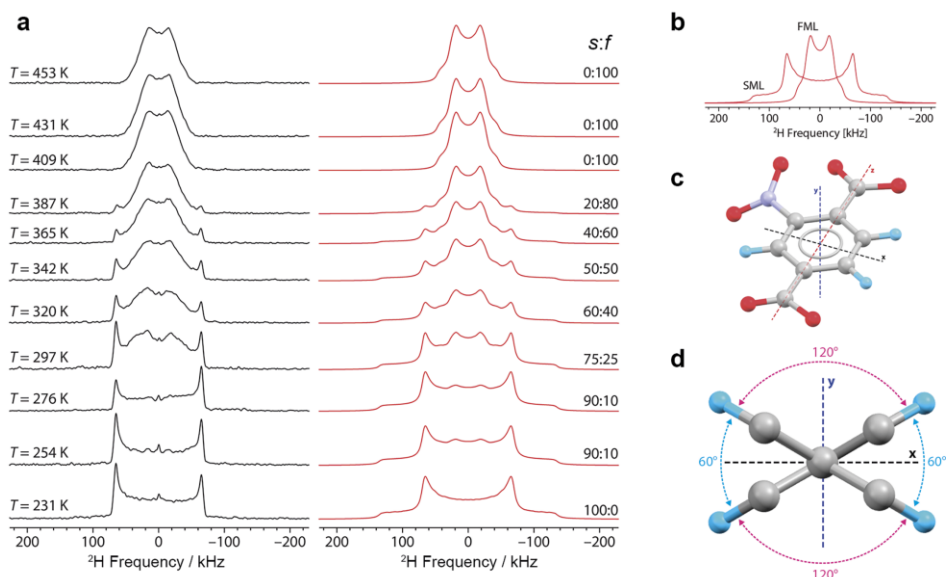


**Figure 2.4.** Solid-state <sup>2</sup>H NMR studies of NO<sub>2</sub>-MIL-53(Al)-d<sub>3</sub>. **a**, Experimental (black) and simulated (red) variable-temperature <sup>2</sup>H SSNMR spectra of NO<sub>2</sub>-MIL-53(Al)-d<sub>3</sub>. **b**, The spectra are comprised of overlapping patterns representing SML (< 10<sup>3</sup> Hz) and FML (> 10<sup>7</sup>–10<sup>8</sup> Hz) motions, with relative integrated intensities indicated to the right of the simulated spectra. **c**, Cartesian frame of reference for the rotation model. **d**, Representation of <sup>2</sup>H exchange sites and angles used in the model; deuterons are shown in light blue.

Although <sup>2</sup>H NMR signals corresponding to motions in the IMR are not observed due to their low intensities and broad frequency distributions, it is possible to model motions in the FML and obtain simulations that agree well with experimental data.<sup>64</sup> Single rotational angle models (*e.g.*, 60°, 120°, or 180°) do not adequately fit the line shape (Figure A2.22), suggesting a more complex mechanism. A four-site model based on energy minima separated by two distinct jumps of 60° and 120° (as predicted by DFT calculations, Figure 2.4c and d) was successful. The simulated <sup>2</sup>H FML shape was found to be sensitive to small deviations in these angles (Figure A2.23). The complete simulated spectra are shown in Figure 2.4a. For the overlapped spectra at 254–387 K, the appropriate ratios of weighted integrated signal intensities for static and mobile components were selected (*i.e.*, *s*:*f*, corresponding to the SML and FML patterns, Fig 4b) and are included in Figure 2.4a. It should be noted that similar four-site rotations have been observed in *p*-phenylene rotators within branched linkers that cause intra-linker steric interactions.<sup>22,65</sup>

To summarize the NO<sub>2</sub>-MIL-53(Al) experimental results, our BDS and <sup>2</sup>H SSNMR experiments detect dynamics corresponding to complementary portions of the frequency spectrum. BDS only includes the mobile fraction of linkers up to 1 MHz, which is the mean frequency of motion at ca. 250 K. <sup>2</sup>H SSNMR detects all linkers undergoing slow dynamics below 1 kHz as well as all with fast dynamics above ~100 MHz, which go largely unobserved in BDS due to its lower and upper frequency limits. Effectively, the only overlap between the two spectroscopic analyses (*i.e.*, where both methods detect signals) is at 230–250 K. At 250 K, the <sup>2</sup>H SSNMR model indicates that a large majority of the linkers are static, which means the BDS peak at 1 MHz omits information on a significant population of linkers. For this reason, the estimated activation energy should be taken as valid only for this fraction of rotors. In the high-temperature region of the <sup>2</sup>H SSNMR spectra, no signal from the SML is observed, and that all rotational motion likely exists within the FML. Both sets of data provide clear evidence that the rotational motions in NO<sub>2</sub>-MIL-53(Al) are spread along a very broad frequency range, which is a rare phenomenon that can be attributed to the addition of the bulky nitro substituent.

To understand the observed frequency broadening and the effect of temperature on how neighboring linkers influence rotational motion in NO<sub>2</sub>-MIL-53(Al), *ab initio* molecular dynamics (MD) simulations were carried out at 300, 450, 700, and 1200 K. The higher temperatures are not directly relevant to the physical situation (NO<sub>2</sub>-MIL-53(Al) combusts at ca. 700 K), yet they allow for more rotation events to be observed during shorter simulation times.<sup>66,67</sup> In periodic MD simulations involving a single unit cell (Figure A2.24), clear preferential conformations are observed, consistent with the potential energy minima observed in zero-Kelvin calculations. At lower temperatures (*e.g.*, 300 K), the linkers undergo discrete 60° rotations between 30° to –30°, whose frequency increases with temperature. At higher temperatures, the occurrence of 120° jumps between ±30° and ±150° is also observed. Both motions are consistent with the <sup>2</sup>H SSNMR data and the DFT-predicted energy barriers.

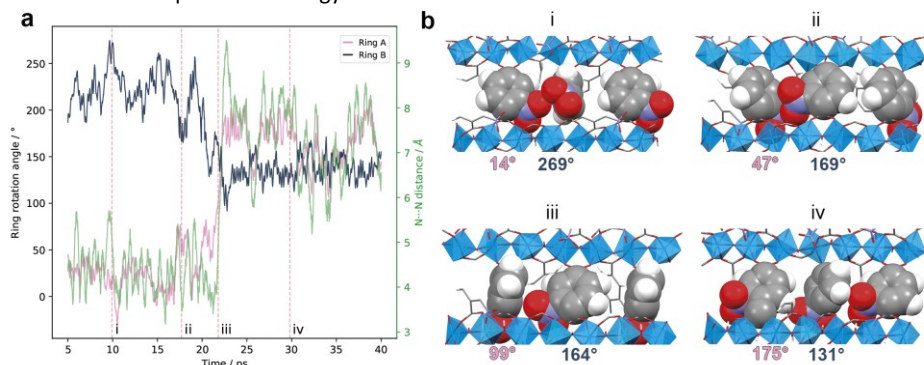


**Figure 2.5.** Cooperative rotation in NO<sub>2</sub>-MIL-53(Al). **a**, Rotation angle traces of two neighboring rings in a 2x1x1 cell MD simulation at 700 K. Correlated motion is observed, with simultaneous angle changes in opposite directions (i,ii,iii), when nitro groups are in proximity (N...N distance ca. 4 Å). **b**, Selected snapshots (i-iv) of linker pair conformation during a cooperative rotation. As ring A rotates in the positive direction, ring B reaches the space originally occupied by ring A.

A similar trend in angular mobility ranges is observed for 2x1x1 supercell simulations. At 300 K, only small angle librations ca. 20° are observed (Figure A2.25). In the mid-temperature range (450-

700 K), two sets of rotational jumps appear, in addition to librations (Figures A2.26–A2.27). At the highest temperature simulated (1200 K), the linkers' motion becomes so fast and extensive that even rotation beyond 180° occurs (Figure A2.28).

Interestingly, barring the 1200 K simulations, the time traces of rotation angles feature repeated occurrences of apparent correlated fluctuations in both librations and jumps of adjacent linker pairs. This is less evident in the 300 K simulations, where rings did not undergo any large-angle jumps. To analyze the relation between this apparent correlated motion and the steric effect of linkers within a row, a comparison of the distance between nitro groups of each pair of neighboring linkers may be insightful. This is defined as the distance between the two nitrogen atoms (see Appendix section A2.3.8). These distances are shown along with the angle traces at 450 K and 700 K in Figure 2.5a and Figures A2.30–A2.33. Indeed, the rings at these temperatures perform mirrored small angle ( $\sim 50^\circ$ ) fluctuations when the distance between their nitro groups is small (Figure 2.5b). In the portions of the simulations where the nitro distances are large enough as to not cause steric effects, the mirrored correlated motion is not present, and faster, shorter fluctuations are observed.

Although large-angle jumps are relatively rare in the supercell simulations, Figures 2.5, A2.31, and A2.33 show examples of correlated large-angle motions that occur when nitro groups are in each other's proximity. A closer analysis of the molecular conformations during a simulation provides a clear example of these cooperative dynamics, presented in Figure 2.5. The snapshot sequence presented in Figure 2.5b illustrates how the limited space of the rotors requires cooperative motion to allow the change in angles from i to iv. In this case, ring A could be seen as rotating cooperatively in the positive direction (most noticeable in snapshots ii to iii) allowing ring B to rotate in the negative direction (i–iv), resulting in the pair performing a gearlike rotation. This correlated motion is facilitated by the neighbors' close arrangement, which implies that, in order to achieve certain conformations, cooperative rotation between neighbors is required.

It can be proposed that this type of complex dynamics is in fact what causes NO<sub>2</sub>-MIL-53(Al) to display the intriguing behavior determined by BDS and <sup>2</sup>H SSNMR analysis. The vast array of possible dynamics observed in this MOF—evidenced by the coexistence of both static and rapidly rotating rings at most temperatures—is a result of functionalizing the phenylene rotators with a substituent that i) drastically decreases the intrinsic rotation barrier and ii) facilitates intra-row steric interactions. Both DFT and ab initio MD methods support the hypothesis that intra-row steric effects lead to cooperative motion for a population of neighboring linkers, while the static rings are the inevitable result of energetically disfavored non-cooperative rotation.

## 2.3. Conclusions

To conclude, the MIL-53 topology, where the distance between the rotational axes of phenylene rings along the pore direction is only  $\sim 6.6 \text{ \AA}$ , has proven to be an excellent example of a framework whose rotational mobility can be tuned to different dynamic regimes. At the two extremes, there are (i) unfunctionalized phenylene units that can rotate independently, with specific temperature-dependent rates, and (ii) amino-functionalized phenylene units that cannot rotate at all, due to hydrogen bonding and increased steric hindrance from the narrow-pore configuration. Between

these extremes, for nitrophenylene linkers, complex rotational dynamics that evolve with temperature are observed, spanning a broad frequency range. Among these, the emergence of cooperative rotational dynamics between neighboring linkers in MOFs was identified. This discovery paves the way to engineering gearlike functional motion in MOFs, if linker dynamics can also be controlled externally, e.g. by electric fields.

## 2.4. Code availability

The Python code used to analyze the ring rotation angles from MD simulation data is available online at <https://github.com/srinidhimula/supplementary-data>. A detailed description of the code's functionality is provided in Appendix section A2.3.9.

## 2.5. References

1. van Meer, G., Voelker, D. R. & Feigenson, G. W. Membrane lipids: where they are and how they behave. *Nat. Rev. Mol. Cell Biol.* **9**, 112–124 (2008).
2. Duncan, A. L., Reddy, T., Koldsø, H., Hélie, J., Fowler, P. W., Chavent, M. & Sansom, M. S. P. Protein crowding and lipid complexity influence the nanoscale dynamic organization of ion channels in cell membranes. *Sci. Rep.* **7**, 16647 (2017).
3. van der Kooij, H. M., Semerzhiev, S. A., Buijs, J., Broer, D. J., Liu, D. & Sprakel, J. Morphing of liquid crystal surfaces by emergent collectivity. *Nat. Commun.* **10**, 1–9 (2019).
4. Catalano, L. & Naumov, P. Exploiting rotational motion in molecular crystals. *CrystEngComm* **20**, 5872–5883 (2018).
5. Vogelsberg, C. S. & Garcia-Garibay, M. A. Crystalline molecular machines: function, phase order, dimensionality, and composition. *Chem. Soc. Rev.* **41**, 1892–1910 (2012).
6. Khuong, T.-A. V., Nunez, J. E., Godínez, C. E., Garcia-Garibay, M. A., Nuñez, J. E., Godínez, C. E. & Garcia-Garibay, M. A. Crystalline molecular machines: A quest toward solid-state dynamics and function. *Acc. Chem. Res.* **39**, 413–422 (2006).
7. Deng, H., Olson, M. A., Stoddart, J. F. & Yaghi, O. M. Robust dynamics. *Nat. Chem.* **2**, 439–443 (2010).
8. Gonzalez-Nelson, A., Coudert, F.-X. & van der Veen, M. Rotational Dynamics of Linkers in Metal–Organic Frameworks. *Nanomaterials* **9**, 330 (2019).
9. Martinez-Bulit, P., Stirk, A. J. & Loeb, S. J. Rotors, Motors, and Machines Inside Metal–Organic Frameworks. *Trends in Chemistry* vol. 1 588–600 (2019).
10. Gee, J. A. & Sholl, D. S. Effect of Framework Flexibility on C 8 Aromatic Adsorption at High Loadings in Metal–Organic Frameworks. *J. Phys. Chem. C* **120**, 370–376 (2016).
11. Park, J., Agrawal, M., Sava Gallis, D. F., Harvey, J. A., Greathouse, J. A. & Sholl, D. S. Impact of intrinsic framework flexibility for selective adsorption of sarin in non-aqueous solvents using metal–organic frameworks. *Phys. Chem. Chem. Phys.* **22**, 6441–6448 (2020).
12. Agrawal, M., Bhattacharyya, S., Huang, Y., Jayachandrababu, K. C., Murdock, C. R., Bentley, J. A., Rivas-Cardona, A., Mertens, M. M., Walton, K. S., Sholl, D. S. & Nair, S. Liquid-Phase Multicomponent Adsorption and Separation of Xylene Mixtures by Flexible MIL-53 Adsorbents. *J. Phys. Chem. C* **122**, 386–397 (2018).
13. Verploegh, R. J., Kulkarni, A., Boulfelfel, S. E., Haydak, J. C., Tang, D. & Sholl, D. S. Screening Diffusion of Small Molecules in Flexible Zeolitic Imidazolate Frameworks Using a DFT-Parameterized Force Field. *J. Phys. Chem. C* **123**, 9153–9167 (2019).

14. Witman, M., Ling, S., Jawahery, S., Boyd, P. G., Haranczyk, M., Slater, B. & Smit, B. The Influence of Intrinsic Framework Flexibility on Adsorption in Nanoporous Materials. *J. Am. Chem. Soc.* **139**, 5547–5557 (2017).
15. Lennox, M. J. & Düren, T. Understanding the Kinetic and Thermodynamic Origins of Xylene Separation in UiO-66(Zr) via Molecular Simulation. *J. Phys. Chem. C* **120**, 18651–18658 (2016).
16. Evans, J. D., Krause, S. & Feringa, B. L. Cooperative and synchronized rotation in motorized porous frameworks: Impact on local and global transport properties of confined fluids. *Faraday Discuss.* (2020) doi:10.1039/D0FD00016G.
17. Aprahamian, I. The Future of Molecular Machines. *ACS Cent. Sci.* **6**, 347–358 (2020).
18. Vogelsberg, C. S., Uribe-Romo, F. J., Lipton, A. S., Yang, S., Houk, K. N., Brown, S. & Garcia-Garibay, M. A. Ultrafast rotation in an amphidynamic crystalline metal organic framework. *Proc. Natl. Acad. Sci.* **114**, 13613–13618 (2017).
19. Bracco, S., Castiglioni, F., Comotti, A., Galli, S., Negroni, M., Maspero, A. & Sozzani, P. Ultrafast Molecular Rotors and Their CO<sub>2</sub>Tuning in MOFs with Rod-Like Ligands. *Chem. - A Eur. J.* **23**, 11210–11215 (2017).
20. Danowski, W., van Leeuwen, T., Abdolazadeh, S., Roke, D., Browne, W. R., Wezenberg, S. J. & Feringa, B. L. Unidirectional rotary motion in a metal–organic framework. *Nat. Nanotechnol.* **14**, 488–494 (2019).
21. Kottas, G. S., Clarke, L. I., Horinek, D. & Michl, J. Artificial Molecular Rotors. *Chem. Rev.* **105**, 1281–1376 (2005).
22. Yan, Y., Kolokolov, D. I., da Silva, I., Stepanov, A. G., Blake, A. J., Dailly, A., Manuel, P., Tang, C. C., Yang, S. & Schröder, M. Porous Metal–Organic Polyhedral Frameworks with Optimal Molecular Dynamics and Pore Geometry for Methane Storage. *J. Am. Chem. Soc.* **139**, 13349–13360 (2017).
23. Sokolov, A. N., Swenson, D. C. & MacGillivray, L. R. Conformational polymorphism in a heteromolecular single crystal leads to concerted movement akin to collective rack-and-pinion gears at the molecular level. *Proc. Natl. Acad. Sci.* **105**, 1794–1797 (2008).
24. Jarowski, P. D., Houk, K. N. & Garcia-Garibay, M. A. Importance of correlated motions on the low barrier rotational potentials of crystalline molecular gyroscopes. *J. Am. Chem. Soc.* **129**, 3110–3117 (2007).
25. Howe, M. E. & Garcia-Garibay, M. A. The Roles of Intrinsic Barriers and Crystal Fluidity in Determining the Dynamics of Crystalline Molecular Rotors and Molecular Machines. *J. Org. Chem.* **84**, 9835–9849 (2019).
26. Lemouchi, C., Iliopoulos, K., Zorina, L., Simonov, S., Wzietek, P., Cauchy, T., Rodríguez-Fortea, A., Canadell, E., Kaleta, J., Michl, J., Gindre, D., Chrysos, M. & Batail, P. Crystalline Arrays of Pairs of Molecular Rotors: Correlated Motion, Rotational Barriers, and Space-Inversion Symmetry Breaking Due to Conformational Mutations. *J. Am. Chem. Soc.* **135**, 9366–9376 (2013).
27. Damron, J. T., Ma, J., Kurz, R., Saalwächter, K., Matzger, A. J. & Ramamoorthy, A. The Influence of Chemical Modification on Linker Rotational Dynamics in Metal–Organic Frameworks. *Angew. Chemie - Int. Ed.* **57**, 8678–8681 (2018).
28. Zhou, W. & Yildirim, T. Lattice dynamics of metal-organic frameworks: Neutron inelastic scattering and first-principles calculations. *Phys. Rev. B* **74**, 180301 (2006).
29. Ryder, M. R., Van De Voorde, B., Civalleri, B., Bennett, T. D., Mukhopadhyay, S., Cinque, G., Fernandez-Alonso, F., De Vos, D., Rudić, S. & Tan, J. C. Detecting Molecular Rotational Dynamics Complementing the Low-Frequency Terahertz Vibrations in a Zirconium-Based Metal-Organic Framework. *Phys. Rev. Lett.* **118**, 1–6 (2017).
30. Liepuoniute, I., Huynh, C. M., Perez-Estrada, S., Wang, Y., Khan, S., Houk, K. N. & Garcia-Garibay, M. A. Enhanced Rotation by Ground State Destabilization in Amphidynamic

- Crystals of a Dipolar 2,3-Difluorophenylene Rotator as Established by Solid State <sup>2</sup>H NMR and Dielectric Spectroscopy. *J. Phys. Chem. C* **124**, 15391–15398 (2020).
31. Kolokolov, D. I., Jobic, H., Stepanov, A. G., Guillermin, V., Devic, T., Serre, C. & Férey, G. Dynamics of benzene rings in MIL-53(Cr) and MIL-47(V) frameworks studied by <sup>2</sup>H NMR spectroscopy. *Angew. Chemie - Int. Ed.* **49**, 4791–4794 (2010).
  32. Kolokolov, D. I., Stepanov, A. G. & Jobic, H. Guest controlled rotational dynamics of terephthalate phenylenes in metal-organic framework MIL-53(Al): Effect of different xylene loadings. *J. Phys. Chem. C* **118**, 15978–15984 (2014).
  33. Khudozhitkov, A. E., Jobic, H., Freude, D., Haase, J., Kolokolov, D. I. & Stepanov, A. G. Ultraslow Dynamics of a Framework Linker in MIL-53 (Al) as a Sensor for Different Isomers of Xylene. *J. Phys. Chem. C* **120**, 21704–21709 (2016).
  34. Khudozhitkov, A. E., Kolokolov, D. I., Stepanov, A. G., Bolotov, V. A. & Dybtsev, D. N. Metal-Cation-Independent Dynamics of Phenylene Ring in Microporous MOFs: A <sup>2</sup>H Solid-State NMR Study. *J. Phys. Chem. C* **119**, 28038–28045 (2015).
  35. Gould, S. L., Tranchemontagne, D., Yaghi, O. M. & Garcia-Garibay, M. A. Amphidynamic character of crystalline MOF-5: Rotational dynamics of terephthalate phenylenes in a free-volume, sterically unhindered environment. *J. Am. Chem. Soc.* **130**, 3246–3247 (2008).
  36. Kolokolov, D. I., Stepanov, A. G., Guillermin, V., Serre, C., Frick, B. & Jobic, H. Probing the dynamics of the porous Zr terephthalate UiO-66 framework using <sup>2</sup>H NMR and neutron scattering. *J. Phys. Chem. C* **116**, 12131–12136 (2012).
  37. Biswas, S., Ahnfeldt, T. & Stock, N. New functionalized flexible Al-MIL-53-X (X = -Cl, -Br, -CH<sub>3</sub>, -NO<sub>2</sub>, -(OH)<sub>2</sub>) solids: Syntheses, characterization, sorption, and breathing behavior. *Inorg. Chem.* **50**, 9518–9526 (2011).
  38. Loiseau, T., Serre, C., Huguenard, C., Fink, G., Taulelle, F., Henry, M., Bataille, T. & Férey, G. A rationale for the large breathing of the porous aluminum terephthalate (MIL-53) upon hydration. *Chemistry* **10**, 1373–1382 (2004).
  39. Munn, A. S., Pillai, R. S., Biswas, S., Stock, N., Maurin, G. & Walton, R. I. The flexibility of modified-linker MIL-53 materials. *Dalt. Trans.* **45**, 4162–4168 (2016).
  40. Stavitski, E., Pidko, E. A., Couck, S., Remy, T., Hensen, E. J. M., Weckhuysen, B. M., Denayer, J., Gascon, J. & Kapteijn, F. Complexity behind CO<sub>2</sub> capture on NH<sub>2</sub>-MIL-53(Al). *Langmuir* **27**, 3970–3976 (2011).
  41. Shustova, N. B., Ong, T.-C., Cozzolino, A. F., Michaelis, V. K., Griffin, R. G. & Dincă, M. Phenyl Ring Dynamics in a Tetraphenylethylene-Bridged Metal–Organic Framework: Implications for the Mechanism of Aggregation-Induced Emission. *J. Am. Chem. Soc.* **134**, 15061–15070 (2012).
  42. Kolokolov, D. I., Stepanov, A. G. & Jobic, H. SI: Guest controlled rotational dynamics of terephthalate phenylenes in metal-organic framework MIL-53(Al): Effect of different xylene loadings. *J. Phys. Chem. C* **118**, 15978–15984 (2014).
  43. Balčiūnas, S., Šimėnas, M., Pavlovaitė, D., Kinka, M., Shieh, F.-K., Wu, K. C.-W., Banys, J. & Grigalaitis, R. Low-Frequency Dipolar Dynamics and Atmospheric Effects in ZIF-90 Metal–Organic Framework. *J. Phys. Chem. C* **123**, 631–636 (2019).
  44. Winston, E. B., Lowell, P. J., Vacek, J., Chocholoušová, J., Michl, J. & Price, J. C. Dipolar molecular rotors in the metal–organic framework crystal IRMOF-2. *Phys. Chem. Chem. Phys.* **10**, 5188 (2008).
  45. Devautour-Vinot, S., Maurin, G., Serre, C., Horcajada, P., Paula Da Cunha, D., Guillermin, V., De Souza Costa, E., Taulelle, F. & Martineau, C. Structure and dynamics of the functionalized MOF type UiO-66(Zr): NMR and dielectric relaxation spectroscopies coupled with DFT calculations. *Chem. Mater.* **24**, 2168–2177 (2012).
  46. Kremer, F. & Schonhals, A. *Broadband Dielectric Spectroscopy*. (Springer-Verlag: Berlin,

- Heidelberg, 2003).
47. Frunza, S., Schönhal, A., Frunza, L., Ganea, P., Kosslick, H., Harloff, J. & Schulz, A. Molecular relaxation processes in a MOF-5 structure revealed by broadband dielectric spectroscopy: Signature of phenylene ring fluctuations. *J. Phys. Chem. B* **114**, 12840–12846 (2010).
  48. Knebel, A., Geppert, B., Volgmann, K., Kolokolov, D. I., Stepanov, A. G., Twiefel, J., Heitjans, P., Volkmer, D. & Caro, J. Defibrillation of soft porous metal-organic frameworks with electric fields. *Science* **358**, 347–351 (2017).
  49. Horansky, R. D., Clarke, L. I., Price, J. C., Khuong, T. A. V., Jarowski, P. D. & Garcia-Garibay, M. A. Dielectric response of a dipolar molecular rotor crystal. *Phys. Rev. B - Condens. Matter Mater. Phys.* **72**, 1–5 (2005).
  50. Horansky, R. D., Clarke, L. I., Winston, E. B., Price, J. C., Karlen, S. D., Jarowski, P. D., Santillan, R. & Garcia-Garibay, M. A. Dipolar rotor-rotor interactions in a difluorobenzene molecular rotor crystal. *Phys. Rev. B - Condens. Matter Mater. Phys.* **74**, 1–12 (2006).
  51. Jiang, X., O'Brien, Z. J., Yang, S., Lai, L. H., Buenaflor, J., Tan, C., Khan, S., Houk, K. N. & Garcia-Garibay, M. A. Crystal Fluidity Reflected by Fast Rotational Motion at the Core, Branches, and Peripheral Aromatic Groups of a Dendrimeric Molecular Rotor. *J. Am. Chem. Soc.* **138**, 4650–4656 (2016).
  52. Hansen, M. R., Graf, R. & Spiess, H. W. Solid-State NMR in Macromolecular Systems: Insights on How Molecular Entities Move. *Acc. Chem. Res.* **46**, 1996–2007 (2013).
  53. Spiess, H. W. Molecular dynamics of solid polymers as revealed by deuterium NMR. *Colloid Polym. Sci* **261**, 193–209 (1983).
  54. Khudozhnikov, A. E., Jobic, H., Freude, D., Haase, J., Kolokolov, D. I. & Stepanov, A. G. Ultraslow Dynamics of a Framework Linker in MIL-53 (Al) as a Sensor for Different Isomers of Xylene. **53**, (2016).
  55. Serra-Crespo, P., Van Der Veen, M. A., Gobechiya, E., Houthoofd, K., Filinchuk, Y., Kirschhock, C. E. A., Martens, J. A., Sels, B. F., De Vos, D. E., Kapteijn, F. & Gascon, J. NH<sub>2</sub>-MIL-53(Al): A high-contrast reversible solid-state nonlinear optical switch. *J. Am. Chem. Soc.* **134**, 8314–8317 (2012).
  56. Spiess, H. W. Deuterium NMR — a new tool for studying chain mobility and orientation in polymers. in 23–58 (1985). doi:10.1007/3-540-13779-3\_16.
  57. Gedat, E., Schreiber, A., Albrecht, J., Emmler, T., Shenderovich, I., Findenegg, G. H., Limbach, H. H. & Buntkowsky, G. 2H-solid-state NMR study of benzene-d<sub>6</sub> confined in mesoporous silica SBA-15. *J. Phys. Chem. B* **106**, 1977–1984 (2002).
  58. Larsen, F. H. Simulation of Molecular Motion of Quadrupolar Nuclei in Solid-State NMR Spectra. in *Annual Reports on NMR Spectroscopy* vol. 71 103–137 (Elsevier Ltd, 2010).
  59. Aliev, A. E., Mann, S. E., Rahman, A. S., McMillan, P. F., Cora, F., Iuga, D., Hughes, C. E. & Harris, K. D. M. High-Resolution Solid-State H-2 NMR Spectroscopy of Polymorphs of Glycine. *J. Phys. Chem. A* **115**, 12201–12211 (2011).
  60. Schadt, R. J., Cain, E. J. & English, A. D. Simulation of one-dimensional deuterium NMR line shapes. *J. Phys. Chem.* **97**, 8387–8392 (1993).
  61. Leisen, J., Ohlemacher, A., Boeffel, C. & Spiess, H. W. Molecular Dynamics in Side-Group Polymers with and without Liquid Crystalline Phases from 2H NMR. *Berichte der Bunsengesellschaft für Phys. Chemie* **97**, 1306–1311 (1993).
  62. Pschorn, U., Spiess, H. W., Hisgen, B. & Ringsdorf, H. Deuterium NMR study of molecular order and motion of the mesogenic side groups in liquid-crystalline polymers. *Die Makromol. Chemie* **187**, 2711–2723 (1986).
  63. Wehrle, M., Hellmann, G. P. & Spiess, H. W. Phenylene motion in polycarbonate and polycarbonate/additive mixtures. *Colloid Polym. Sci.* **265**, 815–822 (1987).

64. Wasylishen, R. E., Ashbrook, S. E. & Wimperis, S. *NMR of Quadrupolar Nuclei in Solid Materials*. (John Wiley & Sons, 2012).
65. Moreau, F., Kolokolov, D. I., Stepanov, A. G., Easun, T. L., Dailly, A., Lewis, W., Blake, A. J., Nowell, H., Lennox, M. J., Besley, E., Yang, S. & Schröder, M. Tailoring porosity and rotational dynamics in a series of octacarboxylate metal-organic frameworks. *Proc. Natl. Acad. Sci.* **114**, 3056–3061 (2017).
66. Haigis, V., Coudert, F.-X., Vuilleumier, R., Boutin, A. & Fuchs, A. H. Hydrothermal Breakdown of Flexible Metal–Organic Frameworks: A Study by First-Principles Molecular Dynamics. *J. Phys. Chem. Lett.* **6**, 4365–4370 (2015).
67. Gaillac, R., Pullumbi, P., Beyer, K. A., Chapman, K., Keen, D. A., Bennett, T. D. & Coudert, F. X. Liquid metal–organic frameworks. *Nat. Mater.* **16**, 1149–1155 (2017).

# Appendix to Chapter 2

---

## Contents

|  |    |
|--|----|
| A2.1. Methods .....  | 72 |
| A2.1.1. MOF synthesis .....  | 72 |
| A2.1.2. Deuterium-labeled MOF synthesis.....                               | 73 |
| A2.1.3. Routine characterization .....                                     | 76 |
| A2.1.4. Broadband dielectric spectroscopy.....                             | 77 |
| A2.1.5. Solid-state $^2\text{H}$ NMR spectroscopy.....                     | 77 |
| A2.2. Computational methods.....   | 77 |
| A2.2.1. Density functional theory calculations.....                        | 77 |
| A2.2.2. Ab initio molecular dynamics simulations.....                      | 78 |
| A2.3. Supplementary information .....                                      | 78 |
| A2.3.1. DFT structural details .....                                       | 78 |
| A2.3.2. Periodic DFT details.....  | 80 |
| A2.3.3. Rotation angle definitions .....                                   | 80 |
| A2.3.4. $\text{NO}_2$ -MIL-53 2x1x1 supercell DFT calculations.....        | 81 |
| A2.3.5. Supplementary BDS data .....                                       | 84 |
| A2.3.6. Supplementary solid-state $^2\text{H}$ NMR spectroscopy data ..... | 86 |
| A2.3.7. Ab initio molecular dynamics simulations.....                      | 90 |
| A2.3.8. Correlated motion between pairs of linkers .....                   | 93 |
| A2.3.9. Rotation angle pseudocode .....                                    | 95 |
| A2.4. Appendix references .....  | 96 |

## A2.1. Methods

### A2.1.1. MOF synthesis

**MIL-53(Al):**  $\text{AlCl}_3 \cdot 6\text{H}_2\text{O}$  (1.97 g, 8.2 mmol) was added to 30 mL demineralized water inside a 45 mL Teflon liner. The solution was homogenized by stirring. Terephthalic acid (1.36 g, 8.2 mmol) was added to the solution, and the mixture was stirred again (terephthalic acid does not completely dissolve in these conditions). The liner was sealed inside a steel autoclave and placed in an oven at 220 °C for 72 h.

To remove unreacted terephthalic acid from the pores, solvent exchange with DMF was performed at 120 °C overnight, followed by exchange with MeOH at 80 °C for 5 h. The residual solvent is removed by heating in an oven at 120 °C for 3 h. MOF characterization is shown in Figures A2.1–A2.3.

**$\text{NO}_2$ -MIL-53(Al):**  $\text{Al}(\text{NO}_3)_3 \cdot 9\text{H}_2\text{O}$  (1.49 g, 3.97 mmol) was dissolved in 50 mL demineralized water inside a 125 mL Teflon liner. 2-Nitroterephthalic acid (0.92 g, 4.36 mmol) was added to the solution. The liner was sealed inside a steel autoclave and placed in an oven at 170 °C for 12 h.

After cooling to room temperature, the white product was collected by filtration and placed in 60 mL MeOH to 80 °C for 20 h. This solvent exchange was performed twice. The product was then dried in an oven at 100 °C for 3 h. MOF characterization is shown in Figures A2.1–A2.3.

**$\text{NH}_2$ -MIL-53(Al):**  $\text{AlCl}_3 \cdot 6\text{H}_2\text{O}$  (2.9 g, 12.0 mmol) was dissolved in 30 mL demineralized water inside a 45 mL Teflon liner. 2-Aminoterephthalic acid (2.2 g, 12.1 mmol) was added to the solution. The liner was sealed inside a steel autoclave and placed in an oven at 150 °C for 10 h. After cooling, the yellow solids were filtered and washed with DMF (30 mL), and then transferred to the autoclave together with 20 mL DMF, and kept at 130 °C for 16 h. The DMF was subsequently exchanged by methanol at 80 °C for 5 h. After filtration the residual solvent is removed by heating the sample in the vacuum oven at 150 °C overnight. MOF characterization is shown in Figures A2.1–A2.3.

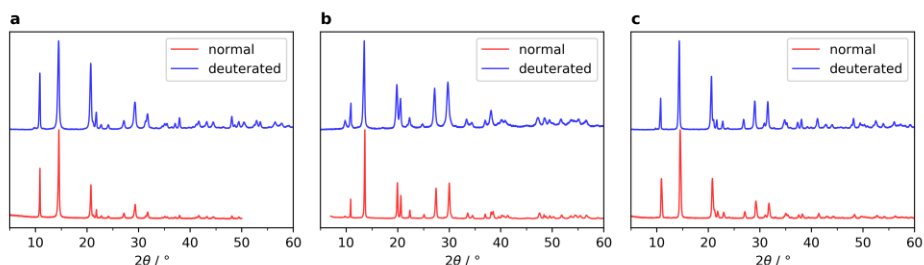


**Figure A2.1.** Powder X-ray diffraction patterns of normal and deuterated MIL-53(Al) (a),  $\text{NO}_2$ -MIL-53(Al) (b),  $\text{NH}_2$ -MIL-53(Al) (c).

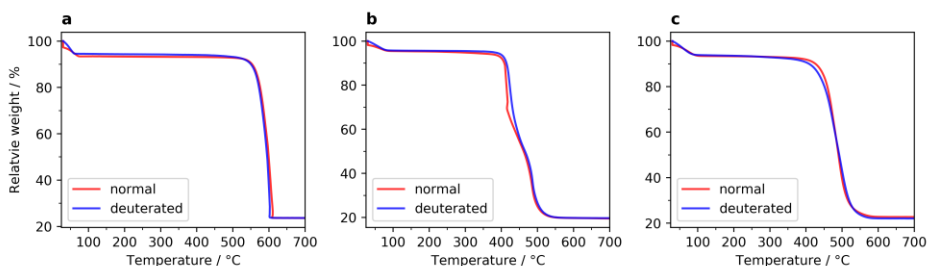


**Figure A2.2.** Thermogravimetric traces of normal and deuterated MIL-53(Al) (a), NO<sub>2</sub>-MIL-53(Al) (b), NH<sub>2</sub>-MIL-53(Al) (c).

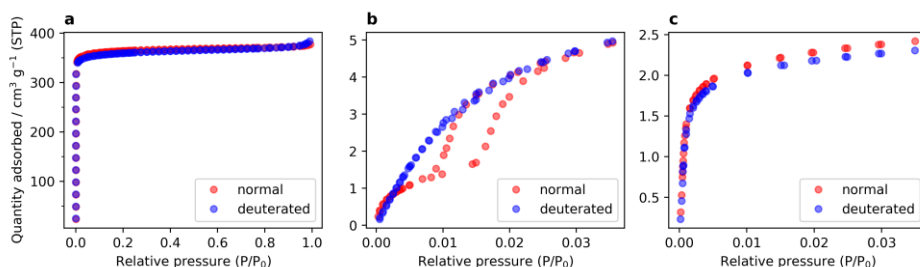


**Figure A2.3.** a, N<sub>2</sub> sorption isotherms at 77 K of normal and deuterated MIL-53(Al); b,c, CO<sub>2</sub> sorption isotherms at 273 K of NO<sub>2</sub>-MIL-53(Al) (b) and NH<sub>2</sub>-MIL-53(Al) (c).

### A2.1.2. Deuterium-labeled MOF synthesis

**MIL-53(Al)-d<sub>4</sub>:** Al(NO<sub>3</sub>)<sub>3</sub>·9H<sub>2</sub>O (0.44 g, 1.17 mmol) was added to 20 mL demineralized water inside a 45 mL Teflon liner. The solution was homogenized by stirring.) Terephthalic acid-d<sub>4</sub> (0.349 g, 2.05 mmol, 98%, Eurisotop) was added to the solution, and the mixture was stirred again. The liner was sealed inside a steel autoclave and placed in an oven at 220 °C for 72 h.

To remove unreacted terephthalic acid from the pores, we performed solvent exchange with DMF at 120 °C for 16 h, followed by exchange with methanol at 80 °C for 13 h. The residual solvent is removed by heating in an oven at 120 °C for 3 h. The product was finally activated in a vacuum oven at 100 °C for 4 h. Final yield 0.187 g (0.88 mmol, 75%). MOF characterization is shown in Figures A2.1–A2.3.

**NO<sub>2</sub>-MIL-53(Al)-d<sub>3</sub>:** Nitration of dimethyl terephthalate-d<sub>4</sub> (1.258 g, 6.35 mmol; ABCR, 95%) in 3.1 mL conc. H<sub>2</sub>SO<sub>4</sub>. The mixture was stirred until completely dissolved, cooled to 0 °C in an ice bath, and a mixture of 0.87 mL 65% HNO<sub>3</sub> and 0.62 mL 98% H<sub>2</sub>SO<sub>4</sub> was added dropwise while stirring. The reaction was then allowed to reach room temperature gradually. After 2.5 h, the solution was poured into 200 mL ice-water mixture and filtered over a Nylon membrane (0.45 μm). Yield: quantitative.

Dimethyl nitroterephthalate-d<sub>3</sub> (1.53 g, 6.3 mmol) was dissolved by stirring in 24 mL methanol. NaOH solution (6.6 ml of 2 M, 528 mg, 13 mmol NaOH) was added, producing an intense yellow color and some precipitation. The mixture was heated to 60 °C for 16 h. An additional 6.6 ml of

NaOH 2 M solution was added to the mixture and the reaction was continued for 5 h. Heating was stopped and the solvent was removed by vacuum evaporation. The solids were dissolved in 3 mL water, neutralized with conc. HCl, and cooled. The precipitated 2-nitroterephthalic acid-d<sub>3</sub> was collected by vacuum filtration, washed with ice water, and dried in a vacuum oven at 90 °C for one hour. Yield: 0.933 g (4.36 mmol; overall 69%). The <sup>1</sup>H and <sup>13</sup>C NMR spectra of 2-nitroterephthalic acid-d<sub>3</sub> are shown in Figures A2.4 and A2.5.

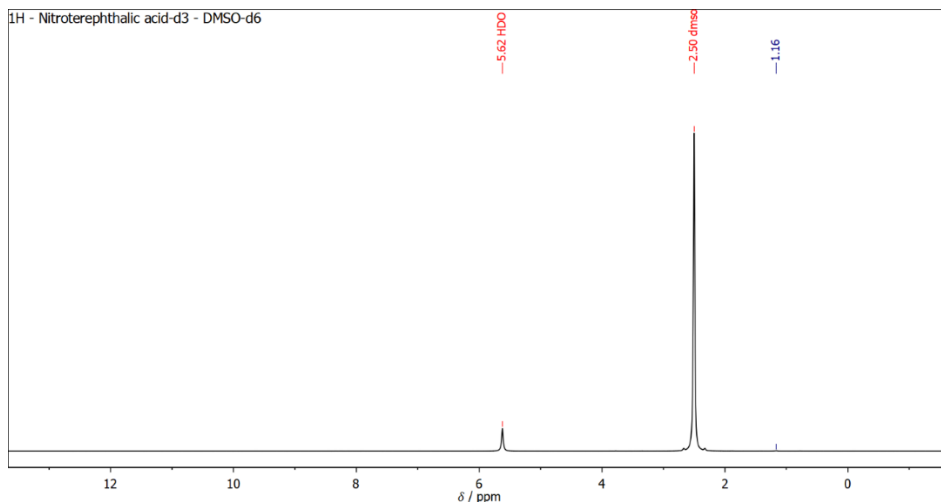


Figure A2.4. Proton NMR spectrum of the deuterium-labelled nitroterephthalic acid-d<sub>3</sub>.

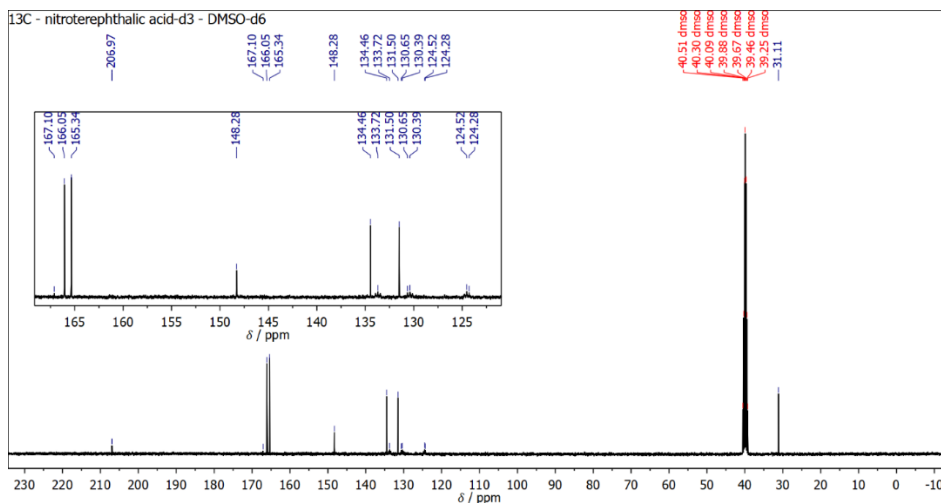


Figure A2.5. <sup>13</sup>C NMR spectrum of the deuterium-labelled nitroterephthalic acid-d<sub>3</sub>.

Al(NO<sub>3</sub>)<sub>3</sub>·9H<sub>2</sub>O (0.896 g, 2.4 mmol) was dissolved in 30 mL demineralized water inside a 45 mL Teflon liner. 2-Nitroterephthalic acid-d<sub>3</sub> (0.91 g, 4.2 mmol) was added to the solution. The liner was sealed inside a steel autoclave and placed in an oven at 170 °C for 12 h. After cooling to room temperature, the white product was collected by filtration and placed in 60 mL MeOH to 80 °C for

20 h. This solvent exchange was performed twice. The product was then dried in an oven at 100 °C for 5 h. Yield: 254 mg (1 mmol; 24%). MOF characterization is shown in Figures A2.1–A2.3.

**NH<sub>2</sub>-MIL-53(Al)-d<sub>3</sub>**: 2-aminoterephthalic acid-d<sub>3</sub> was prepared by reduction of dimethyl nitroterephthalate-d<sub>3</sub> (synthesized as described above). Dimethyl nitroterephthalate-d<sub>3</sub> (1.26 g, 5.2 mmol) was dissolved by stirring in 14 mL ethanol at 45 °C, while nitrogen was bubbled through the solution. SnCl<sub>2</sub>·H<sub>2</sub>O (4.93 g, 26 mmol) was added, turning the solution to an opaque yellow mixture. The reaction became clear after reaching to reflux temperature, and was left for 16 h under nitrogen flow.

The solution was cooled down and poured into 50 mL ethyl acetate. A 5% NaHCO<sub>3</sub> aqueous solution was added dropwise while swirling to neutralize pH, which brought the formation a gel in the aqueous phase. The organic phase was kept. The aqueous phase (gel) was separated and filtered over Celite, washing four times with 20 mL ethyl acetate. The organic fractions were combined, dried over MgSO<sub>4</sub>, and evaporated. The solids were purified by silica column to remove remaining Sn-based impurities, using ethyl acetate as solvent. Yield: 0.926 g (4.36 mmol; 84%).

Hydrolysis of dimethyl aminoterephthalate-d<sub>3</sub>. Dimethyl aminoterephthalate-d<sub>3</sub> (913 mg, 4.3 mmol) was added to a mixture of 32 mL MeOH and 13 mL H<sub>2</sub>O. NaOH (1.68 g) was added. The solution was stirred at room temperature for 16 h. The solvent was removed by evaporation, solids were dissolved in minimal water (8.8 ml). Added 2 M HCl (20 mL, dropwise), until pH starts to decrease. At pH between 4 and 5 a yellow precipitate is formed. Continued adding drops of acid until no more precipitated was formed. The precipitate was recovered by vacuum filtration. The procedure was repeated on the filtrate, washing the solids several times with ice-cold water to remove all salts. The combined solids were dried in a vacuum oven at 100 °C for 5 h. Final yield: 676.2 mg, 3.67 mmol, 85%. The <sup>1</sup>H and <sup>13</sup>C NMR spectra of 2-aminoterephthalic acid-d<sub>3</sub> are shown in Figures A2.6 and A2.7.

AlCl<sub>3</sub>·6H<sub>2</sub>O (857 mg, 3.5 mmol) was dissolved in 10 mL deuterium oxide inside a 45 mL Teflon liner. 2-Aminoterephthalic acid-d<sub>3</sub> (632 mg, 3.4 mmol) was added to the solution. The liner was sealed inside a steel autoclave and placed in an oven at 150 °C for 10 h. After cooling, the yellow solids were filtered and washed with DMF (30 mL), and then transferred to the autoclave together with 25 mL DMF, and kept at 120 °C for 15 h. The DMF was subsequently exchanged by methanol (20 mL) at 80 °C for 4 h. After filtration the residual solvent is removed by heating the sample in the vacuum oven at 150 °C overnight. MOF characterization is shown in Figures A2.1–A2.3.

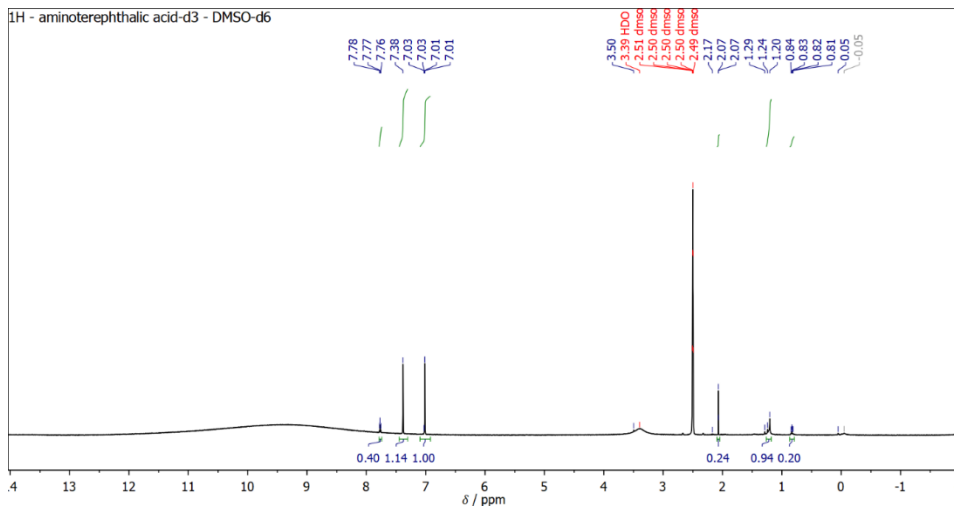


**Figure A2.6.** Proton NMR spectrum of the deuterium-labelled aminoterephthalic acid-d<sub>3</sub>.

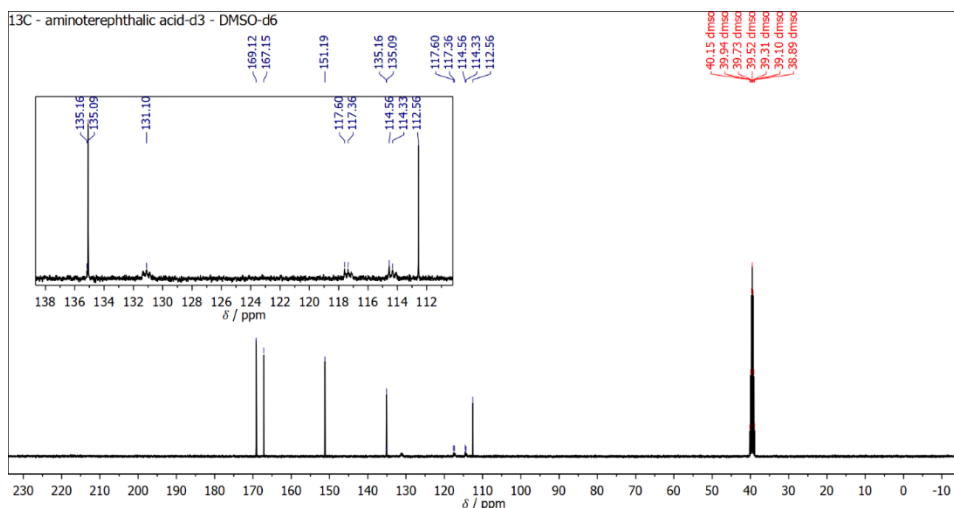


**Figure A2.7.** <sup>13</sup>C NMR spectrum of the deuterium-labelled aminoterephthalic acid-d<sub>3</sub>.

### A2.1.3. Routine characterization

Powder X-ray diffraction was acquired in Bragg–Brentano geometry using a Bruker-AXS D5005 equipped with a Co  $K\alpha$  source operating at 35 kV and 40 mA; a variable divergence slit was used. Thermogravimetric analysis (TGA) was performed using a Mettler Toledo TGA/SDTA 851e under 100 mL min<sup>-1</sup> air flow, from 30 to 700 °C with a heating rate of 5 °C min<sup>-1</sup>. Adsorption/desorption isotherms were measured volumetrically in a Tristar II 3020 Micromeritics instrument. N<sub>2</sub> sorption was performed at 77 K and CO<sub>2</sub> at 273 K. The samples were degassed before measurements under N<sub>2</sub> flow at 433 K for 16 h. The pore volume values were obtained from the N<sub>2</sub> sorption data at

$P/P_0=0.95$ .  $^1\text{H}$  and  $^{13}\text{C}$  NMR spectra were acquired in  $\text{DMSO-d}_6$  using an Agilent 400-MR DD2 equipped with a 5 mm ONE probe.

#### A2.1.4. Broadband dielectric spectroscopy

Dielectric measurements of MIL-53(Al),  $\text{NH}_2\text{-MIL-53(Al)}$  and  $\text{NO}_2\text{-MIL-53(Al)}$  powders were performed using a HP 4284A precision LCR meter in 85–425 K temperature and  $10^2\text{--}10^6$  Hz frequency ranges. The powder was pressed (35 kPa) between two round brass electrodes (diameter = 1 cm) in a custom-made cryostat. Temperature was measured using a Keithley 2700 multimeter with a T-type thermocouple. The samples in the measurement cell were kept under constant dry  $\text{N}_2$  flow. All heating and cooling cycles were done at  $1\text{ K min}^{-1}$ . Low temperatures were achieved using liquid  $\text{N}_2$ . The dielectric permittivity data were acquired during heating at  $1\text{ K min}^{-1}$ , preceded by a full activation cycle (heating to ca. 450 K and cooling down to starting temperature ca. 100 K).

#### A2.1.5. Solid-state $^2\text{H}$ NMR spectroscopy

$^2\text{H}$  NMR spectra were acquired using a Bruker Avance III HD console and a 9.4 T Oxford wide-bore magnet at a resonance frequency of  $\nu_0(^2\text{H}) = 61.422\text{ MHz}$ . A Revolution 5 mm double-resonance (HX) ultra-low-temperature (ULT) probe was used for  $^2\text{H}$  NMR experiments. All data were collected under static conditions (*i.e.*, stationary samples). Spectra were acquired with continuous-wave (CW)  $^1\text{H}$  decoupling with RF fields ranging between 40 and 50 kHz.

RF pulse powers and the chemical-shift reference frequency were calibrated using neat  $\text{D}_2\text{O}$  ( $l$ ) with  $\delta_{\text{iso}} = 4.8\text{ ppm}$ . Recycle delays used for each sample at each temperature are listed in Tables A2.2–A2.4. Temperatures of the VT unit and probe were calibrated using the temperature-dependent chemical shift of  $\text{Pb}(\text{NO}_3)_2$ .<sup>1,2</sup> The quadrupolar-echo pulse sequence ( $\pi/2 - \tau_1 - \tau_2 - \pi/2 - \tau_2 - \text{acquire}$ ) was used to acquire the full echo, with a  $\pi/2$  pulse length =  $2.5\ \mu\text{s}$ , echo delays  $\tau_1 = 198.75$  or  $298.75\ \mu\text{s}$ , ringdown delay of  $\tau_2 = 30\ \mu\text{s}$ , and 400 or 600  $\mu\text{s}$  echo lengths.<sup>3</sup> The entire echo is acquired and is processed in MATLAB by multiplication with a Gaussian function for line broadening, then Fourier transformation and magnitude calculation. The quadrupolar parameters of the SML spectra were determined with simulations using SOLA in Topspin 3.6.1. Simulations of the IMR and FML spectra were conducted using EXPRESS.<sup>4</sup> All simulations utilized standard  $^2\text{H}$  quadrupolar parameters for a C–D bond in an aromatic ring:  $C_Q = 180\text{ kHz}$ ,  $\eta_Q = 0.0$ .

## A2.2. Computational methods

### A2.2.1. Density functional theory calculations

All density function theory (DFT) calculations were performed using the ab initio CRYSTAL17 code,<sup>5</sup> at the generalized gradient approximation (GGA) level of theory with the PBE exchange–correlation functional.<sup>6</sup> Grimme “D3” dispersion corrections were used.<sup>7,8</sup> Peintinger–Oliveira–Bredow (POB) triple- $\zeta$  valence plus polarization basis sets<sup>9</sup> were used for all atoms.

For molecular systems, full geometry optimizations were performed to obtain the global energy minimum  $E_{\text{min}}$ . The rotary transition state energy ( $E_{90}$ ) was obtained from constrained geometry

optimizations, setting the dihedral angles between carboxylic groups and ring ( $O-C_{\text{carboxylic}}-C_{\text{ring}}-C_{\text{ring}}$ ) to  $90^\circ$ . In the case of non-planar ground state conformations, a forced coplanar carboxyl reference energy ( $E_{\text{anchor}}$ ) was calculated starting from a planar molecule, performed a geometry optimization while applying constraints to the four oxygens to remain coplanar. The reported  $E_{\text{rot}}$  barriers are relative to  $E_{\text{min}}$  or  $E_{\text{anchor}}$  (if applicable).

For periodic MOF systems, experimentally determined unit cell parameters of the guest-free frameworks were used for  $\text{NH}_2\text{-MIL-53(Al)}$  and  $\text{NO}_2\text{-MIL-53(Al)}$  (Table A2.1).<sup>10</sup> The cell parameters were kept constant in all calculations. Global minimum structures of both MOFs were obtained by geometry optimization of the atomic positions without any symmetry constraints ( $P1$  space group). Starting from the minimized structure, one linker in the unit cell was rotated in steps of  $15^\circ$  (for amino) and  $30^\circ$  (for nitro) in either direction (as defined in the main article) using the CrystalMaker software. At each step, the rotating ring was fixed within the unit cell by freezing the four off-axis carbons. A geometry optimization was then performed, relaxing all other atomic positions. Each successive rotation step was started from the geometry of the previous step. The relative energy for each step is reported with respect to the global minimum energy.

### A2.2.2. Ab initio molecular dynamics simulations

The dynamics of linkers of  $\text{NO}_2\text{-MIL-53(Al)}$  was simulated at different temperatures by DFT-based molecular dynamics (MD) using the Quickstep module<sup>11</sup> of the CP2K code package. The geometry-optimized DFT structure with lattice parameters from ref. 12 was used as starting structure for all MD simulations. Simulations were performed in the  $(N,V,T)$  ensemble with fixed size and shape of the unit cell. A timestep of 0.5 fs was used in the MD runs and temperature was controlled by a canonical sampling through velocity rescaling (CSVR) thermostat.<sup>13</sup> MD simulations had an equilibration period of 5 ps and a production period of 35 ps for all temperatures (300 K, 450 K, 700 K and 1200 K). Valence and core electrons were represented by double- $\zeta$  polarized basis sets and Goedecker–Teter–Hutter (GTH)<sup>14</sup> pseudopotentials for all atoms (C, H, O, N, Al). The exchange correlation energy was evaluated in Perdew–Burke–Ernzerhof (PBE)<sup>6</sup> approximation and dispersion interactions were treated at DFT-D3<sup>8</sup> level. Plane wave cutoff energy was set to 900 Ry based on the energy convergence to  $10^{-4}$  Ha and relative cutoff energy was set to 60 Ry. Representative structures and input files for calculations are available online at <https://github.com/fxcoudert/citable-data>.

## A2.3. Supplementary information

### A2.3.1. DFT structural details

A terephthalate rotor can be divided into three constituent parts: the *para*-phenylene moiety acts as the rotator, the carboxylic groups act as stators, and the two C–C single bonds function as the axle. In free terephthalate rotors, a  $180^\circ$  rotation ( $\pi$ -flip) can be seen as a transition between two potential energy minima (*i.e.*, two conformers).

Nitroterephthalic acid presents a strong case of non-coplanarity, as can be seen in the optimized structure (Figure A2.8, *left*). Chloro- and bromoterephthalic acids behave similarly (not shown). A partial optimization with carboxyl groups in coplanar conformation better represents the

anchoring effect that the MOF lattice imposes on the linker (Figure A2.8, *right*). To allow for an adequate comparison between different functional groups, we use this type of constraint for all molecules that deviate from planarity in full geometry optimizations. In the nitro case, the latter structure has an energy penalty of 10 kJ mol<sup>-1</sup> with respect to the former, mainly attributed to the loss of nitro group  $\pi$  electron delocalization.

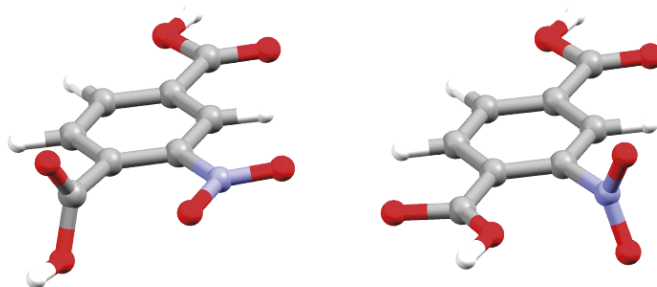


**Figure A2.8.** Nitroterephthalic acid optimized geometries: full optimization (*left*) and coplanar carboxyl partial optimization (*right*).

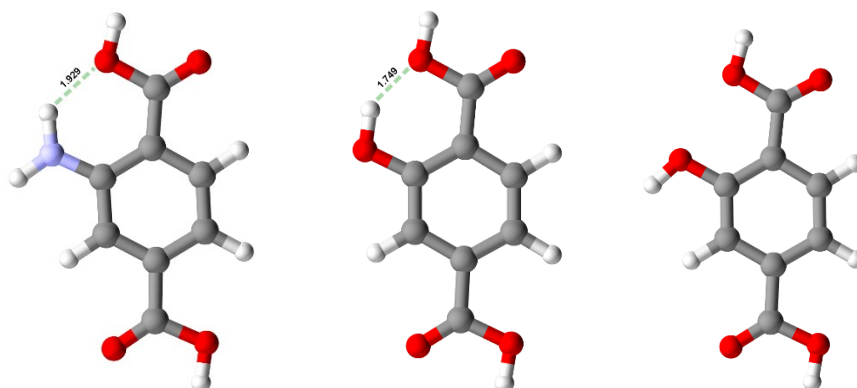


**Figure A2.9.** Geometry-optimized structures of amino- and hydroxyterephthalic acids (*left* and *center*) showing H-bonding distance. Right: Non-H-bonding structure of hydroxyterephthalic acid.

### Free molecule model validation

This simple model estimates a barrier of 48 kJ mol<sup>-1</sup> for the unsubstituted terephthalic acid, which matches the experimentally obtained activation energy of terephthalate linkers in MOF-5 ( $47.3 \pm 8.4$  kJ mol<sup>-1</sup>).<sup>15</sup> This result is not surprising as MOF-5 has a characteristic cubic network with ample free volume surrounding each linker, which prevents inter-linker steric hindrance. Similarly, bromine functionalization yields  $E_{\text{rot}}$  of 25.1 kJ mol<sup>-1</sup>, a reasonable approximation to the experimental value of  $30.5 \pm 0.4$  kJ mol<sup>-1</sup> determined for unhindered IRMOF-2 (bromine-substituted version of MOF-5).<sup>16</sup>

The two functionalizations that increase the barrier with respect to the unfunctionalized linker are amine and hydroxyl (53.7 and 64.2 kJ mol<sup>-1</sup>, respectively). Experimental evidence has shown

similar trends, for example in UiO-66, where an activation energy for linker rotation of  $30 \text{ kJ mol}^{-1}$ ,<sup>17</sup> increased to  $51.9 \text{ kJ mol}^{-1}$  upon amine functionalization.<sup>18</sup> In addition to both these groups being electron donating—which could potentially increase the double bond character of the rotation axis bonds via  $\pi$  electron delocalization—their planar conformations also enable hydrogen bond donation to the adjacent carboxyl oxygen (Figure A2.9).

### A2.3.2. Periodic DFT details

The unit cell parameters of activated frameworks used in DFT calculations are shown in Table A2.1. The rotor spacing (*i.e.*, the distance between the rotation axes of two adjacent linkers in a row) in LP frameworks is defined by the cell parameter  $a$ . For NP conformation, parameter  $c$  defines the spacing. The closest row-to-row distances (presented in Table 2.2 of the main text) for the LP frameworks can be defined as half the cell parameter  $c$  or half of  $b$  for  $\text{NH}_2\text{-MIL-53}$ .

**Table A2.1. Experimental unit cell parameters used in periodic DFT calculations**

| MOF                                      | $a$    | $b$    | $c$    | $\alpha$ | $\beta$ | $\gamma$ |
|--|--------|--------|--------|----------|---------|----------|
| $\text{NO}_2\text{-MIL-53(Al)}^\dagger$  | 6.666  | 16.254 | 13.521 | 90       | 90      | 90       |
| $\text{NH}_2\text{-MIL-53(Al)}^\ddagger$ | 19.722 | 7.692  | 6.578  | 90       | 105.1   | 90       |

<sup>†</sup> Cell parameters from diffraction collected for this work (*vide infra*). <sup>‡</sup>Cell parameters reported in ref. 10.

### $\text{NO}_2\text{-MIL-53(Al)}$ PXRD indexing

The PXRD of activated  $\text{NO}_2\text{-MIL-53(Al)}$  was collected using an Anton–Paar sample cell and heating under  $\text{N}_2$  flow. The diffractogram acquired at  $220^\circ\text{C}$  was indexed using DASH.<sup>19</sup> The obtained cell parameters are shown in Table A2.1.

### A2.3.3. Rotation angle definitions

**$\text{NO}_2\text{-MIL-53(Al)}$ .** The reported rotation angles correspond to the angle between two planes: the best-fitting plane to the benzene ring and the (011) or (0-11) crystallographic plane. The choice between the two crystallographic planes depends on the row to which the rotating linker belongs to. The (011) or (0-11) planes are absolute reference planes as they do not change during geometry optimization or MD simulation. For simplicity, we define the full rotation space around the linker's rotation axis in two halves:  $0^\circ$  to  $180^\circ$  and  $0^\circ$  to  $-180^\circ$ . The positive part of this space corresponds to the orientations pointing in the direction of the normal of the reference plane (see Fig 2a and 2b of the main text), and the negative portion corresponds to those pointing in the opposite direction of the reference plane normal.  $0^\circ$  is defined based on the [100] direction; *i.e.*, the functional group is pointing approximately in the [100] direction of the unit cell.

**$\text{NH}_2\text{-MIL-53(Al)}$ .** The axis of rotation of linkers in  $\text{NH}_2\text{-MIL-53}$  does not correspond to any crystallographic plane. Therefore, we define a reference plane for the rotating linker as the best-fitting plane for its four oxygen atoms in the global minimum structure (see Figure A2.10). The rotation angle is the angle between the best-fitting plane of the rotating ring and the reference

plane. The sign is defined as positive if the functional group points in the general direction of the normal to the reference plane (dashed arrow in Figure A2.10).

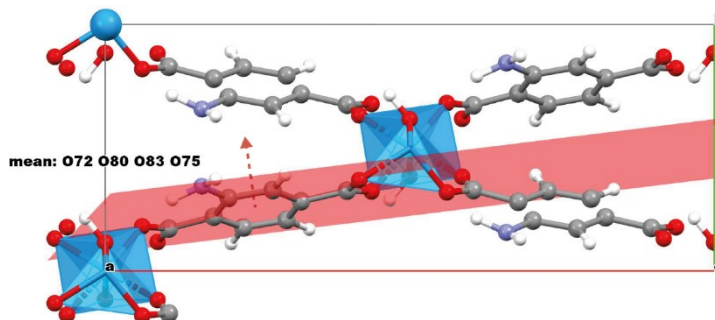


**Figure A2.10.** Reference plane for rotation angle in NH<sub>2</sub>-MIL-53 DFT calculations. Dashed arrow represents the normal vector of the plane, denoting positive angles.

Due to its narrow-pore structure, NH<sub>2</sub>-MIL-53(Al) suffers from strong steric limitations even at small amplitude rotations. An example is shown in Figure A2.11.

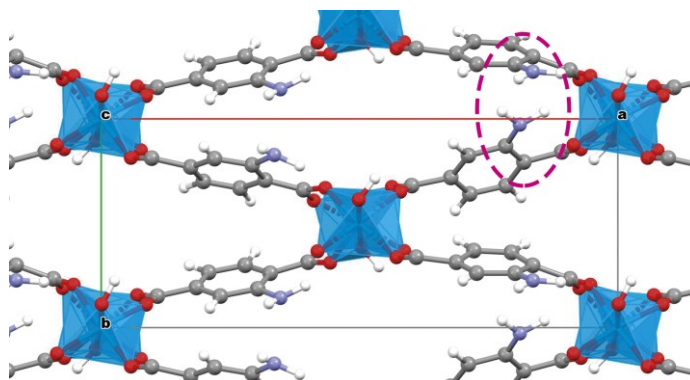


**Figure A2.11.** The linker rotated to ca.  $-30^\circ$  in NH<sub>2</sub>-MIL-53(Al) collides with its neighbor in the closest row.

#### A2.3.4. NO<sub>2</sub>-MIL-53 2x1x1 supercell DFT calculations DFT structure sequence during neighbor “crash”

With the rotating linker (left of the cell) at  $-91^\circ$ , the neighbor is not affected and finds a minimum conformation at ca.  $-12^\circ$  (Figure A2.12). Upon approaching  $-150^\circ$ , the nitro group of the rotating linker begins to overlap with the nitro group of the free neighbor. From the progression seen from  $-145^\circ$  to  $-180^\circ$ , it is clear that the combination of direction of approach of rotating linker and starting conformation of the neighbor (right linker) did not allow for the latter ring to reduce this repulsive interaction by rotating away. This is because this free neighbor is being pushed towards the  $0^\circ$  position, and this represents an increase in energy (note the local maximum at  $0^\circ$ ) before a more energetically favored conformation can be reached. Instead, at  $-180^\circ$  we see the nitro group

of the forced rotated ring is bent to an unfeasible configuration, and the neighbor does not cross the  $0^\circ$  barrier. This leads to the vertical energy increase below  $-145^\circ$  seen in Figure 2c.

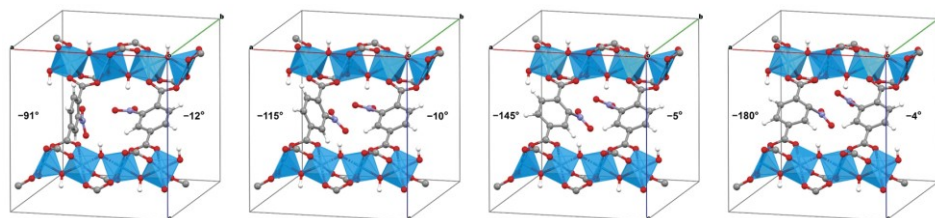


**Figure A2.12.** DFT converged structure sequence for steps from ca.  $-90^\circ$  to  $-180^\circ$  (left to right), which resemble a head-to-head crash between the neighboring rings. The rotating linker is on the left side of each cell.

### DFT structure sequence during neighbor “push”

Rotation in the opposite direction to reach the same  $-150^\circ$  position is different in that the interaction with the free ring resembles a gear; the “push” from the rotating nitro ring causes the free ring to adapt by rotating from its initial  $-15^\circ$  conformation to a larger negative value (ca.  $-56^\circ$ ), as shown in Figure A2.13. Once the rotating ring has cleared the shared space between the pair, the neighbor returned to its minimum ( $-12^\circ$ ). We note that the structure at  $-115^\circ$  for this direction of rotation is still a maximum in the potential energy curve, yet feasible in comparison to the previous rotation direction. This result further illustrates the importance of cooperative motion between neighbor linkers.

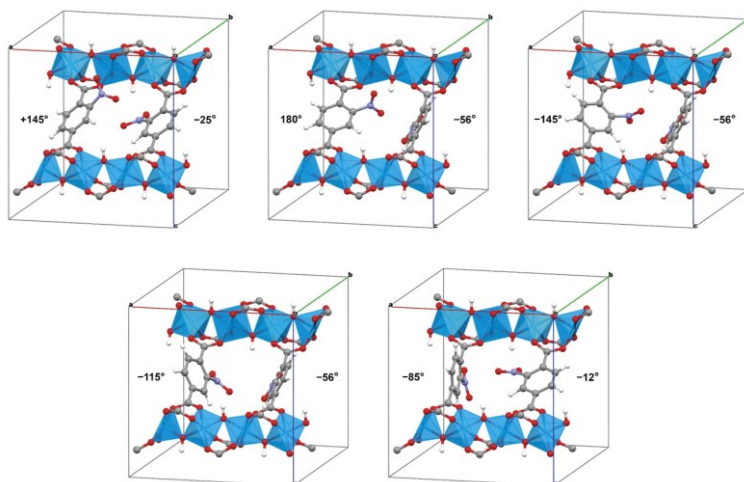


**Figure A2.13.** DFT converged structure sequence for steps from ca.  $+145^\circ$  to  $-85^\circ$  (left to right), which resemble a head-to-head push between the neighboring rings. The free neighbor ring cooperates by swinging out of the rotating linker’s trajectory. The rotating linker is on the left side of each cell.

### Alternative nitro group positions

Even when considering only the pair participating in forced rotation, there are four possible nitro positions for each ring. This results in 16 possible combinations in the  $2 \times 1 \times 1$  supercell calculations,

and although some of them may result in similar energy curves, none of them is equal (due to the effect of the remaining linker's nitro positions). Although a great number of combinations are likely present in a real system, the case we show in the main text was chosen due to it being the most impacted by steric effects between rotors. In addition to the original set of DFT calculations (case 1), we performed calculations using alternative nitro positions: case 2 and case 3, as shown in Figure A2.14.

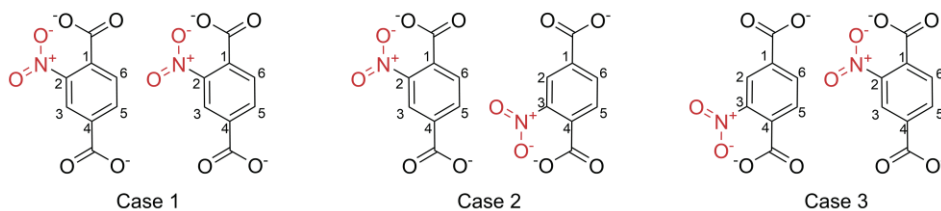


**Figure A2.14.** The three studied cases in 2x1x1 NO<sub>2</sub>-MIL-53 supercell. The rotating ring is on the left for each pair.

These additional calculations focus on the portion of the rotational space most relevant to nitro-nitro interactions. Case 2 and 3 resulted in significantly lower energies at angles where nitro-nitro interactions in case 1 were highly disfavored (see Figure A2.15). Importantly, the unfeasible energy increase observed when rotating below  $-115^\circ$  in case 1 was absent in the two alternative cases, for which a maximum of 50–60 kJ mol<sup>-1</sup> was found. These results indicate that, in contrast to case 1, independent rotation of alternatively positioned nitrophenylene neighbors should not be ruled out.

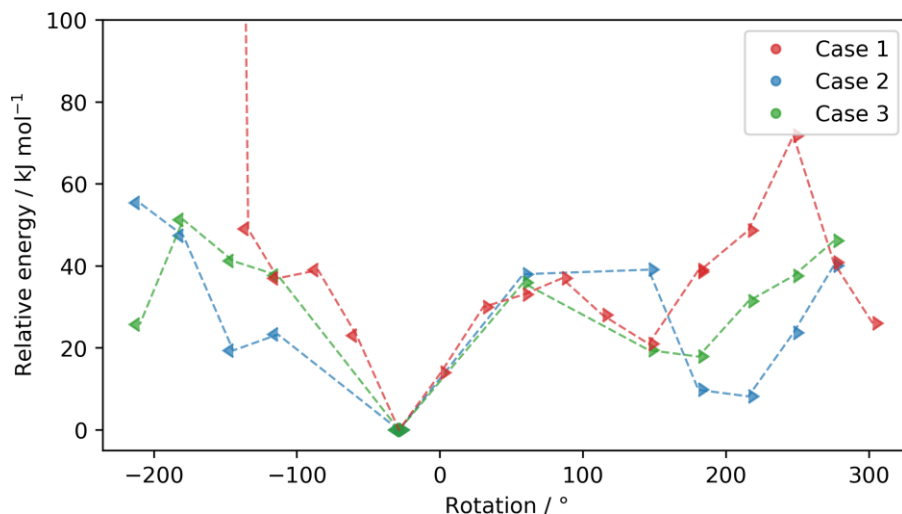


**Figure A2.15.** Potential energy profiles of the three studied cases in 2x1x1 NO<sub>2</sub>-MIL-53 supercell.

The marked difference between the first case and the latter two suggests that a large variability can be expected from a real population of disordered linkers, ranging from linkers whose

neighbors impede rotations (causing slow or no motion) and linkers whose neighbors cooperate (whether by correlated motion or by favorable arrangement) allowing for relatively fast rotation.

### A2.3.5. Supplementary BDS data

We performed BDS measurements on activated powder samples of MIL-53(Al), NO<sub>2</sub>-MIL-53(Al), and NH<sub>2</sub>-MIL-53(Al) under dry N<sub>2</sub> flow. The Cole–Cole equation (Eq. 1) was used to fit the NO<sub>2</sub>-MIL-53(Al) dielectric relaxation. Both  $\epsilon'$  and  $\epsilon''$  parts of the complex dielectric permittivity  $\epsilon^*$  were fitted simultaneously.

$$\epsilon^* = \epsilon_\infty + \frac{\Delta\epsilon}{1+(i\tau\omega)^{1-\alpha}} \quad (1)$$

where  $\epsilon_\infty$  is the high frequency limit of the dielectric permittivity,  $\Delta\epsilon$  is the relaxation strength,  $\omega$  denotes the angular frequency,  $\tau$  is the mean relaxation time, and parameter  $\alpha$  describes the width of the relaxation. For  $\alpha = 0$ , Eq. (1) reduces to the Debye relaxation of non-interacting electric dipoles in a uniform environment. The obtained  $\alpha$  values are presented in Figure A2.18. The relaxation strength remained roughly 1.4 in the whole investigated temperature range.

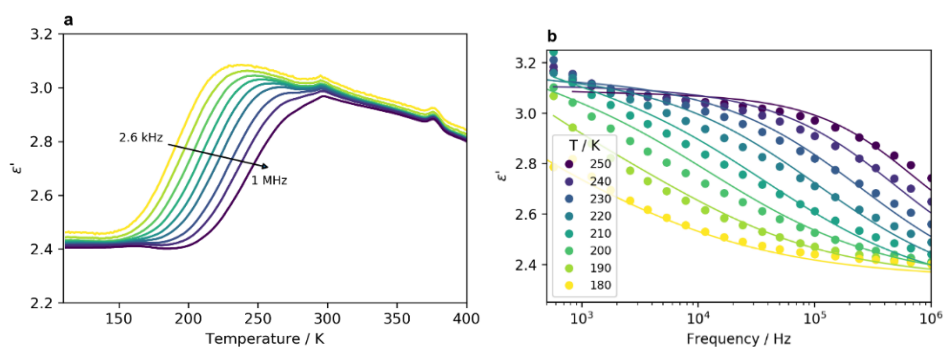


**Figure A2.16.** Real part ( $\epsilon'$ ) of NO<sub>2</sub>-MIL-53(Al) with respect to (a) temperature and (b) frequency. The latter includes the fitted Cole-Cole model (eq. 1) as continuous lines.

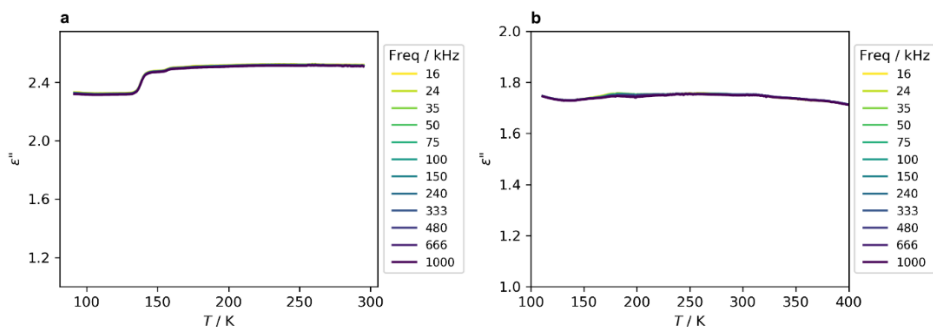


**Figure A2.17.** Temperature domain of  $\epsilon'$  for (a) NH<sub>2</sub>-MIL-53(Al) and (b) MIL-53(Al).

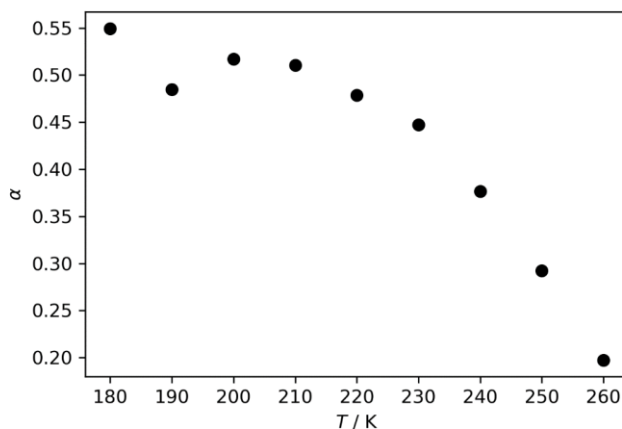


**Figure A2.18.** The  $\alpha$  parameters from the Cole-Cole fit for  $\text{NO}_2$ -MIL-53(Al) relaxation at different temperatures.

The Arrhenius equation (2) was used to fit the determined mean relaxation times  $\tau$ .

$$\tau = \tau_0 e^{E_a/k_b T} \quad (2)$$

where  $E_a$  is the activation energy of the process,  $\tau_0$  denotes the attempt time, and  $k_b$  is the Boltzmann constant. The best fit and determined values of the fit parameters are shown in Figure A2.19.

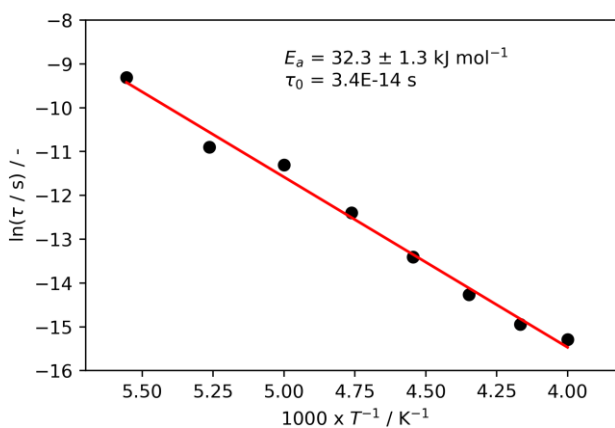


**Figure A2.19.** Fit of the Arrhenius equation (eq. 2) to the mean relaxation times of  $\text{NO}_2$ -MIL-53(Al) obtained from the Cole-Cole fit. The confidence interval corresponds to the standard deviation of the fit.

The obtained pre-exponential factor is equivalent to  $2.9 \times 10^{13}$  Hz. As explained in the main text, a rotator of the dimensions of nitro-*p*-phenylene is expected to present an attempt or libration frequency in the order of  $10^{12}$  Hz, based on a simple assessment of its rotational inertia.<sup>20</sup>

However, it is not uncommon to find pre-exponential factors that deviate from the theoretical expectation to higher values, particularly in studies of more complex rotors, such as functionalized p-phenylene rotators.<sup>18,20–22</sup>

This deviation to higher attempt frequencies has been interpreted as an indication of a temperature dependence of the rotational energy barrier.<sup>20</sup> The reasoning is that the observable  $E_a$  and pre-exponential factor should be taken as effective values, and by fixing the “true” pre-exponential factor as the expected attempt frequency (estimated at  $10^{12}$  Hz), the “true” barriers at each temperature can be derived. After applying this analysis to our data, we found the slope of the barrier to be  $-0.028$  kJ mol<sup>-1</sup> K<sup>-1</sup>, which is in between of the two slopes reported by Horansky et al. for their molecular crystal rotors.<sup>20,21</sup> Phenomena that could be accountable of this effective decrease in rotation barrier with temperature are indeed expected in a framework where linkers influence each other during rotational motion, similar to some that have been reported for other complex solid-state rotor systems.<sup>23–25</sup>

### A2.3.6. Supplementary solid-state <sup>2</sup>H NMR spectroscopy data

**Table A2.2. Experimental Parameters for <sup>2</sup>H NMR Experiments of MIL-53(Al)-d<sub>4</sub>.**

| Temperature (K) | Recycle Delay (s) | Number of Scans |
|-----------------|-------------------|-----------------|
| 453             | 1                 | 4096            |
| 431             | 2                 | 512             |
| 387             | 5                 | 3072            |
| 319             | 60                | 256             |
| 298             | 140               | 50              |
| 277             | 200               | 32              |

**Table A2.3. Experimental Parameters for <sup>2</sup>H NMR Experiments of NH<sub>2</sub>-MIL-53(Al)-d<sub>3</sub>.**

| Temperature (K) | Recycle Delay (s) | Number of Scans |
|-----------------|-------------------|-----------------|
| 453             | 20                | 625             |
| 431             | 20                | 600             |
| 387             | 40                | 256             |
| 298             | 60                | 80              |

**Table A2.4. Experimental Parameters for <sup>2</sup>H NMR Experiments of NO<sub>2</sub>-MIL-53(Al)-d<sub>3</sub>.**

| Temperature (K) | Recycle Delay (s) | Number of Scans |
|-----------------|-------------------|-----------------|
| 453             | 1                 | 512             |
| 431             | 2                 | 512             |
| 409             | 4                 | 512             |

|     |    |      |
|-----|----|------|
| 387 | 6  | 512  |
| 365 | 7  | 512  |
| 342 | 8  | 512  |
| 320 | 10 | 512  |
| 297 | 10 | 1024 |
| 276 | 10 | 1600 |
| 254 | 20 | 1080 |
| 231 | 20 | 768  |

Our data for this system (Figure A2.20**Figure A2.a**) mirror those of Kolokolov *et al.*,<sup>26</sup> where the phenylene rings are observed to undergo an increased rate of 180° reorientations (“ $\pi$ -flips”) at increased temperatures. The modeled rates fitted to an Arrhenius equation yielded an activation energy of 35 kJ mol<sup>-1</sup> (Figure A2.20**b**). It is noted that the fast motion limit (FML, *i.e.*,  $k > 100$  MHz) is not reached, even at temperatures as high as *ca.* 453 K.

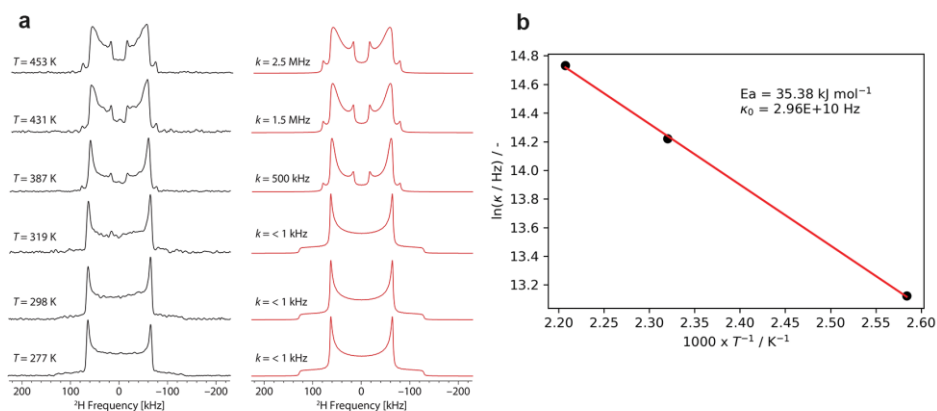


**Figure A2.20.** **a**, Variable-temperature <sup>2</sup>H NMR spectra of MIL-53(Al)-d<sub>4</sub> acquired (left column) at 9.4 T and simulated (right column) with the 180°-flip exchange model described in the text, using different exchange rates, *k*. **b**, Arrhenius fit of the obtained exchange rates.

ND<sub>2</sub>-MIL-53(Al) (a deuterated amine version of the MOF) was investigated by Gascon *et al.*,<sup>27</sup> who found that the aromatic rings remain stationary across a temperature range from 298 to 423 K. Our experiments on ring-labelled NH<sub>2</sub>-MIL-53(Al)-d<sub>3</sub> (Figure A2.21) reveal similar spectra and static behavior of the phenylene rings. This is evidenced by a constant Pake doublet up to 453 K that matches a slow motion limit (SML, *i.e.*, < 1 kHz) C–H bond model.

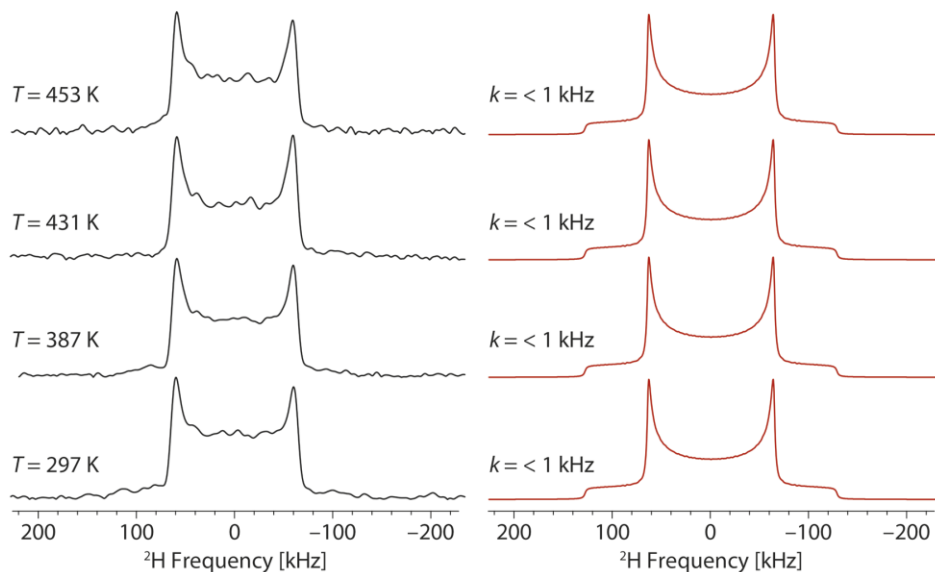


**Figure A2.21.** Variable-temperature  $^2\text{H}$  NMR spectra of  $\text{NH}_2\text{-MIL-53(Al)-d}_3$  acquired (left column) at 9.4T and simulated (right column) with no exchange/low exchange rates (*i.e.*, slow-motion limit spectra). In each case, exchange rate,  $k$ , has an upper limit of 1 kHz.

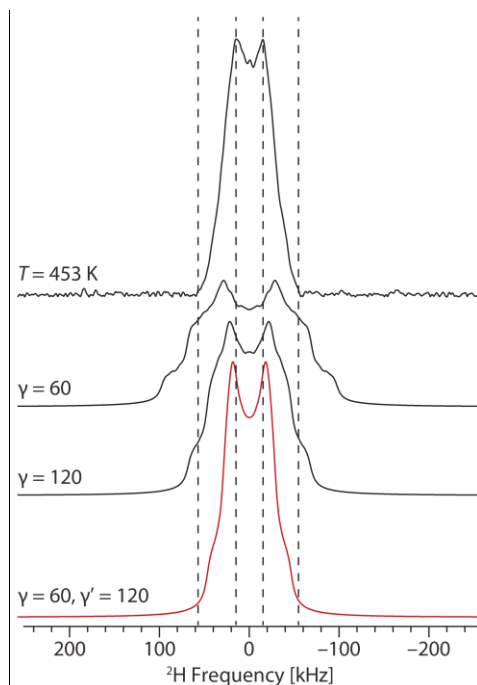


**Figure A2.22.**  $^2\text{H}$  NMR spectra of  $\text{NO}_2\text{-MIL-53(Al)-d}_3$  acquired at 453 K (top) and simulated (below) using a two-site exchange model with a single reorientation of the ring described by the angle  $\gamma$ . The red spectrum is simulated with the four-site exchange model described in the main text and is used in Figure 2.4a (main chapter).

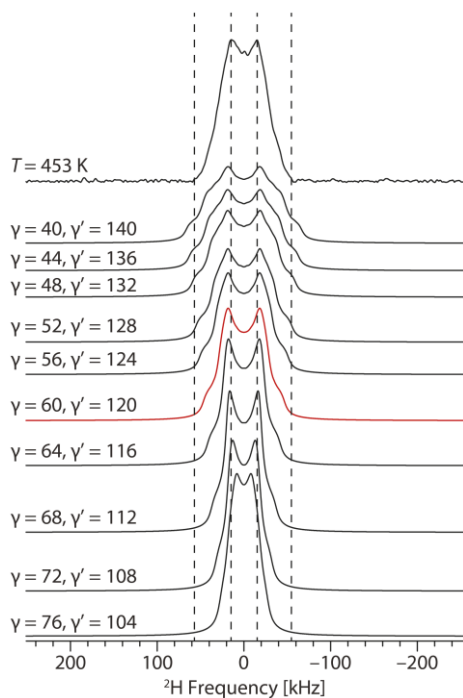


**Figure A2.23.**  $^2\text{H}$  NMR spectra of  $\text{NO}_2\text{-MIL-53(Al)-d}_3$  acquired at 453 K (top spectrum) and simulated (below) using a four-site exchange model described in the main article. In each case, the two relative orientations of the phenyl ring planes vary according to the angles  $\gamma$  and  $\gamma'$ . The simulated spectrum in red is in best agreement with the experimental spectrum and is used in Figure 2.4a (main chapter).

## A2.3.7. Ab initio molecular dynamics simulations

Using the MD trajectory structures, rotation angles of all *p*-phenylene rings (Figures A2.24–A2.28) were obtained using a simple Python code described in Appendix section A2.3.9 and available online at <https://github.com/srinidhimula/supplementary-data>.

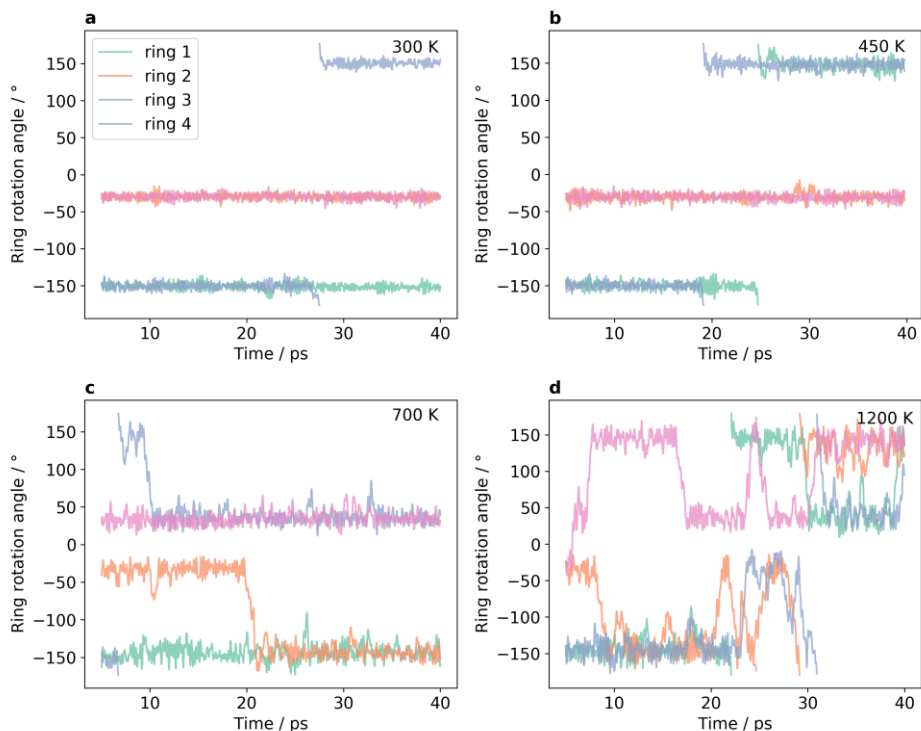


**Figure A2.24.** a-d, Rotation angle traces vs. simulation time for all linkers in a unit cell at different temperatures.

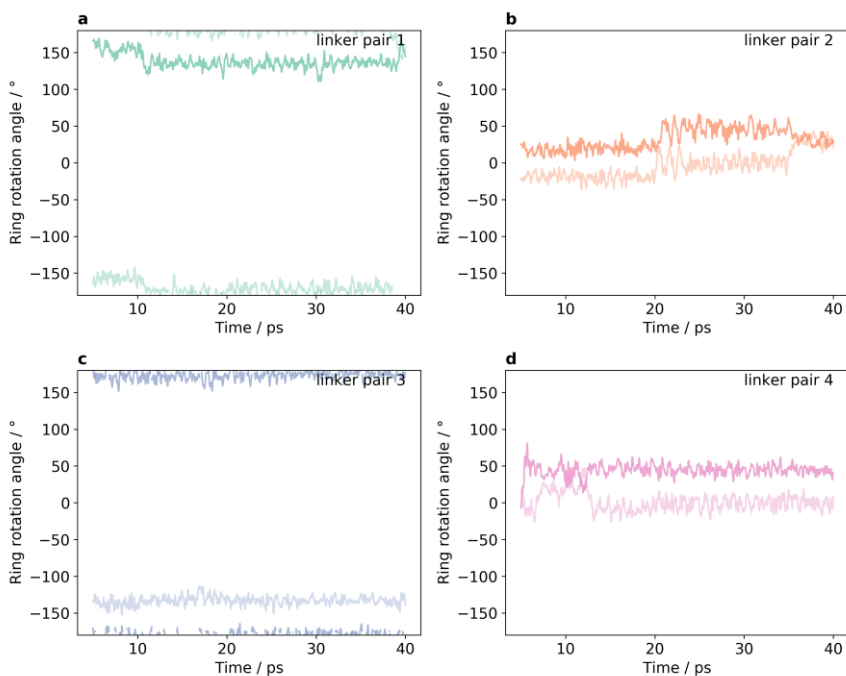


Figure A2.25. a-d, Rotation angle traces vs. simulation time for same-row pairs in a 2x1x1 simulation at 300 K.

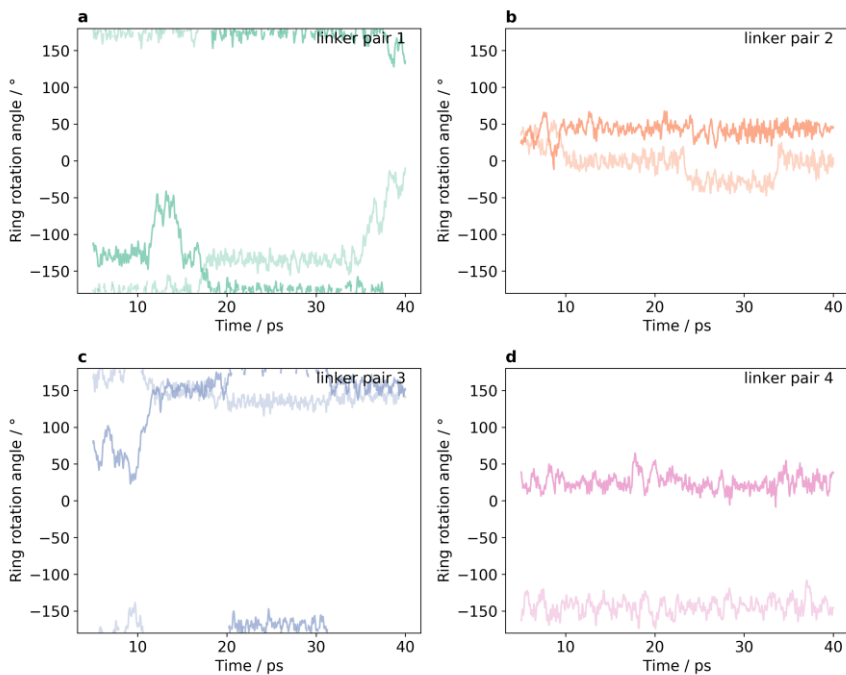


Figure A2.26. a-d, Rotation angle traces vs. simulation time for same-row pairs in a 2x1x1 simulation at 450 K.

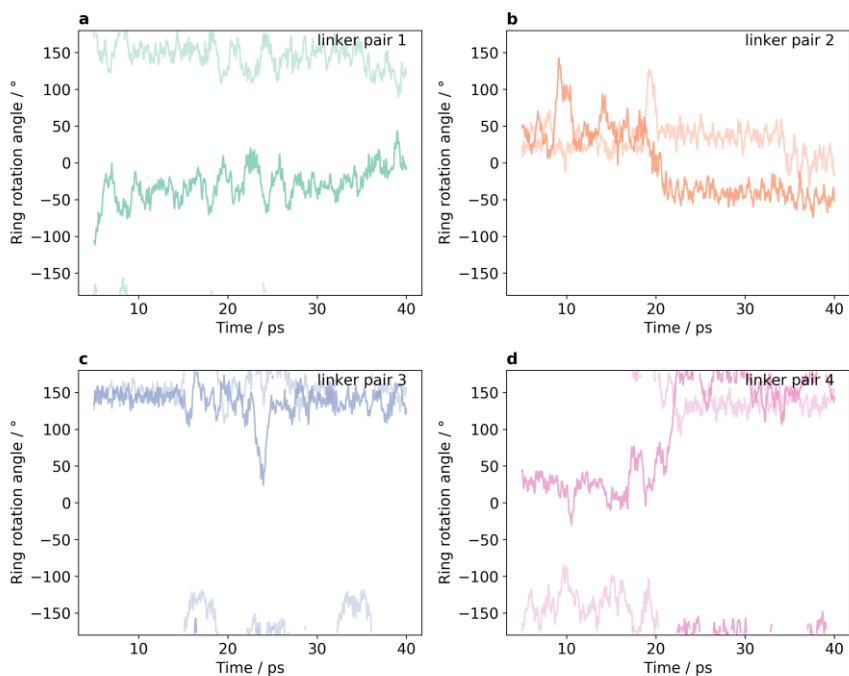


Figure A2.27. a-d, Rotation angle traces vs. simulation time for same-row pairs in a 2x1x1 simulation at 700 K.

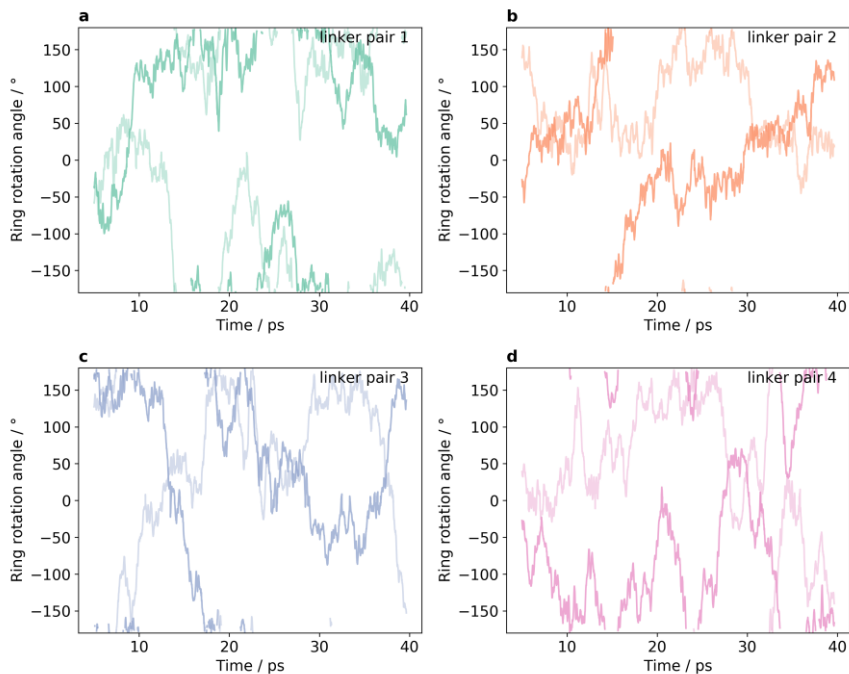
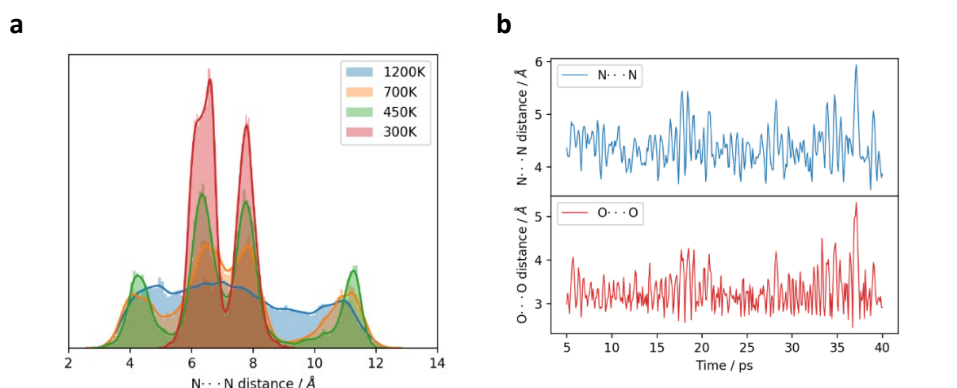


Figure A2.28. a-d, Rotation angle traces vs. simulation time for same-row pairs in 2x1x1 simulation at 1200 K.

### A2.3.8. Correlated motion between pairs of linkers

We present the rotation angle traces of all four same row pairs from the 2x1x1 supercell simulations at 450 K and 700 K along with the corresponding N···N distances between their nitro groups (Figures A2.30–A2.33). The minimum N···N distance seen in the data is approximately 4 Å, as seen in the distributions at all temperatures (Figure A2.29a). Figure A2.b shows that this N···N distance is a reasonable approximation to the closest O···O contact of ca. 3 Å. When N···N distances approach this value, it can be inferred that steric effects between nitro groups start to play a significant role. We highlighted such regions of interest in Figures A2.30–A2.33. In these regions we see that inversely correlated small-angle oscillations occur, such that one trace seems to roughly mirror the other. However, outside these windows, where N···N distance is larger, this correlation is absent, and in fact the frequency of the oscillations is visibly higher (*e.g.*, at 450 K, pair 4 shows correlated fluctuations with lower frequency, while pairs 2 and 3 do not).

Additionally, although rarely observed large-angle jumps occasionally show correlation between same-row pairs when the N···N distance is close to 4 Å. The clearest examples of this are seen at 700 K for pair 2 at ca. 20 ps and pair 4 at ca. 22 ps.



**Figure A2.29.** **a**, Distribution of N···N distances in 2x1x1 simulations. **b**, Comparison between N···N and shortest O···O distances; N···N represents well enough the steric interactions between nitro groups of neighbor pairs of linkers.

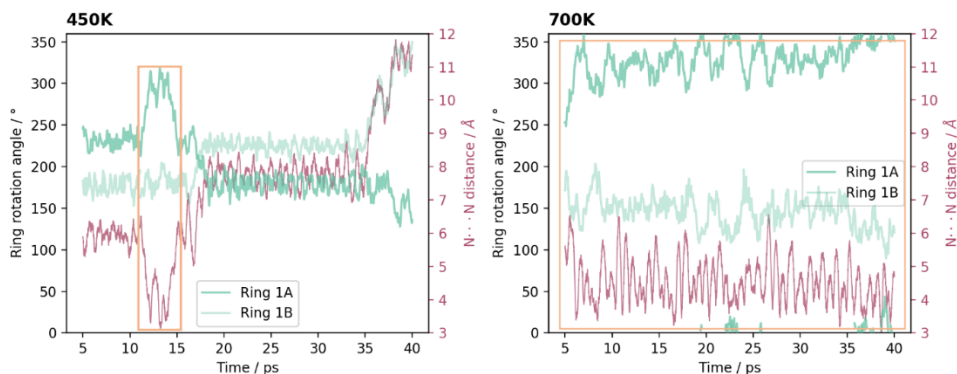


**Figure A2.30.** Rotation angle and N···N distance traces for linker pair 1.

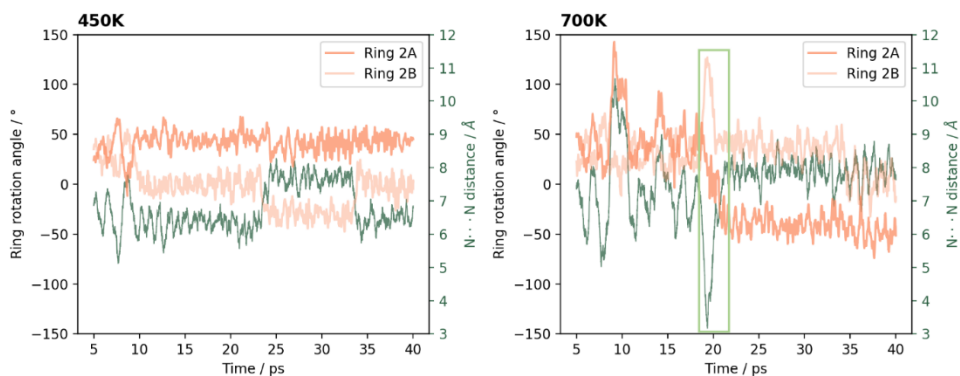


Figure A2.31. Rotation angle and N...N distance traces for linker pair 2.

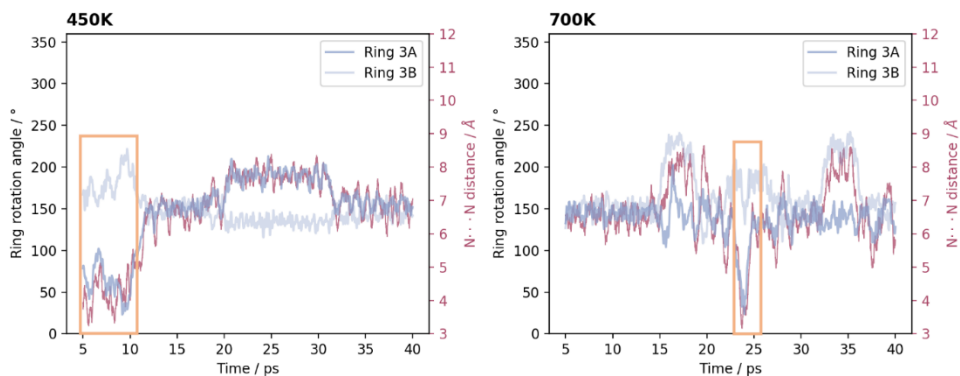


Figure A2.32. Rotation angle and N...N distance traces for linker pair 3.

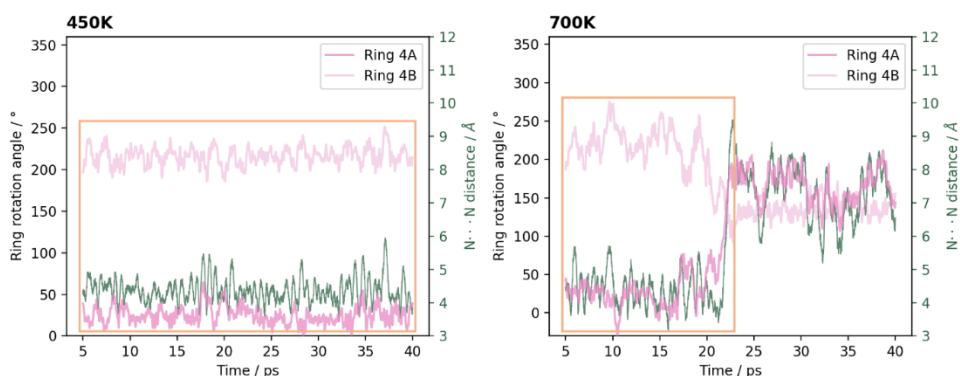


Figure A2.33. Rotation angle and N...N distance traces for linker pair 4.

### A2.3.9. Rotation angle pseudocode

A Python code was used to obtain the rotation angles of all benzene rings in the MD simulation structures. This section includes a detailed description of the code's functionality. The code is available online at <https://github.com/srinidhimula/supplementary-data>.

#pseudocode

**start**= Initial timestep at which rotation angle calculation starts from

**end**= Final timestep at which rotation angle calculation has to be ended

**Function load\_data\_fromxyz:**

Takes the path where MD trajectory file is located as input  
*returns filename and path*

**Function get\_num\_steps:**

Filename from load\_data\_fromxyz is given as input  
for timesteps in (start, end)  
Lines where timestep is specified in the file is read and stored into an array  
*returns timesteps array*

**Function ring(a)\_rotation:**

Filename from load\_data\_fromxyz is given as input  
ring\_carbon = Contains the 6 carbon labels of that specific benzene ring  
ref\_plane = Normal vector ( $\mathbf{N}_{ref}$ ) of reference crystallographic plane based on which row the rotating linker belongs to.  
for timesteps in (start, end)  
    Read cartesian coordinates of the specified ring labels from the MD trajectory file  
    Cell parameters are added for specific cases to correct for periodicity.  
    Call *angle\_calculate* function with inputs : cartesian coordinates of 6 carbons,  $\mathbf{N}_{ref}$  and cartesian coordinates of 3 specific carbons (a, b, c)  
    # Last input(a, b, c) is to have consistent ring normal direction and sign for the rotation angle based on notation in Figure 2 of article  
*returns rotation angle array*

**Function angle\_calculate:**

Inputs: ring carbon cartesian coordinates at each time step,  $\mathbf{N}_{ref}$ , cartesian coordinates of 3 specific carbons (**a, b, c**)  
Normal vector ( $\mathbf{N}$ ) of best fitting plane of benzene carbons is calculated from singular value decomposition  
Ring plane normal vector direction is made consistent by taking cross product  $\mathbf{C1}=(\mathbf{a} \times \mathbf{b})$   
a, b inputs depends on the benzene ring.  
Direction corrected normal vector  $\mathbf{N}_{final}=\mathbf{C1}\cdot\mathbf{N}$   
Rotation angle=  $\cos^{-1}(\mathbf{N}_{final}\cdot\mathbf{N}_{ref})$

Sign for the angle based on notation in Figure 2 is corrected by sign of  $((N_{\text{final}} \times N_{\text{ref}}) \cdot \text{Coord of c})$   
 returns rotation angle

## A2.4. Appendix references

- van Gorkom, L. C. M., Hook, J. M., Logan, M. B., Hanna, J. V. & Wasylshen, R. E. Solid-state lead-207 NMR of lead(II) nitrate: Localized heating effects at high magic angle spinning speeds. *Magn. Reson. Chem.* **33**, 791–795 (1995).
- Bielecki, A. & Burum, D. P. Temperature Dependence of 207Pb MAS Spectra of Solid Lead Nitrate. An Accurate, Sensitive Thermometer for Variable-Temperature MAS. *J. Magn. Reson. Ser. A* **116**, 215–220 (1995).
- Hung, I. & Gan, Z. On the practical aspects of recording wideline QCPMG NMR spectra. *J. Magn. Reson.* **204**, 256–265 (2010).
- Vold, R. L. & Hoatson, G. L. Effects of jump dynamics on solid state nuclear magnetic resonance line shapes and spin relaxation times. *J. Magn. Reson.* **198**, 57–72 (2009).
- Dovesi, R., Erba, A., Orlando, R., Zicovich-Wilson, C. M., Civalleri, B., Maschio, L., Rérat, M., Casassa, S., Baima, J., Salustro, S. & Kirtman, B. Quantum-mechanical condensed matter simulations with CRYSTAL. *Wiley Interdiscip. Rev. Comput. Mol. Sci.* **8**, e1360 (2018).
- Perdew, J. P., Burke, K. & Ernzerhof, M. Generalized Gradient Approximation Made Simple. *Phys. Rev. Lett.* **77**, 3865–3868 (1996).
- Grimme, S., Ehrlich, S. & Goerigk, L. Effect of the damping function in dispersion corrected density functional theory. *J. Comput. Chem.* **32**, 1456–1465 (2011).
- Grimme, S., Antony, J., Ehrlich, S. & Krieg, H. A consistent and accurate ab initio parametrization of density functional dispersion correction (DFT-D) for the 94 elements H-Pu. *J. Chem. Phys.* **132**, 154104 (2010).
- Peintinger, M. F., Oliveira, D. V. & Bredow, T. Consistent Gaussian basis sets of triple-zeta valence with polarization quality for solid-state calculations. *J. Comput. Chem.* **34**, 451–459 (2013).
- Ahnfeldt, T., Gunzermann, D., Loiseau, T., Hirsemann, D., Senker, J., Férey, G. & Stock, N. Synthesis and Modification of a Functionalized 3D Open-Framework Structure with MIL-53 Topology. *Inorg. Chem.* **48**, 3057–3064 (2009).
- VandeVondele, J., Krack, M., Mohamed, F., Parrinello, M., Chassaing, T. & Hutter, J. Quickstep: Fast and accurate density functional calculations using a mixed Gaussian and plane waves approach. *Comput. Phys. Commun.* **167**, 103–128 (2005).
- Biswas, S., Ahnfeldt, T. & Stock, N. New Functionalized Flexible Al-MIL-53-X (X = -Cl, -Br, -CH<sub>3</sub>, -NO<sub>2</sub>, -(OH)<sub>2</sub>) Solids: Syntheses, Characterization, Sorption, and Breathing Behavior. *Inorg. Chem.* **50**, 9518–9526 (2011).
- Bussi, G., Donadio, D. & Parrinello, M. Canonical sampling through velocity rescaling. *J. Chem. Phys.* **126**, 014101 (2007).
- Goedecker, S., Teter, M. & Hutter, J. Separable dual-space Gaussian pseudopotentials. *Phys. Rev. B* **54**, 1703–1710 (1996).
- Gould, S. L., Tranchemontagne, D., Yaghi, O. M. & Garcia-Garibay, M. A. Amphidynamic character of crystalline MOF-5: Rotational dynamics of terephthalate phenylenes in a free-volume, sterically unhindered environment. *J. Am. Chem. Soc.* **130**, 3246–3247 (2008).
- Winston, E. B., Lowell, P. J., Vacek, J., Chocholoušová, J., Michl, J. & Price, J. C. Dipolar molecular rotors in the metal–organic framework crystal IRMOF-2. *Phys. Chem. Chem.*

- Phys.* **10**, 5188 (2008).
17. Kolokolov, D. I., Stepanov, A. G., Guillermin, V., Serre, C., Frick, B. & Jolic, H. Probing the dynamics of the porous Zr terephthalate UiO-66 framework using <sup>2</sup>H NMR and neutron scattering. *J. Phys. Chem. C* **116**, 12131–12136 (2012).
  18. Devautour-Vinot, S., Maurin, G., Serre, C., Horcajada, P., Paula Da Cunha, D., Guillermin, V., De Souza Costa, E., Taulelle, F. & Martineau, C. Structure and dynamics of the functionalized MOF type UiO-66(Zr): NMR and dielectric relaxation spectroscopies coupled with DFT calculations. *Chem. Mater.* **24**, 2168–2177 (2012).
  19. David, W. I. F., Shankland, K., van de Streek, J., Pidcock, E., Motherwell, W. D. S. & Cole, J. C. *DASH* : a program for crystal structure determination from powder diffraction data. *J. Appl. Crystallogr.* **39**, 910–915 (2006).
  20. Horansky, R. D., Clarke, L. I., Winston, E. B., Price, J. C., Karlen, S. D., Jarowski, P. D., Santillan, R. & Garcia-Garibay, M. A. Dipolar rotor-rotor interactions in a difluorobenzene molecular rotor crystal. *Phys. Rev. B - Condens. Matter Mater. Phys.* **74**, 1–12 (2006).
  21. Horansky, R. D., Clarke, L. I., Price, J. C., Khuong, T. A. V., Jarowski, P. D. & Garcia-Garibay, M. A. Dielectric response of a dipolar molecular rotor crystal. *Phys. Rev. B - Condens. Matter Mater. Phys.* **72**, 1–5 (2005).
  22. Liepuoniute, I., Huynh, C. M., Perez-Estrada, S., Wang, Y., Khan, S., Houk, K. N. & Garcia-Garibay, M. A. Enhanced Rotation by Ground State Destabilization in Amphidynamic Crystals of a Dipolar 2,3-Difluorophenylene Rotator as Established by Solid State <sup>2</sup>H NMR and Dielectric Spectroscopy. *J. Phys. Chem. C* **124**, 15391–15398 (2020).
  23. Jiang, X., O'Brien, Z. J., Yang, S., Lai, L. H., Buenaflor, J., Tan, C., Khan, S., Houk, K. N. & Garcia-Garibay, M. A. Crystal Fluidity Reflected by Fast Rotational Motion at the Core, Branches, and Peripheral Aromatic Groups of a Dendrimeric Molecular Rotor. *J. Am. Chem. Soc.* **138**, 4650–4656 (2016).
  24. Vogelsberg, C. S., Bracco, S., Beretta, M., Comotti, A., Sozzani, P. & Garcia-Garibay, M. A. Dynamics of Molecular Rotors Confined in Two Dimensions: Transition from a 2D Rotational Glass to a 2D Rotational Fluid in a Periodic Mesoporous Organosilica. *J. Phys. Chem. B* **116**, 1623–1632 (2012).
  25. Jiang, X., Duan, H.-B., Khan, S. I. & Garcia-Garibay, M. A. Diffusion-Controlled Rotation of Triptycene in a Metal–Organic Framework (MOF) Sheds Light on the Viscosity of MOF-Confined Solvent. *ACS Cent. Sci.* **2**, 608–613 (2016).
  26. Kolokolov, D. I., Stepanov, A. G. & Jolic, H. Guest controlled rotational dynamics of terephthalate phenylenes in metal-organic framework MIL-53(Al): Effect of different xylene loadings. *J. Phys. Chem. C* **118**, 15978–15984 (2014).
  27. Serra-Crespo, P., Van Der Veen, M. A., Gobechiya, E., Houthoofd, K., Filinchuk, Y., Kirschhock, C. E. A., Martens, J. A., Sels, B. F., De Vos, D. E., Kapteijn, F. & Gascon, J. NH<sub>2</sub>-MIL-53(Al): A high-contrast reversible solid-state nonlinear optical switch. *J. Am. Chem. Soc.* **134**, 8314–8317 (2012).



# Chapter 3

## Overcoming crystallinity limitations of aluminum metal–organic frameworks by oxalic acid modulated synthesis

---

A modulated synthesis approach based on the chelating properties of oxalic acid ( $\text{H}_2\text{C}_2\text{O}_4$ ) is presented as a robust and versatile method to achieve highly crystalline Al-based metal–organic frameworks. A comparative study on this method and the already established modulation by hydrofluoric acid was conducted using MIL-53 as test system. The superior performance of oxalic acid modulation in terms of crystallinity and absence of undesired impurities is explained by assessing the coordination modes of the two modulators and the structural features of the product. The validity of our approach was confirmed for a diverse set of Al-MOFs, namely X-MIL-53 ( $X = \text{OH}, \text{CH}_3\text{O}, \text{Br}, \text{NO}_2$ ), CAU-10, MIL-69, and Al(OH)ndc (ndc = 1,4-naphthalenedicarboxylate), highlighting the potential benefits of extending the use of this modulator to the synthesis of other coordination materials.

---

This chapter is based on the following publication:

Stefano Canossa,<sup>‡</sup> Adrian Gonzalez-Nelson,<sup>‡</sup> Leonid Shupletsov, Maria del Carmen Martin, and Monique A. Van der Veen, Overcoming Crystallinity Limitations of Aluminium Metal–Organic Frameworks by Oxalic Acid Modulated Synthesis, *Chem. Eur. J.* **26**, 3564–3570 (2020). (<sup>‡</sup> Equal contribution to this publication: experimental design, synthesis, characterization, and analysis).

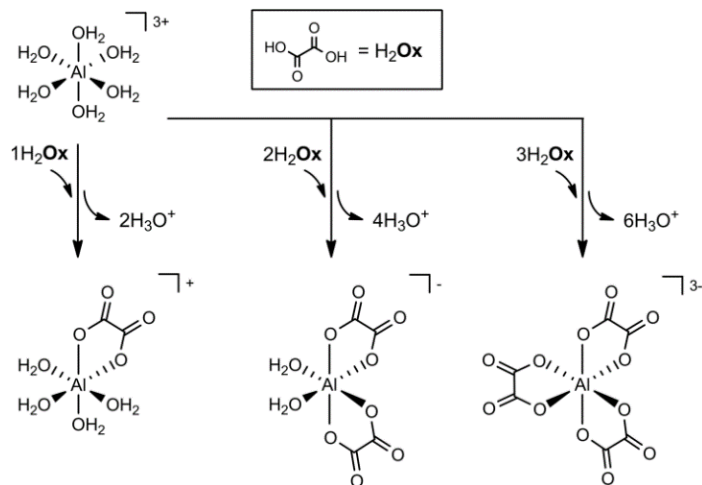
### 3.1. Introduction

Among porous materials, metal–organic frameworks (MOFs) stand out for the extraordinary diversity of their applications. Such versatility arises from the combined use of a virtually endless variety of inorganic and organic building units (known as IBUs and linkers, respectively). Although this hybrid structure can endow MOFs with an outstanding number of functionalities, it also limits their chemical and thermal stabilities, which are substantially lower compared to already established porous inorganic materials such as zeolites<sup>1–3</sup> and porous metal oxides.<sup>4</sup> For this reason, the research of stable MOFs is of utmost importance to guarantee long-term unaltered performance, especially for applications involving non-standard conditions such as catalysis or gas separation. In this regard, Al-MOFs are of special interest as they combine high operating temperatures,<sup>5</sup> convenient syntheses in aqueous media,<sup>6–8</sup> and high natural abundance of the metal sources. Moreover, their exceptional chemical stability<sup>9,10</sup> in both aqueous and organic media make this class of materials ideal for applications that are unsuitable for most MOFs, such as moisture harvesting,<sup>11,12</sup> adsorption-driven heat exchange,<sup>13–15</sup> and water remediation.<sup>16</sup> Unfortunately, the synthesis of highly crystalline Al-MOFs is a long-standing challenge as most of these can only be obtained as nanocrystalline powders<sup>17–19</sup> and such limitations are known to have detrimental effects on MOFs' porosity and sorption capacity.<sup>20–22</sup> Importantly, increasing the achievable crystal size of MOFs enables the detailed description of their structural features by single-crystal X-ray diffraction (SCXRD) and the investigation of functional properties of interest, such as mechanical response<sup>23–26</sup> and electronic behavior.<sup>27–29</sup>

A synthetic strategy that has been successful in modifying the average size of MOF crystals is known as coordination modulation. This method often relies on the addition of a monotopic ligand with the same coordination group as the linker, which act as capping reagents impeding the coordination between metal cations and linkers, effectively slowing down the reaction rate.<sup>30</sup> Although this method of kinetic control has shown positive results in increasing crystal size of some MOFs,<sup>31,32</sup> it carries the potentially undesired effect of producing large amounts of missing linker defects.<sup>33</sup> This is a direct result of the modulator ligand substituting linkers in the final product. Moreover, the addition of monocarboxylic acids to Al-MOF syntheses has not been found to increase crystal size as significantly as in other systems.<sup>34</sup> To date, the only effective approach that has been reported for the synthesis of highly crystalline Al-MOFs is based on the use of hydrofluoric acid (HF),<sup>35–38</sup> borrowing from its well-documented use as mineralizer to improve the crystallinity of microporous inorganic materials.<sup>39</sup> Its widespread use, however, raises concerns both on safety and on the possible fluoride inclusion into the framework's structure.

In this context, this chapter presents a versatile and efficient modulated synthesis approach able to improve substantially the crystallinity of Al-MOFs while maintaining their structure and composition unaltered. This method is based on the use of a natural and abundant molecule: oxalic acid (chemical formula:  $\text{H}_2\text{C}_2\text{O}_4$ ; Scheme 3.1). The high stability of this molecule's hetero- and homoleptic aluminum complexes has long been known in environmental and geological sciences,<sup>40,41</sup> yet its potential as synthesis modulator has never been studied. The formation of aluminum complexes in solution may provide a similar beneficial effect on MOF formation as HF. The coordination of fluoride to the metal cations is thought to reduce the rate of MOF formation by limiting the availability of metal cations.<sup>42</sup> This action differs from the capping effect attributed

to monocarboxylic modulators. In a similar way, the formation of strong complexes with oxalate is expected to reduce the effective concentration of  $\text{Al}^{3+}$ , therefore resulting in slower nucleation and growth, producing a smaller number of single crystals.



**Scheme 3.1.** The possible hetero- and homoleptic complexes formed in water by  $\text{Al}^{3+}$  and oxalic acid.

### 3.2. Results and discussion

First, the effects of this molecule in the synthesis of the widely researched MIL-53( $\text{Al}$ )<sup>43</sup> (chemical formula  $\text{Al}(\text{OH})\text{bdc}$ ;  $\text{bdc} = 1,4\text{-benzdicarboxylate}$ ) were compared, under equal synthetic conditions, with those of other modulators, namely  $\text{HCl}$ ,  $\text{HF}$ ,  $\text{NH}_4\text{F}$ , and sodium oxalate. This choice allows the decoupling of the effects of acidity and coordination modulation, and the evaluation of the advantages of this approach over the already established use of  $\text{HF}$ . Whereas the increase of  $\text{H}_3\text{O}^+$  concentration has positive effects on the crystallinity in general, the  $\sim 10\ \mu\text{m}$  average crystal size observed by using  $\text{HCl}$  increases 4-fold with  $\text{HF}$  and 8-fold with oxalic acid (Figure 3.1a, Figures A3.3–A3.8), suggesting that the anion’s coordinative capabilities have the most significant influence. However, in the case of fluoride modulation, the crystal size was not the only observed change as powder X-ray diffraction (PXRD) patterns show the presence of a secondary phase (Figure 3.1a). This is supported by the appearance of a secondary combustion process in the thermogravimetric profiles (Figure A3.37). These differences agree with the formation of a fluorine-substituted form of MIL-53,  $\text{Al}(\text{F})\text{bdc}$ , whose properties differ significantly from those of the fluorine-free material, especially concerning its renowned breathing behaviour.<sup>44</sup>

This compound, first reported by Liu et al,<sup>45</sup> has also been observed as impurity in a recent paper on the use of  $\text{HF}$  to increase the crystallinity of MIL-53.<sup>36</sup> Energy dispersive X-ray spectroscopy (EDX) analysis on rinsed product obtained by  $\text{HF}$ -modulated synthesis shows that all the observed crystals are contaminated with fluoride inclusions (Figures 3.1b and A3.36). This evidence indicates that  $\text{Al}(\text{F})\text{bdc}$  is present as crystalline domains within MIL-53 crystals rather than as a pure phase. This is further corroborated by the absence of structured diffuse scattering in high-

resolution SCXRD data from contaminated crystals (Figures A3.53 and A3.54).<sup>46,47</sup> Additionally, a minor fraction of the crystals exhibit a higher density of aluminum and fluorine, in line with the previously reported presence of undesired  $\text{AlF}_3$  (Figure 3.1b, Figure A3.36, and Table A3.3).<sup>37</sup> Considering all the evidence, it can be concluded that the use of fluoride modulation in MIL-53 synthesis yields crystals with inclusions of  $\text{Al}(\text{F})\text{bdc}$ , and  $\text{AlF}_3$  as by-product.

The oxalate-modulated syntheses, on the other hand, yielded pure MIL-53 crystals as evidenced by PXRD analysis (Figure 3.1a). Their thermogravimetric profiles show no sign of oxalate species in the framework or missing linker defects (Figure A3.37). Moreover, nitrogen sorption measurements show no substantial difference, in terms of BET area and pore volume, between the unmodulated and the oxalic acid-modulated products. By comparison, the products obtained by using HF show instead a loss of BET area and pore volume of approximately 10%. Since this difference is mainly attributable to the presence of impurities of non-porous  $\text{AlF}_3$  in the sample ( $\sim 4.5\%$  w/w calculated from the TGA profile), it is not possible to assess with precision the effects of the fluoride inclusions in the MIL-53 framework based on the sorption behavior. Nevertheless, these results further demonstrate the detrimental effects of fluoride-based synthesis modulation and the capability of oxalic acid to increase the MOF's crystallinity without causing compositional modifications. In other words, oxalic acid offers the kinetic control over nucleation and growth, similar to HF, by decreasing the availability of metal cations, without undesired structural changes in the framework.

The main reason for these effects can be found in the characteristic  $\kappa^2$  chelation mode of oxalic acid and the high stability of the resulting five-membered ring (Scheme 3.2a), which results in the kinetic control of nucleation and crystal growth during synthesis. The participation of oxalate in the framework would require it either to adopt a poorly stable  $\mu_2$ -1,3 coordination using only one of its carboxylate groups or to bridge the aluminum centers using both groups (*i.e.*,  $\mu_2$ -1,4 bridging), which is incompatible with the MIL-53 structure both in terms of charge and IBU coordination geometry. This is further supported by the absence of both types of oxalate–aluminum coordination geometries in the CSD database (see Appendix section A3.6).<sup>48</sup>

On the contrary, fluoride coordination to aluminum is fully compatible with the substitution of hydroxy groups in the framework since both anions are monodentate, have similar size, and feature the same charge and number of valence electron pairs (Scheme 3.2b). For similar reasons, the use of short-chain monocarboxylic acids as synthesis modulators should be considered only in cases where inducing linker-replacement defects is pursued, as evidenced by previous studies.<sup>49,50</sup>

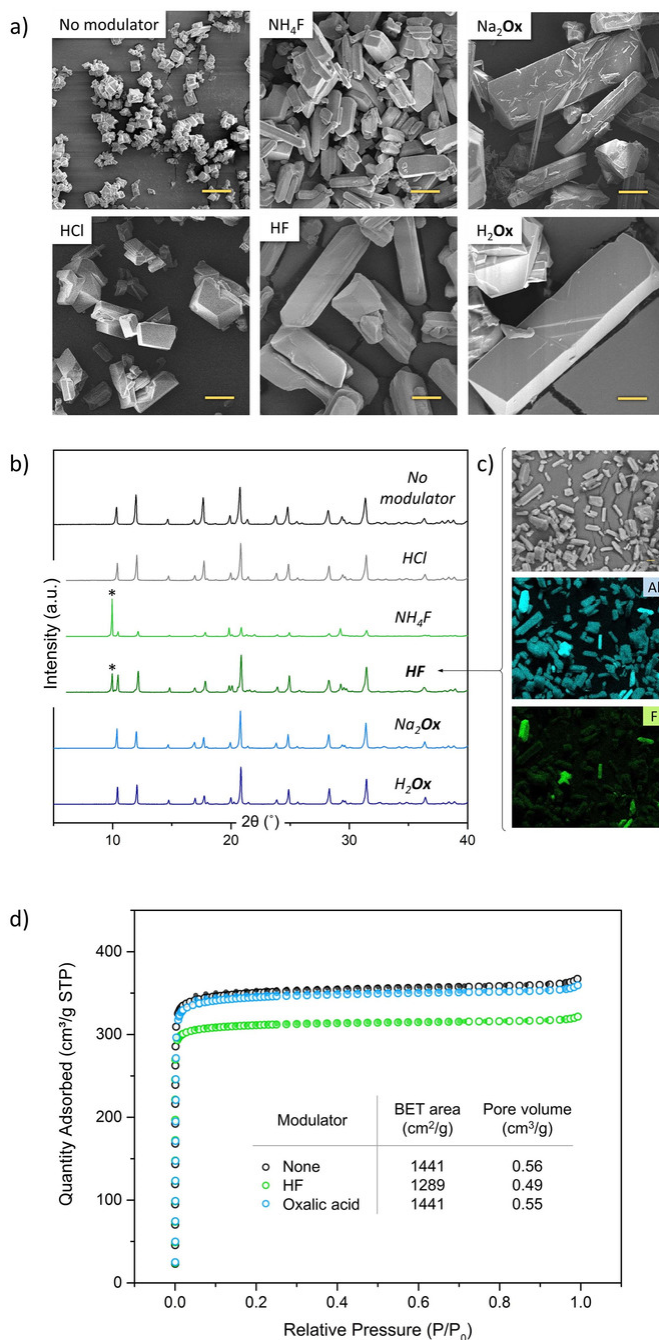
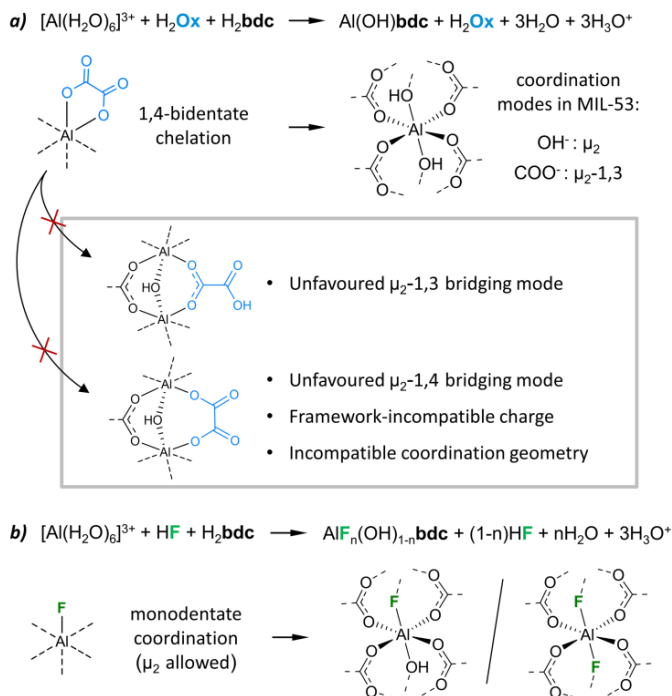


**Figure 3.1.** Comparison of oxalic acid as modulator of MIL-53(Al) versus other modulators. a, SEM micrographs of MIL-53 crystals obtained by normal and modulated syntheses (scale bar = 10 μm). b, c, PXRD and EDX analysis (c) show the presence of Al(F)bc (marked \*) and AlF<sub>3</sub> when a fluoride-based modulator is used. (d) N<sub>2</sub> adsorption (open symbols) and desorption (closed symbols) isotherms showing a decrease of BET area and micropore volume for HF-modulated MIL-53.



**Scheme 3.2.** The reaction formulas for MIL-53 synthesis modulated by oxalic acid (a) and hydrofluoric acid (b).

The benefits of oxalic acid modulation are not limited to MIL-53, as they were also observed for its analogues with OH-, CH<sub>3</sub>O-, Br-, and NO<sub>2</sub>-functionalised linkers. These MOFs were synthesized using 0.5, 1, and 1.5 oxalic acid:Al ratios to study how the amount of modulator affects the crystallinity of the products. In all the studied systems, oxalic acid leads to an increased crystal size with respect to the unmodulated synthesis (Figure 3.2, Figures A3.9–A3.23). In contrast to studies using other modulators,<sup>34,51,52</sup> which have found an effect on the crystal shape of the product, there are no drastic differences when using oxalic acid as modulator beyond slightly more elongated morphology. Interestingly, a higher modulator-to-Al ratio does not always result in improved crystallinity. Indeed, in the cases of OH- and CH<sub>3</sub>O-MIL-53, an excessive amount of modulator leads to the stabilization of a specific size or the absence of solid products, respectively. This behavior can be attributed to the electron-donor character of OH and CH<sub>3</sub>O groups,<sup>53</sup> which lowers the acidity of terephthalic acid by destabilizing its conjugated base.<sup>54</sup> Additionally, the pH decrease due to the MOF synthesis and to the formation of aluminum oxalate complexes further disfavors the deprotonation of the linkers, thus diminishing their reactivity. Our results show that the combination of these effects can allow for the tuning of the product's size distribution, in addition to its crystallinity. However, to achieve such control several aspects should be considered, in particular the modulator concentration, the species formed during the synthesis, and the chemical properties of the linker. Therefore, the adequate conditions to stabilize a specific size must be optimized for every system.

A peculiar behavior is observed for NO<sub>2</sub>-MIL-53, whose crystal size and quality (*i.e.*, single crystals) increases progressively with the use of 0.5 and 1 modulator:Al molar ratios, but drops significantly when a ratio of 1.5 is used (Figure 3.2 and Figures A3.20–A3.23). Using the highest ratio, irregular crystals with rough surfaces were obtained, suggesting a large amount of intergrowth. The PXRD patterns of all NO<sub>2</sub>-MIL-53 products (Figure A3.48) show broad diffuse reflections, also observed by SCXRD (Figure A3.55). These signals are attributable to a local ordering of the NO<sub>2</sub> groups, which can be found disordered in four equivalent positions for every linker after the MOF assembly. The effect of the modulator in slowing the crystal growth can favor this ordering and allow the formation of larger ordered domains, which could grow clustered in polycrystalline aggregates like those observed by SEM for the products obtained with the highest modulator concentration. Further experiments to confirm this hypothesis and determine the ordering of the NO<sub>2</sub> groups will be the focus of our future research.

Having confirmed the effectiveness of oxalic acid in the synthesis of functionalized MIL-53, we extended its use to additional Al-MOFs with varying linker molecules and IBUs, namely CAU-10,<sup>55</sup> MIL-69,<sup>56</sup> and Al(OH)ndc<sup>57</sup> (ndc = 1,4-naphthalenedicarboxylate). These three materials were obtained as nanocrystalline powders by conventional synthesis, whereas the introduction of oxalic acid modulation afforded crystals up to 5 μm for CAU-10, 20 μm for MIL-69, and 70 μm for Al(OH)ndc (Figure 3.2, Figures A3.24–A3.35). Although the performance of the modulator depends strongly on the type of material, the oxalic acid modulation method proved its validity on these systems despite their different structure and assembly. Even in the case of the notably different linker geometry and IBU structure of CAU-10, the kinetic control introduced by oxalate coordination to the metals improves the crystallinity while limiting the occurrence of intergrown domains.

### 3.3. Conclusions

In conclusion, the use of oxalic acid as synthesis modulator for various Al-MOFs affords products with an unprecedented crystallinity without affecting the materials' structure and composition. Although the outcome of this approach is highly dependent on the framework's structure as well as on the synthetic conditions, its efficacy has been confirmed for all the examined systems regardless of linker functionalization or type of material. In the most successful cases, single crystal size were found to have increased up to tenfold. We attribute the remarkable versatility of oxalic acid as crystal size modulator to the synergistic action in both binding the metals and protonating the linkers, which introduce a substantial kinetic control over the MOF nucleation and crystal growth. Furthermore, the strong differences between its characteristic five-membered ring chelation and the linker's coordination mode in the studied materials allow a crystallization modulating function without causing substitutional defects. These advantages do not apply in the case of modulators whose coordination capabilities are compatible with those found in the IBUs, such as fluoride or monocarboxylate species. Further applications of oxalic acid modulation to other Al-MOFs, as well as frameworks based on different metals, will be crucial to assess more thoroughly its validity and highlight additional MOF-specific particularities and advantages associated with its use.

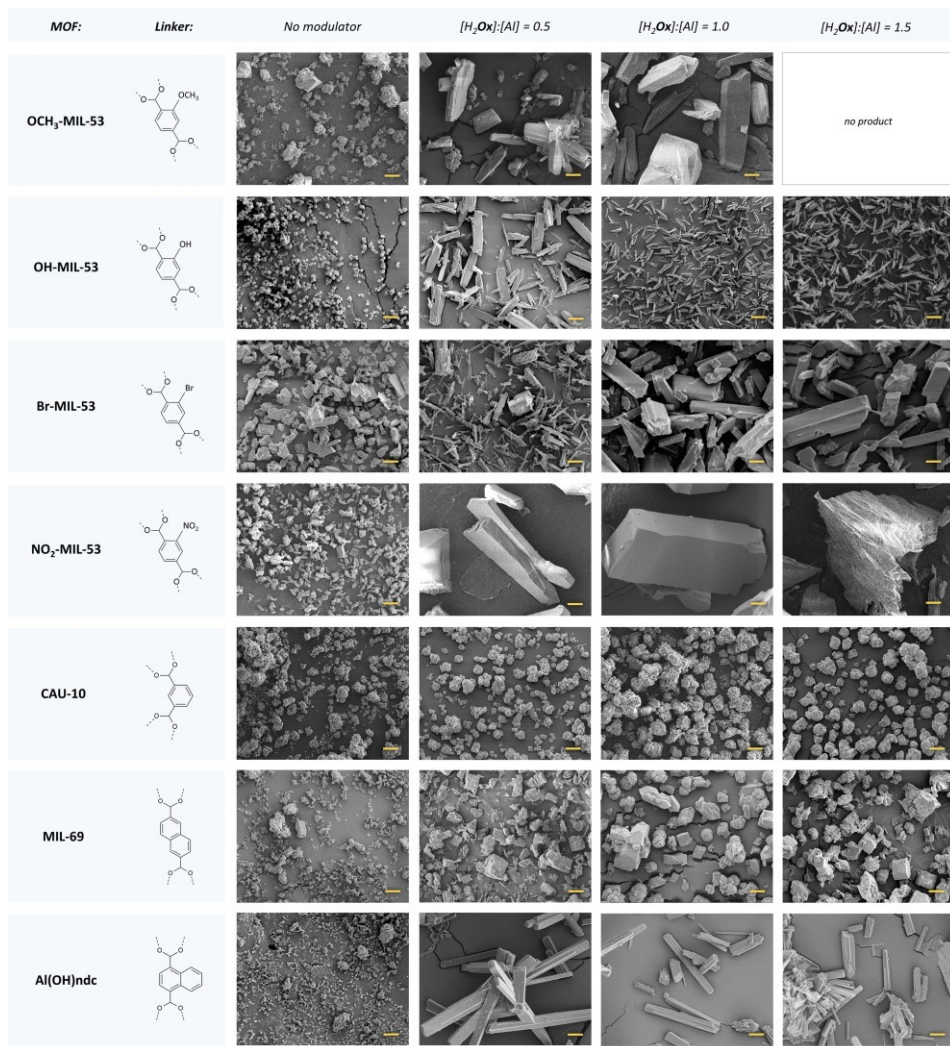


**Figure 3.2.** SEM micrographs of functionalized MIL-53, CAU-10, MIL-69, and Al(OH)ndc crystals synthesized without oxalic acid modulator and with different modulator concentrations (scale bar = 10  $\mu$ m).

### 3.4. References

1. Masters, A. F. & Maschmeyer, T. Zeolites – From curiosity to cornerstone. *Microporous Mesoporous Mater.* **142**, 423–438 (2011).
2. Wang, Z., Yu, J. & Xu, R. Needs and trends in rational synthesis of zeolitic materials. *Chem. Soc. Rev.* **41**, 1729–1741 (2012).
3. Vermeiren, W. & Gilson, J.-P. Impact of Zeolites on the Petroleum and Petrochemical Industry. *Top. Catal.* **52**, 1131–1161 (2009).
4. Ren, Y., Ma, Z. & Bruce, P. G. Ordered mesoporous metal oxides: synthesis and applications. *Chem. Soc. Rev.* **41**, 4909 (2012).
5. Yuan, S., Feng, L., Wang, K., Pang, J., Bosch, M., Lollar, C., Sun, Y., Qin, J., Yang, X.,

- Zhang, P., Wang, Q., Zou, L., Zhang, Y., Zhang, L., Fang, Y., Li, J. & Zhou, H.-C. Stable Metal–Organic Frameworks: Design, Synthesis, and Applications. *Adv. Mater.* **30**, 1704303 (2018).
6. Sánchez-Sánchez, M., Getachew, N., Díaz, K., Díaz-García, M., Chebude, Y. & Díaz, I. Synthesis of metal–organic frameworks in water at room temperature: salts as linker sources. *Green Chem.* **17**, 1500–1509 (2015).
  7. Biswas, S., Ahnfeldt, T. & Stock, N. New Functionalized Flexible Al–MIL-53-X (X = -Cl, -Br, -CH<sub>3</sub>, -NO<sub>2</sub>, -(OH)<sub>2</sub>) Solids: Syntheses, Characterization, Sorption, and Breathing Behavior. *Inorg. Chem.* **50**, 9518–9526 (2011).
  8. Wang, S. & Serre, C. Toward Green Production of Water-Stable Metal–Organic Frameworks Based on High-Valence Metals with Low Toxicities. *ACS Sustain. Chem. Eng.* **7**, 11911–11927 (2019).
  9. Devic, T. & Serre, C. High valence 3p and transition metal based MOFs. *Chem. Soc. Rev.* **43**, 6097–6115 (2014).
  10. Low, J. J., Jakubczak, P., Abrahamian, J. F., Faheem, S. A., Willis, R. R., Benin, A. I., Low, J. J., Willis, R. R., Abrahamian, J. F., Jakubczak, P., Abrahamian, J. F., Faheem, S. A. & Willis, R. R. Virtual High Throughput Screening Confirmed Experimentally : Porous Coordination Polymer Hydration. *J. Am. Chem. Soc.* **131**, 15834–15842 (2009).
  11. Tannert, N., Jansen, C., Nießing, S. & Janiak, C. Robust synthesis routes and porosity of the Al-based metal–organic frameworks Al-fumarate, CAU-10-H and MIL-160. *Dalt. Trans.* **48**, 2967–2976 (2019).
  12. Fathieh, F., Kalmutzki, M. J., Kapustin, E. A., Waller, P. J., Yang, J. & Yaghi, O. M. Practical water production from desert air. *Sci. Adv.* **4**, eaat3198 (2018).
  13. Lenzen, D., Bendix, P., Reinsch, H., Fröhlich, D., Kummer, H., Möllers, M., Hügenell, P. P. C., Gläser, R., Henninger, S. & Stock, N. Scalable Green Synthesis and Full-Scale Test of the Metal–Organic Framework CAU-10-H for Use in Adsorption-Driven Chillers. *Adv. Mater.* **30**, 1705869 (2018).
  14. Lenzen, D., Zhao, J., Ernst, S.-J., Wahiduzzaman, M., Ken Inge, A., Fröhlich, D., Xu, H., Bart, H.-J., Janiak, C., Henninger, S., Maurin, G., Zou, X. & Stock, N. A metal–organic framework for efficient water-based ultra-low-temperature-driven cooling. *Nat. Commun.* **10**, 3025 (2019).
  15. Permyakova, A., Skrylnyk, O., Courbon, E., Affram, M., Wang, S., Lee, U. H., Valekar, A. H., Nouar, F., Mouchaham, G., Devic, T., De Weireld, G., Chang, J. S., Steunou, N., Frère, M. & Serre, C. Synthesis Optimization, Shaping, and Heat Reallocation Evaluation of the Hydrophilic Metal–Organic Framework MIL-160(Al). *ChemSusChem* **10**, 1419–1426 (2017).
  16. Samokhvalov, A. Aluminum metal–organic frameworks for sorption in solution: A review. *Coord. Chem. Rev.* **374**, 236–253 (2018).
  17. Devic, T. & Serre, C. High valence 3p and transition metal based MOFs. *Chem. Soc. Rev.* **43**, 6097–6115 (2014).
  18. Feng, D., Wang, K., Wei, Z., Chen, Y.-P., Simon, C. M., Arvapally, R. K., Martin, R. L., Bosch, M., Liu, T.-F., Fordham, S., Yuan, D., Omary, M. A., Haranczyk, M., Smit, B. & Zhou, H.-C. Kinetically tuned dimensional augmentation as a versatile synthetic route towards robust metal–organic frameworks. *Nat. Commun.* **5**, 5723 (2014).
  19. Millange, F. & Walton, R. I. MIL-53 and its Isorecticular Analogues: a Review of the Chemistry and Structure of a Prototypical Flexible Metal–Organic Framework. *Isr. J. Chem.* **58**, 1019–1035 (2018).
  20. Farha, O. K., Spokoyny, A. M., Mulfort, K. L., Galli, S., Hupp, J. T. & Mirkin, C. A. Gas-Sorption Properties of Cobalt(II)-Carborane-Based Coordination Polymers as a Function of Morphology. *Small* **5**, 1727–1731 (2009).

21. Lee, H. J., We, J., Kim, J. O., Kim, D., Cha, W., Lee, E., Sohn, J. & Oh, M. Morphological and Structural Evolutions of Metal-Organic Framework Particles from Amorphous Spheres to Crystalline Hexagonal Rods. *Angew. Chemie Int. Ed.* **54**, 10564–10568 (2015).
22. Tanaka, S., Fujita, K., Miyake, Y., Miyamoto, M., Hasegawa, Y., Makino, T., Van Der Perre, S., Cousin Saint Remi, J., Van Assche, T., Baron, G. V. & Denayer, J. F. M. Adsorption and Diffusion Phenomena in Crystal Size Engineered ZIF-8 MOF. *J. Phys. Chem. C* **119**, 28430–28439 (2015).
23. Cai, W., Gładysiak, A., Aniola, M., Smith, V. J., Barbour, L. J. & Katrusiak, A. Giant Negative Area Compressibility Tunable in a Soft Porous Framework Material. *J. Am. Chem. Soc.* **137**, 9296–9301 (2015).
24. Henke, S., Li, W. & Cheetham, A. K. Guest-dependent mechanical anisotropy in pillared-layered soft porous crystals – a nanoindentation study. *Chem. Sci.* **5**, 2392 (2014).
25. Gagnon, K. J., Beavers, C. M. & Clearfield, A. MOFs Under Pressure: The Reversible Compression of a Single Crystal. *J. Am. Chem. Soc.* **135**, 1252–1255 (2013).
26. Kapustin, E. A., Lee, S., Alshammari, A. S. & Yaghi, O. M. Molecular Retrofitting Adapts a Metal–Organic Framework to Extreme Pressure. *ACS Cent. Sci.* **3**, 662–667 (2017).
27. Mon, M., Ferrando-Soria, J., Verdaguer, M., Train, C., Paillard, C., Dkhil, B., Versace, C., Bruno, R., Armentano, D. & Pardo, E. Postsynthetic Approach for the Rational Design of Chiral Ferroelectric Metal–Organic Frameworks. *J. Am. Chem. Soc.* **139**, 8098–8101 (2017).
28. Yoon, S. M., Warren, S. C. & Grzybowski, B. A. Storage of electrical information in metal-organic-framework memristors. *Angew. Chemie - Int. Ed.* **53**, 4437–4441 (2014).
29. Bunzen, H., Javed, A., Klawinski, D., Lamp, A., Grzywa, M., Kalytta-Mewes, A., Tiemann, M., von Nidda, H.-A. K., Wagner, T. & Volkmer, D. Anisotropic Water-Mediated Proton Conductivity in Large Iron(II) Metal–Organic Framework Single Crystals for Proton-Exchange Membrane Fuel Cells. *ACS Appl. Nano Mater.* **2**, 291–298 (2019).
30. Tsuruoka, T., Furukawa, S., Takashima, Y., Yoshida, K., Isoda, S. & Kitagawa, S. Nanoporous Nanorods Fabricated by Coordination Modulation and Oriented Attachment Growth. *Angew. Chemie Int. Ed.* **48**, 4739–4743 (2009).
31. Diring, S., Furukawa, S., Takashima, Y., Tsuruoka, T. & Kitagawa, S. Controlled Multiscale Synthesis of Porous Coordination Polymer in Nano/Micro Regimes. *Chem. Mater.* **22**, 4531–4538 (2010).
32. Schaate, A., Roy, P., Godt, A., Lippke, J., Waltz, F., Wiebcke, M. & Behrens, P. Modulated Synthesis of Zr-Based Metal-Organic Frameworks: From Nano to Single Crystals. *Chem. - A Eur. J.* **17**, 6643–6651 (2011).
33. Wu, H., Chua, Y. S., Krungleviciute, V., Tyagi, M., Chen, P., Yildirim, T. & Zhou, W. Unusual and highly tunable missing-linker defects in zirconium metal-organic framework UiO-66 and their important effects on gas adsorption. *J. Am. Chem. Soc.* **135**, 10525–10532 (2013).
34. Carmona, F. J., Maldonado, C. R., Ikemura, S., Romão, C. C., Huang, Z., Xu, H., Zou, X., Kitagawa, S., Furukawa, S. & Barea, E. Coordination Modulation Method to Prepare New Metal-Organic Framework-Based CO-Releasing Materials. *ACS Appl. Mater. Interfaces* **10**, 31158–31167 (2018).
35. Wang, X. & Jacobson, A. J. Hydrothermal crystal growth and Vernier structures of the metal benzenedicarboxylates MIL-47 and MIL-53 containing guest molecules of benzenecarboxylic acid. *J. Solid State Chem.* **236**, 230–235 (2016).
36. Guo, Y., Zhang, J., Dong, L.-Z., Xu, Y., Han, W., Fang, M., Liu, H.-K., Wu, Y. & Lan, Y.-Q. Syntheses of Exceptionally Stable Aluminum(III) Metal-Organic Frameworks: How to Grow High-Quality, Large, Single Crystals. *Chem. - A Eur. J.* **23**, 15518–15528 (2017).
37. Vougo-Zanda, M., Huang, J., Anokhina, E., Wang, X. & Jacobson, A. J. Tossing and

- turning: Guests in the flexible frameworks of metal(III) dicarboxylates. *Inorg. Chem.* **47**, 11535–11542 (2008).
38. Loiseau, T., Lecroq, L., Volkringer, C., Marrot, J., Férey, G., Haouas, M., Taulelle, F., Bourrelly, S., Llewellyn, P. L. & Latroche, M. MIL-96, a Porous Aluminum Trimesate 3D Structure Constructed from a Hexagonal Network of 18-Membered Rings and  $\mu$  3 -Oxo-Centered Trinuclear Units. *J. Am. Chem. Soc.* **128**, 10223–10230 (2006).
  39. Caultet, P., Paillaud, J.-L., Simon-Masseron, A., Soulard, M. & Patarin, J. The fluoride route: a strategy to crystalline porous materials. *Comptes Rendus Chim.* **8**, 245–266 (2005).
  40. Fein, J. B. & Hestrin, J. E. Experimental studies of oxalate complexation at 80 °C: Gibbsite, amorphous silica, and quartz solubilities in oxalate-bearing fluids. *Geochim. Cosmochim. Acta* **58**, 4817–4829 (1994).
  41. Thomas, F., Masion, A., Bottero, J. Y., Rouiller, J., Genevrièr, F. & Boudot, D. Aluminum(III) speciation with acetate and oxalate. A potentiometric and aluminum-27 NMR study. *Environ. Sci. Technol.* **25**, 1553–1559 (1991).
  42. Han, Y., Liu, M., Li, K., Zuo, Y., Wei, Y., Xu, S., Zhang, G., Song, C., Zhang, Z. & Guo, X. Facile synthesis of morphology and size-controlled zirconium metal–organic framework UiO-66: the role of hydrofluoric acid in crystallization. *CrystEngComm* **17**, 6434–6440 (2015).
  43. Loiseau, T., Serre, C., Huguenard, C., Fink, G., Taulelle, F., Henry, M., Bataille, T. & Férey, G. A Rationale for the Large Breathing of the Porous Aluminum Terephthalate (MIL-53) Upon Hydration. *Chem. - A Eur. J.* **10**, 1373–1382 (2004).
  44. Nanthamathee, C., Ling, S., Slater, B. & Attfield, M. P. Contradistinct thermoresponsive behavior of isostructural MIL-53 type metal-organic frameworks by modifying the framework inorganic anion. *Chem. Mater.* **27**, 85–95 (2015).
  45. Liu, L., Wang, X. & Jacobson, A. J. AlF-1,4-benzenedicarboxylate: synthesis and absorption properties. *Dalt. Trans.* **39**, 1722–1725 (2010).
  46. Cliffe, M. J., Wan, W., Zou, X., Chater, P. A., Kleppe, A. K., Tucker, M. G., Wilhelm, H., Funnell, N. P., Coudert, F.-X. & Goodwin, A. L. Correlated defect nanoregions in a metal–organic framework. *Nat. Commun.* **5**, 4176 (2014).
  47. Balestri, D., Bassanetti, I., Canossa, S., Gazzurelli, C., Bacchi, A., Bracco, S., Comotti, A. & Pelagatti, P. Changing the Dress to a MOF through Fluorination and Transmetalation. Structural and Gas-Sorption Effects. *Cryst. Growth Des.* **18**, 6824–6832 (2018).
  48. Groom, C. R., Bruno, I. J., Lightfoot, M. P. & Ward, S. C. The Cambridge structural database. *Acta Crystallogr. Sect. B Struct. Sci. Cryst. Eng. Mater.* **72**, 171–179 (2016).
  49. Carmona, F. J., Maldonado, C. R., Ikemura, S., Romão, C. C., Huang, Z., Xu, H., Zou, X., Kitagawa, S., Furukawa, S. & Barea, E. Coordination Modulation Method to Prepare New Metal–Organic Framework-Based CO-Releasing Materials. *ACS Appl. Mater. Interfaces* **10**, 31158–31167 (2018).
  50. Wu, H., Chua, Y. S., Krungleviciute, V., Tyagi, M., Chen, P., Yildirim, T. & Zhou, W. Unusual and Highly Tunable Missing-Linker Defects in Zirconium Metal–Organic Framework UiO-66 and Their Important Effects on Gas Adsorption. *J. Am. Chem. Soc.* **135**, 10525–10532 (2013).
  51. Zuo, Y., Zhang, Z., Wei, Y., Liu, M., Song, C., Guo, X., Xu, S., Han, Y., Li, K. & Zhang, G. Facile synthesis of morphology and size-controlled zirconium metal–organic framework UiO-66: the role of hydrofluoric acid in crystallization. *CrystEngComm* **17**, 6434–6440 (2015).
  52. Tsuruoka, T., Furukawa, S., Takashima, Y., Yoshida, K., Isoda, S. & Kitagawa, S. Nanoporous nanorods fabricated by coordination modulation and oriented attachment growth. *Angew. Chemie - Int. Ed.* **48**, 4739–4743 (2009).

53. Ozimiński, W. P. & Dobrowolski, J. C.  $\sigma$  - and  $\pi$ -electron contributions to the substituent effect: natural population analysis. *J. Phys. Org. Chem.* **22**, 769–778 (2009).
54. Hollingsworth, C. A., Seybold, P. G. & Hadad, C. M. Substituent effects on the electronic structure and pKa of benzoic acid. *Int. J. Quantum Chem.* **90**, 1396–1403 (2002).
55. Reinsch, H., van der Veen, M. A., Gil, B., Marszalek, B., Verbiest, T., de Vos, D. & Stock, N. Structures, Sorption Characteristics, and Nonlinear Optical Properties of a New Series of Highly Stable Aluminum MOFs. *Chem. Mater.* **25**, 17–26 (2013).
56. Loiseau, T., Mellot-Draznieks, C., Muguerra, H., Férey, G., Haouas, M. & Taulelle, F. Hydrothermal synthesis and crystal structure of a new three-dimensional aluminum-organic framework MIL-69 with 2,6-naphthalenedicarboxylate (ndc), Al(OH)(ndc)·H<sub>2</sub>O. *Comptes Rendus Chim.* **8**, 765–772 (2005).
57. Comotti, A., Bracco, S., Sozzani, P., Horike, S., Matsuda, R., Chen, J., Takata, M., Kubota, Y. & Kitagawa, S. Nanochannels of Two Distinct Cross-Sections in a Porous Al-Based Coordination Polymer. *J. Am. Chem. Soc.* **130**, 13664–13672 (2008).

# Appendix to Chapter 3

---

## Contents

|  |     |
|--|-----|
| A3.1. Experimental details .....   | 112 |
| A3.1.1. Synthesis details .....  | 112 |
| A3.1.2. Analytical techniques .....  | 114 |
| A3.2. SEM micrographs .....  | 116 |
| A3.2.1. MIL-53 .....   | 116 |
| A3.2.2. X-MIL-53 (X = CH <sub>3</sub> O, OH, Br, NO <sub>2</sub> ) .....               | 118 |
| A3.2.3. CAU-10 .....   | 123 |
| A3.2.4. MIL-69 .....   | 125 |
| A3.2.5. Al(OH)ndc .....  | 126 |
| A3.2.6. EDX analysis .....   | 127 |
| A3.3. Thermogravimetric analysis (TGA) .....   | 129 |
| A3.3.1. TGA curves of MIL-53 .....   | 129 |
| A3.3.2. TGA curves of X-MIL-53 (X = CH <sub>3</sub> O, OH, Br, NO <sub>2</sub> ) ..... | 130 |
| A3.3.3. TGA curves of CAU-10, MIL-69, Al(OH)ndc .....                                  | 132 |
| A3.4. Powder X-ray diffraction .....   | 133 |
| A3.5. Single-crystal X-ray diffraction .....   | 137 |
| A3.6. Database searches .....  | 138 |
| A3.7. Appendix references .....  | 139 |

## A3.1. Experimental details

### A3.1.1. Synthesis details

#### Reagents and solvents

All solvents and reagents, except for 2-methoxyterephthalic acid and sodium oxalate anhydrous, were purchased by commercial suppliers and used as-received.

#### Synthesis of 2-methoxyterephthalic acid

2-Methoxyterephthalic acid was synthesized according to a reported method.<sup>1</sup> A mixture of 2,5-dimethylanisole (7.76 g, 57 mmol),  $\text{KMnO}_4$  (25.0 g, 158 mmol), and NaOH (3.10 g, 77.5 mmol) in water (500 mL) was heated to 60 °C. After 5h, an additional amount of  $\text{KMnO}_4$  (25.0 g, 158 mmol) was added, and refluxed for 1 h. The mixture was cooled to room temperature and filtered over paper. The filtrate was acidified with conc. HCl (37%), and the resulting white precipitate was collected by filtration and dried under vacuum at 60 °C for 12 h. Yield: 4.5 g, 40%.  $^1\text{H}$  NMR (400 MHz, DMSO- $d_6$ )  $\delta$  13.12 (br. s, 2H, COOH), 7.68 (d,  $J$  = 7.8 Hz, 1H,  $\text{C}_{\text{Ar}}\text{H}$ ), 7.57 (d,  $J$  = 1.4 Hz, 1H,  $\text{C}_{\text{Ar}}\text{H}$ ), 7.55 (dd,  $J$  = 7.8, 1.4 Hz, 1H,  $\text{C}_{\text{Ar}}\text{H}$ ), 3.87 (s, 3H,  $\text{CH}_3$ ), Figure A3.1.

#### Synthesis of anhydrous sodium oxalate

Oxalic acid dihydrate (5 g, 39.7 mmol) was dissolved in 60 mL  $\text{H}_2\text{O}$  by stirring. NaOH (3.17 g, 79.3 mmol) was dissolved in 50 mL  $\text{H}_2\text{O}$ , and slowly added to the first solution while stirring. The resulting mixture was left to evaporate overnight at 80 °C, and then dried in an oven at 260 °C for 5 h. Thermogravimetric analysis of the product (Figure A3.2) agrees with anhydrous sodium oxalate decomposition step at ca. 560 °C (exp. 21.0%, calc. 20.9%), yielding an equimolar amount of  $\text{Na}_2\text{CO}_3$ .<sup>2</sup> Diffuse reflectance FTIR spectroscopy: 3101, 3053, 2929, 2764, 2484, 1882, 1761, 1651, 1622, 1572, 1416, 1335, 1311, 1250, 771, 617, 517  $\text{cm}^{-1}$ .

#### Synthesis of MIL-53

$\text{AlCl}_3 \cdot 6\text{H}_2\text{O}$  (966 mg, 4 mmol) was added to 30 ml demineralized  $\text{H}_2\text{O}$  inside a 45 mL Teflon liner. For modulated syntheses, 4 mmol of modulator was added (Table A3.1) and the solution was homogenized by stirring. Terephthalic acid (665 mg, 4 mmol) was added to the solution, and the mixture was stirred again (terephthalic acid is not completely dissolved in these conditions). The liner was sealed inside a steel autoclave and placed in an oven at 220 °C for 72 h.

**Table A3.1. Amount of modulator used for the syntheses of MIL-53.**

| Modulator  | Amount  |
|--|---------|
| HCl 37%  | 0.33 mL |
| $\text{NH}_4\text{F}$ anhydrous                            | 148 mg  |
| HF 40%   | 0.17 mL |
| $\text{Na}_2\text{C}_2\text{O}_4$ anhydrous                | 536 mg  |
| $\text{H}_2\text{C}_2\text{O}_4 \cdot 2\text{H}_2\text{O}$ | 504 mg  |

### Synthesis of X-MIL-53 (X = CH3O, OH, Br, NO2)

All reagent amounts and reaction temperatures are given in Table A3.2. A synthesis-specific amount of  $\text{AlCl}_3 \cdot 6\text{H}_2\text{O}$  was added to 30 ml demineralized  $\text{H}_2\text{O}$  inside a 45 mL Teflon liner. Oxalic acid dihydrate was added in a specific stoichiometric amount and the solution was homogenized by stirring. An amount of linker in molar ratio 1:1 to  $\text{AlCl}_3 \cdot 6\text{H}_2\text{O}$  was added and the solution was stirred again. The liner was sealed inside a steel autoclave and placed in an oven at a given temperature for 72 h.

### Synthesis of CAU-10

Four different syntheses were performed using a general procedure adapted from the one reported by Reinsch *et al.*<sup>3</sup> by using different amounts of oxalic acid: 0 mmol, 0.6 mmol (53 mg), 1.2 mmol (105 mg), and 1.8 mmol (158 mg). The general procedure is reported as follows.

$\text{Al}_2(\text{SO}_4)_3 \cdot 18\text{H}_2\text{O}$  (802 mg, 1.2 mmol) was dissolved in 10 ml of a 1:4 DMF– $\text{H}_2\text{O}$  mixture in a 45 mL Teflon liner. A certain stoichiometric amount of oxalic acid dihydrate was added and the solution was homogenized by stirring. Isophthalic acid (199 mg, 1.2 mmol) was added and the solution was stirred again. The liner was sealed inside a steel autoclave and placed in an oven at 135 °C for 24 h.

### Synthesis of MIL-69

Four different syntheses were performed using a general procedure adapted from the one reported by Loiseau *et al.*<sup>4</sup> by using different amounts of oxalic acid: 0 mmol, 1.75 mmol (221 mg), 3.5 mmol (441 mg), and 5.25 mmol (662 mg). The general procedure is reported as follows.

$\text{Al}(\text{NO}_3)_3 \cdot 9\text{H}_2\text{O}$  (1313 mg, 3.5 mmol) was added to 5 ml  $\text{H}_2\text{O}$  inside a 45 mL Teflon liner. A certain stoichiometric amount of oxalic acid dihydrate was added and the solution was homogenized by stirring. 2,6-Naphthalenedicarboxylic acid (378 mg, 1.75 mmol) and KOH (236 mg, 4.2 mmol) were added and the solution was stirred again (the linker is not completely dissolved in these conditions). The liner was sealed inside a steel autoclave and placed in an oven at 210 °C for 16 h.

### Synthesis of $\text{Al}(\text{OH})\text{ndc}$

Four different syntheses were performed using a general procedure adapted from the one reported by Comotti *et al.*<sup>5</sup> by using different amounts of oxalic acid: 0 mmol, 0.5 mmol (63 mg), 1.0 mmol (126 mg) and 1.5 mmol (189 mg). The general procedure is reported as follows.

$\text{Al}(\text{NO}_3)_3 \cdot 9\text{H}_2\text{O}$  (375 mg, 1 mmol) was added to 10 ml  $\text{H}_2\text{O}$  inside a 45 mL Teflon liner. A certain stoichiometric amount of oxalic acid dihydrate was added and the solution was homogenized by stirring. 1,4-Naphthalenedicarboxylic acid (108 mg, 0.5 mmol) was added and the solution was stirred again (the linker is not completely dissolved in these conditions). The liner was sealed inside a steel autoclave and placed in an oven at 180 °C for 24 h.

### Post-synthesis treatment

After every MOF synthesis, the same treatment was applied to the products. The autoclave was cooled down slowly to room temperature and the solids were removed from the mother liquor by centrifugation. The products were subsequently rinsed three times: with 10mL of DMF, with

10 mL demineralized water, and with 10 mL ethanol. The washed solids were placed in a glass vial and dried in a vacuum oven at 40 °C for 12 h.

### A3.1.2. Analytical techniques

SEM analyses were performed using a JEOL JSM-6010LA InTouchScope scanning electron microscope. Morphological micrographs were obtained using a secondary electron detector and an acceleration voltage of 5 kV. X-ray microanalyses were obtained by energy-dispersive X-ray (EDX) spectra acquired with an acceleration voltage of 20 kV. All samples underwent a gold-coating preparation prior to the analysis. SEM micrographs and EDX spectra were processed using the InTouchScope software Version 1.12.

Thermogravimetric analyses (TGA) were performed using a Mettler Toledo TGA/SDTA 851e under 100 mL/min air flow from 30 to 700 °C with a heating rate of 5 °C/min. The data were processed using the STARE SW 14.00 software.

Nitrogen adsorption/desorption isotherms were measured volumetrically in a Tristar II 3020 Micromeritics instrument at 77 K. The samples were activated by thermal treatment at 603 K for 72 h and degassed before the measurement at 433 K under N<sub>2</sub> flow for 16 h. The pore volume values were obtained from the data at  $P/P_0=0.95$ .

X-ray powder diffractograms of the products were collected in Bragg-Brentano geometry using a Bruker-AXS D5005 equipped with a Co K $\alpha$  source operating at 35 kV and 40 mA. Data collections were performed using a variable divergence slit and a step size of 0.02° in 2 $\theta$ . Single-crystal XRD experiments on MIL-53 and NO<sub>2</sub>-MIL-53 were performed at the XRD1 beamline of the Elettra Synchrotron facility (CNR Trieste, Basovizza, Italy).<sup>6</sup> Diffraction data were collected using a monochromatic 0.61 Å wavelength at 250 K (MIL-53) and 100 K (NO<sub>2</sub>-MIL-53), using a cold nitrogen stream produced with an Oxford Cryostream 700 (Oxford Cryosystems Ltd., Oxford, United Kingdom). Diffraction datasets have been processed using the Rigaku CrysAlisPro version 1.171.38.43 software (Rigaku Corporation, Oxford, United Kingdom), which was also used for the reconstruction of the reciprocal space and precession images.

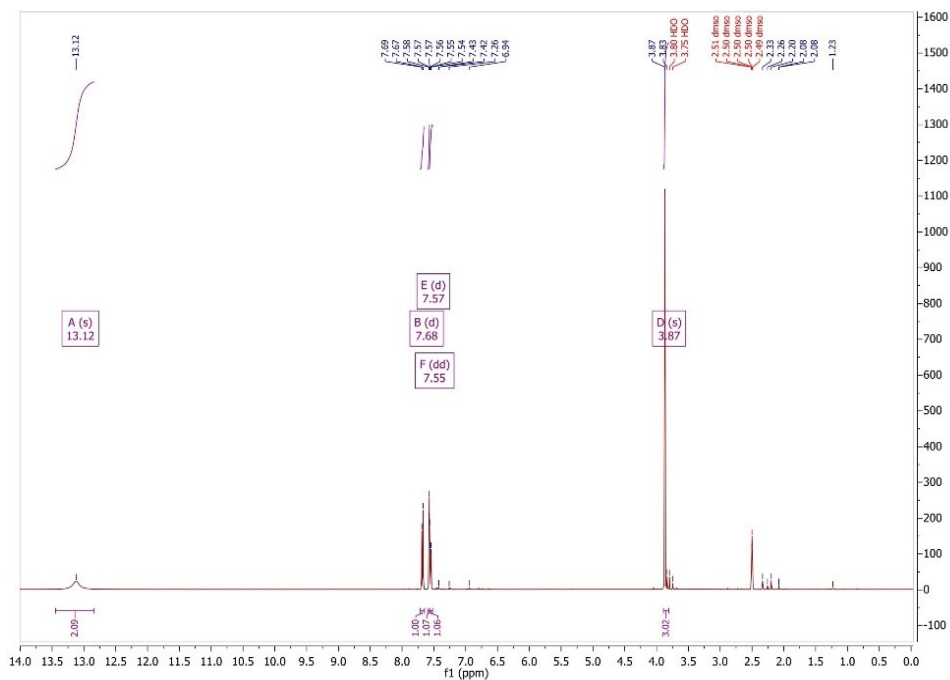


Figure A3.1.  $^1\text{H}$  NMR spectrum of synthesized 2-methoxyterephthalic acid.

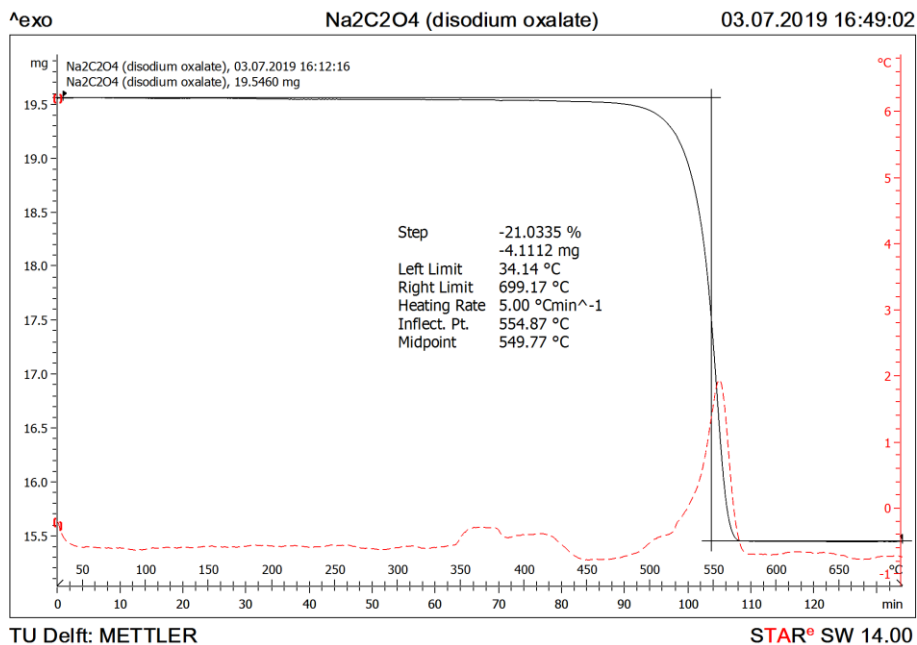


Figure A3.2. Thermogravimetric curve of the prepared sodium oxalate.

Table A3.2. Parameters for the synthesis of X-MIL-53 (X = CH<sub>3</sub>O, OH, Br, NO<sub>2</sub>).

| Product                  | Modulator : Al ratio | AlCl <sub>3</sub> · 6H <sub>2</sub> O amount | linker amount   | T (°C) | Modulator amount |
|--------------------------|----------------------|--|-----------------|--------|------------------|
| CH <sub>3</sub> O-MIL-53 | 0.0                  | 2 mmol (483 mg)                              | 2 mmol (392 mg) | 160    | 0 mmol (0 mg)    |
|                          | 0.5                  | 2 mmol (483 mg)                              | 2 mmol (392 mg) | 160    | 1 mmol (126 mg)  |
|                          | 1.0                  | 2 mmol (483 mg)                              | 2 mmol (392 mg) | 160    | 2 mmol (252 mg)  |
|                          | 1.5                  | 2 mmol (483 mg)                              | 2 mmol (392 mg) | 160    | 3 mmol (378 mg)  |
| OH-MIL-53                | 0.0                  | 2 mmol (483 mg)                              | 2 mmol (364 mg) | 170    | 0 mmol (0 mg)    |
|                          | 0.5                  | 2 mmol (483 mg)                              | 2 mmol (364 mg) | 170    | 1 mmol (126 mg)  |
|                          | 1.0                  | 2 mmol (483 mg)                              | 2 mmol (364 mg) | 170    | 2 mmol (252 mg)  |
|                          | 1.5                  | 2 mmol (483 mg)                              | 2 mmol (364 mg) | 170    | 3 mmol (378 mg)  |
| Br-MIL-53                | 0.0                  | 4 mmol (966 mg)                              | 4 mmol (980 mg) | 210    | 0 mmol (0 mg)    |
|                          | 0.5                  | 4 mmol (966 mg)                              | 4 mmol (980 mg) | 210    | 2 mmol (252 mg)  |
|                          | 1.0                  | 4 mmol (966 mg)                              | 4 mmol (980 mg) | 210    | 4 mmol (504 mg)  |
|                          | 1.5                  | 4 mmol (966 mg)                              | 4 mmol (980 mg) | 210    | 6 mmol (756 mg)  |
| NO <sub>2</sub> -MIL-53  | 0.0                  | 4 mmol (966 mg)                              | 4 mmol (845 mg) | 170    | 0 mmol (0 mg)    |
|                          | 0.5                  | 4 mmol (966 mg)                              | 4 mmol (845 mg) | 170    | 2 mmol (252 mg)  |
|                          | 1.0                  | 4 mmol (966 mg)                              | 4 mmol (845 mg) | 170    | 4 mmol (504 mg)  |
|                          | 1.5                  | 4 mmol (966 mg)                              | 4 mmol (845 mg) | 170    | 6 mmol (756 mg)  |

## A3.2. SEM micrographs

### A3.2.1. MIL-53

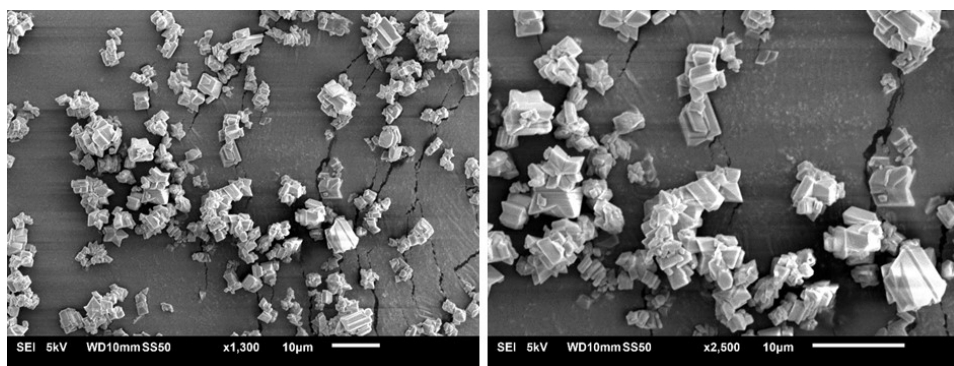
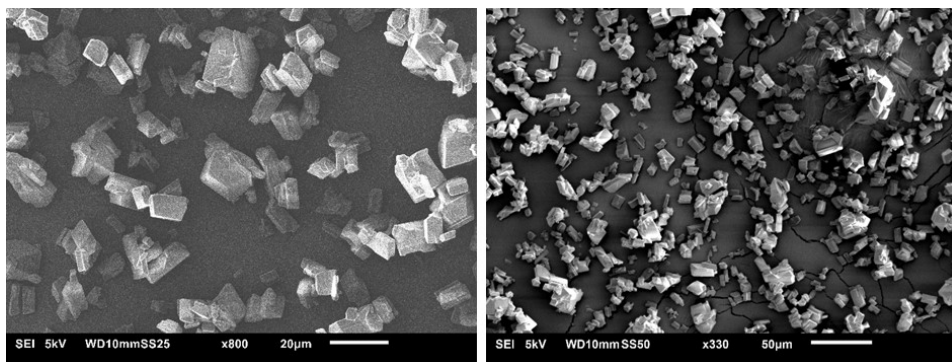
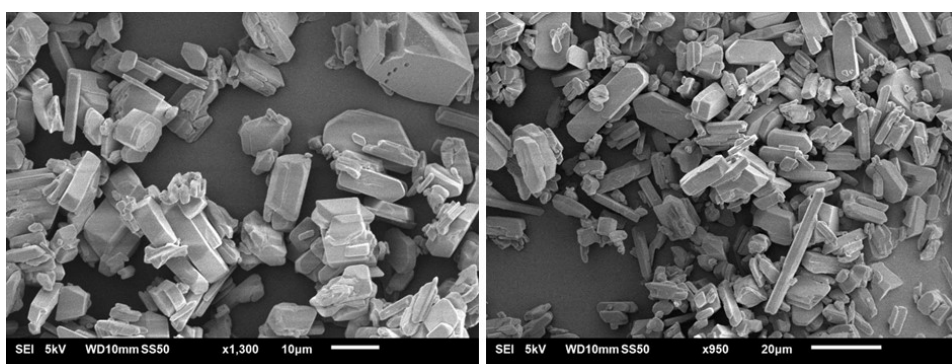


Figure A3.3. SEM micrographs of MIL-53 crystals obtained without synthesis modulator.



**Figure A3.4.** SEM micrographs of MIL-53 crystals obtained by using HCl as synthesis modulator.



**Figure A3.5.** SEM micrographs of MIL-53 crystals obtained by using  $\text{NH}_4\text{F}$  as synthesis modulator.

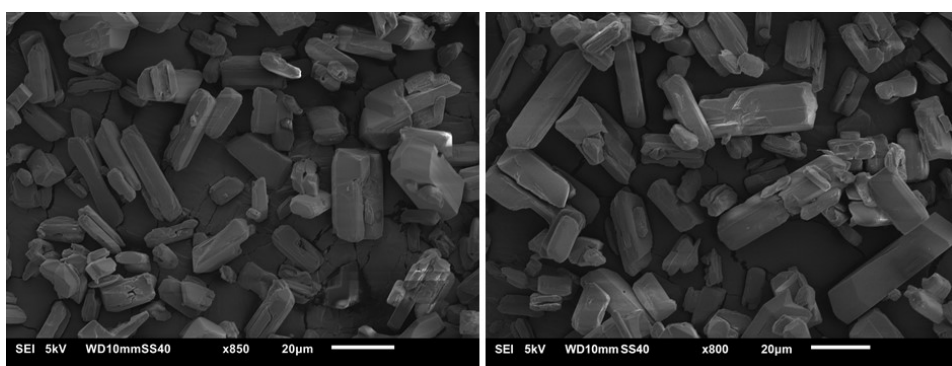


**Figure A3.6.** SEM micrographs of MIL-53 crystals obtained by using HF as synthesis modulator.

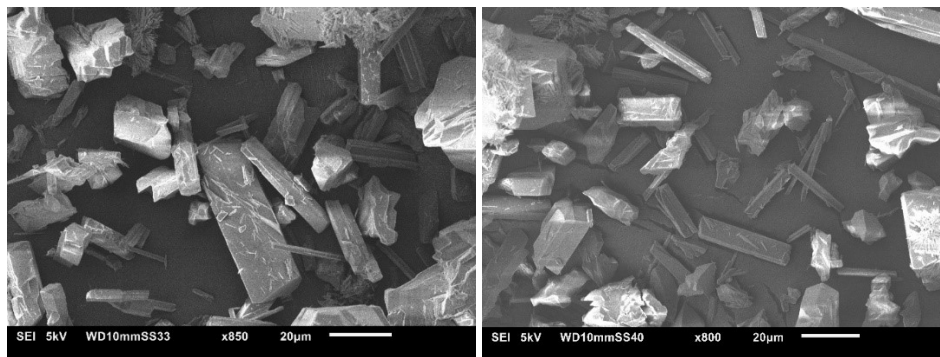


**Figure A3.7.** SEM micrographs of MIL-53 crystals obtained by using  $\text{Na}_2\text{C}_2\text{O}_4$  as synthesis modulator.

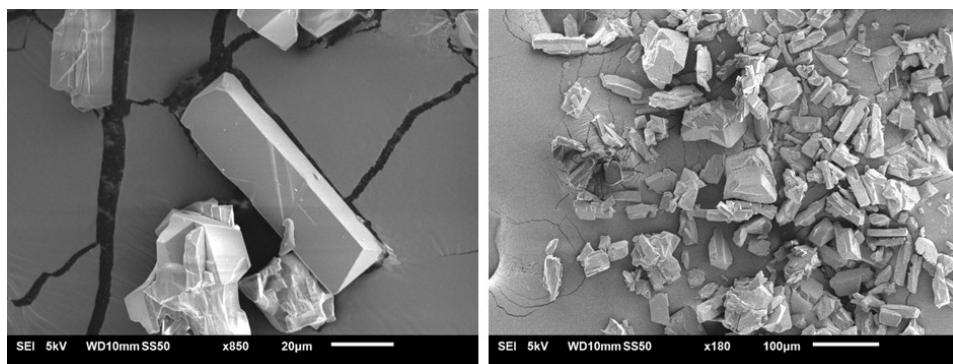


**Figure A3.8.** SEM micrographs of MIL-53 crystals obtained by using  $\text{H}_2\text{C}_2\text{O}_4$  as synthesis modulator.

### A3.2.2. X-MIL-53 ( $\text{X} = \text{CH}_3\text{O}, \text{OH}, \text{Br}, \text{NO}_2$ )

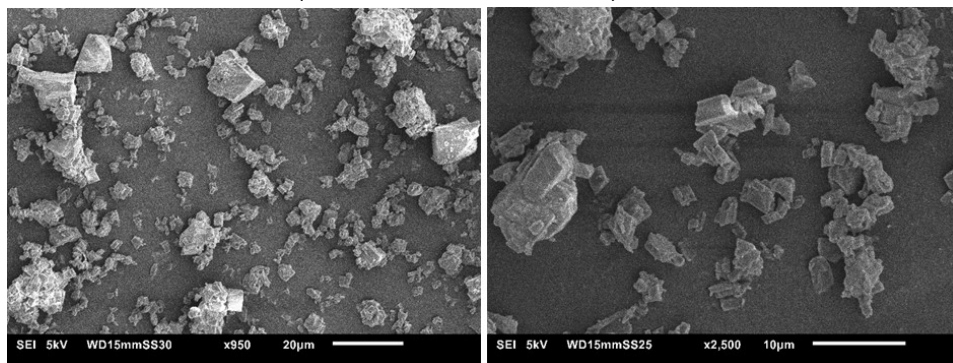


**Figure A3.9.** SEM micrographs of  $\text{CH}_3\text{O}$ -MIL-53 crystals obtained by unmodulated synthesis.

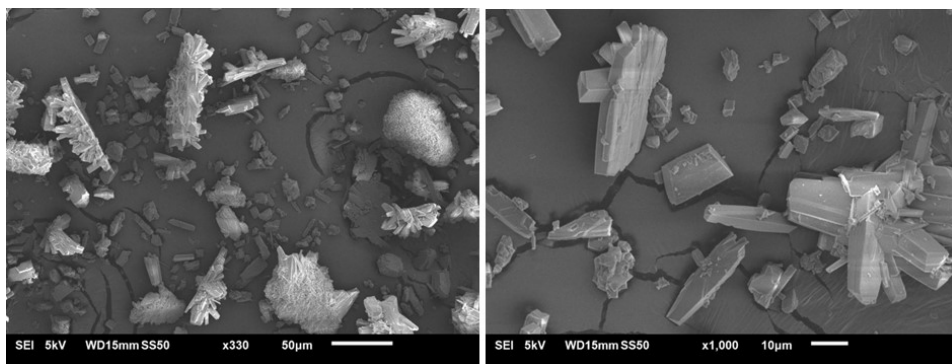


Figure A3.10. SEM micrographs of CH<sub>3</sub>O-MIL-53 crystals obtained by using an oxalic acid:Al ratio of 0.5.

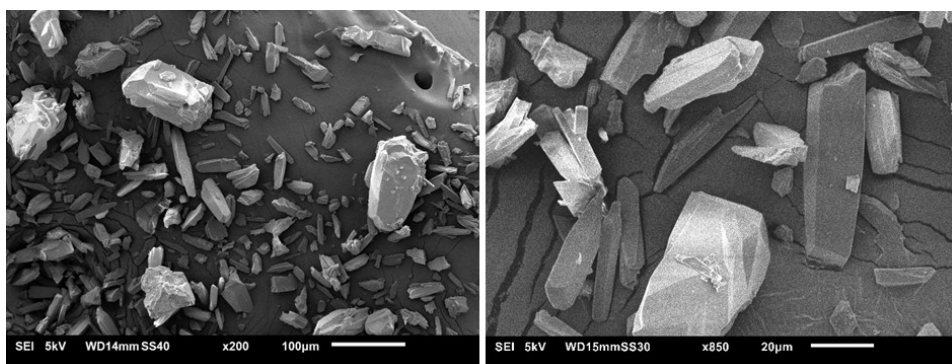


Figure A3.11. SEM micrographs of CH<sub>3</sub>O-MIL-53 crystals obtained by using an oxalic acid:Al ratio of 1.0.

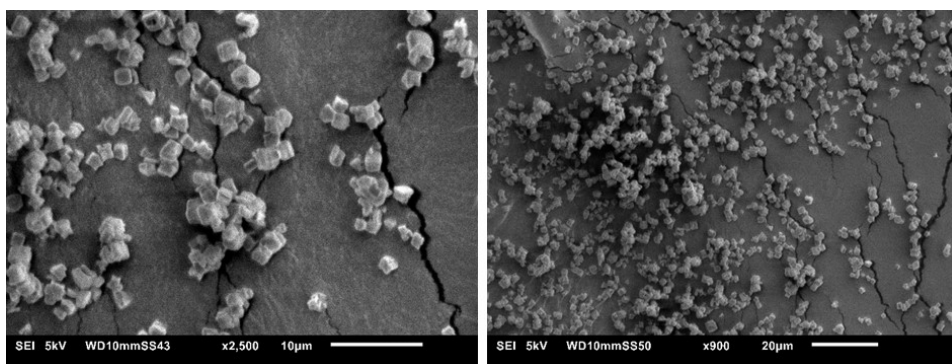


Figure A3.12. SEM micrographs of OH-MIL-53 crystals obtained by unmodulated synthesis.

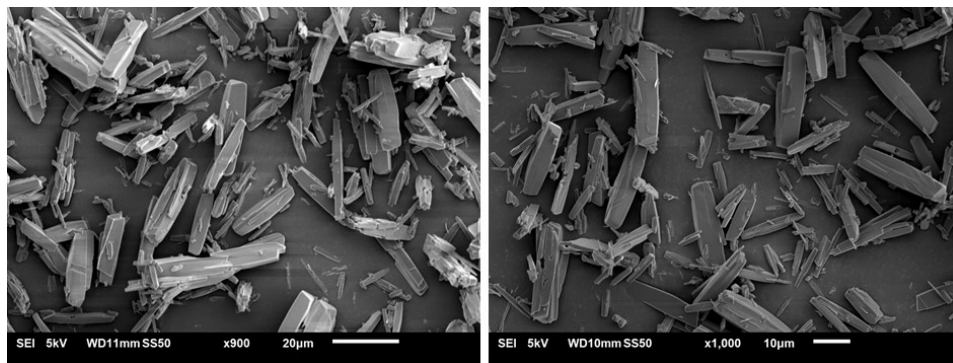


Figure A3.13. SEM micrographs of OH-MIL-53 crystals obtained by using an oxalic acid:Al ratio of 0.5.

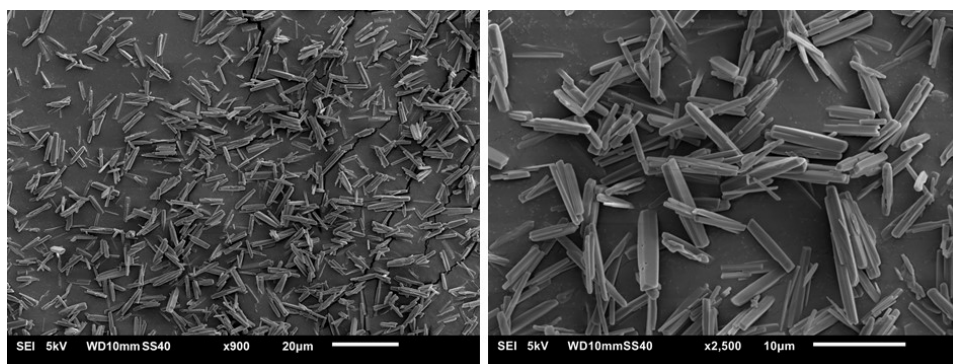


Figure A3.14. SEM micrographs of OH-MIL-53 crystals obtained by using an oxalic acid:Al ratio of 1.0.

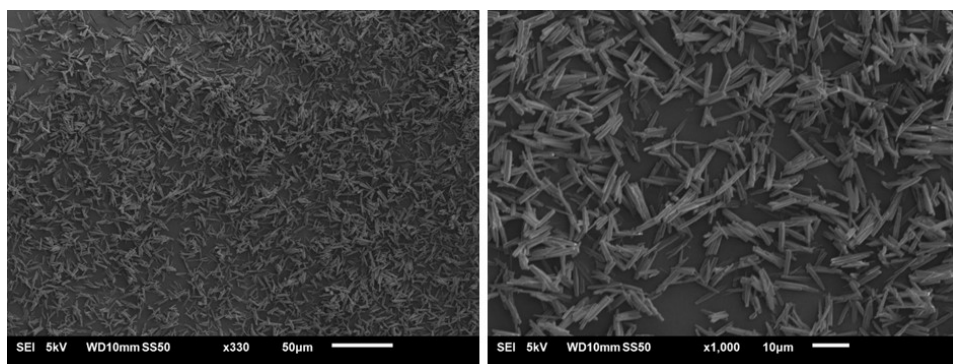


Figure A3.15. SEM micrographs of OH-MIL-53 crystals obtained by using an oxalic acid:Al ratio of 1.5.

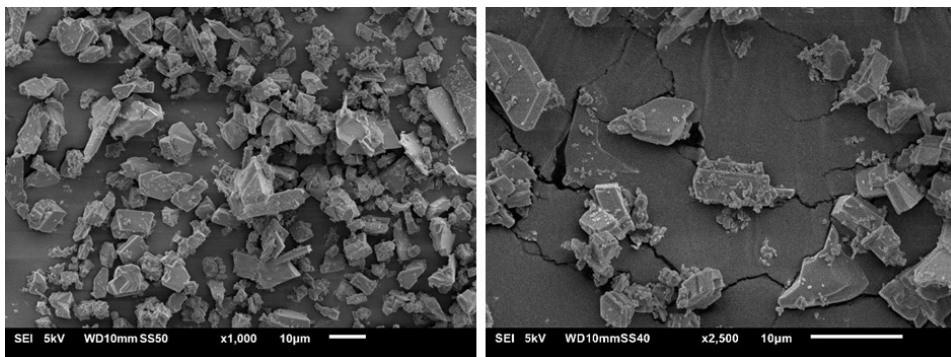


Figure A3.16. SEM micrographs of Br-MIL-53 crystals obtained by unmodulated synthesis.

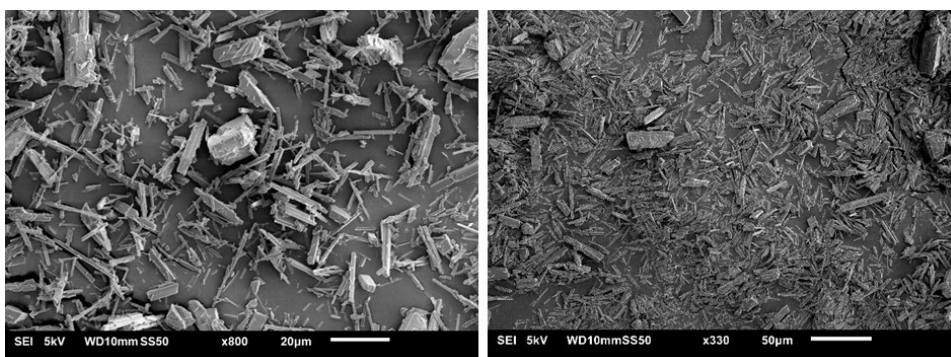


Figure A3.17. SEM micrographs of Br-MIL-53 crystals obtained by using an oxalic acid:Al ratio of 0.5.

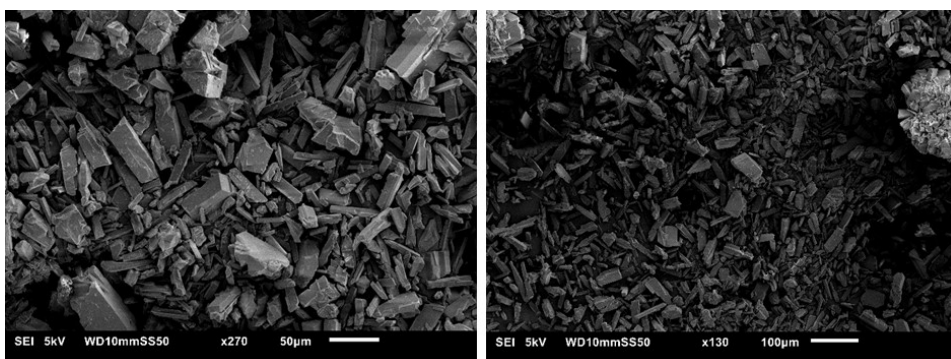


Figure A3.18. SEM micrographs of Br-MIL-53 crystals obtained by using an oxalic acid:Al ratio of 1.0.

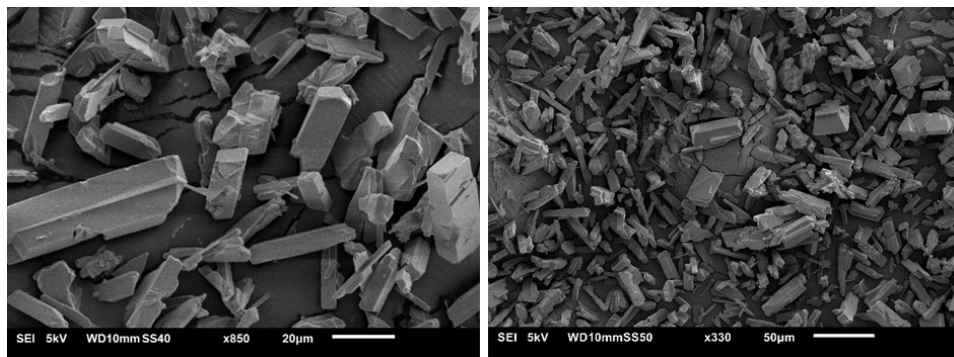


Figure A3.19. SEM micrographs of Br-MIL-53 crystals obtained by using an oxalic acid:Al ratio of 1.5.

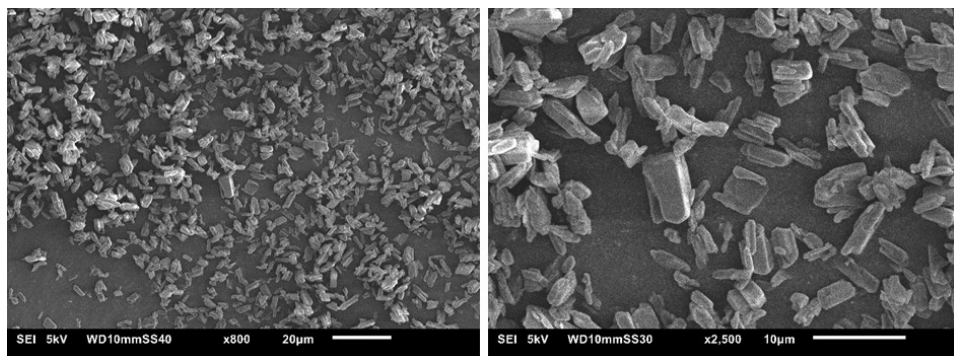


Figure A3.20. SEM micrographs of NO<sub>2</sub>-MIL-53 crystals obtained by unmodulated synthesis.

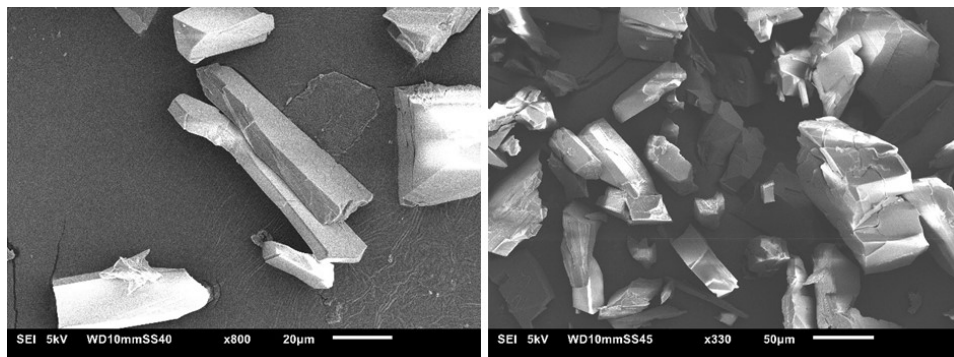
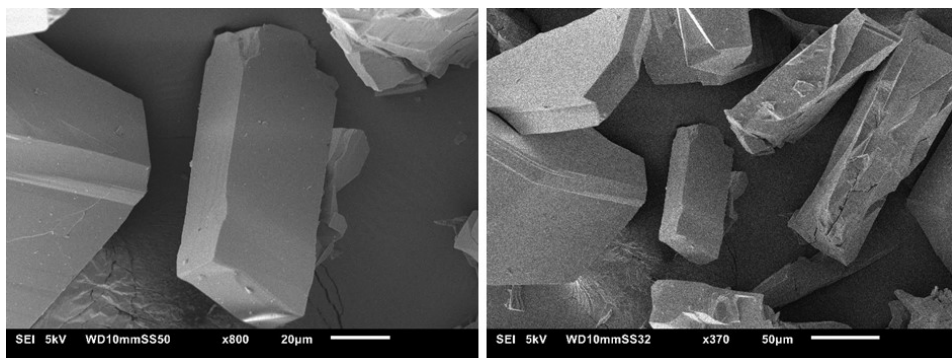
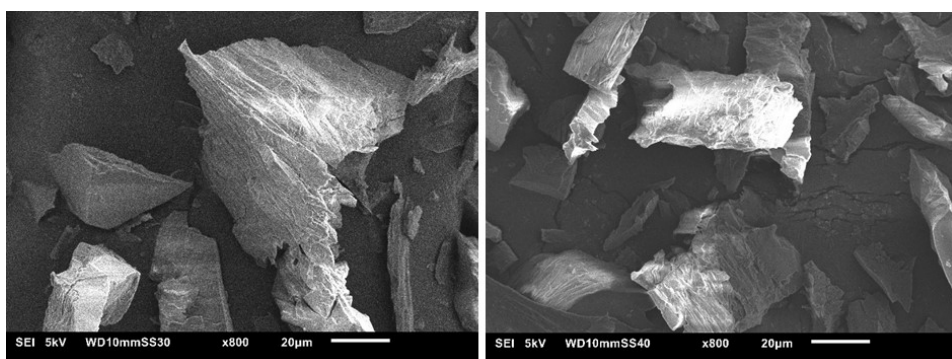


Figure A3.21. SEM micrographs of NO<sub>2</sub>-MIL-53 crystals obtained by using an oxalic acid:Al ratio of 0.5.



**Figure A3.22.** SEM micrographs of NO<sub>2</sub>-MIL-53 crystals obtained by using an oxalic acid:Al ratio of 1.0.



**Figure A3.23.** SEM micrographs of NO<sub>2</sub>-MIL-53 crystals obtained by using an oxalic acid:Al ratio of 1.5.

### A3.2.3. CAU-10

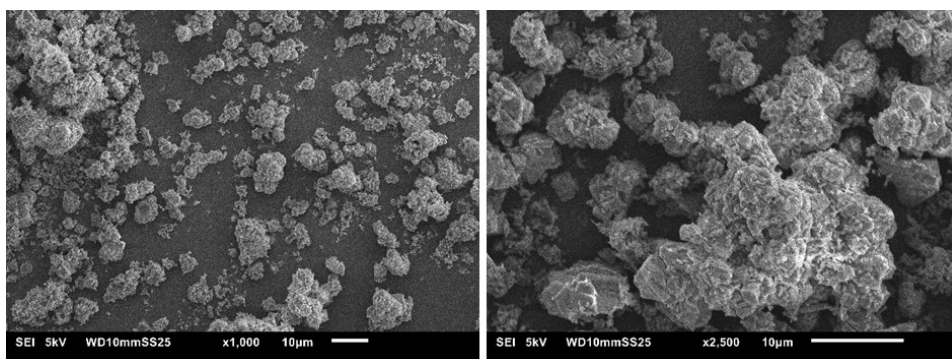


**Figure A3.24.** SEM micrographs of CAU-10 crystals obtained by unmodulated synthesis.

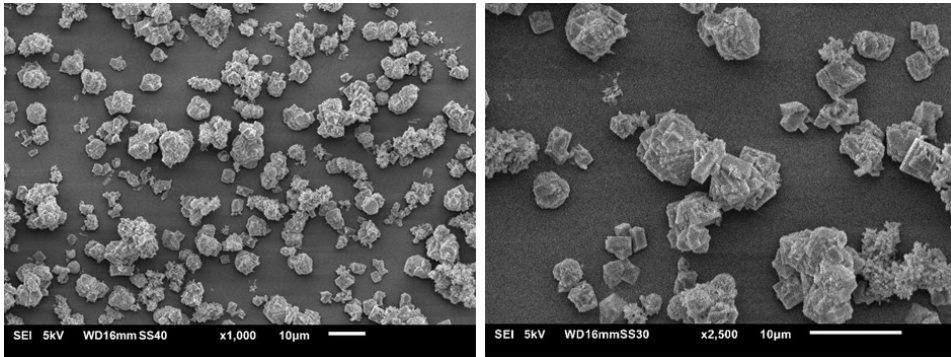


Figure A3.25. SEM micrographs of CAU-10 crystals obtained by using an oxalic acid:Al ratio of 0.5.

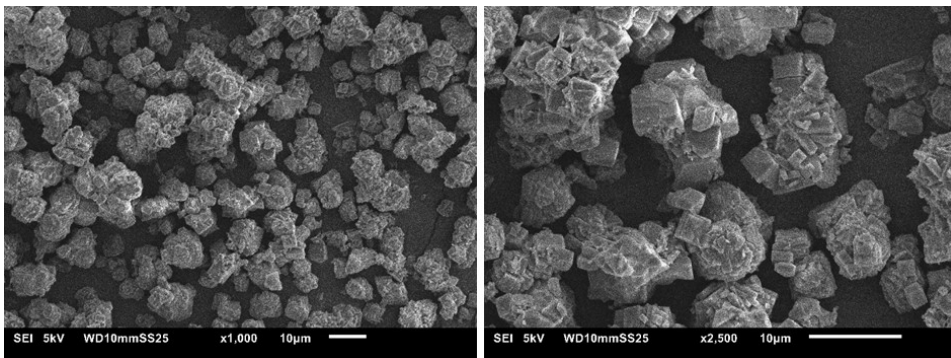


Figure A3.26. SEM micrographs of CAU-10 crystals obtained by using an oxalic acid:Al ratio of 1.0.

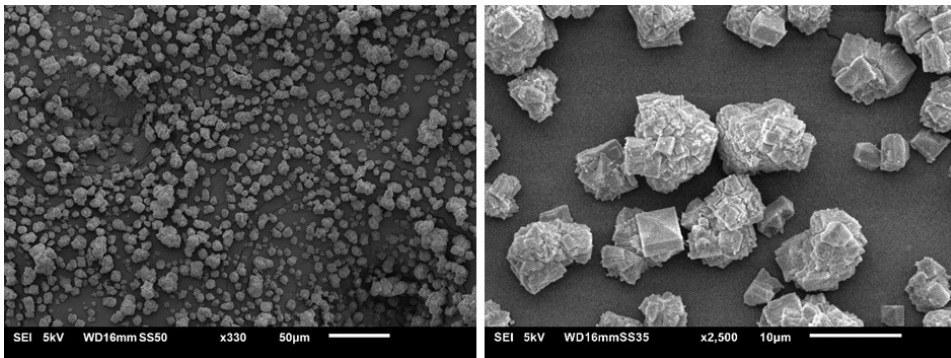
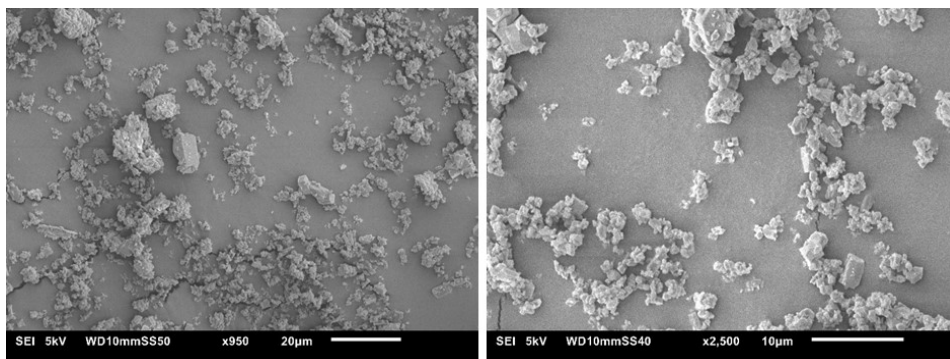
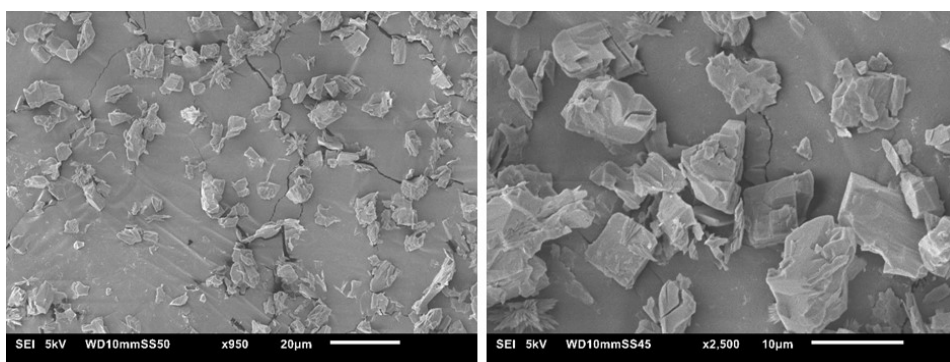


Figure A3.27. SEM micrographs of CAU-10 crystals obtained by using an oxalic acid:Al ratio of 1.5.

#### A3.2.4. MIL-69



**Figure A3.28.** SEM micrographs of MIL-69 crystals obtained by unmodulated synthesis.



**Figure A3.29.** SEM micrographs of MIL-69 crystals obtained by using an oxalic acid:Al ratio of 0.5.

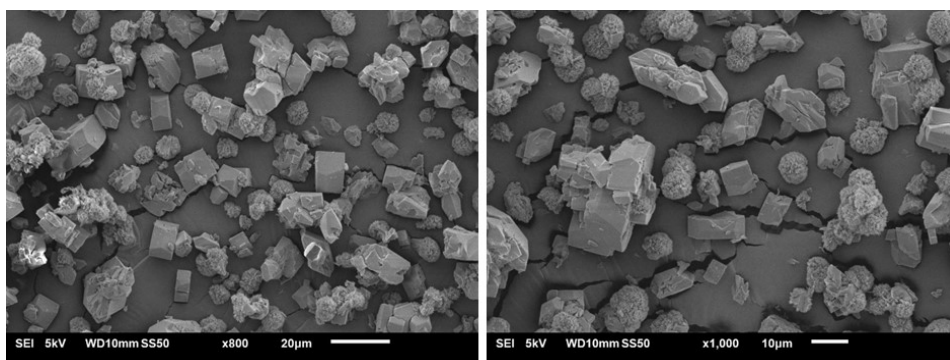


**Figure A3.30.** SEM micrographs of MIL-69 crystals obtained by using an oxalic acid:Al ratio of 1.0.

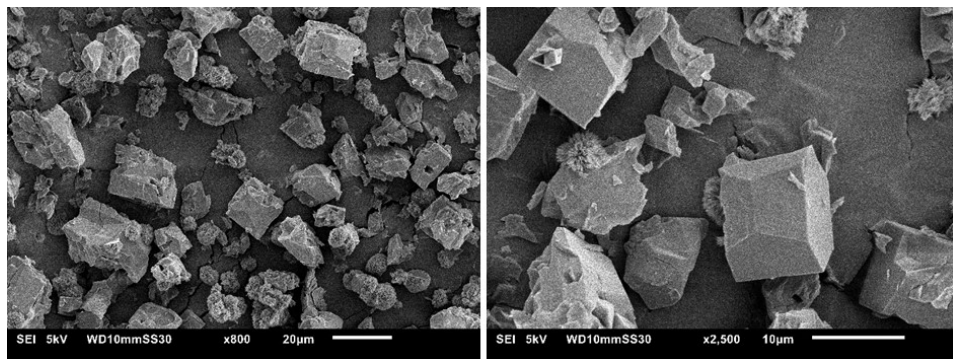


Figure A3.31. SEM micrographs of MIL-69 crystals obtained by using an oxalic acid:Al ratio of 1.5.

### A3.2.5. Al(OH)ndc

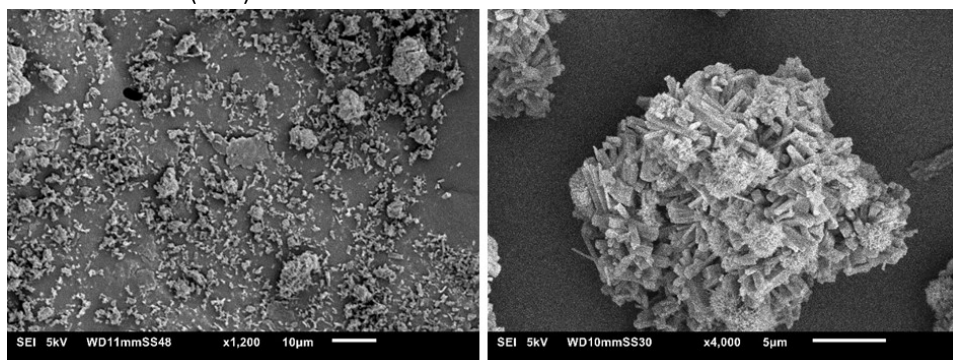


Figure A3.32. SEM micrographs of Al(OH)ndc crystals obtained by unmodulated synthesis.

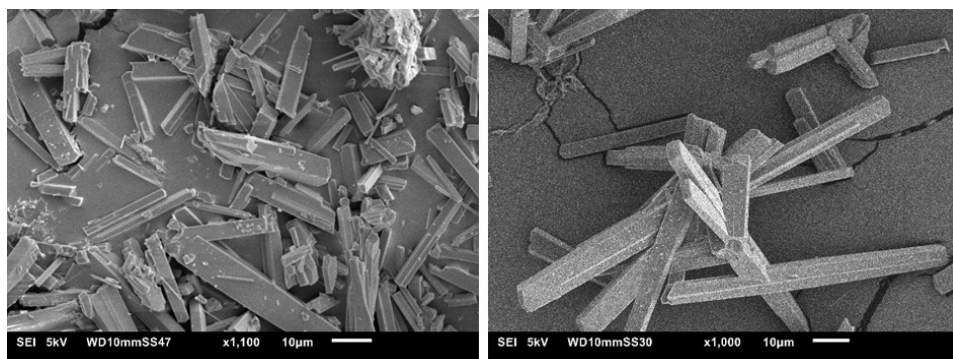


Figure A3.33. SEM micrographs of Al(OH)ndc crystals obtained by using an oxalic acid:Al ratio of 0.5.

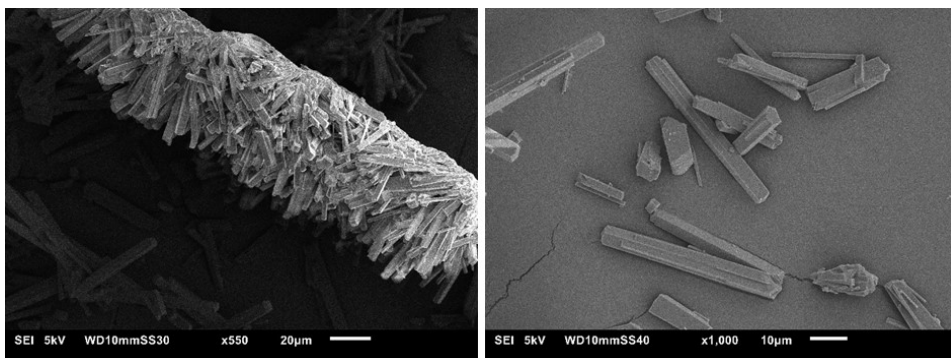


Figure A3.34. SEM micrographs of Al(OH)ndc crystals obtained by using an oxalic acid:Al ratio of 1.0.

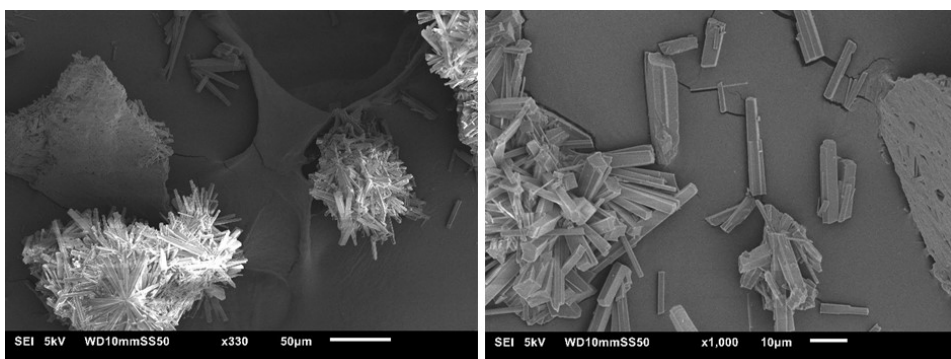


Figure A3.35. SEM micrographs of Al(OH)ndc crystals obtained by using an oxalic acid:Al ratio of 1.5.

### A3.2.6. EDX analysis

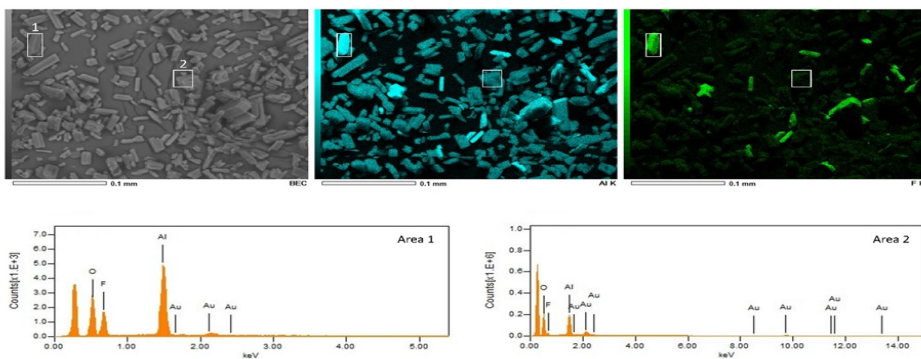


Figure A3.36. EDX microanalysis of the product obtained by the HF-modulated synthesis of MIL-53. Above, from the left: SEM micrograph, aluminium map, and fluorine map. Below: spectra recorded over the areas marked in the upper pictures with white rectangles.

Table A3.3. Elementary quantification relative to the EDX spectra shown in Figure A3.36.

|        | Element       | mass%      | Atom%      | Line |
|--------|---------------|------------|------------|------|
| Area 1 | C             | 47.45      | 58.1       | K    |
|        | O             | 27.42      | 25.21      | K    |
|        | F             | 15.27      | 11.82      | K    |
|        | Al            | 8.81       | 4.8        | K    |
|        | Au            | 1.06       | 0.08       | M    |
|        | <b>Total:</b> | <b>100</b> | <b>100</b> |      |
| Area 2 | C             | 56         | 65.4       | K    |
|        | O             | 34.85      | 30.56      | K    |
|        | F             | 1.64       | 1.21       | K    |
|        | Al            | 5.13       | 2.67       | K    |
|        | Au            | 2.38       | 0.17       | M    |
|        | <b>Total:</b> | <b>100</b> | <b>100</b> |      |

### A3.3. Thermogravimetric analysis (TGA)

#### A3.3.1. TGA curves of MIL-53

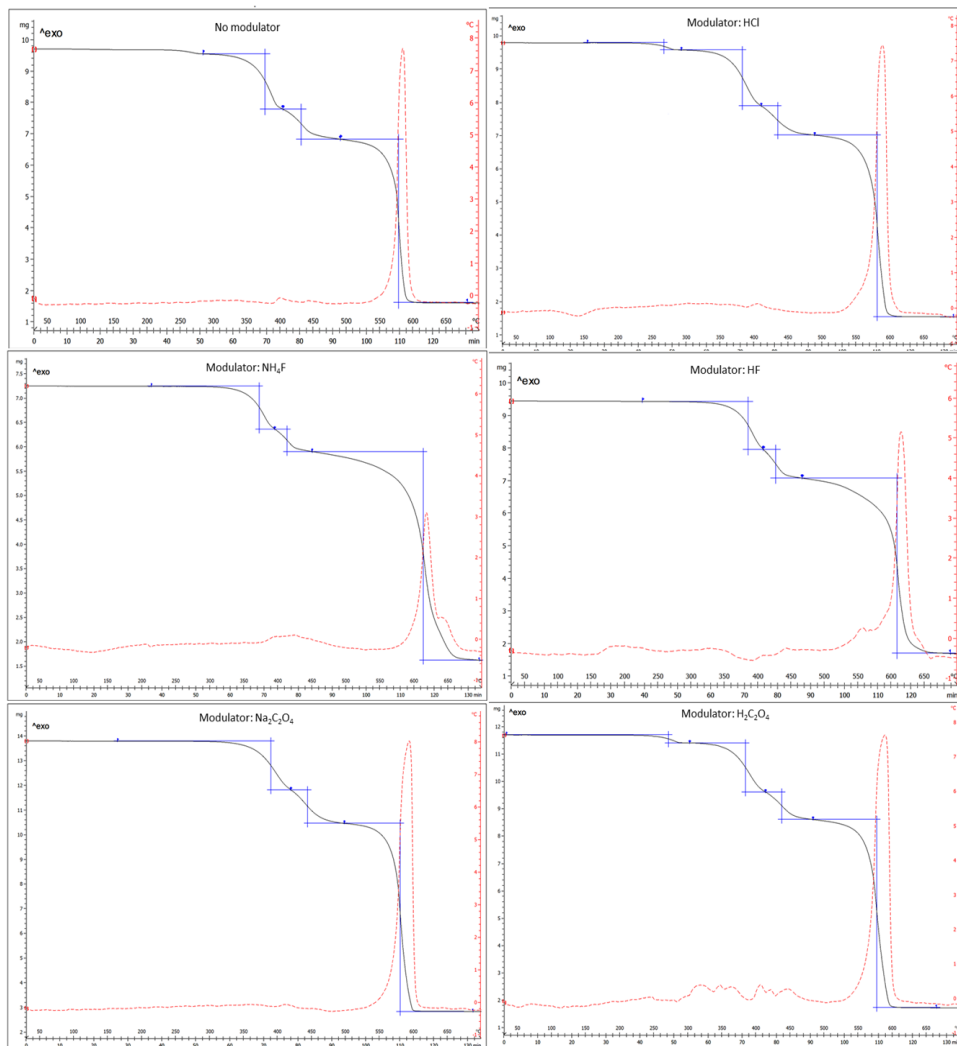


Figure A3.37. TGA curves of the products of MIL-53 synthesis (unmodulated and with different modulators).

### A3.3.2. TGA curves of X-MIL-53 (X = CH<sub>3</sub>O, OH, Br, NO<sub>2</sub>)

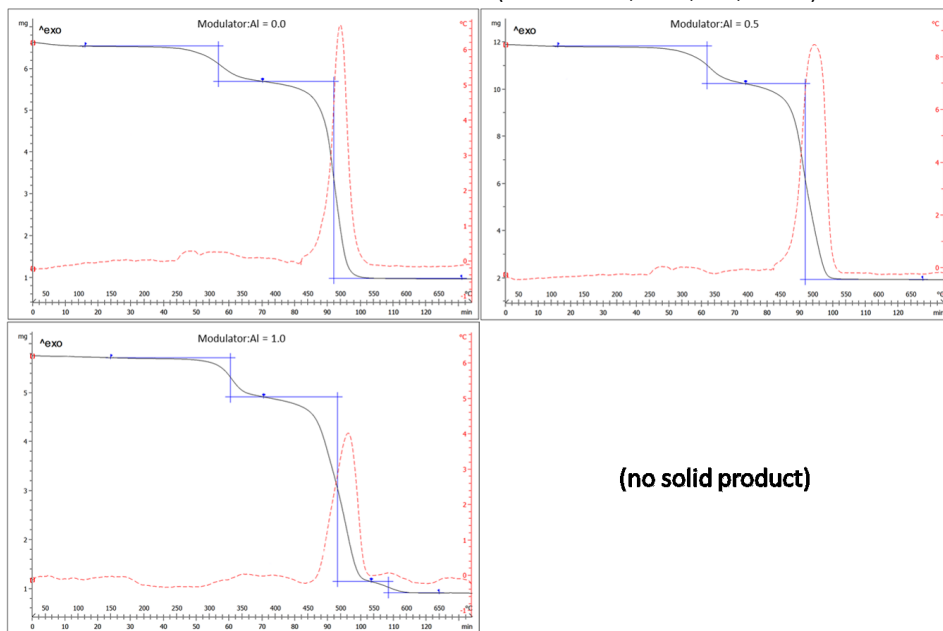


Figure A3.38. TGA curves of CH<sub>3</sub>O-MIL-53 synthesized with different oxalic acid:Al ratios.

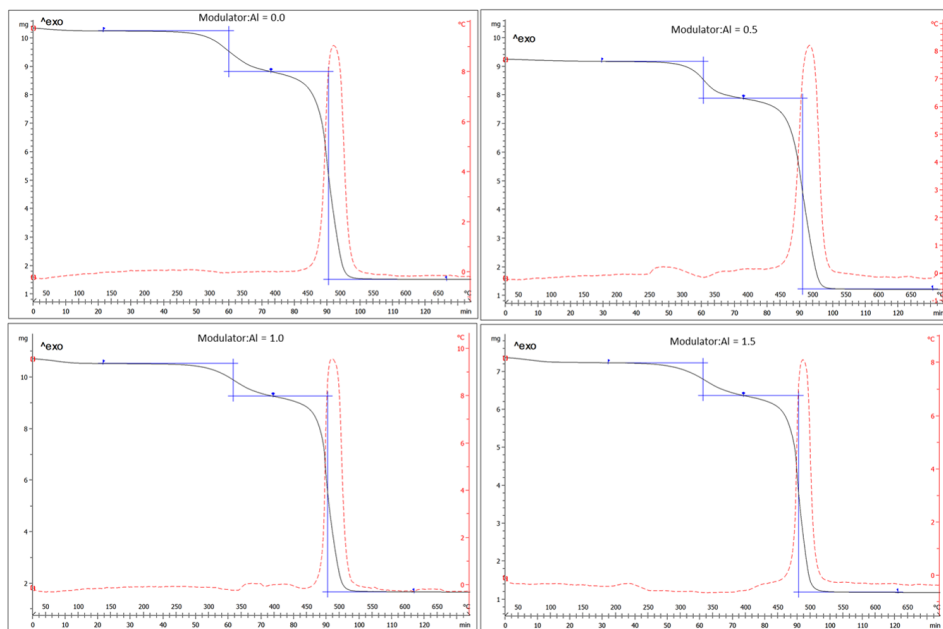


Figure A3.39. TGA curves of OH-MIL-53 synthesized with different oxalic acid:Al ratios.

# Overcoming crystallinity limitations of aluminum metal–organic frameworks by oxalic acid modulated synthesis

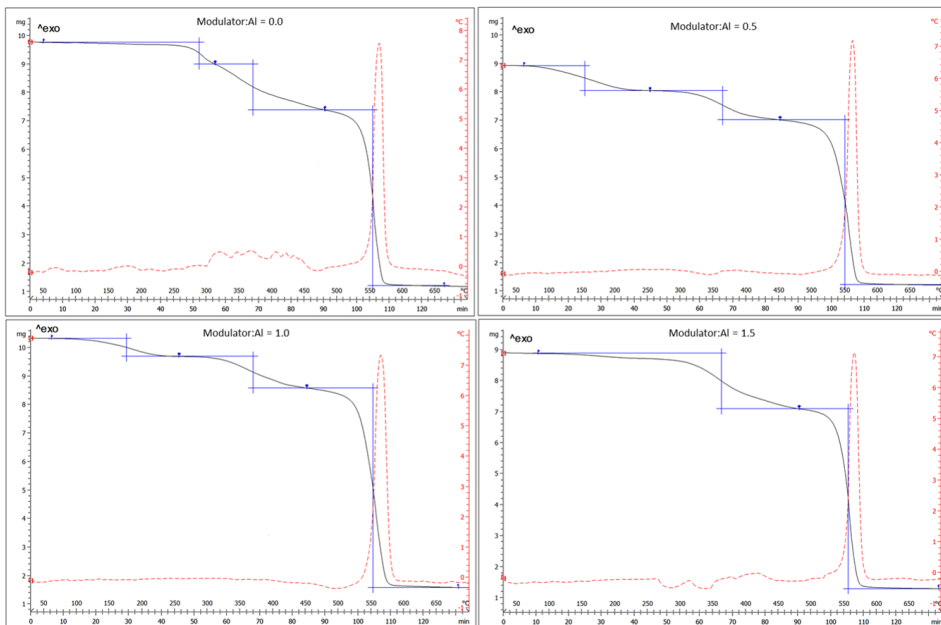


Figure A3.40. TGA curves of Br-MIL-53 synthesized with different oxalic acid:Al ratios.

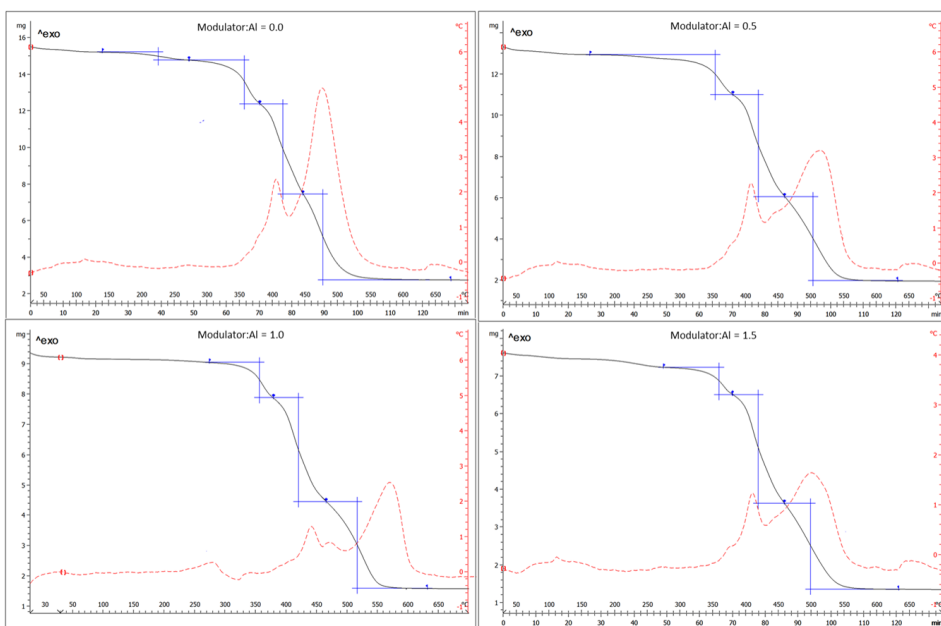


Figure A3.41. TGA curves of NO<sub>2</sub>-MIL-53 synthesized with different oxalic acid:Al ratios.

### A3.3.3. TGA curves of CAU-10, MIL-69, Al(OH)ndc

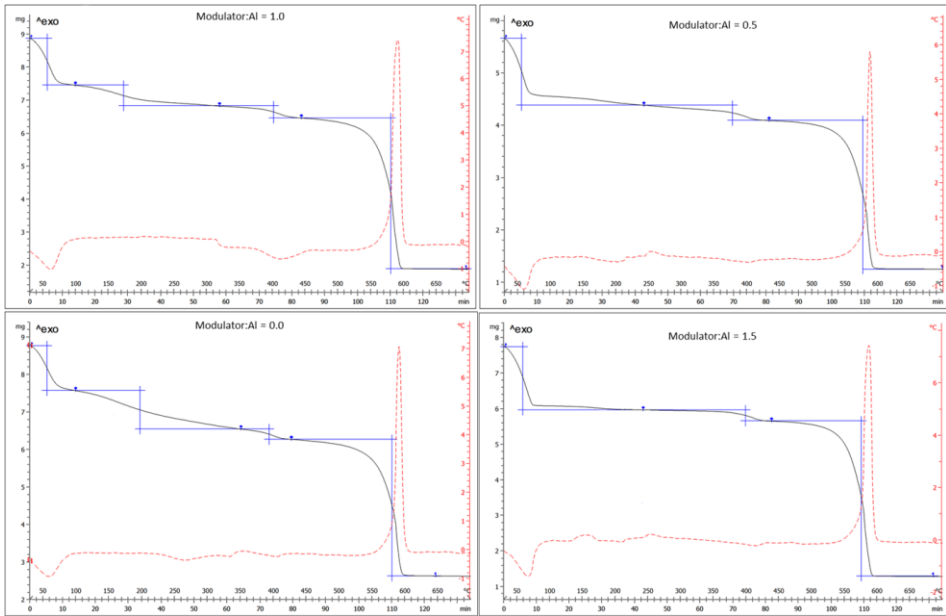


Figure A3.42. TGA curves of CAU-10 synthesized with different oxalic acid:Al ratios.

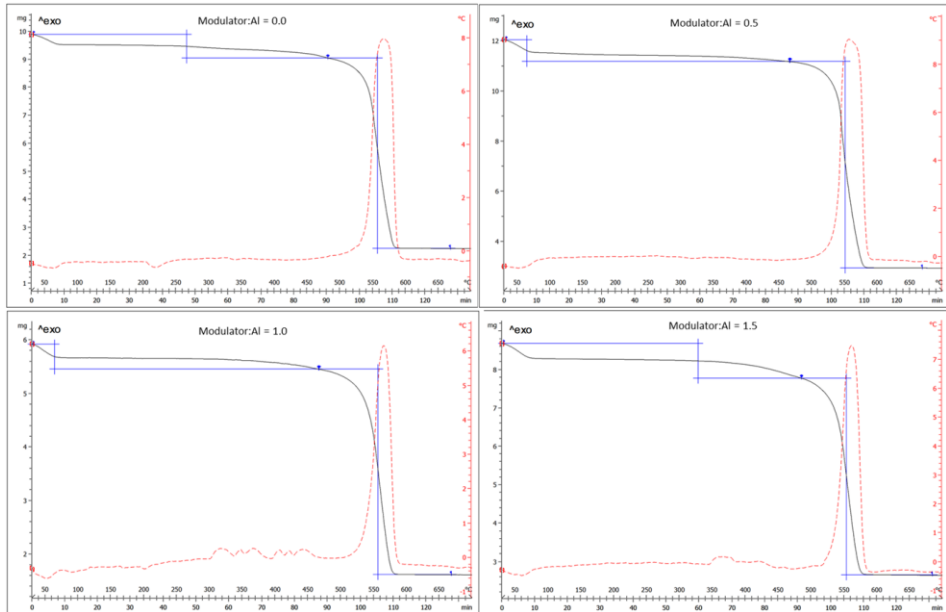


Figure A3.43. TGA curves of MIL-69 synthesized with different oxalic acid:Al ratios.

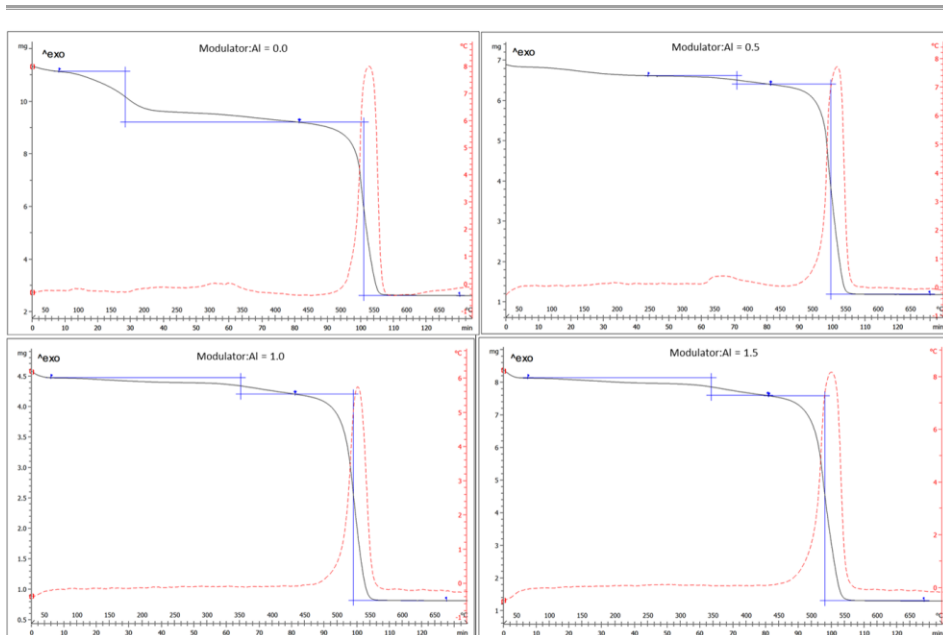


Figure A3.44. TGA curves of Al(OH)ndc synthesized with different oxalic acid:Al ratios.

### A3.4. Powder X-ray diffraction

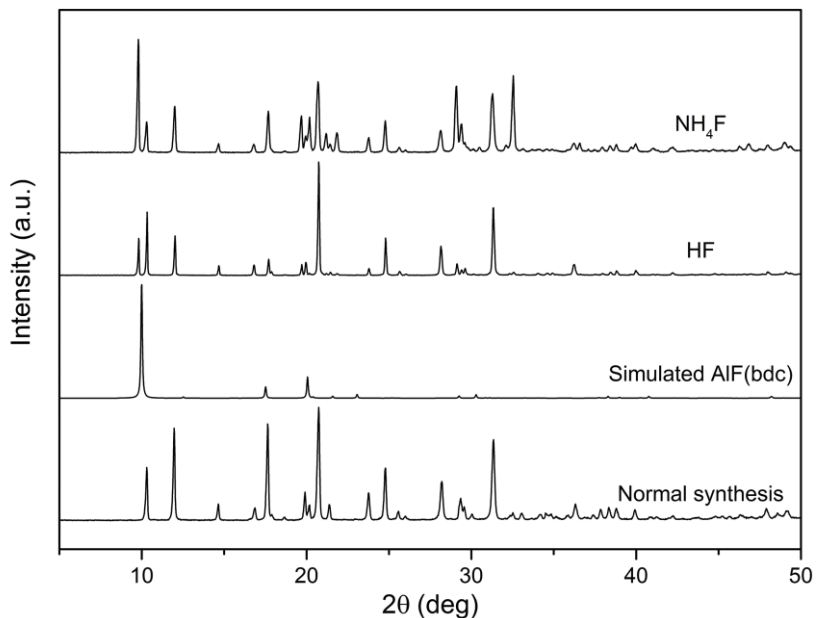
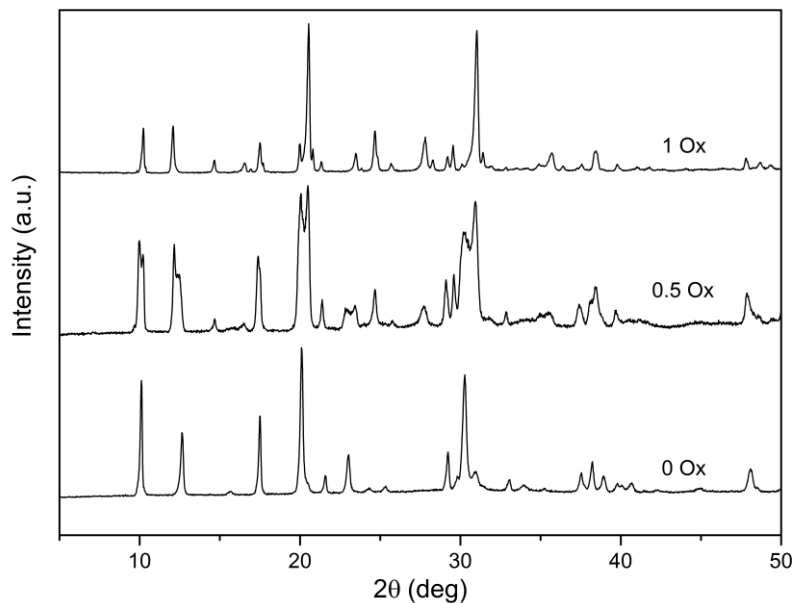
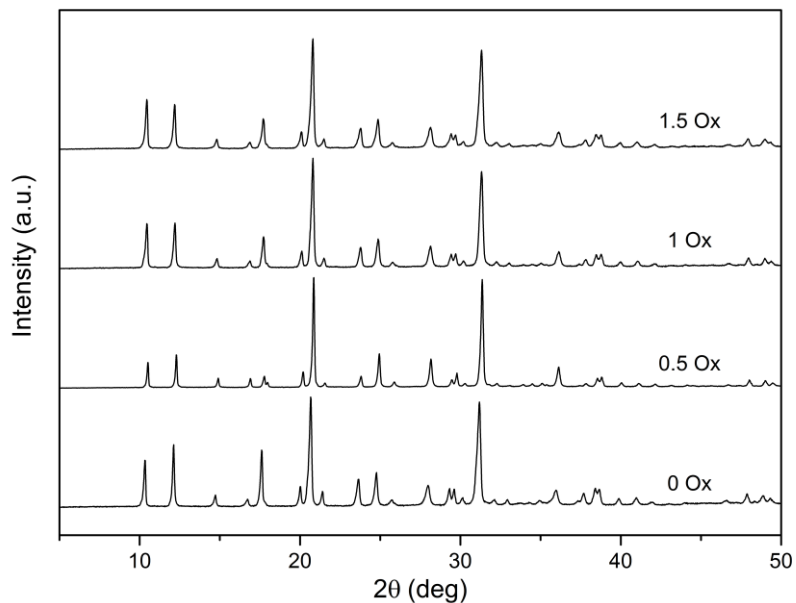


Figure A3.45. PXRD diffractograms of the products of fluoride modulators compared with a simulated pattern from AlF(bdc) reported by Nanthamathee *et al.*<sup>7</sup> The diffractogram of the product of non-modulated synthesis is shown for comparison.



**Figure A3.46.** PXRD diffractograms of CH<sub>3</sub>O-MIL-53 synthesized with different modulator:Al molar ratios. The peak shift from the “no modulator” and the “mod.:Al = 1.0” patterns is due to the different conformation of the framework, whose cavities have a more closed configuration in the latter case. The pattern of “mod.:Al = 0.5” shows the combined presence of both conformations.



**Figure A3.47.** PXRD diffractograms of OH-MIL-53 synthesized with different modulator:Al molar ratios.

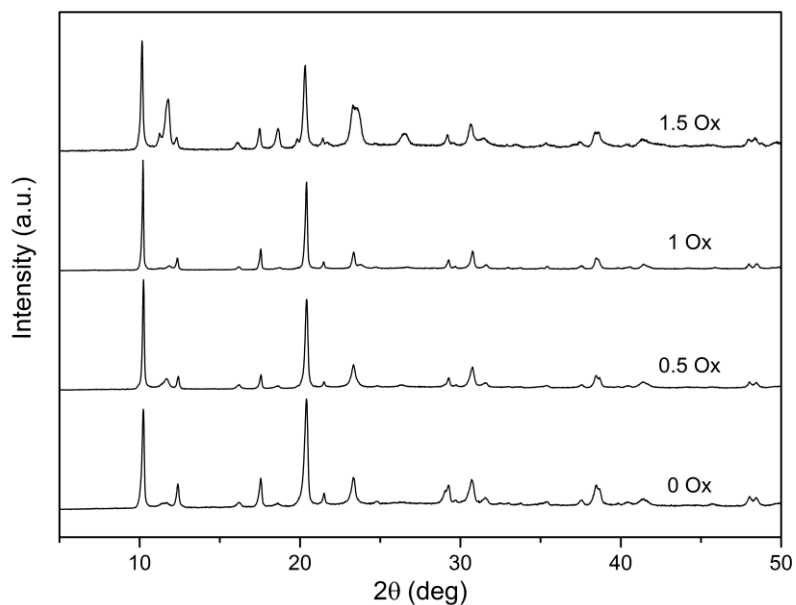


**Figure A3.48.** PXRD diffractograms of NO<sub>2</sub>-MIL-53 synthesized with different modulator:Al molar ratios.

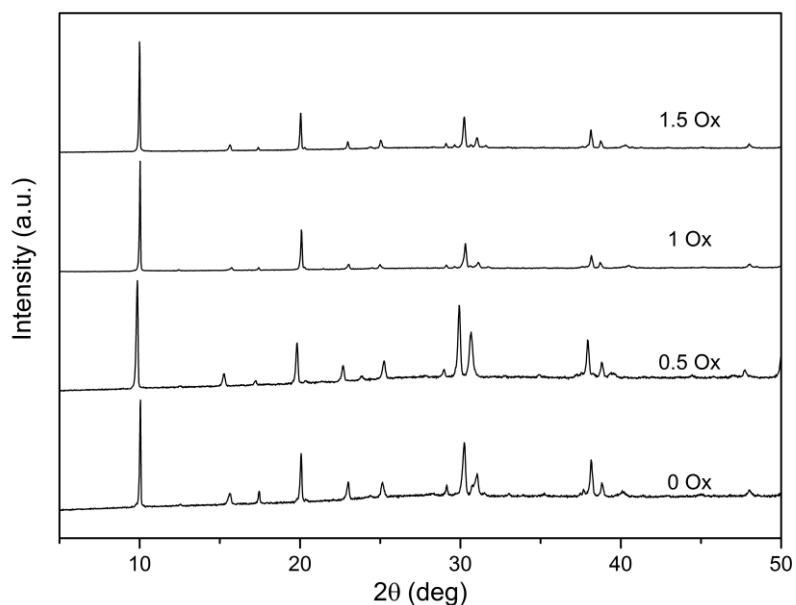


**Figure A3.49.** PXRD diffractograms of Br-MIL-53 synthesized with different modulator:Al molar ratios.

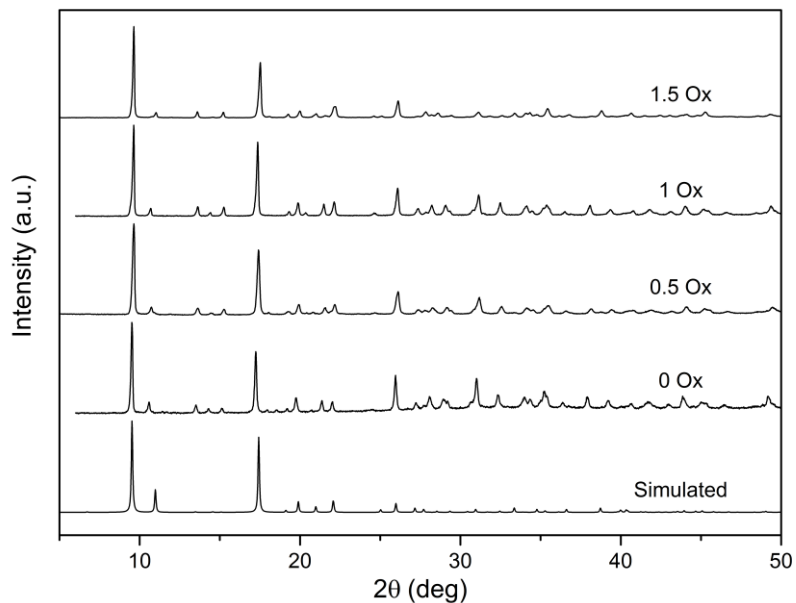


**Figure A3.50.** PXRD diffractograms of CAU-10 synthesized with different modulator:Al molar ratios. The bottom pattern was simulated from crystallographic data reported by Reinsch *et al.*<sup>3</sup>

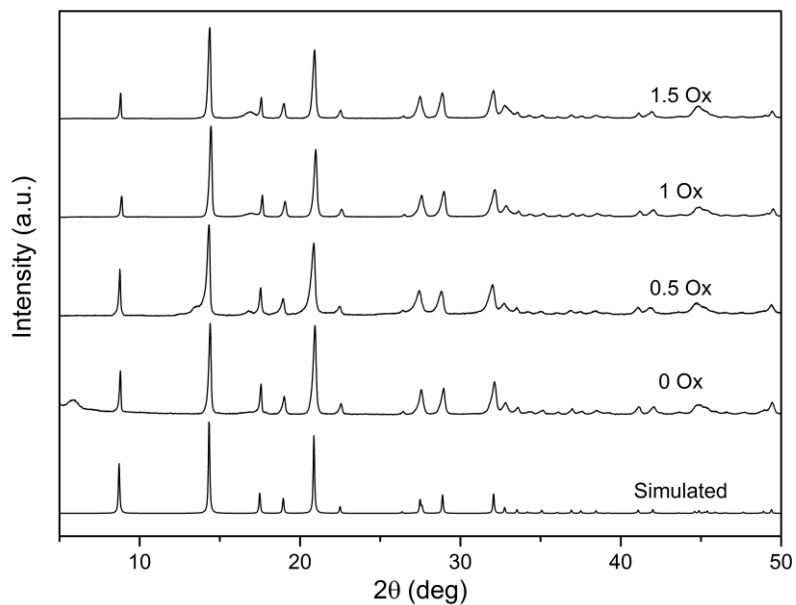


**Figure A3.51.** PXRD diffractograms of MIL-69 synthesized with different oxalic acid ratios. The bottom pattern was simulated from crystallographic data reported by Loiseau *et al.*<sup>4</sup>

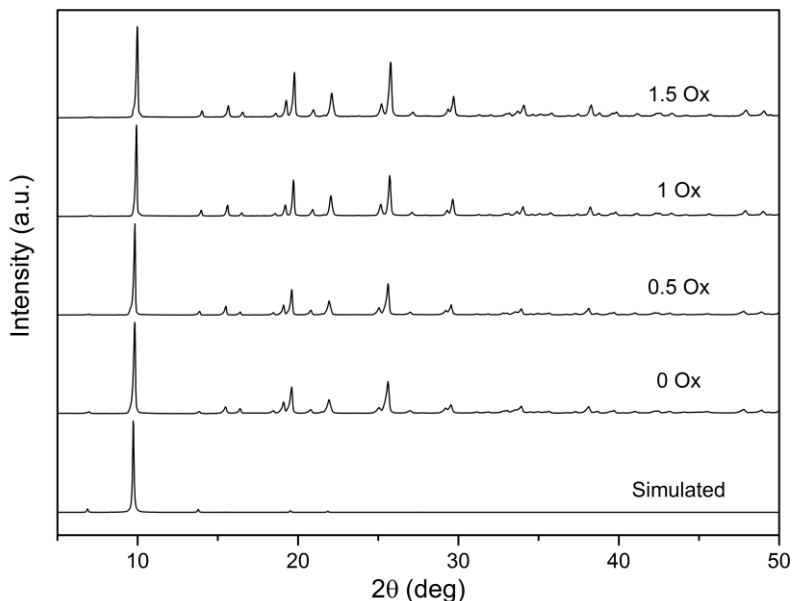


**Figure A3.52.** PXRD diffractograms of Al(OH)ndc synthesized with different oxalic acid ratios. The bottom pattern was simulated from crystallographic data reported by Comotti *et al.*<sup>5</sup>

### A3.5. Single-crystal X-ray diffraction

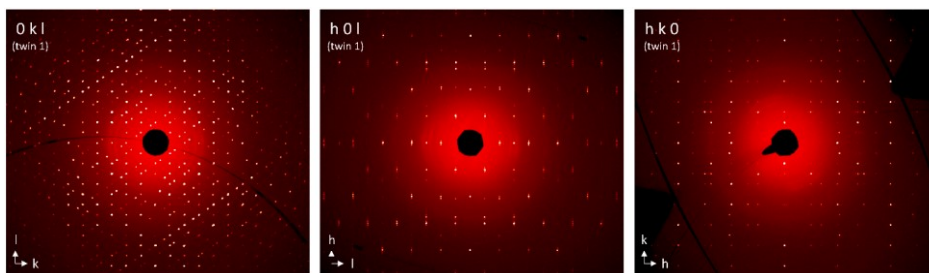


**Figure A3.53.** Precession images of a MIL-53 crystal synthesized using oxalic acid as synthesis modulator in a modulator-Al ratio of 1:1. The precession images' reconstruction is based on the orientation matrix of the domain identified as "twin 1" based on the percentage of the indexed reflections with respect to the total number of harvested reflections.

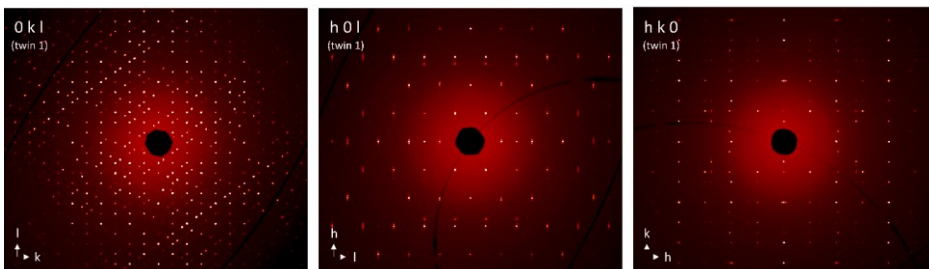


**Figure A3.54.** Precession images of a MIL-53 crystal synthesized using HF as synthesis modulator in a modulator:Al ratio of 1:1. The precession images' reconstruction is based on the same criteria described for the previous figure.

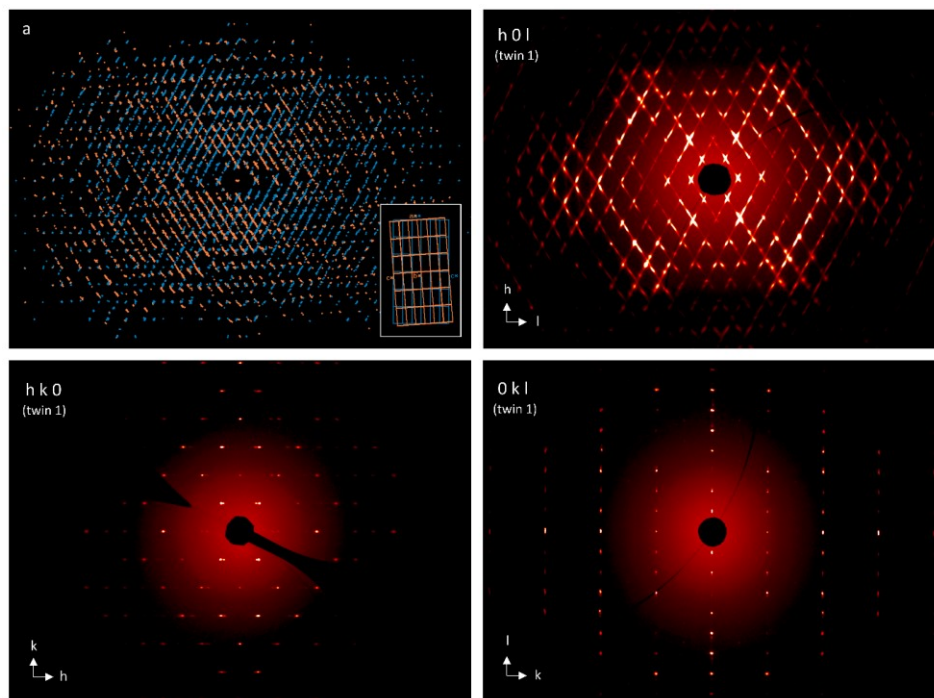


**Figure A3.55.** Reciprocal space reconstruction (a) and precession images of  $\text{NO}_2$ -MIL-53 synthesized using oxalic acid as synthesis modulator with modulator:Al ratio of 0.5:1. The crystal is affected by non-merohedral twinning by rotation of  $179.9726^\circ$  around  $1.00\ 0.00\ -0.08$  vector in reciprocal space ( $1.00\ 0.00\ -0.02$  in direct space); the two domains are marked with a blue and an orange colour.

The precession images' reconstruction is based on the orientation matrix of the domain identified as "twin 1" based on the percentage of the indexed reflections with respect to the total number of harvested reflections.

Diffuse scattering streaks due to correlated disorder are present in the  $(h\ 0\ l)$  plane, distributed along the  $a^*+c^*$  direction for each domain. No structured diffuse scattering is observed in the  $(h\ k\ 0)$  and  $(0\ k\ l)$  planes; the presence of satellite peaks is due to the contribution of the secondary domain.

### A3.6. Database searches

To confirm the rarity of the MIL-53 linker's bridging coordination mode for oxalate, two searches were conducted in the Cambridge Structural Database (CSD version 5.40, Updated May 2019). The search structural criteria are reported in the figure below.

Search 1 resulted in zero entries, and Search 2 in four entries with refcodes: QOBVOT, RAPBOZ, TAFPOG, TAFPOG01 (in Figure A3.56). In all these structures, oxalate anions perform stable five-membered ring metal chelation with all four oxygens and no  $\mu_2$ -1,3 bridging coordination is present.

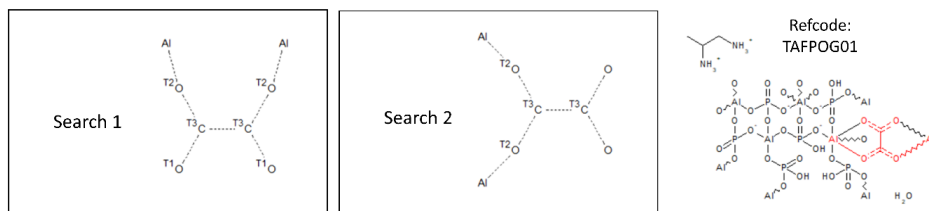


**Figure A3.56.** CSD searches for two possible oxalate coordination modes.

### A3.7. Appendix references

1. Otake, K., Matsumoto, M., Tanaka, S., Uchida, S., Goseki, R., Hirao, A. & Ishizone, T. Anionic Polymerization of Divinylbenzenes Possessing Methoxy Group. *Macromol. Chem. Phys.* **218**, 1–13 (2017).
2. Suba, K. & Udupa, M. R. Solid state reaction between dichromates and oxalates. *J. Therm. Anal.* **35**, 1197–1203 (1989).
3. Reinsch, H., van der Veen, M. A., Gil, B., Marszalek, B., Verbiest, T., de Vos, D. & Stock, N. Structures, Sorption Characteristics, and Nonlinear Optical Properties of a New Series of Highly Stable Aluminum MOFs. *Chem. Mater.* **25**, 17–26 (2013).
4. Loiseau, T., Mellot-Draznieks, C., Muguerra, H., Férey, G., Haouas, M. & Taulelle, F. Hydrothermal synthesis and crystal structure of a new three-dimensional aluminum-organic framework MIL-69 with 2,6-naphthalenedicarboxylate (ndc),  $\text{Al}(\text{OH})(\text{ndc})\cdot\text{H}_2\text{O}$ . *Comptes Rendus Chim.* **8**, 765–772 (2005).
5. Comotti, A., Bracco, S., Sozzani, P., Horike, S., Matsuda, R., Chen, J., Takata, M., Kubota, Y. & Kitagawa, S. Nanochannels of Two Distinct Cross-Sections in a Porous Al-Based Coordination Polymer. *J. Am. Chem. Soc.* **130**, 13664–13672 (2008).
6. Lausi, A., Polentarutti, M., Onesti, S., Plaisier, J. R., Busetto, E., Bais, G., Barba, L., Cassetta, A., Campi, G., Lamba, D., Pifferi, A., Mande, S. C., Sarma, D. D., Sharma, S. M. & Paolucci, G. Status of the crystallography beamlines at Elettra. *Eur. Phys. J. Plus* **130**, (2015).
7. Nanthamathee, C., Ling, S., Slater, B. & Attfield, M. P. Contradistinct thermo-responsive behavior of isostructural MIL-53 type metal-organic frameworks by modifying the framework inorganic anion. *Chem. Mater.* **27**, 85–95 (2015).



# Chapter 4

## Pillared cobalt metal–organic frameworks act as chromatic polarizers

---

The ease with which molecular building blocks can be ordered in metal–organic frameworks is an invaluable asset for many potential applications. In this chapter, this inherent order is shown to result in materials that could be used as chromatic polarizers based on visible-light linear dichroism via cobalt paddlewheel chromophores.

---

This chapter is based on the following publication:

Adrian Gonzalez-Nelson, Chaitanya Joglekar, and Monique A. van der Veen, Pillared cobalt metal–organic frameworks act as chromatic polarizers, *Chemical Communications* **57**, 1022-1025 (2021)

## 4.1. Introduction

Linear dichroism can be defined as the anisotropic absorption of light by a material.<sup>1</sup> This phenomenon is observed in materials that, due to their crystalline or partially ordered structure, show an overall alignment of the transition dipole moments or of nanostructured features on substrates.<sup>2–4</sup> This results in different degrees of light absorption depending on the relative orientation of the polarization direction of light.<sup>2</sup> For this reason, linear dichroic spectroscopy is often used to determine the structural orientation of molecules in matter.<sup>5–9</sup>

In terms of application, the main interest for dichroic materials is their potential use in polarization-sensitive light detectors<sup>2,3,10</sup> and optical components (*e.g.*, polarizers, filters, and waveplates).<sup>11</sup> The search for new dichroic materials is ongoing, arguably dominated by 2D inorganic materials,<sup>3,10–13</sup> which offer the advantage of strong light–matter interactions.<sup>14,15</sup> However, this family of materials entails difficulties in processing and obtaining high-quality crystals.<sup>3</sup> Among alternatives proposed to overcome these challenges are hybrid perovskites<sup>3,16</sup> and organic molecular crystals.<sup>17,18</sup> While the dichroism of the former type relies on the strongly anisotropic crystal structure (*i.e.*, stacked 2D layers),<sup>19</sup> the latter focuses on engineering molecular interactions to achieve a precise alignment of chromophores within the crystal structure. So far, most materials that show intrinsic dichroism are monochromatic, that is, an increase or decrease of the intensity of a single absorption mode simply results in the apparent change of the color's saturation. In contrast, photonic metamaterials, whose properties follow from their nanostructured surfaces,<sup>20</sup> are capable of showing a dichromatic linear dichroism, where changing the polarization of incident light the material leads to two distinct material colors.<sup>21–24</sup> This is a key advantage towards their application in polarimetry spectroscopy, security tags, and hyperspectral imaging, among others.<sup>21,23,25</sup>

Interestingly, with regard to dichroic molecular crystals, the reticular chemistry concept behind metal–organic frameworks (MOFs) may offer a further degree of control over the orientation of molecules while simultaneously facilitating the use of well-known coordination complexes as chromophores. MOFs are based on highly directional coordination bonding between organic and inorganic building blocks. Thorough research in the past two decades has provided an immense library of node and linker geometries which can be rationally selected to achieve desired properties.<sup>26,27</sup> Although the dichroic effect due to guest molecule alignment inside MOF pores has been reported,<sup>28</sup> to the best of our knowledge inherent linear dichroism has surprisingly not been studied in this type of materials.

This chapter constitutes an example of how well-defined MOF structures may be exploited to gain more control over the orientation of chromophores in crystal structures. In particular, a rare example of dichromatic dichroism is achieved as an *intrinsic* materials' property, which provides the potential for easier large-scale processing when compared to metamaterials. By selecting the tetragonal dabco-MOF (DMOF) architecture,  $[M_2(1,4\text{-bdc})_2(\text{dabco})]$  (1,4-bdc = 1,4-benzene dicarboxylate, dabco = 1,4-diazabicyclo[2.2.2]octane, and  $M = \text{Cu}^{2+}$ ,<sup>29</sup>  $\text{Zn}^{2+}$ ,<sup>30</sup> and  $\text{Co}^{2+}$ ,<sup>31,32</sup> among others), where 2D sheets of divalent transition metal carboxylate paddlewheels are stacked via dabco ligands functioning as pillars (Figure 4.1), a complete anisotropic alignment of the metal

paddlewheels is attained.  $\text{Co}^{2+}$  was chosen as the metal center due to its attractive chromophoric properties, which have already been demonstrated in other MOFs.<sup>33,34</sup>

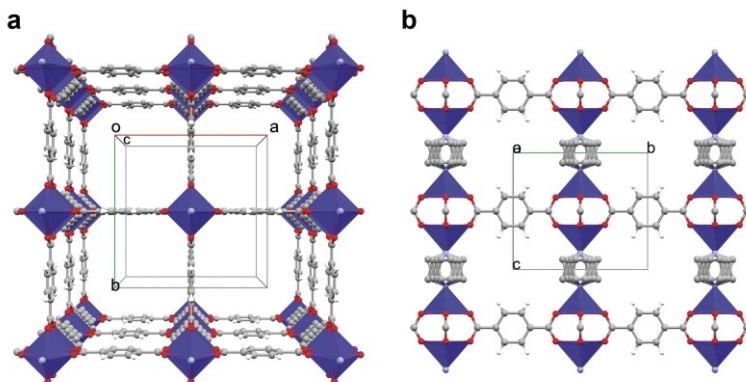


**Figure 4.1.** Structure of **1**. **a**, View along [001] direction, *i.e.*, the pillaring axis. **b**, View along [100] direction. Unit cell dimensions are  $a = b = 10.963 \text{ \AA}$  and  $c = 9.469 \text{ \AA}$ .

## 4.2. Results and discussion

Large single crystals of  $[\text{Co}_2(1,4\text{-bdc})_2(\text{dabco})]$  (**1**) were obtained in the range of  $500 \mu\text{m}$  long  $\times 50 \mu\text{m}$  wide by modifying a previously reported synthesis.<sup>31</sup> As explained in Chapter 3, pH modulation is a known approach to improve the crystallinity of MOFs.<sup>35,36</sup> During synthesis, protons in solution slow down the kinetics of ligand coordination reactions, thus decreasing nucleation and crystal growth rates. pH modulation was employed here by first mixing equimolar amounts of dabco and nitric acid, in order to obtain a monoprotonated dabco- $\text{H}^+$  salt, which was then allowed to react with terephthalic acid and  $\text{Co}(\text{NO}_3)_2 \cdot \text{H}_2\text{O}$  in DMF (see Appendix section A4.1 for experimental details). The powder XRD pattern of the product is shown in Figure A4.1, alongside the pattern computed from the reported crystallographic structure.

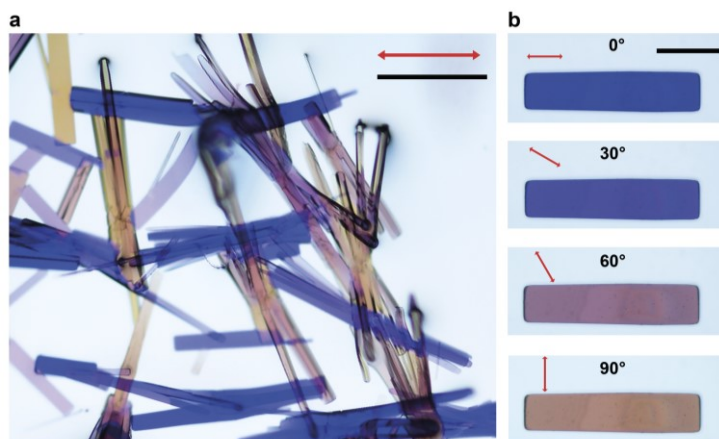


**Figure 4.2.** Optical images of **1**. **a**, Various relative orientations with respect to the polarization direction (red arrow) transmit different ranges of visible light. **b**, View of an isolated crystal of **1** whose long axis is  $0^\circ$ ,  $30^\circ$ ,  $60^\circ$ , and  $90^\circ$  relative to the polarized light orientation (red arrows); scale bars are  $200 \mu\text{m}$ .

When observed under polarized light, crystals of **1** transmit various colors (blue, purple, orange, yellow, see Figure 4.2) depending on their relative orientation to the polarization plane of light. The blue color corresponds to an orientation of the plane of polarization parallel ( $0^\circ$ ) to the long axis of the crystal, and the yellow color is observed when the crystals are perpendicular to the polarization plane ( $90^\circ$ ). Intermediate angles result in the combination of both colors. Compared to organic crystals, where dichroism simply manifests as a change in degree of transparency, this change between different colors, is an extraordinary case of dichroism.

To understand the origins of this remarkable dichroism, it is essential to study the visible light absorption of the MOF. Using diffuse reflectance UV-visible absorption spectroscopy on powdered samples, absorption bands are identified at 450, 540, and 580 nm, as well as a broader band around 700 nm (Figure 4.3). These absorption bands correspond to electronic transitions that are not present in the uncoordinated organic linkers, which do not absorb visible light. Rather, they are related to d-d transitions of electrons in the Co-dimers.<sup>37,38</sup> In fact, the absorption bands are very close to those reported for similar Co-paddlewheel MOFs,<sup>33,39–41</sup> as well as for cobalt complexes with a comparable coordination environment.<sup>42–44</sup>

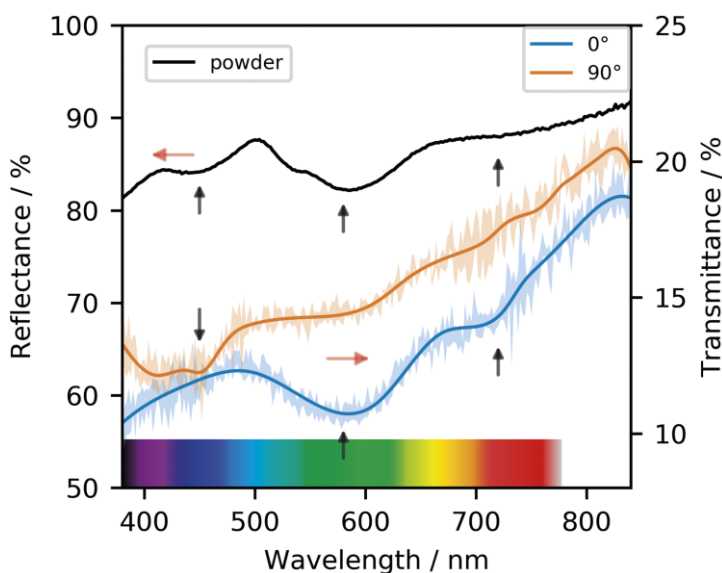


**Figure 4.3.** UV-visible spectra of **1** as powder in diffuse reflectance mode (black) and in single-crystal transmission mode with two relative polarization directions ( $0^\circ$  shown in blue and  $90^\circ$  in orange). The shaded area corresponds to one standard deviation (see Appendix section A4.1 for details).

The tetragonal crystal structure of the framework suggests that the distinct axis (*i.e.*, *c*) corresponds to the long dimension of their square prism habit. This means that the long axis of each crystal corresponds to the [Co-DABCO-Co] direction.

Polarization-dependent UV-visible absorbance spectroscopy on single crystals in transmission allows to understand how the different absorption bands are involved in the dichroic effect.

Although the transmittance of corresponding to the single-crystal spectra in Figure 4.3 seems low, it is important to remark that reflectance on the crystal surfaces may play a role in addition to absorbance, as the reference in the UV-Vis spectroscopy measurements entailed a cell without a crystal present. Nevertheless, the reflectance is expected to be similar in both polarization orientations, meaning that the relative change between the two single-crystal spectra is due to the dichroic effect. This spectrum shows that a clear change governing the transition from blue to yellow is the relative strength of the absorption bands (*i.e.*, dips in transmittance) centered around 580 and 700 nm. At 0°, this absorption is at its maximum, meaning that a larger fraction of yellow and red light is absorbed, causing the crystal to appear blue.<sup>45</sup> At 90°, absorption of the 580 and 700 nm bands is drastically decreased, implying that this wavelength's transmittance through the crystal increases, which results in it dominating the optical appearance. An apparent inverse effect may be inferred from the 450 nm absorption band (corresponding to the absorption of blue light), but the limited signal-to-noise ratio of these experiments does not allow us to conclude this with certainty. Also note that the yellow color of the crystals under 90° implies significant absorption of blue light (the 450 nm band), in contrast to the blue crystals at 0° where blue light is the least absorbed.

These observations can be rationalized by considering the framework's crystal structure. Within the pillared structure, the cobalt dimers are aligned along the *c*-axis, which corresponds to the longest dimension of the crystal habit. Therefore, in combination with the UV-visible absorption evidence, it can be proposed that the transition dipole moment corresponding to the 580 nm centered transition, as well as the broad 700 nm transition, are located along this axis. The higher energy absorption around 450 nm remains present at 90° polarization angle, causing the crystal to appear yellow.<sup>46</sup> This particular transition between two modes of visible light absorption is uncommon in dichroic materials, which are often monochromatic.<sup>17,18,28,47</sup>

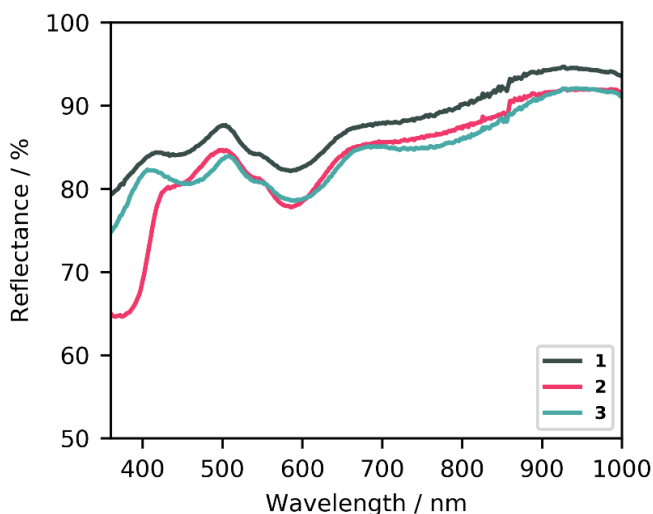


**Figure 4.4.** Diffuse reflectance UV-visible spectra of **1**, **2**, and **3**. Barring the absorption at 375 nm for **2**, the same absorption bands are observed for all frameworks, with slight shifts with respect to **1**.

The dichromatic dichroic effect is retained upon functionalization of the BDC linkers with nitro and amino groups (compounds  $[\text{Co}_2(1,4\text{-bdc-NH}_2)_2(\text{dabco})]$  (**2**) and  $[\text{Co}_2(1,4\text{-bdc-NO}_2)_2(\text{dabco})]$  (**3**); synthesis and characterization in Appendix). Only slight shifts in the location of absorption bands are observed (Figure 4.4), as well as the appearance of a new absorption band in the case of the amino functionalization (at ca. 375 nm), assigned to an  $n\text{-}\pi^*$  transition in previous work with the same linker.<sup>48</sup> The visible light dichroic effect in these two MOFs is very similar to that of the unfunctionalized framework, with the largest difference between  $0^\circ$  and  $90^\circ$  polarization being the absorption at 580 and 700 nm, producing a change from blue to yellow appearance under the optical microscope, respectively (Figures A4.2 and A4.3). This is not unexpected, because the coordination geometry of the Co-paddlewheel chromophore likely remains unchanged, and the electronic effects of the benzene ring substituent only have an indirect impact on the energy levels of the  $d\text{-}d$  transitions responsible for the dichroic absorption of visible light. The linkers, however, do provide a handle for additional dichroism in the near UV-range.

Since the observed dichroism is a result of  $d\text{-}d$  transitions from the cobalt coordination environment, the substitution of this metal should lead to a modification of the effect. A mixed-metal version of the DMOF was synthesized using equal parts of Zn and Co (**4**; characterization in Figures A4.4 and A4.5). While the dichroic effect is still present, crystals of **4** contain regions where light is better transmitted regardless of the thickness (Figure 4.5), likely due to a larger content of the complete  $d$  subshell  $\text{Zn}^{2+}$  cations. Although these results offer only a qualitative insight into the modification of the dichroic properties of **1**, this pillared structure provides an excellent playground to tune the dichroism to different combinations of colors. Potential pathways for such tunability would include the substitution of the metal cations (*e.g.*, with  $\text{Cu}^{2+}$  or  $\text{Mn}^{2+}$ ), or of the pillaring linker with a different nitrogen donor ligand, which can be expected to modify the splitting of the visible-light transitions significantly.

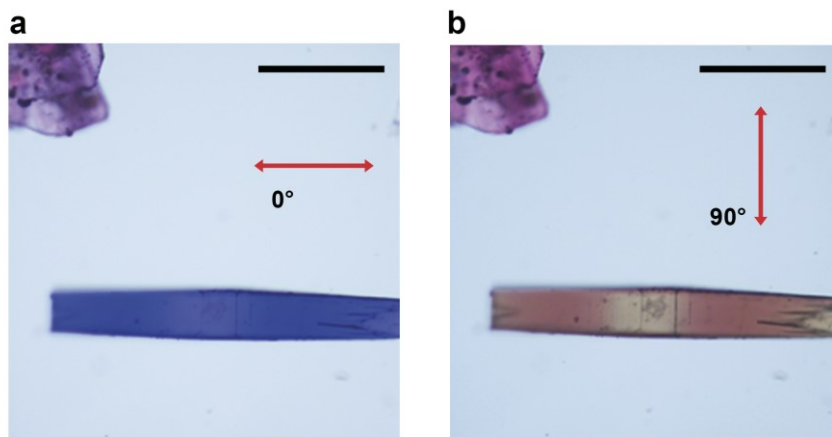


**Figure 4.5.** Polarized optical microscope images of a crystal of **4**, showing similar dichroic behavior as **1**. A region in the middle of the crystal clearly displays less visible light absorption both at parallel and perpendicular polarization orientations (**a** and **b**, respectively). Scale bars are 300  $\mu\text{m}$ . The pink crystals are an unidentified secondary product of the synthesis of **4**, also accountable for additional diffraction peaks in the PXRD pattern (Figure A4.4).

### 4.3. Conclusions

The ordered structure and specific orientation of building blocks are exceptional features with a tunable character in MOFs, which enable the development of new materials with desirable light-matter interactions. In the case of Co-based DMOFs, an anisotropic family of pillared frameworks, an unprecedented visible-light dichroic behavior is found, with a transition from blue to yellow. So far, to the best of our knowledge, such properties have only been achieved by applying nanostructured metamaterials as chromatic plasmonic polarizers.<sup>25</sup> MOFs may therefore be an attractive alternative to the complex nanopatterning processes currently needed for plasmonic polarizers.<sup>20</sup> The results presented here are the first example of dichromatic dichroism being an intrinsic material property. This strategy can be used to produce versatile dichroic materials active in other ranges of the electromagnetic spectrum, provided that the linker (or linkers), the inorganic building units, and therefore the topology, are selected accordingly.

### 4.4. References

1. Nordén, B. Applications of linear Dichroism Spectroscopy. *Appl. Spectrosc. Rev.* **14**, 157–248 (1978).
2. Yuan, H., Liu, X., Afshinmanesh, F., Li, W., Xu, G., Sun, J., Lian, B., Curto, A. G., Ye, G., Hikita, Y., Shen, Z., Zhang, S. C., Chen, X., Brongersma, M., Hwang, H. Y. & Cui, Y. Polarization-sensitive broadband photodetector using a black phosphorus vertical p-n junction. *Nat. Nanotechnol.* **10**, 707–713 (2015).
3. Liu, Y., Wu, Z., Liu, X., Han, S., Li, Y., Yang, T., Ma, Y., Hong, M., Luo, J. & Sun, Z. Intrinsic Strong Linear Dichroism of Multilayered 2D Hybrid Perovskite Crystals toward Highly Polarized-Sensitive Photodetection. *Adv. Opt. Mater.* **7**, 2–7 (2019).
4. Liu, Y., Wang, J., Han, S., Liu, X., Li, M., Xu, Z., Guo, W., Hong, M., Luo, J. & Sun, Z. Multilayered 2D Cesium-Based Hybrid Perovskite with Strong Polarization Sensitivity: Dimensional Reduction of CsPbBr<sub>3</sub>. *Chem. – A Eur. J.* **26**, 3494–3498 (2020).
5. Rocha, S., Kogan, M., Beke-Somfai, T. & Nordén, B. Probing Microscopic Orientation in Membranes by Linear Dichroism. *Langmuir* **32**, 2841–2846 (2016).
6. Hicks, M. R., Kowalski, J. & Rodger, A. LD spectroscopy of natural and synthetic biomaterials. *Chem. Soc. Rev.* **39**, 3380–3393 (2010).
7. Biver, T. Use of UV-Vis Spectrometry to Gain Information on the Mode of Binding of Small Molecules to DNAs and RNAs. *Appl. Spectrosc. Rev.* **47**, 272–325 (2012).
8. Persson, N. E., Engmann, S., Richter, L. J. & DeLongchamp, D. M. In Situ Observation of Alignment Templating by Seed Crystals in Highly Anisotropic Polymer Transistors. *Chem. Mater.* **31**, 4133–4147 (2019).
9. Qiao, J., Kong, X., Hu, Z.-X., Yang, F. & Ji, W. High-mobility transport anisotropy and linear dichroism in few-layer black phosphorus. *Nat. Commun.* **5**, 4475 (2014).
10. Zhou, Z., Long, M., Pan, L., Wang, X., Zhong, M., Blei, M., Wang, J., Fang, J., Tongay, S., Hu, W., Li, J. & Wei, Z. Perpendicular Optical Reversal of the Linear Dichroism and Polarized Photodetection in 2D GeAs. *ACS Nano* **12**, 12416–12423 (2018).
11. Yu, J., Kuang, X., Gao, Y., Wang, Y., Chen, K., Ding, Z., Liu, J., Cong, C., He, J., Liu, Z. & Liu, Y. Direct Observation of the Linear Dichroism Transition in Two-Dimensional Palladium Diselenide. *Nano Lett.* **20**, 1172–1182 (2020).
12. Wang, X., Li, Y., Huang, L., Jiang, X.-W., Jiang, L., Dong, H., Wei, Z., Li, J. & Hu, W. Short-Wave Near-Infrared Linear Dichroism of Two-Dimensional Germanium Selenide. *J. Am. Chem. Soc.* **139**, 14976–14982 (2017).

13. Yang, S., Hu, C., Wu, M., Shen, W., Tongay, S., Wu, K., Wei, B., Sun, Z., Jiang, C., Huang, L. & Wang, Z. In-Plane Optical Anisotropy and Linear Dichroism in Low-Symmetry Layered TlSe. *ACS Nano* **12**, 8798–8807 (2018).
14. Long, M., Wang, P., Fang, H. & Hu, W. Progress, Challenges, and Opportunities for 2D Material Based Photodetectors. *Adv. Funct. Mater.* **29**, 1803807 (2019).
15. Koppens, F. H. L., Mueller, T., Avouris, P., Ferrari, A. C., Vitiello, M. S. & Polini, M. Photodetectors based on graphene, other two-dimensional materials and hybrid systems. *Nat. Nanotechnol.* **9**, 780–793 (2014).
16. Zhao, Y.-Q., Ma, Q.-R., Liu, B., Yu, Z.-L., Yang, J. & Cai, M.-Q. Layer-dependent transport and optoelectronic property in two-dimensional perovskite: (PEA) <sub>2</sub> PbI<sub>4</sub>. *Nanoscale* **10**, 8677–8688 (2018).
17. Christopherson, J.-C., Potts, K. P., Bushuyev, O. S., Topić, F., Huskić, I., Rissanen, K., Barrett, C. J. & Friščić, T. Assembly and dichroism of a four-component halogen-bonded metal–organic cocrystal salt solvate involving dicyanoaurate(I) acceptors. *Faraday Discuss.* **203**, 441–457 (2017).
18. Bushuyev, O. S., Friščić, T. & Barrett, C. J. Controlling Dichroism of Molecular Crystals by Cocrystallization. *Cryst. Growth Des.* **16**, 541–545 (2016).
19. Li, L., Liu, X., Li, Y., Xu, Z., Wu, Z., Han, S., Tao, K., Hong, M., Luo, J. & Sun, Z. Two-Dimensional Hybrid Perovskite-Type Ferroelectric for Highly Polarization-Sensitive Shortwave Photodetection. *J. Am. Chem. Soc.* **141**, 2623–2629 (2019).
20. Tong, X. C. Photonic Metamaterials and Metadevices. In: *Functional Metamaterials and Metadevices*. Springer Series in Materials Science, vol 262. Springer, Cham.
21. Jia, H., Wu, Q. J., Jiang, C., Wang, H., Wang, L. Q., Jiang, J. Z. & Zhang, D. X. High-transmission polarization-dependent active plasmonic color filters. *Appl. Opt.* **58**, 704 (2019).
22. Jung, Y., Jung, H., Choi, H. & Lee, H. Polarization Selective Color Filter Based on Plasmonic Nanograting Embedded Etalon Structures. *Nano Lett.* **20**, 6344–6350 (2020).
23. Li, Z., Clark, A. W. & Cooper, J. M. Dual Color Plasmonic Pixels Create a Polarization Controlled Nano Color Palette. *ACS Nano* **10**, 492–498 (2016).
24. Franklin, D., Frank, R., Wu, S.-T. & Chanda, D. Actively addressed single pixel full-colour plasmonic display. *Nat. Commun.* **8**, 15209 (2017).
25. Ellenbogen, T., Seo, K. & Crozier, K. B. Chromatic Plasmonic Polarizers for Active Visible Color Filtering and Polarimetry. *Nano Lett.* **12**, 1026–1031 (2012).
26. Yaghi, O. M. Reticular Chemistry in All Dimensions. *ACS Central Science* **5**, 1295–1300 (2019).
27. Yaghi, O. M., O’Keeffe, M., Ockwig, N. W., Chae, H. K., Eddaoudi, M. & Kim, J. Reticular synthesis and the design of new materials. *Nature* **423**, 705–714 (2003).
28. Walton, I. M., Cox, J. M., Coppin, J. A., Linderman, C. M., Patel, D. G. (Dan) & Benedict, J. B. Photo-responsive MOFs: light-induced switching of porous single crystals containing a photochromic diarylethene. *Chem. Commun.* **49**, 8012 (2013).
29. Seki, K., Takamizawa, S. & Mori, W. Design and Gas Adsorption Property of a Three-Dimensional Coordination Polymer with a Stable and Highly Porous Framework. *Chem. Lett.* **30**, 332–333 (2001).
30. Dybtsev, D. N., Chun, H. & Kim, K. Rigid and flexible: A highly porous metal-organic framework with unusual guest-dependent dynamic behavior. *Angew. Chemie - Int. Ed.* **43**, 5033–5036 (2004).
31. Wang, H., Getzschmann, J., Senkovska, I. & Kaskel, S. Structural transformation and high pressure methane adsorption of Co<sub>2</sub>(1,4-bdc)<sub>2</sub>dabco. *Microporous Mesoporous Mater.* **116**, 653–657 (2008).
32. Takei, T., Li, T., Kawashima, J., Ohmura, T., Ichikawa, M., Hosoe, M., Shinya, Y., Kanoya, I.

- & Mori, W. Hydrogen-adsorption properties of a novel lantern-type dinuclear Co(BDC)(DABCO)1/2. *Chem. Lett.* **36**, 1136–1137 (2007).
33. Ehrling, S., Senkovska, I., Bon, V., Evans, J. D., Petkov, P., Krupskaya, Y., Kataev, V., Wulf, T., Krylov, A., Vtyurin, A., Krylova, S., Adichtchev, S., Slyusareva, E., Weiss, M. S., Büchner, B., Heine, T. & Kaskel, S. Crystal size versus paddle wheel deformability: selective gated adsorption transitions of the switchable metal–organic frameworks DUT-8(Co) and DUT-8(Ni). *J. Mater. Chem. A* **7**, 21459–21475 (2019).
34. Andrzejewski, M. & Katrusiak, A. Piezochromic Porous Metal–Organic Framework. *J. Phys. Chem. Lett.* **8**, 279–284 (2017).
35. Canossa, S., Gonzalez-Nelson, A., Shupletsov, L., del Carmen Martin, M. & Van der Veen, M. A. Overcoming Crystallinity Limitations of Aluminium Metal–Organic Frameworks by Oxalic Acid Modulated Synthesis. *Chem. - A Eur. J.* **26**, 3564–3570 (2020).
36. Zhao, Y., Zhang, Q., Li, Y., Zhang, R. & Lu, G. Large-Scale Synthesis of Monodisperse UiO-66 Crystals with Tunable Sizes and Missing Linker Defects via Acid/Base Co-Modulation. *ACS Appl. Mater. Interfaces* **9**, 15079–15085 (2017).
37. Benbellat, N., Gavrilenco, K. S., Le Gal, Y., Cador, O., Golhen, S., Gouasmia, A., Fabre, J. M. & Ouahab, L. Co(II)-Co(II) paddlewheel complex with a redox-active ligand derived from TTF. *Inorg. Chem.* **45**, 10440–10442 (2006).
38. *Conducting and Magnetic Organometallic Molecular Materials*, M. Fourmigué and L. Ouahab, (Springer Berlin Heidelberg, 2009).
39. Zhu, J., Chen, J., Qiu, T., Deng, M., Zheng, Q., Chen, Z., Ling, Y. & Zhou, Y. Cobalt substitution in a flexible metal–organic framework: modulating a soft paddle-wheel unit for tunable gate-opening adsorption. *Dalt. Trans.* **48**, 7100–7104 (2019).
40. Gupta, V. & Mandal, S. K. A robust and water-stable two-fold interpenetrated metal–organic framework containing both rigid tetrapodal carboxylate and rigid bifunctional nitrogen linkers exhibiting selective CO<sub>2</sub> capture. *Dalt. Trans.* **48**, 415–425 (2019).
41. Yang, X., Zhang, Y., Li, F., Guo, T., Wu, Y., Jin, F., Fang, M., Lan, Y., Li, Y., Zhou, Y. & Zou, Z. Theoretical and experimental studies on three water-stable, isostructural, paddlewheel based semiconducting metal–organic frameworks. *Dalt. Trans.* **46**, 8204–8218 (2017).
42. Hudák, J., Boča, R., Dlháň, Ľ., Kožíšek, J. & Moncoř, J. Structure and magnetism of mono-, di-, and trinuclear benzoato cobalt(II) complexes. *Polyhedron* **30**, 1367–1373 (2011).
43. Catterick, J. & Thornton, P. Mononuclear and polynuclear complexes of cobalt(II) carboxylates with pyridine and other heterocyclic bases. *J. Chem. Soc. Dalt. Trans.* 1634 (1976).
44. Ciampolini, M. & Bertini, I. A ligand-field model for high-spin five-co-ordinate complexes of cobalt(II). *J. Chem. Soc. A Inorganic, Phys. Theor.* 2241 (1968).
45. Cenens, J. & Schoonheydt, R. A. Visible Spectroscopy of Methylene Blue on Hectorite, Laponite B, and Barasym in Aqueous Suspension. *Clays Clay Miner.* **36**, 214–224 (1988).
46. Šuleková, M., Hudák, A. & Smřcová, M. The determination of food dyes in vitamins by RP-HPLC. *Molecules* **21**, (2016).
47. Walton, I. M., Cox, J. M., Mitchell, T. B., Bizier, N. P. & Benedict, J. B. Structural response to desolvation in a pyridyl-phenanthrene diarylethene-based metal–organic framework. *CrystEngComm* **18**, 7972–7977 (2016).
48. Sun, D., Fu, Y., Liu, W., Ye, L., Wang, D., Yang, L., Fu, X. & Li, Z. Studies on Photocatalytic CO<sub>2</sub> Reduction over NH<sub>2</sub>-Uio-66(Zr) and Its Derivatives: Towards a Better Understanding of Photocatalysis on Metal–Organic Frameworks. *Chem. - A Eur. J.* **19**, 14279–14285 (2013).

# Appendix to Chapter 4

---

## A4.1. Experimental details

### Materials

Preparation of protonated dabco-H<sup>+</sup> salt: 22.4 g (0.2 mol) 1,4-diazabicyclo[2.2.2]octane (dabco) was dissolved in an aqueous solution of nitric acid (1 M, 200 mL) using magnetic stirring. The solution was allowed to evaporate at 80 °C overnight.

Synthesis of **1**: Cobalt(II) nitrate hexahydrate (436 mg, 1.5 mmol) and terephthalic acid (249 mg, 1.5 mmol) were dissolved in N,N-dimethylformamide (DMF; 30 mL) together with 168 mg of dabco-H<sup>+</sup> salt. To promote heterogeneous nucleation, a clean glass slide was added to the reaction vessel. The solution was sealed in a 45 mL Teflon-lined autoclave and placed in an oven at 110 °C for 48 h. The autoclave was allowed to cool down to room temperature, and the product was filtered and washed with 30 mL DMF. The solid product was then dried at room temperature under vacuum for 12 h.

Synthesis of **2**: Cobalt(II) nitrate hexahydrate (218.5 mg, 0.75 mmol) and 2-aminoterephthalic acid (135.8 mg, 0.75 mmol) were dissolved in DMF (30 mL) together with 84 mg of dabco-H<sup>+</sup> salt. To promote heterogeneous nucleation, a clean glass slide was added to the reaction vessel. The solution was sealed in a 45 mL Teflon-lined autoclave and placed in an oven at 125 °C for 48 h. The autoclave was allowed to cool down to room temperature, and the product was filtered and washed with 30 mL DMF. The solid product was then dried at room temperature under vacuum for 12 h.

Synthesis of **3**: Cobalt(II) nitrate hexahydrate (218.5 mg, 0.75 mmol) and 2-nitroterephthalic acid (158.3 mg, 0.75 mmol) were dissolved in DMF (30 mL) together with 84 mg of protonated dabco-H<sup>+</sup> salt. To promote heterogeneous nucleation, a clean glass slide was added to the reaction vessel. The solution was sealed in a 45 mL Teflon-lined autoclave and placed in an oven at 125 °C for 48 h. The autoclave was allowed to cool down to room temperature, and the product was filtered and washed with 30 mL DMF. The solid product was then dried at room temperature under vacuum for 12 h.

Synthesis of **4**: Cobalt(II) nitrate hexahydrate (109.2 mg, 0.375 mmol), zinc(II) nitrate hexahydrate (111.5 mg, 0.375 mmol), dabco (67.3 mg, 0.6 mmol), and terephthalic acid (124.5 mg, 0.75 mmol) were dissolved in DMF (30 mL). To promote heterogeneous nucleation, a clean glass slide was added to the reaction vessel. The solution was sealed in a 45 mL Teflon-lined autoclave and placed in an oven at 110 °C for 48 h. The autoclave was allowed to cool down to room temperature, and the product was filtered and washed with 30 mL DMF. The solid product was then dried at room temperature under vacuum for 12 h.

### Measurements

The powder XRD patterns were measured with a Bruker-AXS D5005 diffractometer, equipped with a Co-K $\alpha$  source ( $\lambda=1.789$  nm). The measurements were conducted with a step size of 0.02°

with a  $2\theta$  range of  $5^\circ$ – $50^\circ$ , and variable divergence slit. Polarized light microscopy images were taken using a Nikon Eclipse E600 POL microscope fitted with Nikon DS-Ri1 camera. A JEOL JSM-6010LA scanning electron microscope was used to perform energy dispersive X-ray spectroscopy using the backscatter electron detector and 20 kV acceleration voltage. Samples were deposited on conductive adhesive carbon tape and sputtered with a layer of gold to avoid charging effects.

**Ultraviolet-Visible (UV-Vis) Spectroscopy:** A Perkin-Elmer Lambda-900 spectrophotometer equipped with an integration sphere was used. For diffuse reflectance measurements, spectra were referenced to a blank reading of BaSO<sub>4</sub>. An acquisition time of 200 nm/min was used. Sample preparation included grinding and dilution with BaSO<sub>4</sub>. Single-crystal measurements were performed by mounting a large single crystal in a demountable quartz cuvette (Hellma 26  $\mu$ L) using Fluorolube oil as a medium. The separation between front and back sides of the cuvette was maintained constant by placing a 100  $\mu$ m spacer in between. A mask with a 200  $\mu$ m diameter pinhole was placed on the front side of the cuvette, centered on the crystal to reduce the incident light area. Spectra were acquired with the polarizer set at  $0^\circ$  and  $90^\circ$  with respect to the long edge of the crystal. Blank measurements (i.e., the same cuvette, mask, and medium without the crystal) were subtracted from all single crystal measurements for both polarization angles. Acquisition times of 15 nm/min or 30 nm/min were used depending on the quality of the spectra. The data reported in Figures 4.3, A4.2 and A4.3 correspond to the average of five acquisitions, with the shaded area representing the confidence interval of one standard deviation.

## A4.2. Supporting Figures

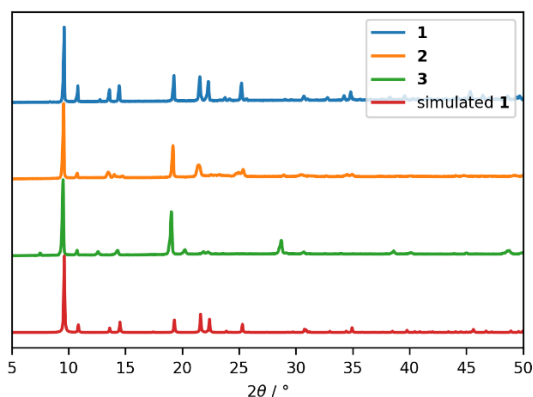


**Figure A4.1.** Powder XRD patterns of 1, 2, and 3, compared to the simulated pattern from the reported structure of 1 with CCDC Refcode: TORXEE.

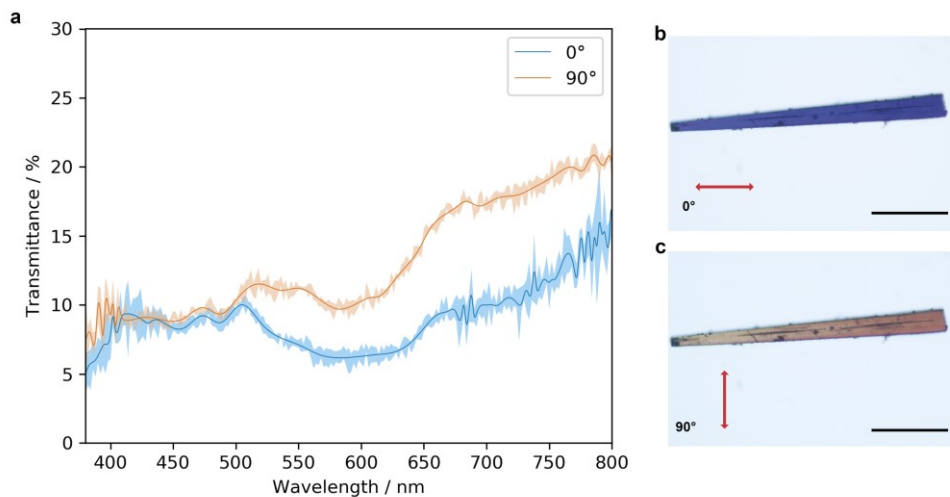


**Figure A4.2.** (a) UV-visible spectra of **2** in single-crystal transmission mode with two relative polarization directions ( $0^\circ$  shown in blue and  $90^\circ$  in orange). The shaded area corresponds to one standard deviation. (b and c) Optical microscope images of an isolated crystal of **2** whose long axis is parallel and perpendicular to the polarized light orientation (red arrows); scale bar represents  $200\ \mu\text{m}$ .

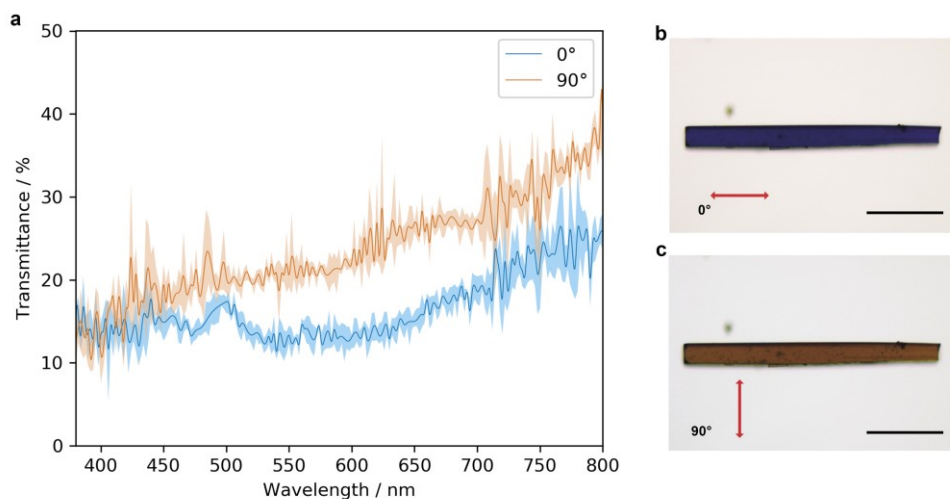


**Figure A4.3.** (a) UV-visible spectra of **3** in single-crystal transmission mode with two relative polarization directions ( $0^\circ$  shown in blue and  $90^\circ$  in orange). The shaded area corresponds to one standard deviation. (b and c) Optical microscope images of an isolated crystal of **3** whose long axis is parallel and perpendicular to the polarized light orientation (red arrows); scale bar represents  $200\ \mu\text{m}$ .

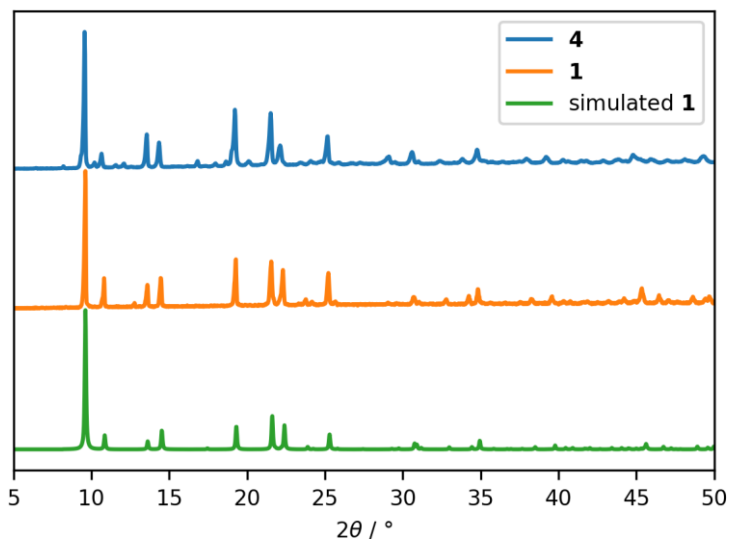


**Figure A4.4.** Powder XRD pattern of 4 compared to the experimental and simulated patterns of 1. Synthesis of 4 produced a secondary product, whose diffraction pattern is slightly visible, seen also in Figure 4.5 (pink crystals).

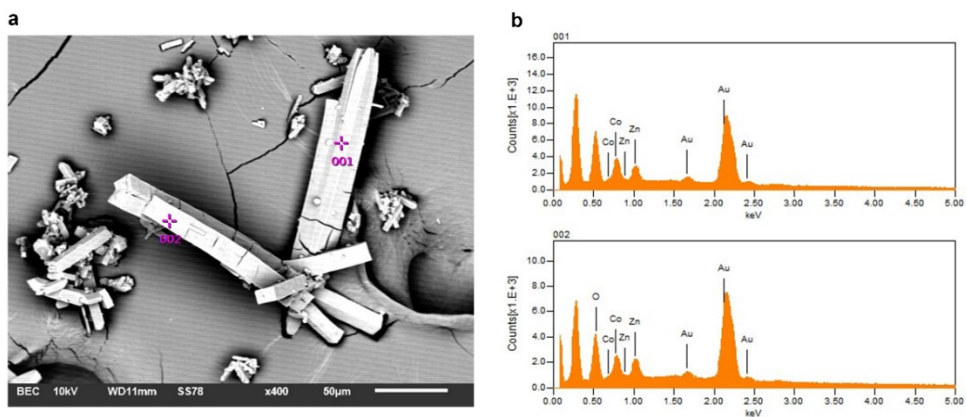


**Figure A4.5.** (a) SEM image of 4, showing the presence of both Co and Zn in two different points by energy dispersive X-ray spectroscopy (b).



# Summary

Metal–organic frameworks (MOFs) are ordered arrays of polytopic organic ligands, commonly called linkers, which interconnect metal-based inorganic building units via coordination bonds. The highly precise assembly of well-defined building blocks into extended 3-D networks, known as reticular chemistry, has allowed researchers in this field to produce tens of thousands of different frameworks. As an obvious consequence of their unprecedented porosity and tunability, these versatile materials are continuously studied with various potential applications in mind. An important portion of MOF research has been invested in the interaction between molecules and the framework, aiming for applications such as gas storage and separation, as well as catalysis, drug delivery, heat exchange, and water harvesting.

MOFs are considered soft or flexible materials, a characteristic that includes structural dynamics or large amplitude deformations. This flexibility can usually be attributed to the framework's topology and the degrees of freedom of some of its bonds. However, the linkers themselves may also have degrees of freedom allowing independent molecular dynamics, in particular in the form of rotation. This type of dynamics is particularly common in MOFs because their porous architectures often provide enough space for the rotation of a molecular fragment to occur. It is this type of dynamics that this thesis is centered on, starting from the fact that, although it is an intriguing phenomenon that occurs in MOFs, it has remained relatively unexplored.

Nevertheless, the past four years have seen an increase in researchers' interest in rotational dynamics in MOFs. This may be due to two main reasons: First, linker rotation influences MOF properties, not only when guest molecule interactions are involved, but also in optical and mechanical properties. Development of our knowledge on linker rotation is therefore essential for a more complete understanding of these materials' properties and how they may be modified to enhance a specific trait. Second, the exploitation of linkers' rotational freedom could potentially lead to important technological advances. The latter category includes various innovative ideas, such as the design of ferroelectric MOFs by means of controllable dipolar rotors, or the realization of crystalline molecular machines able to produce useful work.

**Chapter 1** is an introduction into rotational linker dynamics literature, which covers the different types of rotation that have been demonstrated, as well as an overview of the techniques used and the applications the research is aimed towards. Rotational linker dynamics in MOFs may be categorized into four types based on geometric and energetic considerations. From the amount of work that has been published on the topic, it is evident that rotational motions are commonplace in MOFs, with a rich diversity of mechanisms of rotation, as well as complex interplays between the rotor framework and guest molecules. The electronic configuration of the rotor and the steric environment inside the framework are the two main factors determining the torsional potential, and they are therefore key parameters in the design of rotor MOF systems. Rotational motions can have a drastic impact on their properties and on their performance in several applications. So far, research has primarily analyzed the properties that derive from

rotation, but growth is expected in the exploitation of rotation as a valuable design factor in functional nanomaterials.

From the literature it appears that due to its specificity and relative ease of interpretation,  $^2\text{H}$  NMR is the most prominent experimental technique in the study of MOF linker rotation. It has been used successfully to determine rotation steps, rates, and barriers of numerous and often diverse MOFs. Other methods, such as  $^1\text{H}$  NMR spin-lattice relaxation, dielectric spectroscopy, and THz spectroscopy, are becoming more commonplace, but may need further development and/or combination with supporting techniques to avoid ambiguity. Molecular modeling techniques can also be used to provide information on the dynamic nature of the frameworks.

In order to fully exploit linker rotation, it is necessary to engineer correlated linker dynamics to achieve their cooperative functional motion. Linkers in MOFs are separated from each other by tunable free space, and by modifying this space a large variety of dynamic behavior can emerge. In **Chapter 2**, I discuss the intricate effects that linker functionalization may have on the dynamic behavior in a family of MOFs that allows steric interactions between linkers. The work presented in this chapter involves the MIL-53 family, which has a conveniently small distance between its linkers. The functionalization of the rotating phenylene groups allows for the tuning of the rotors' steric environment, shifting linker rotation from completely static to rapid motions at frequencies above 100 MHz, as measured by solid-state  $^2\text{H}$  NMR spectroscopy. When a bulkier nitro group is placed on the rotors, steric interactions start to inhibit their independent motion, and a more complex dynamic behavior emerges. By combining solid-state  $^2\text{H}$  NMR and broadband dielectric spectroscopies with DFT and ab initio molecular dynamics, correlated rotation between linkers was confirmed. These findings pave the way for function-specific engineering of gear-like cooperative motion in MOFs.

Moving to a more general territory in the second part of the thesis, the following two chapters address the necessity for large single crystals in MOF research. Even more detailed understanding of a MOF structure, including its dynamics, could be obtained if large single MOF crystals are available. Several important characterization techniques then become applicable. Perhaps the most fundamental is single-crystal XRD, which enables us to obtain the average periodic structure of a framework with great resolution, as well as, in some cases, revealing more local structural details such as correlated defects or other types of domains.

**Chapter 3** presents a new synthesis modulation approach developed for large single crystal aluminum MOFs, which are notoriously difficult to obtain. Typical MOF synthesis modulation methods are based on the addition of a capping agent with the same coordination mode as the linker. In this way, modulator and linker ligands compete during MOF formation and growth, which reduces the rate of reaction and in some cases leads to increase in crystal size. However, the modulator's compatibility ensures that certain amounts of missing linker defects are formed whenever the capping agent is not substituted by a linker.

In contrast to this, the new oxalic acid-based method relies on a ligand that does not coordinate with the same geometry as the linker, bypassing the aforementioned pitfall. Oxalic acid forms stable chelates with  $\text{Al}^{3+}$  in solution, which decreases the nucleation and growth rates but does not affect the final product's structure. A comparative study on this method and the already

established modulation by hydrofluoric acid was conducted using MIL-53 as test system. The validity of this approach was further confirmed for a diverse set of Al-MOFs, namely X-MIL-53 (X = OH, CH<sub>3</sub>O, Br, NO<sub>2</sub>), CAU-10, MIL-69, and Al(OH)ndc (ndc = 1,4-naphthalenedicarboxylate), highlighting the potential benefits of extending the use of this versatile modulator to other coordination materials.

In **Chapter 4**, a different modulation approach, namely pH modulation, was used to obtain large single crystals of Co-based pillared MOFs. These were found to possess an intriguing and unusual optical property: dichromatic dichroism, where different portions of the visible light spectrum are absorbed depending on the relative orientation of the light's polarization plane and the crystal. The pillared structure of these MOFs is such that all Co dimers, known as paddlewheel clusters, are oriented along the long axis of the crystal. Single-crystal UV-Vis absorption measurements showed that when the polarization direction is parallel to this axis, a strong absorption of yellow and red regions of the spectrum occurs, resulting in the transmission of mainly blue light. At 90°, said absorption disappears, and the absorption of blue light at 450 nm dominates, producing a yellow appearance. This dichromatic effect stands out from most conventional dichroic molecular materials, which usually rely on absorption of a single color, resulting in only a change in transparency upon changing the polarization of incident light. The results presented here are the first example of dichromatic dichroism being an intrinsic material property. This strategy can be used to produce versatile dichroic materials active in other ranges of the electromagnetic spectrum, provided that the linker (or linkers), the inorganic building units, and therefore the topology, are selected accordingly.

# Samenvatting

Metaal-organische roosters (Engels: *metal-organic frameworks*, MOFs) zijn geordende reeksen van polytopische organische liganden, gewoonlijk linkers genoemd, die op metaalionen gebaseerde anorganische bouwstenen verbinden via coördinatiebindingen. De zeer nauwkeurige aaneenschakeling van goed gedefinieerde bouwstenen tot uitgebreide 3D-netwerken, bekend als *reticulaire chemie*, heeft het voor onderzoekers in dit veld mogelijk gemaakt om tienduizenden verschillende roosters te produceren. Als vanzelfsprekend gevolg van hun ongekende porositeit en afstembaarheid, worden deze veelzijdige materialen voortdurend onderzocht met het oog op verschillende mogelijke toepassingen. Een belangrijk deel van MOF-onderzoek betreft de interactie tussen geadsorbeerde moleculen en het rooster, gericht op toepassingen zoals gasopslag en -scheiding, evenals katalyse, medicijnafgifte, warmtewisseling en wateroogsten in droge gebieden.

MOFs worden beschouwd als zachte of flexibele materialen, een kenmerk dat structurele dynamica of vervormingen met grote amplitudes omvat. Deze flexibiliteit kan meestal worden toegeschreven aan de topologie van het rooster en de vrijheidsgraden van sommige van zijn bindingen. De linkers zelf kunnen echter ook vrijheidsgraden hebben die onafhankelijke moleculaire dynamica mogelijk maken, in het bijzonder in de vorm van rotatie. Dit type dynamica komt vaak voor in MOFs omdat hun poreuze architecturen vaak voldoende ruimte bieden om rotatie van een moleculair fragment te laten plaatsvinden. Het is dit soort dynamiek waar dit proefschrift zich op richt, uitgaande van het feit dat, hoewel het een intrigerend, vaak voorkomend fenomeen is in MOFs, het relatief onontgonnen is gebleven.

Desalniettemin is de afgelopen vier jaar de belangstelling van onderzoekers voor rotatiedynamica in MOFs toegenomen. Dit kan toegeschreven worden aan twee hoofdredenen: ten eerste worden de eigenschappen van MOFs beïnvloed door linker-rotatie, niet alleen als er interacties met gastmoleculen bij betrokken zijn, maar ook wat betreft optische en mechanische eigenschappen. Ontwikkeling van onze kennis over de rotatie van linkers is daarom essentieel voor een vollediger begrip van de eigenschappen van deze materialen en hoe ze kunnen worden aangepast om een specifiek kenmerk te versterken. Ten tweede zou de exploitatie van de rotatievrijheid van linkers mogelijk kunnen leiden tot belangrijke technologische vooruitgang. Dit laatste omvat verschillende innovatieve ideeën, zoals het ontwerp van ferro-elektrische MOFs met aanstuurbare dipolaire rotoren, of de realisatie van kristallijne moleculaire machines die nuttige arbeid kunnen leveren.

**Hoofdstuk 1** is een inleiding tot de literatuur over de rotatiedynamica van linkers, waarin de verschillende soorten rotatie die zijn aangetoond worden behandeld, met daarnaast een overzicht van de gebruikte technieken en de toepassingen waar het onderzoek op is gericht. De dynamica van roterende linkers in MOFs kan worden onderverdeeld in vier types op basis van geometrische en energetische beschouwingen. Uit de hoeveelheid werk die over dit onderwerp is gepubliceerd, is het duidelijk dat rotatiebewegingen normaal zijn in MOFs, met een rijke diversiteit aan rotatiemechanismen, evenals complexe wisselwerkingen tussen het rotorraamwerk en

gastmoleculen. De elektronische configuratie van de rotor en de sterische omgeving binnen het raamwerk zijn de twee belangrijkste factoren die de torsiepotentiaal bepalen, en ze zijn daarom belangrijke parameters bij het ontwerp van rotor-MOF-systemen. Rotatiebewegingen kunnen een drastische impact hebben op hun eigenschappen en op hun prestaties in verschillende toepassingen. Tot nu toe heeft onderzoek voornamelijk de eigenschappen geanalyseerd die voortvloeien uit rotatie, maar verwacht wordt dat de benutting van rotatie als een waardevolle ontwerpfactor van functionele nanomaterialen zal groeien.

Uit de literatuur blijkt dat vaste-stof  $^2\text{H}$ -NMR de meest prominente experimentele techniek is in de studie van linker-rotatie, vanwege zijn specificiteit en relatief gemakkelijke interpretatie. Het is met succes gebruikt om rotatiestappen, -snelheden en -barrières van talrijke en vaak uiteenlopende MOFs te bepalen. Andere methoden, zoals  $^1\text{H}$ -NMR spin-roosterrelaxatie, diëlektrische spectroscopie en THz-spectroscopie, worden steeds gebruikelijker, maar moeten wellicht verder worden ontwikkeld en/of gecombineerd worden met ondersteunende technieken om meerduidigheid te voorkomen. Moleculaire modelleringstechnieken kunnen ook gebruikt worden om informatie te verschaffen over de dynamische aard van de roosters.

Om de rotatie van de linker volledig te benutten moet gecorreleerde linkerdynamica ontwikkeld worden om hun coöperatieve functionele beweging te realiseren. Linkers in MOFs worden van elkaar gescheiden door afstembare vrije ruimte, en door deze ruimte aan te passen kan een grote verscheidenheid aan dynamisch gedrag ontstaan. In **Hoofdstuk 2** bespreek ik de ingewikkelde effecten van linkerfunctionalisatie op hun dynamisch gedrag in een familie van MOFs die sterische interacties tussen linkers mogelijk maakt. Het werk dat in dit hoofdstuk wordt gepresenteerd betreft de MIL-53-familie, die een gunstige kleine afstand tussen zijn linkers heeft. De functionalisering van de roterende fenyleengroepen maakt het mogelijk om de sterische omgeving van de rotors te variëren, waardoor de linker-rotatie verschuift van volledig statisch naar snelle bewegingen met frequenties boven 100 MHz, zoals gemeten door middel van vaste-stof  $^2\text{H}$ -NMR-spectroscopie. Als een grotere nitrogroep op de rotoren wordt geplaatst beginnen sterische interacties hun onafhankelijke beweging te onderdrukken en ontstaat er een complexer dynamisch gedrag. Door vaste-stof  $^2\text{H}$ -NMR en breedband diëlektrische spectroscopie te combineren met DFT en *ab initio* moleculaire dynamica, werd gecorreleerde rotatie tussen linkers bevestigd. Deze bevindingen banen de weg voor functiespecifieke ontwikkeling van tandwielachtige coöperatieve beweging in MOFs.

Doorgaand naar een meer algemeen territorium in het tweede deel van het proefschrift, behandelen de volgende twee hoofdstukken de noodzaak van grote éénkristallen in MOF-onderzoek. Een nog gedetailleerder begrip van een MOF-structuur, inclusief de dynamiek ervan, zou kunnen worden verkregen als er grote MOF-éénkristallen beschikbaar zijn. Verschillende belangrijke karakteriseringstechnieken worden dan toepasbaar. Misschien wel de meest fundamentele is éénkristal XRD, waarmee we in hoge resolutie de gemiddelde periodieke structuur van een raamwerk kunnen verkrijgen, en in sommige gevallen zelfs meer lokale structurele details kunnen onthullen, zoals gecorreleerde defecten of andere soorten domeinen.

**Hoofdstuk 3** presenteert een nieuwe synthesesmodulatiebenadering die is ontwikkeld voor grote éénkristallen van aluminium MOFs, die notoir moeilijk te verkrijgen zijn. Typische MOF-

synthesemodulatiemethoden zijn gebaseerd op de toevoeging van een molecuul (modulator) dat dezelfde coördinerende groep als de linker bezit, maar slechts één hiervan (bekend als *capping agent*). Op deze manier concurreren modulator- en linkerliganden tijdens MOF-vorming en groei, wat de reactiesnelheid vermindert en in sommige gevallen leidt tot een toename van de kristalgrootte. De compatibiliteit van de modulator zorgt er echter voor dat bepaalde hoeveelheden ontbrekende-linkerdefecten worden gevormd wanneer de modulator niet wordt vervangen door een linker.

In tegenstelling hiermee is onze nieuwe methode gebaseerd op een ligand (oxaalzuur) dat niet met dezelfde geometrie coördineert als de linker, waardoor de bovengenoemde valkuil wordt omzeild. Oxaalzuur vormt stabiele chelaten met  $\text{Al}^{3+}$  in oplossing, wat de kiemvorming en groeisnelheid verlaagt, maar geen invloed heeft op de structuur van het eindproduct. Een vergelijkende studie van deze methode en de reeds gevestigde modulatie door fluorwaterstof werd uitgevoerd met MIL-53 als testsysteem. De validiteit van deze benadering werd verder bevestigd voor een reeks uiteenlopende Al-MOFs, namelijk X-MIL-53 ( $X = \text{OH}, \text{CH}_3\text{O}, \text{Br}, \text{NO}_2$ ), CAU-10, MIL-69 en  $\text{Al}(\text{OH})\text{ndc}$  ( $\text{ndc} = 1,4\text{-naftaleendicarboxylaats}$ ), wat de potentiële voordelen benadrukt van het gebruik van deze veelzijdige modulator voor andere coördinatie-materialen.

In **Hoofdstuk 4** werd een andere modulatiebenadering gebruikt, namelijk pH modulatie, om grote éénkristallen van Co-gebaseerde 'pilaar'-MOFs te verkrijgen. Deze bleken een intrigerende en ongebruikelijke optische eigenschap te bezitten: dichromatisch dichroïsme, waarbij verschillende delen van het zichtbare lichtspectrum worden geabsorbeerd afhankelijk van de oriëntatie van het polarisatievlak van het licht ten opzichte van het kristal. De pilarenstructuur van deze MOFs is zodanig dat alle Co-dimeren georiënteerd zijn langs de lange as van het kristal. Monokristallijne UV-Vis absorptiemetingen toonden aan dat wanneer de polarisatie-richting parallel is aan deze as, er een sterke absorptie van gele en rode gebieden van het spectrum optreedt, wat resulteert in de transmissie van voornamelijk blauw licht. Bij  $90^\circ$  verdwijnt deze absorptie en domineert de absorptie van blauw licht bij 450 nm, waardoor een geel uiterlijk ontstaat. Dit dichromatische effect onderscheidt zich van de meeste conventionele dichroïsche moleculaire materialen, die meestal afhankelijk zijn van absorptie van een enkele kleur, wat alleen resulteert in een verandering in transparantie bij verandering van de polarisatie van invallend licht. De hier gepresenteerde resultaten zijn het eerste voorbeeld van dichromatisch dichroïsme als intrinsieke materiaaleigenschap. Deze strategie kan worden gebruikt om veelzijdige dichroïsche materialen te produceren die actief zijn in verschillende gebieden van het elektromagnetische spectrum, op voorwaarde dat overeenkomstige anorganische bouweenheden, de linker (of linkers), en daarmee de topologie worden geselecteerd.

# Outlook

Even though rotational dynamics are fairly prevalent in MOFs, their impact is often understated or entirely overlooked. Other emerging families of related microporous materials, like porous organic frameworks (POFs) and porous organic cages are expected to exhibit similar behavior. So far, research has primarily analyzed the properties that derive from rotation, but we should expect to see progress in the exploitation of rotation as a valuable design factor in functional nanomaterials. In particular, more explicit cases of modulation of gas adsorption based on tunable rotational dynamics can be forecast, as the interplay between these two phenomena is becoming better understood.

In addition, the exploitation of the rotation-related conformational degrees of freedom of linkers is a goal in the mind of many research groups. An interesting example of this is the control of pore accessibility by external stimuli-responsive linker rotation. In the case of electric field stimulus to a dipolar linker, the result could be electrically controllable gates for gas diffusion, aiming for externally switchable gas separation or storage. Another milestone in the electric field control of rotor linker orientation are ferroelectric MOFs, where stable, ordered, and reversible dipole orientations are needed in order to achieve a macroscopic polarization of the crystal. Other types of materials have demonstrated a similar effect based on rotating units within the crystalline structure, although to date there is no definitive proof of this type of ferroelectric mechanism in MOFs.<sup>1-3</sup>

For MOFs to be successfully developed as artificial nanomachine systems<sup>4,5</sup> that can produce useful work based on their linker dynamics, coherent motion of these units needs to be attained.<sup>6,7</sup> One recent demonstration of ordered linker motion is the light-driven unidirectional rotation of side groups.<sup>8</sup> Although using molecular rotors as linkers in MOFs already solves the need for well-defined spatial arrangement, and in fact bypasses the challenges of crystallization in conventional molecular crystals, the proper structure needs to be selected in order to achieve any meaningful inter-rotor communication.<sup>5</sup> An additional factor that has been highlighted recently in the context of rotor-enhanced diffusion through a pore is the relation between the pore and the rotor's sizes.<sup>9</sup>

The work presented in Chapter 2 is particularly exciting in this context, because it suggests that simple steric interactions between linkers may be a means of introducing complex cooperative rotation in an otherwise simple framework. At a first glance, this might be as simple as finding an appropriate ratio between rotor diameter and rotor spacing.

Regardless of the great versatility available in MOF design, the field still faces many challenges related to developing or adapting the appropriate experimental techniques in the study and applications of linker rotation. An important but not often discussed limitation is crystal size. The approach to growth modulation presented in Chapter 3 differs fundamentally from the more conventional method used in MOFs, namely capping agent modulation. Capping agents have only been shown to increase crystal sizes moderately, and are often accompanied by the introduction of missing linker defects. The chelating approach manages to avoid defect formation because the

agent's coordination mode is not compatible with those found in most frameworks. This method should be further developed for frameworks with other topologies and metal ions. In most cases appropriate chelating agents (*i.e.*, stable complex but not compatible with framework incorporation) are likely already known, and most of the work would need to be focused into the optimization of reaction conditions.

The dichroic properties of the Co-DMOF presented in Chapter 4 are an intriguing addition to the field of dichroic materials, especially when comparing the visible light ranges involved (*i.e.*, transmission of blue or yellow light, meaning this is a dichromatic property). Organic dichroic crystals seem to only present a single color variation, and the only dichromatic dichroic materials currently known are based on nanosurface patterning (*i.e.*, metamaterials). MOF dichroism could potentially lead to improved properties, especially considering the further opportunities for tuning the property, which may also be beneficial in the fabrication of color filters and optical data storage devices.<sup>10,11</sup> For example, the use of a chromophoric linker would add another range of light absorption, as well as the inclusion of dyes inside the pores, as long as the constrained pore space ensures anisotropic alignment of the guest molecules.

## References

1. Akutagawa, T., Koshinaka, H., Sato, D., Takeda, S., Noro, S.-I., Takahashi, H., Kumai, R., Tokura, Y. & Nakamura, T. Ferroelectricity and polarity control in solid-state flip-flop supramolecular rotators. *Nat. Mater.* **8**, 342–347 (2009).
2. Fu, D.-W., Zhang, W., Cai, H.-L., Zhang, Y., Ge, J.-Z., Xiong, R.-G. & Huang, S. D. Supramolecular Bola-Like Ferroelectric: 4-Methoxyanilinium Tetrafluoroborate-18-crown-6. *J. Am. Chem. Soc.* **133**, 12780–12786 (2011).
3. Liao, W.-Q., Zhang, Y., Hu, C.-L., Mao, J.-G., Ye, H.-Y., Li, P.-F., Huang, S. D. & Xiong, R.-G. A lead-halide perovskite molecular ferroelectric semiconductor. *Nat. Commun.* **6**, 7338 (2015).
4. Browne, W. R. & Feringa, B. L. Making molecular machines work. *Nat. Nanotechnol.* **1**, 25–35 (2006).
5. Aprahamian, I. The Future of Molecular Machines. *ACS Cent. Sci.* **6**, 347–358 (2020).
6. Kottas, G. S., Clarke, L. I., Horinek, D. & Michl, J. Artificial Molecular Rotors. *Chem. Rev.* **105**, 1281–1376 (2005).
7. Vogelsberg, C. S. & Garcia-Garibay, M. A. Crystalline molecular machines: function, phase order, dimensionality, and composition. *Chem. Soc. Rev.* **41**, 1892–1910 (2012).
8. Danowski, W., van Leeuwen, T., Abdolazadeh, S., Roke, D., Browne, W. R., Wezenberg, S. J. & Feringa, B. L. Unidirectional rotary motion in a metal–organic framework. *Nat. Nanotechnol.* **14**, 488–494 (2019).
9. Evans, J. D., Krause, S. & Feringa, B. L. Cooperative and synchronized rotation in motorized porous frameworks: impact on local and global transport properties of confined fluids. *Faraday Discuss.* **225**, 286–300 (2021).
10. Ellenbogen, T., Seo, K. & Crozier, K. B. Chromatic Plasmonic Polarizers for Active Visible Color Filtering and Polarimetry. *Nano Lett.* **12**, 1026–1031 (2012).
11. Jung, Y., Jung, H., Choi, H. & Lee, H. Polarization Selective Color Filter Based on Plasmonic Nanograting Embedded Etalon Structures. *Nano Lett.* **20**, 6344–6350 (2020).

# Acknowledgements

## Supervisors

I thank Monique for her supervision, support, understanding, ideas, and enthusiasm on this project. Freek, thanks for taking the role of promotor and for your input towards the final version of this thesis. Having a more external point of view was very useful.

## Unofficial mentors

The following people were key in helping me tackle some crucial knowledge needed for this thesis. Sonia (organic chemistry, spectroscopy, and all kinds of much needed PhD advice), Stefano (crystallography, large crystal synthesis, crystal whispering, crystal management, and even crystal surgery), Han (all types of synthetic chemistry tricks and Python help, and lots of patience in dealing with us non-chemists), FX (a welcoming research stay in Paris, advice and supervision on all computational-MOF-related things – and Romain for his initial support and introduction to DFT).

## Collaborators

Many thanks to all the people who actively collaborated in this project, many of whom are coauthors of the resulting papers. Special thanks to the researchers who directly contributed to some of the most important work presented in this thesis: FX (supervision of DFT and MD work), Mantas (BDS experiments and always interesting discussions), Rob Schurko ( $^2\text{H}$  NMR), Pim (ferroelectric materials advice), Stefano (XRD and crystal growth), and Srinidhi (MD simulations).

## General support

Management support from Caroline and Els is greatly appreciated. Technical support from Bart, Willy, Liliana, Ben, Stephen, Jos, Reiner, and Ruben was essential to the successful completion of all the experimental work I did in the department.

## Group

Thanks to all the members of the CE group, for discussions, ideas, and help around the lab. Special mention to Eduardo for his great efforts to sustain group social activities among all the members of CE. Thanks to the members who have taken up the challenge of organizing socially distant yet really fun activities for the past year. Thanks to Monique's team for all the help, brainstorming, and especially for all the nice time we spent together. I thank also all the students who participated in this project: Aron, Daniëlle, Anthony, Martin, Ruben, Chaitanya, Mari, Marc, Matthijs, Rei, and Jeannet. Thank you for your interest in the project, and for your effort.

# List of publications

## Peer-reviewed papers:

A. Gonzalez-Nelson, S. Mula, M. Šimėnas, S. Balčiūnas, A.R. Altenhof, C.S. Vojvodin, S. Canossa, J. Banys, R. W. Schurko, F.-X. Coudert, and M.A. van der Veen, Emergence of coupled rotor dynamics in metal–organic frameworks via tuned steric interactions, in review for *J. Am. Chem. Soc.* (2021)

A. Gonzalez-Nelson, C. Joglekar, and M.A. van der Veen, Pillared cobalt metal–organic frameworks act as chromatic polarizers, *Chemical Communications* **57**, 1022–1025 (2021)

S. Canossa, A. Gonzalez-Nelson, L. Shupletsov, M. Martin, and M.A. Van der Veen, Overcoming Crystallinity Limitations of Aluminium Metal–Organic Frameworks by Oxalic Acid Modulated Synthesis, *Chemistry - A European Journal* **26**, 3564–3570 (2020)

M. Šimėnas, S. Balčiūnas, A. Gonzalez-Nelson, M. Kinka, M. Ptak, M.A. van der Veen, M. Mączka, and J. Banys, Preparation and Dielectric Characterization of P(VDF–TrFE) Copolymer-Based Composites Containing Metal–Formate Frameworks, *J. Phys. Chem. C* **123**, 16380–16387 (2019)

A. Gonzalez-Nelson, F.-X. Coudert, and M.A. van der Veen, Rotational Dynamics of Linkers in Metal–Organic Frameworks, *Nanomaterials* **9**, 330 (2019)

J.G. Santaclara, A.I. Olivos-Suarez, A. Gonzalez-Nelson, D. Osadchii, M.A. Nasalevich, M.A. van der Veen, F. Kapteijn, A.M. Sheveleva, S.L. Veber, M.V. Fedin, A.T. Murray, C.H. Hendon, A. Walsh, and J. Gascon, Revisiting the Incorporation of Ti(IV) in UiO-type Metal–Organic Frameworks: Metal Exchange versus Grafting and Their Implications on Photocatalysis, *Chem. Mater.* **29**, 8963–8967 (2017)

## Poster presentations:

A. Gonzalez-Nelson, S. Balciunas, M. Simenas, A. Altenhof, C. Vojvodin, R. Schurko, J. Banys, F.-X. Coudert, and M.A. van der Veen, Tunable Polar Linker Dynamics in Metal–Organic Frameworks, 32<sup>nd</sup> European Crystallographic Meeting, Vienna, Austria, 2019

A. Gonzalez-Nelson, F.-X. Coudert, and M.A. van der Veen, Understanding rotational energy barriers of polar linkers, MOFSIM2019, Ghent, Belgium, 2019

A. Gonzalez-Nelson, S. Canossa, M. Martin-Asensio, L. Shupletsov, and M.A. van der Veen, A Versatile Coordination Modulator for the Growth of Aluminum MOFs, 1<sup>st</sup> MOFSchool, Como, Italy, 2019

A. Gonzalez-Nelson, M.A. van der Veen, Rotational dynamics of functionalized linkers in MIL-53(Al), EuroMOF2019, Paris, France, 2019

A. Gonzalez-Nelson, P. Groen, F. Kapteijn, and M.A. van der Veen, Dynamics of metal-organic frameworks: polar linker rotation and the influence of guest molecules, Gordon Research Conference on Crystal Engineering, NH, USA, 2018

A. Gonzalez-Nelson, P. Groen, F. Kapteijn, and M.A. van der Veen, Intraframework dynamics of MOFs: how fast do polar linkers rotate?, EuroMOF2017, Delft, The Netherlands, 2017